THESE EN CO-TUTELLE

entre l'Université de Lyon délivrée par l'Ecole Centrale de Lyon (France)
et l'Université Taras Chevchenko de Kyiv (Ukraine)

Spécialité : Physique et Science des matériaux

Soutenue publiquement le 22 Juin 2011

par

M. Maksym Iazykov

Préparée aux Laboratoires: Institut des Nanotechnologies de Lyon
et Institute of High Technologies Taras Shevchenko National University of Kyiv

Titre:

Growth of pentacene on parylene and on BCB for organic transistors application, and DNA-based nanostructures studied by Amplitude –Modulation Atomic Force Microscopy in air and in liquids

Ecole doctorale Matériaux de Lyon

Composition du jury:

Mme Cendrine MOSKALENKO	en qualité de Rapporteur
M. Philippe LECLERE	en qualité de Rapporteur
M. Jacques TARDY	en qualité d'Examinateur
M. Jean Paul RIEU	en qualité d'Examinateur
M. Valeriy SKRYSHEVSKIY	en qualité de co-Directeur de thèse
Mme Magali PHANER-GOUTORBE	en qualité de co-Directrice de thèse

UNIVERSITÉ DE LYON

Liste des personnes Habilitées à Diriger des Recherches en poste à l'Ecole Centrale de Lyon

Nom-Prénom	Corps grade	Laboratoire ou à défaut département ECL	Etablissement
AURIOL Philippe	professeur	AMPERE	ECL
BEROUAL Abderrahmane	professeur	AMPERE	ECL
BURET François	professeur	AMPERE	ECL
JAFFREZIC-RENAULT Nicole	directeur de recherche	AMPERE	CNRS/ECL
KRÄHENBÜHL Laurent	directeur de recherche	AMPERE	CNRS/ECL
MARTELET Claude	professeur	AMPERE	ECL
NICOLAS Alain	professeur	AMPERE	ECL
NICOLAS Laurent	directeur de recherche	AMPERE	CNRS/ECL
SCORLETTI Gérard	professeur	AMPERE	ECL
SIMONET Pascal	chargé de recherche	AMPERE	CNRS/ECL
THOMAS Gérard	professeur	AMPERE	ECL
VOLLAIRE Christian	professeur	AMPERE	ECL

Nbre Ampère 12

HELLOUIN Yves	maître de conférences	DER EEA	ECL
LE HELLEY Michel	professeur	DER EEA	ECL

Nbre DER EEA 2

GUIRALDENQ Pierre	professeur émérite	DER STMS	ECL
VINCENT Léo	professeur	DER STMS	ECL

Nbre DER STMS 2

LOHEAC Jean-Pierre	maître de conférences	ICJ	ECL
MAITRE Jean-François	professeur émérite	ICJ	ECL
MARION Martine	professeur	ICJ	ECL
MIRONESCU Elisabeth	professeur	ICJ	ECL
MOUSSAOUI Mohand	professeur	ICJ	ECL
MUSY François	maître de conférences	ICJ	ECL
ZINE Abdel-Malek	maître de conférences	ICJ	ECL

Nbre ICJ 7

DAVID Bertrand	professeur	ICTT	ECL

Nbre ICTT 1

CALLARD Anne-Ségolène	professeur	INL	ECL
CLOAREC Jean-Pierre	maître de conférences	INL	ECL
GAFFIOT Frédéric	professeur	INL	ECL
GAGNAIRE Alain	maître de conférences	INL	ECL
GARRIGUES Michel	directeur de recherche	INL	CNRS/ECL
GENDRY Michel	directeur de recherche	INL	CNRS/ECL
GRENET Geneviève	directeur de recherche	INL	CNRS/ECL
HOLLINGER Guy	directeur de recherche	INL	CNRS/ECL

JOSEPH Jacques	professeur	INL	ECL
KRAWCZYK Stanislas	directeur de recherche	INL	CNRS/ECL
LETARTRE Xavier	chargé de recherche	INL	CNRS/ECL
MARTIN Jean-René	professeur émérite	INL	ECL
O'CONNOR Ian	professeur	INL	ECL
PHANER-GOUTORBE Magali	professeur	INL	ECL
ROBACH Yves	professeur	INL	ECL
SAINT-GIRONS Guillaume	chargé de recherche	INL	CNRS/ECL
SEASSAL Christian	chargé de recherche	INL	CNRS/ECL
SOUTEYRAND Eliane	directeur de recherche	INL	CNRS/ECL
TARDY Jacques	directeur de recherche	INL	CNRS/ECL
VIKTOROVITCH Pierre	directeur de recherche	INL	CNRS/ECL

Nbre INL 20

CHEN Liming	professeur	LIRIS	ECL

Nbre LIRIS 1

BAILLY Christophe	professeur	LMFA	ECL
BERTOGLIO Jean-Pierre	directeur de recherche	LMFA	CNRS/ECL
BLANC-BENON Philippe	directeur de recherche	LMFA	CNRS/ECL
BOGEY Christophe	chargé de recherche	LMFA	CNRS/ECL
CAMBON Claude	directeur de recherche	LMFA	CNRS/ECL
CARRIERE Philippe	chargé de recherche	LMFA	CNRS/ECL
CHAMPOUSSIN J-Claude	professeur émérite	LMFA	ECL
COMTE-BELLOT geneviève	professeur émérite	LMFA	ECL
FERRAND Pascal	directeur de recherche	LMFA	CNRS/ECL
GALLAND Marie-Annick	professeur	LMFA	ECL
GODEFERD Fabien	chargé de recherche	LMFA	CNRS/ECL
GOROKHOVSKI Mikhail	professeur	LMFA	ECL
HENRY Daniel	directeur de recherche	LMFA	CNRS/ECL
JEANDEL Denis	professeur	LMFA	ECL
JUVE Daniel	professeur	LMFA	ECL
LE RIBAULT Catherine	chargée de recherche	LMFA	CNRS/ECL
LEBOEUF Francis	professeur	LMFA	ECL
PERKINS Richard	professeur	LMFA	ECL
ROGER Michel	professeur	LMFA	ECL
SCOTT Julian	professeur	LMFA	ECL
SHAO Liang	chargé de recherche	LMFA	CNRS/ECL
SIMOENS Serge	chargé de recherche	LMFA	CNRS/ECL
TREBINJAC Isabelle	maître de conférences	LMFA	ECL

Nbre LMFA 23

BENAYOUN Stéphane	professeur	LTDS	ECL
CAMBOU Bernard	professeur	LTDS	ECL
COQUILLET Bernard	maître de conférences	LTDS	ECL
DANESCU Alexandre	maître de conférences	LTDS	ECL
FOUVRY Siegfrid	chargé de recherche	LTDS	CNRS/ECL
GEORGES Jean-Marie	professeur émérite	LTDS	ECL
GUERRET Chrystelle	chargé de recherche	LTDS	CNRS/ECL
HERTZ Dominique	past	LTDS	ECL
ICHCHOU Mohamed	professeur	LTDS	ECL
JEZEQUEL Louis	professeur	LTDS	ECL
JUVE Denyse	ingénieur de recherche	LTDS	ECL
KAPSA Philippe	directeur de recherche	LTDS	CNRS/ECL
LE BOT Alain	chargé de recherche	LTDS	CNRS/ECL

LOUBET Jean-Luc	directeur de recherche	LTDS	CNRS/ECL
MARTIN Jean-Michel	professeur	LTDS	ECL
MATHIA Thomas	directeur de recherche	LTDS	CNRS/ECL
MAZUYER Denis	professeur	LTDS	ECL
PERRET-LIAUDET Joël	maître de conférences	LTDS	ECL
SALVIA Michelle	maître de conférences	LTDS	ECL
SIDOROFF François	professeur	LTDS	ECL
SINOU Jean-Jacques	maître de conférences	LTDS	ECL
STREMSDOERFER Guy	professeur	LTDS	ECL
THOUVEREZ Fabrice	professeur	LTDS	ECL
TREHEUX Daniel	professeur	LTDS	ECL
VANNES André-Bernard	professeur émérite	LTDS	ECL
VINCENS Eric	maître de conférences	LTDS	ECL

Nbre LTDS 26

Total HdR ECL	91

Acknowledgments

The present work was carried out in the laboratory Institut des Nanotechnologies de Lyon of Ecole Centrale de Lyon in collaboration with the Institute of High Technologies Taras Shevchenko National University of Kyiv, Ukraine.

I would like to thank my French supervisor Pr. Magali Phaner-Goutorbe and director of our team "Chimie et biotechnologies" Eliane Souteyrand for accepting me in INL for my co-tutorial thesis. I am very grateful for their confidence in me, comprehending, patience and scientific cooperation during this period.

I also thank Pr. Valeriy Skryshevskiy for the proposal of my candidature for this PhD position, for his support and supervising of this work from the part of the Institute of High technologies.

I acknowledge Pr. Jean Paul Rieu for accepting to be a president of the examination panel. I warmly thank DR.Cendrine Moskalenko, Pr. Philippe Leclère, DR. Jacques Tardy for accepting to judge my thesis, for their opinions and comments which helped me to improve a description of the results presented in this manuscript.

I am grateful to Pr.Yves Robach, Dr.Yann Chevolot, MC. Jean-Pierre Cloarec, Pr.François Morvan, MC.Naoufel Haddour, Dr. Abdou Karim Diallo, Pr. Elisabeth Charlaix, IR. Agnes Piednoir for their professional assistance and fruitful collaboration.

I warmly thank Aziz Benamrouche, Pierre Cremillieu, Claude Botella, Brice Devif, Philippe Regreny, Brice Gautier, David Albertini, Armel Descamps-Mandine for their help and technical assistance.

Many thanks to my colleagues and friends with which I passed these three years: Michel Garrigues, Virginie Monnier, Thomas Gehin, Emmanuelle Laurenceau, Isabelle Nabeth, Mariline Diserio, Marie Trévisan, Zing Zhang, Richard Villey, Rémy Beland, Delphine Sicard, Alice Goudot, Zhugen Yang, Ning Sui, Dimitri Charrier.

I also thank Mme. Anne Zucco, Mme. Therèse Martin and Mme. Nicole Durand for their help in my administrative adventures.

I am wery grateful to Ambassade de France, CROUS de Lyon and to Région Rhone-Alpes for financial support, without which this thesis would not be possible.

Particular thanks to the team "Chimie et biotechnologies" in the person of Eliane Souteyrand and Magali Phaner-Goutorbe for their continued assistance in funding of my thesis.

Table of contents

Acronyms

AFM – Atomic Force Microscop

AM-AFM – Amplitude Modulated Atomic Force Microscopy

BB – bottom-contact bottom gate configuration of the field effect transistor

BCB – benzocyclobutene

CVD – chemical vapour deposition

DLG – Diffusion Limited Growth

DLVO – Derjaguin, Landau, Verwey and Overbeek theory

DMT – Derjaguin Muller Toporov theory

DNA – Deoxyribonucleic acid

FM-AFM – Frequency Modulated Atomic Force Microscopy

HEPES – 4-(2-hydroxyethyl)-1-piperazineethanesulfon acid

HOMO – highest occupied molecular orbital

JKR – Johnson-Kendall-Roberts theory

LUMO – lowest occupied molecular orbital

NCM – non contact mode

OFET – organic field effect transistor

OLED – organic light-emitting device

OPVC – organic photovoltaic cell

OTFT – organic thin film transistor

PBS – phosphate buffer solution

PMMA – polymethyl methacrylate

PSD – power spectral density

PVD – physical vapour deposition

PVP – polyvinyl phenol

RMS – root mean square deviation

SEM – scanning electron microscope

SPM – scanning probe microscopy

STM – scanning tunnelling microscope

TB – top-contact bottom gate configuration of the field effect transistor

TM – temperature of melting

Tris – tris(hydroxymethyl)aminomethane

TTF – tetrathiafulvalene

UHV – ultra high vacuum

XRD – x-ray diffraction

General introduction

The emergence of SPM followed the development of the nanotechnologies, for which a direct visualization or manipulation of surfaces and interfaces is essential. Nowadays, SPM techniques go on to be developed because they also offer the ability to obtain local information on the physical, chemical and mechanical properties of isolated nanostructures or surfaces. In comparison to other techniques, SPM and especially atomic force microscopy (AFM) provides extremely high lateral and vertical resolution that puts it out of competition with commonly used the scanning electron microscopy (SEM) and optical microscopy. In addition, AFM offers the opportunity to operate in vacuum, gas or liquid environment that makes it irreplaceable in such domains of applications as physics, biology, chemistry, medicine etc…

A large variety of operation modes makes AFM technique easy adaptable to a wide range of samples under different experimental conditions. Generally, there are no special requirement for sample preparation and they can be scanned in their native environment *in situ*.

Nowadays, many works are devoted to investigations of organic materials which may, in the nearest future, become an alternative to actually widely used inorganic materials in scientific and industrial applications. That's why there are more and more researches devoted to fundamental studies in organic and particularly biological materials with the wide use of ample opportunities of the atomic force microscopy.

This thesis deals with various aspects of the application of AFM, for the characterization of organic semiconductors and DNA-based arrays, as promising candidates in organic electronics and biological applications. This work includes the question of the theoretical study of the optimal conditions for non-destructive investigation of such samples in different environments. For this reason, we used the versatility of the AFM technique to explore the regime of the tip-surface interaction by controlling the dynamics of the dissipative processes, during scanning, on one example of a DNA chip. Moreover, we propose to use the AFM contact spectroscopy as an alternative method for the local study of the surface energy of organic thin films. Added to advanced methods of statistical image analysis, in reciprocal Fourier space, it provides an exhaustive description not only of the accessible surface of the sample but also of its inner structural properties.

The particular design of the experimental liquid cell of our AFM makes it possible to perform a comparative study of the molecular assembling of DNA-based macromolecules in air and liquid media. This allows to compare the theoretically expected and experimentally observed results under controllable conditions at the molecular scale.

This memory is organized in the following manner:

In the first chapter we give a general introduction to Atomic Force Microscopy. The description of the principle together with a close look at the different operation modes allow to explain the physics of the processes responsible of the high accuracy and versatility of the AFM.

In this chapter, it is also discussed on the different forces which inevitably involved in the imaging process and in a large extent, which are responsible for the image contrast. A peculiar attention is also given

to specificities of working in gas and liquid environments. Their respective advantages and fundamental limitations are also reviewed.

A particular attention is focused on the practical application of the dynamic phase and amplitude spectroscopy. It provides a quantitative description of dissipative processes during AFM mapping and allows to prevent damages of fragile biological materials. For this purpose, a specific study of the AFM parameters is presented on a DNA chip substrate.

Finally, an alternative method of statistical image analysis is described, which gives a more complete description of the surface in comparison with the conventional method of analysis.

In the <u>second chapter</u>, we focus on the AFM study of the pentacene which is the most promising organic semiconductors among other organic compounds. In this chapter, we explain the structure an electronic properties of the pentacene, and then we perform the AFM study of the thickness-driven pentacene growth on two polymeric substrates, parylene and benzocyclobutene (BCB). Therefore, we discuss the morphology of the pentacene thin films by means of conventional methods of analysis which showed a nonlinear dependence of the pentacene grain sizes on the equivalent film thickness. Then, we perform the measurement of the pentacene surface energy in alternative to the drop sessile method, by the contact mode AFM spectroscopy.

In this chapter, we also describe a power density method (PSD) to analyse obtained pentacene morphologies. Based on the transformation of AFM image in 2D reciprocal Fourier space represented as 1D graph (PSD curve) we show that an appropriate analysis of the experimental PSD curves together with determined pentacene surface energy, provides a complete description of both surface properties and the properties of the sample as a whole.

Therefore, we propose the model of the pentacene growth, upon which the electrical performances of an experimental pentacene-based organic field effect transistor (OFET) are discussed.

In the last <u>third chapter</u> we focus on the study of the possible assembling of DNA-based X1+X2, Y1+Y2 and X1+20 bases molecules. First of all, we discuss their hybridization and thermal stability by measuring experimentally the melting temperatures (TM) and comparing them with theoretically calculated values. Then, theoretically possible assembling of X1+X2, Y1+Y2 and X1+20bases molecules is also reviewed. Therefore, we describe AFM imaging of DNA-based samples deposited on chemically modified and non modified muscovite mica surface in air and in two liquids: Tris and HEPES. For AFM imaging in liquid, the goal was to study the influence of the ionic strength of both solutions on the molecular assembling and compare it with the molecular assembling in air. An interpretation was proposed.

In addition, there are also three annexes which complement this manuscript. Annexe I is used in the second chapter and gives explanation of surface energy measurements with the drop sessile technique. Annexes II and III refer to the third chapter. Annexe II describes in detail the scheme of chemical synthesis of X1+X2, Y1+Y2 and X1+20bases molecules and gives their structural formulas. Annexe III provides an explanation of methods used for deducting of convolution effect of the AFM tip with a DNA molecule.

Chapter I

Atomic Force Microscopy

I - Introduction

I-1 Scanning probe microscopies among microscopies

Scanning probe microscopy (SPM) includes a large family of microscopy techniques for the characterisation of surfaces at the micro and nano scale. The emergence of SPM followed the development of the nanotechnologies, for which a direct visualization or manipulation of surfaces or interfaces, at high resolution, is essential. Nowadays, SPM techniques go on to be developed because they also offer the ability to obtain local information on the physical chemical and mechanical properties of isolated nanostructures or surfaces.

Before SPM, there were two means to observe surfaces or interfaces: with the optical microscope and its derivatives (confocal, fluorescent, phase microscopes) and the electronic microscope, specifically the scanning electron microscope (SEM) for surface observation.

Optical microscopes present the advantage of a surface observation, in environmental media, air or liquids, on any surfaces provided that it is not totally transparent, (chemical and fluorescent dye are used to colour surface) [1]. However, the resolution of such microscopes is limited by the Rayleigh criteria to half the wave-length and then to hundreds nanometers.

The SEM microscope uses an electron beam to probe the surface, this allows to reach subnanometric wave length and then a high resolution (de Broglie theory). However, due to aberration in the electrostatic lens system, the better value reached today is of 0.4nm [2]. This technique has a great field depth and is really appropriate to study nanostructures.

However, a vacuum environment is necessary due to the small electron mean path and only conductive or semiconductive surfaces can be imaged because secondary electrons are emitted from the surface. Isolated surface must be previously prepared, recovered by a conductive layer. These limitations make it difficult to image biological systems in their physiological environment. One should notice that progress have been made and environmental SEM exists today [3].

In comparison to these microscopies, SPM and especially atomic force microscopy (AFM) offers the opportunity to observe surfaces in air and liquid environment such as an optical microscopy, with a high-resolution similar to the one of the electron microscopy (SEM).

Figure I-1 shows the principal characteristics of these different microscopical methods.
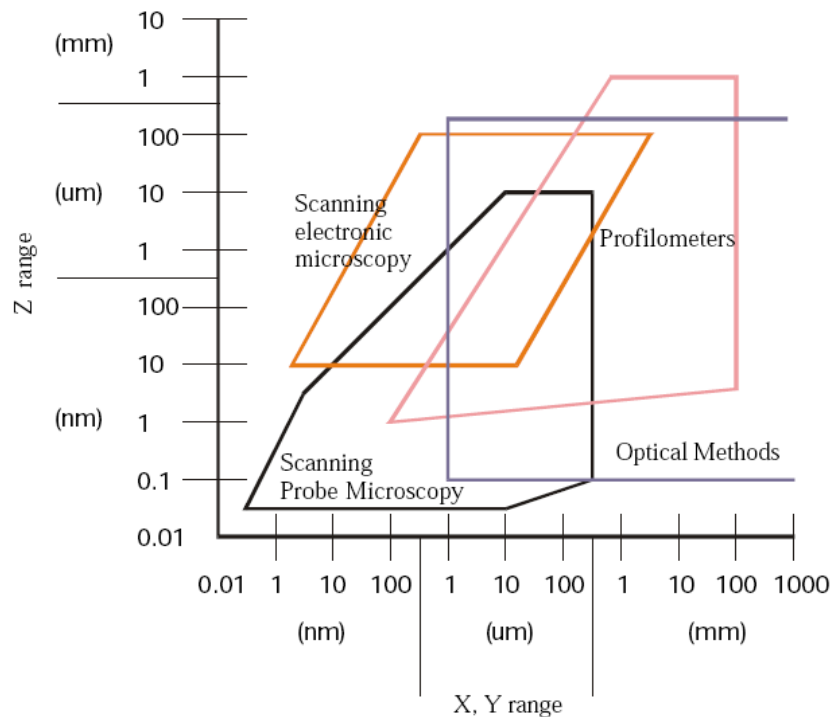
Figure I-1. Comparison of most popular microscopical techniques [4]

The fundamental principle of all scanning probe microscopes is to observe the so called *near- field interactions* that occur between a sharp tip and the surface of a sample. To form an image the tip with a curvature radius of few nanometres is swept across the surface, line by line, making a map of the interactions. During this scanning process, tunnelling current, interaction forces, electromagnetic waves or thermal flux can be monitored and directly used for the surface characterization. Since the invention of the first scanning tunnelling microscope (STM) by Gerd Binnig and Heinrich Rohrer [5], in 1982, SPM techniques were widely popularized and the number of investigations devoted to technical advances and applications has increased rapidly. Now, SPM instruments are commonly used in science of physics, chemistry, biology and related disciplines. This group of microscopies demonstrates the ability to perform experiments in vacuum, air and liquid in the range of temperatures from 4K to over 700K and the diverse range of phenomena can be studied including surface topography, measurements of adhesion and strength of individual chemical bonds, friction, electronic and vibrational properties, electric and magnetic properties, molecular manipulation, and many other phenomena from the micrometer down to the subnanometer scale.

I-2 History of the Atomic Force Microscopy

I-2-1 From stylus profilometer to STM

The operation principle of all SPMs is quite similar. This fact can be explained by a common archetypal instrument which has become an enabling tool for developing modern methods of SPM family. It is useful to follow the development of scanning probe microscopy by the beginning from the first prototypes to clearly understand the background of SPM techniques.

Visualizing the morphology of a surface using a scanning probe is an old idea. In 1929, Schmaltz already invented the Stylus Profilometer [6]. This instrument had lot in common with the modern atomic force microscope (AFM) and can be mentioned as its first prototype. The operation principle was based on the detection of a light beam reflected on a moving probe. The probe was carefully brought into contact with a surface and moved across it. The projection of the light beam reflected by the probe was exposed on a photoemulsion. A magnified profile of the surface was obtained by the optical lever system. However, the scanning and detection systems were not enough isolated from external noise that strongly limited the resolution.

The next step in scanning probe methods was realized by Young in 1971 [7, 8] when he created another type of profiler called "Topographiner". This non-contact profiler is considered as the "father" of the scanning tunnelling microscope (STM). It already had implemented feedback loop to keep the working distance constant during the scanning of a conducting tip above a conducting sample. However, when the STM uses the direct tunnelling to feel the proximity of the surface, the topographiner operated in an emission regime. Such operation regime and the unsubstantial protection from acoustical and thermal noise were responsible to a relatively low resolution comparable to the one of the optical microscope.

In addition, Young also performed spectroscopic measurements with his topographiner in direct tunnelling regime. He has already shown that the detected tunnelling current was in strong dependence on the tip-sample separation. However, no stable imaging was obtained under their experimental conditions [7].

The situation drastically changed since the development of the first STM, which was able to realize the surface visualization in direct space, at a true atomic resolution [8, 9], in 1982. This fundamental achievement of G. Binnig and H. Rohrer was honoured by a Nobel prize in Physics in 1986.

Unlike the previous prototypes, the STM could perform image scanning in a direct tunnelling regime by measuring the tunneling current present through the gap between a sharp tip and a conducting sample surface [10, 11]. The exponential dependence of the current on the distance is responsible of the high sensitivity of the instrument to variation in surface topography (actually electronic density of states). For example, a monoatomic step may cause a change in the tunnel current from 2 to 3 orders of magnitude [9]. That is why the question of stability during imaging was crucial. Fortunately, the solution has been found: this first STM was equipped by improved system of noise reduction, which used the effect of magnetic levitation [8]. The exponential decrease of the current towards distance implies that only the extremity of the

tip apex is involved in the interaction. To reach atomic resolution, only one atom at the extremity of the tip contribute to the current and the tip-surface distance, typically of 1nm, should be controlled at less than 1pm. The tip surface distance can be reached thanks to piezoelectric ceramics actuators which allow displacements of tip and sample at a nanometric scale. The stability can be achieved when controlling displacement, external noise and vibration, electromagnetic perturbations and thermal drift. Thus, STM microscopes are placed in a faraday cage, on an anti-vibration table, and in an air-conditioned room. They are also symmetrically designed to compensate thermal drift.

Unfortunately, few surfaces can be directly observed in air because of their oxidization. The presence of a faradic current, typically of 1 μA, makes the measurement more complex in liquids. Nowadays, the STM is dedicated to high resolution studies in UHV [8, 9].

I-2-2 Basis of Atomic force microscope

In 1986, G.Binnig, C.Quate and C.Gerber invented the Atomic Force Microscope (AFM) [12] which made a breakthrough in the world of microscopy. Since then, the AFM was recognized as a powerful and versatile tool for nanometric scale objects characterization. The AFM allows to image the topography of a wide variety of materials, conducting and insulating, hard or smooth with a relative ease.

The AFM principle is based on the interaction of a tip fixed to a microcantilever with a sample. A typical AFM configuration includes a microcantilever, a detection system, a sample positioner and a control system (Figure I-2).
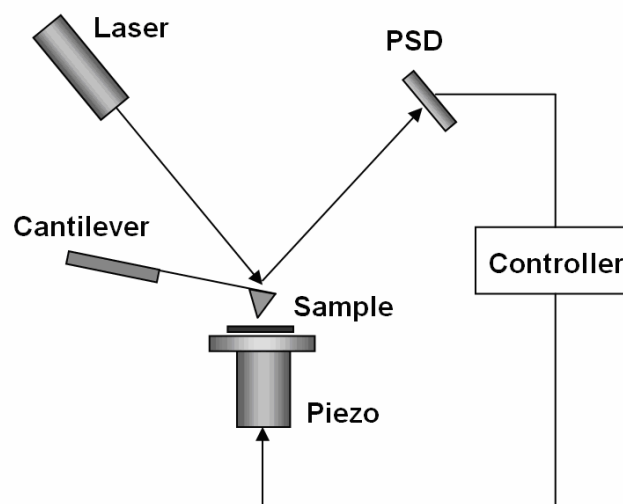

Figure I-2. Schematic representation of the AFM

When the cantilever is close enough to the sample, according to the size of the tip (typical radius are around 10nm), surface forces appear on the nanometric scale. These forces are sufficient to cause a detectable signal in the system of detection. As a measure of the tip-sample interaction, the resonant

frequency or the deflection of the cantilever can be used. In most common cases, the cantilever movement is registered by an optical system which consists of a photodiode array that detects laser beam reflected from the top side of the cantilever. The control system governs the sample position according to the output signal of the photodiode.

An AFM image is obtained by scanning line by line the sample surface. During the scanning, the sample position is adjusted to keep the output signal at the position corresponding to the reference deflection or the reference resonant frequency of the cantilever.

II - The different interaction forces

The tip-sample interaction on which AFM is based involves different forces, attractive and repulsive, and of different intensities. All these forces exhibit different tip surface distance dependence. In external field-free experiments, the dominant forces are van der Waals, chemical forces, short-range repulsive interactions, adhesion and capillary forces.

II-1 Van der Waals force

The van der Waals force is a long-range type force which acts in all media whatever the chemical composition of the surface. This universality is induced by the nature of the van der Waals forces, they are due to the fluctuations of electrical dipole moment between atoms and/or molecules. More precisely, the van der Waals force is the sum of three different forces. Each is proportional to $1/r^6$, where r is the distance between atoms or molecules. Thus, the corresponding total potential is expressed as [13, 14]:

$$U_{VdW} = U_K + U_D + U_L = \left(C_K + C_D + C_L\right)/r^6 \qquad \text{(eq.1.1)}$$

where U_K is the orientation or Keesom potential, U_D is the induction or Debye potential and U_L is the dispersion or London potential, and C_K, C_D, C_L are corresponding constants .

The first and second terms of (eq.1.1) are called Keesom and Debye energies, they manifest only in interaction between atoms or molecules with a permanent or an induced dipole, respectively.
The third term is called the London energy, it manifests between all types of atoms and molecules [15], even the non polar. This London energy mostly contributes to the van der Waals force.

The attractive van der Waals force between atoms is proportional to $1/r^6$, where r is the distance. The empirical potential used to approximate the interaction between a pair of atoms or molecules is the Lennard-Jones potential (Figure I-3) [13]:

$$\phi(r) = -\frac{A}{r^6} + \frac{C}{r^{12}} = 4\varepsilon\left[\left(\frac{\sigma}{r}\right)^{12} - \left(\frac{\sigma}{r}\right)^6\right]; \qquad \sigma = \left(\frac{C}{A}\right)^{1/6}; \quad \varepsilon = \frac{C^2}{4A} \qquad \text{(eq.1.2)}$$

where A is the Hamaker constant, C is the attractive interaction strength.

The empirical constant ε represents the characteristic energy of interaction between molecules, namely the maximum energy of attraction between a pair of molecules. Characteristic diameter of the molecule σ, also called the *collision diameter,* is the distance between two atoms or molecules for $\varphi(r) = 0$. In this expression, only the r^{-6} term, the attractive term corresponds to the van der Waals or dispersive force. The r^{-12} term is the repulsive term and describes the Pauli repulsion at short ranges due to electron orbitals overlapping (Figure I-3):
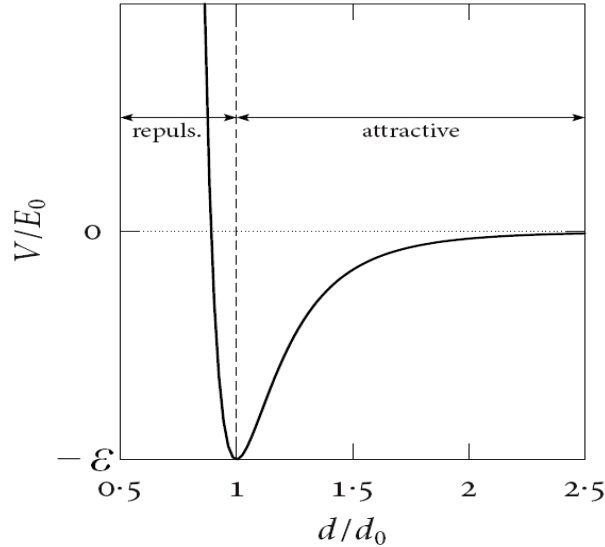
Figure I-3. Lennard-Jones potential with attractive and repulsive parts [13].

Analytical expression for van der Waals force depends on several factors including geometry of interacting surfaces. In AFM, the tip-sample interaction should be considered as an interaction between macroscopic bodies rather than between individual atoms or molecules [13]. In this case, the interacting interface can by approximated by a sphere-plane geometry and the van der Waals force obtained using the Derjaguin's approximation [16] is then expressed as:

$$F_{VdW} = -\frac{AR}{6r^2} \qquad (eq.1.3)$$

where A is the Hamaker constant, R the tip radius and r is the tip-sample separation.

All physico-chemical information about interacting bodies is included in the Hamaker constant which is a measure of the strength of the van der Waals force.

For special applications, other long range forces are considered, electrostatic forces between a conductive tip and sample system and magnetic force between a magnetic tip and surface system. In this work, we do not consider these forces, they lead to specific SPM instruments devoted to the analyse of surface potential, conductance, doping effect or magnetic moment.

II-2 Short-range forces and adhesion

Short-range repulsive forces appear when the separation distance between two objects reaches the magnitude of the interatomic distance. It is the case when they are brought into mechanical contact. Some repulsive forces between molecules or atoms appear due to the Pauli or ionic repulsion. However, for microscopic contact areas consisting of large number of atoms, the effective force can be described without considering Pauli or ionic repulsion. This approach implies that the mechanical contact defo²rms interacting objects and that the deformation depends on the applied load (or force) and on the material properties. Analytical description of the relationship between deformation and applied force is provided by theories of continuum elasticity.

Historically, the first model was proposed by Hertz in 1881 [17]. This model described the deformation without adhesion forces. Other widely used models such as Johnson-Kendall-Roberts (JKR) [18] and Derjaguin-Muller-Toporov (DMT) [19] take into account adhesion inside (JKR) or outside (DMT) the contact area.

In the case of a spherical tip on a flat surface, these three theories give the following relations for the contact radius a, a deformation of the sample δ, an adhesion force F_a, a reduced Young Modulus E_{tot}, a tip radius R and an applied load F. Here W is the thermodynamic work of adhesion.

– according to *Hertz* model:

$$a = \sqrt[3]{\frac{RF}{E_{tot}}} \qquad\qquad \delta = \left(\frac{F^2}{RE_{tot}^2}\right)^{1/3} \qquad\qquad F_{ad} = 0 \qquad\qquad \text{(eq.1.4)}$$

– according to *JKR* model:

$$a = \sqrt[3]{\frac{R}{E_{tot}}(F + 2\pi RW)} \qquad \delta = \frac{(F + 2\pi RW)^{2/3}}{\sqrt[3]{RE_{tot}^2}} \qquad F_{ad} = 2\pi RW \qquad \text{(eq.1.5)}$$

– according to *DMT* model:

$$a = \sqrt[3]{\frac{R}{E_{tot}}\left(F + 3\pi RW + \sqrt{(3\pi RW)^2}\right)} \qquad \delta = \frac{2}{3}\sqrt{\frac{6\pi Wa}{E_{tot}}} \qquad F_{ad} = \frac{3\pi RW}{2} \quad \text{(eq.1.6)}$$

Typically, the Hertz theory can only by applied if the adhesion force F_{ad} is significantly smaller than the maximum applied load F. The JKR model is suitable for describing the contact of soft samples with a large adhesion when a large tip is used. The DMT model can by used for stiff samples with a small adhesion in the case of small tips [20]. Even if these theories are only approximations, they have become standard contact models for AFM studies.

More sophisticated analytical description of the interaction between surfaces has been proposed by Maugis [21]. The contact mechanics of two elastic bodies can be described by the relationship between stress (σ_{ij}) and strain (ε_{ij}) tensors, which for isotropic materials is established by the following equation:

$$\sigma_{ij} = \eta\varepsilon_{ll}\delta_{ij} + G\varepsilon_{ij} \qquad\qquad \text{(eq.1.7)}$$

where η is the Lamé coefficient and G is the shear modulus.

The (eq.1.7), at an equilibrium state, can be parameterized by the elasticity parameter λ, which compares the relative strength of the deformation and the effective range of the surface force:

$$\lambda = \sigma_0\sqrt[3]{\frac{9R}{2\pi WE_{tot}}} \qquad\qquad \text{(eq.1.8)}$$

where σ_0 is the stress at the equilibrium spacing.

As it is shown in the adhesion map of Greenwood and Johnson [22] (Figure I-4), the general solutions can be reduced to the Hertz model for $\lambda=0$, to the DMT model for small λ ($\lambda < 0.1$) and to the JKR model for large λ ($\lambda > 5$).
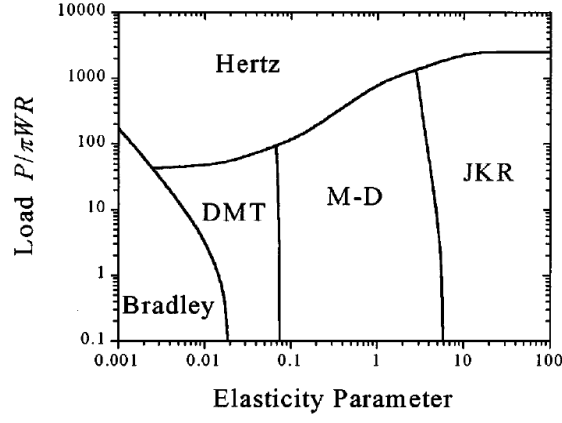
Figure I-4. Adhesion map of Greenwood and Johnson [22]

The Maugis theory, experimentally verified by Lantz et al. [23], settled the dispute between the JKR and DMT models in the 1970s and is now recognized as the general theory fully describing the elastic deformation of samples.

II-3 Capillary forces

Under ambient conditions, in air, a meniscus or liquid bridge may form between tip and sample, due to capillary condensation around the contact (Figure I-5). This meniscus induces an attractive force, dependent on the distance, caused by the pressure difference between the liquid and surrounding vapor phases.
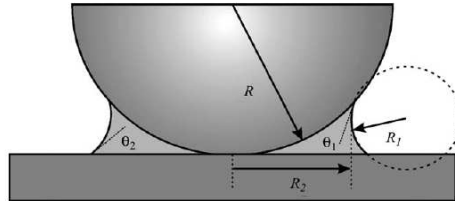
Figure I-5. Schematic of a water meniscus between a plane and a sphere of radius R [4]

The pressure difference is given by the Young-Laplace equation:

$$\Delta P = \gamma \left(\frac{1}{R_1} + \frac{1}{R_2} \right)$$
(eq.1.9)

where γ is the surface tension of the liquid and R_1 and R_2 are the principal radii of curvature of the water meniscus.

The analytical expression of the capillary force F_{cap} between tip and sample of plane-sphere geometry has been developed by O'Brien and Hermann [24]:

$$F_{cap} = 2\pi\gamma\left(\cos\theta_1 + \cos\theta_2\right) \qquad \text{(eq.1.10)}$$

where θ_1 and θ_2 are contact angles between surfaces of tip and sample, and the liquid.

However, (eq.1.10) does not reflect any dependence of the capillary force on the relative humidity. A model including the influence of humidity, of the surface roughness, and also the time in the capillary force expression, was introduced by L. Bocquet and J. L. Barrat [25]:

$$F_{cap}(t) \approx \gamma d \frac{1}{\ln(P_0/P)} \ln\left(\frac{t}{\tau_0}\right) \qquad \text{(eq.1.11)}$$

where d is the effective distance taking into account geometry of the contact, P_0/P is the relative humidity, and τ_0 is a time constant of the order of the condensation time of one liquid layer.

The authors of this model observed good agreements between their experimental results and their theoretical predictions. According to equations (1.10) and (1.11), meniscus forces are expected to increase for hydrophilic surfaces and decrease for hydrophobic surface. This was experimentally observed by many groups [26-29].

The calculations demonstrated that the capillary force is usually more long-ranged than the van der Waals force under moderate humidity conditions as shown in Figure I-6 [30].
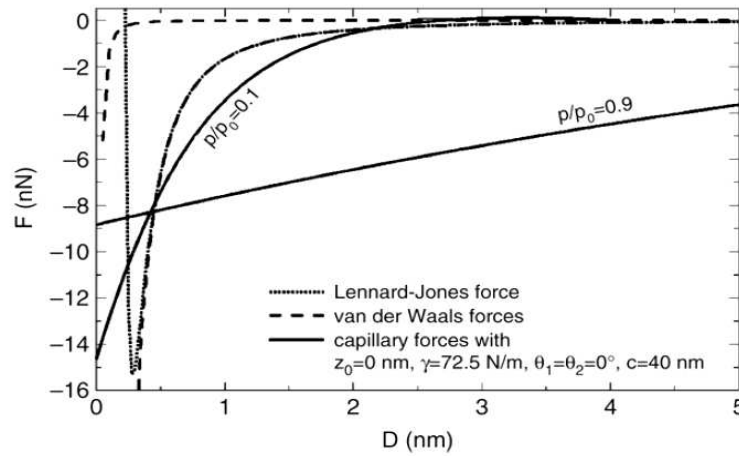
Figure I-6. Comparison of van der Waals and capillary forces at different humidities for an hydrophilic tip with a radius of 20 nm interacting with an hydrophilic flat substrate [30]

The relative contribution of several forces such as van der Waals, capillary and electrostatic forces has been experimentally studied by Ouyang et al. [31]. They performed adhesion measurements of an AFM tip on mica, graphite and MoS_2 surfaces with relative humidity $P_0/P=50\%$ and have found that the capillary force has the largest contribution, in all cases.

II-4 Forces in aqueous medium

Forces acting between an AFM tip and a surface in an aqueous medium can be described by the DLVO theory (*Derjaguin, Landau, Verwey and Overbeek*). This theory is based on the assumption that interaction between two surfaces is governed by the van der Waals attraction and the electrostatic double-layer repulsion [32, 33].

The origin of the van der Waals force has been already described. The electrostatic double-layer force appears due to the interaction between ions of the liquid and surface charges at interfaces. For example, if surfaces approach the concentration of ions between them increases providing a repulsion force [33]. For large separation distance this force decreases exponentially with the characteristic decay length known as the Debye length:

$$\lambda_D = \sqrt{\frac{\varepsilon\varepsilon_0 k_B T}{e^2 \sum c_i Z_i^2}}$$ (eq.1.12)

where ε is the dielectric constant, ε_0 is the electric permittivity of vacuum, k_B is the Boltzmann constant, T is the temperature, e is the electron charge. Term $\Sigma c_i Z_i^2$ is the salt concentration and determines the Debye length λ_D. Here c_i is the partial concentration of ions of higher valency Z_i.

The electrostatic double-layer force can be calculated using the common continuum theory based on the Debye and Hückel [34], and also the Gouy and Chapman [35, 36] theories.

According to continuum theory, the force between an AFM tip and a surface can by calculated in assumption of following boundary conditions: firstly, during the approach, the surface charges are constant (constant charge) and secondly, the surface potentials are constant (constant potentials).

For the tip with a parabolic shape that interacts with a flat surface in the constant potential conditions, the electrostatic double-layer force is given by [37, 38]:

$$F_{el}^{cp} = \frac{2\pi R\varepsilon\varepsilon_0}{\lambda_D}[2\psi_S\psi_T e^{-D/\lambda_D} - \left(\psi_S^2 + \psi_T^2\right)e^{-2D/\lambda_D}],$$ (eq.1.13)

where ψ_S and ψ_T are the surface and tip surface constant potentials, respectively.

For the constant charge conditions, it gives [38, 39]:

$$F_{el}^{cc} = \frac{2\pi R\lambda_D}{\varepsilon\varepsilon_0}[2\sigma_S\sigma_T e^{-D/\lambda_D} + \left(\sigma_S^2 + \sigma_T^2\right)e^{-2D/\lambda_D}],$$ (eq.1.14)

where σ_S and σ_T are the surface and tip charge densities respectively.

These equations are valid in the case of low surface potentials ψ_S, $\psi_T \leq 50\text{mV}$. In addition, both the tip radius and the separation distance must be larger than the Debye length ($R >> \lambda_D$, and $D \geq \lambda_D$).

The choice of the appropriate boundary conditions depends on the surfaces, on the liquid and also on the approach speed. However, the constant potential conditions are more suitable with the so-called charge regulation model, in most cases [40]. According to this model, a surface charge appears due to the dissociation of ions from surface groups and consequently dependent on the potential. This is in agreement with experimental data for which the surface charge is often dependent on the pH of the solution and on the concentration of the ions.

Despite several limitations, the DLVO theory provides a satisfactory description of the electric double-layer force in aqueous solutions for monovalent salts at concentrations below 0.2M and potentials below 50-80mV. For example, it is appropriate to describe pH-determined surface charge such as oxides, mica and biological macromolecules.

This theory is not consistent to describe images in the case of a small separation between interacting surfaces. In fact, the finite size of ions is neglected and the distribution of their charge is considered as continuous. Between two hydrophilic surfaces separated by distances of 1-3nm, repulsive forces appear which are related to strong charge-dipole, dipole-dipole or H-bond interaction of these low energy surfaces with water. These forces are called hydration forces and they are measured for surfaces such as mica, alumina, DNA, proteins etc… demonstrating a short-range behaviour [13]. In contrast to the electrostatic double-layer force, increasing the ionic concentration provides increasing the strength of hydration forces and their range of actions becomes more extended.

Interaction between two hydrophobic surfaces in water is characterized by the so-called *hydrophobic force*. This force has a decaying attractive character and is stronger than the van der Waals interaction, between solid surfaces [41, 42]. In many experiments, short- and long-range attraction components are observed. Short-range component is characterized by an exponential decay length of 2-6nm, whereas long-range may reach 100nm [43, 44].

Several theories have been proposed to explain the nature of the hydrophobic force. Acceptable agreement between theoretically predicted and experimental hydrophobic forces gives the so-called nanobubbles hypothesis. According to this theory, bubbles form bridges between the hydrophobic surfaces. However, it was shown that such mechanism occurs only in the long-range hydrophobic attraction [41].

III - The AFM principle

The AFM is based on the detection of a tip-sample interaction force. To determine the interaction, the AFM measures the deflection or the resonant frequency of a cantilever in a static or a dynamic regime, respectively. In both cases, the probe deflection as well as the probe frequency response must be measured with sufficient accuracy to achieve the expected resolution.

The interaction potential between the tip and the sample includes contributions from different forces described in details in previous section. These forces exhibit power law dependencies on the tip-sample separation. It is necessary to know which forces are involved in the interaction process to control them. However, the tip behavior is defined by the forces, but also by its shape and by the medium between tip and surface.

III -1 The cantilever and the tip

The probe is a key element of the AFM. It consists of a tip attached at the end of a flexible cantilever (Figure I-7) and its mechanical properties are greatly responsible for AFM performance.
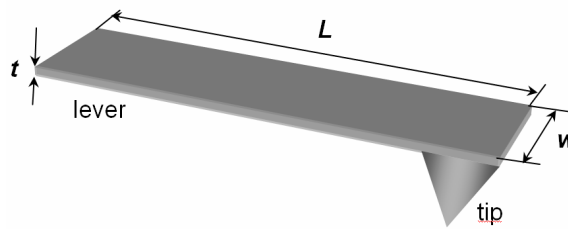
Figure I-7. An atomic force microscopy probe (rectangular cantilever)

Commercial cantilevers are manufactured from a crystalline material, typically from silicon or silicon nitride. The tip is characterized by its shape as well as its electro-chemical and mechanical properties. The curvature radius of the tip is determinant for the resolution and the tip angle defined the probe aspect ratio i.e. the ability of the tip to precisely follow rough surfaces. The cantilever is characterized by its mechanical properties such as the spring constant k and the resonance frequency v_0, which can be calculated from the cantilever dimensions and material properties.

The elastic deformation of the cantilever is used to measure the tip-sample interaction. According to the Hook's law, the deflection z is approximately proportional to the applied force F:

$$F=kz \qquad \text{(eq.1.15)}$$

where k is the stiffness of the cantilever.

For homogeneous rectangular cantilevers with a constant cross-section, the spring constant can be calculated using (eq. 1.16):

$$k = \frac{F}{z} = \frac{Ewt^3}{4L^3}$$ (eq.1.16)

where E is Young's modulus, w, t and L are the cantilever width, thickness and length, respectively (Figure I-7).

In practice, V-shaped cantilevers are also used (Figure I-8). According to Sader [45], such cantilevers are more mechanically stable and more sensitive to lateral force, and their spring constant can be expressed as:

$$k = \frac{Ewt^3}{2L^3}\left(1 + \frac{4w^3}{b^3}\right)^{-1}$$ (eq.1.17)

where b is the distance between levers.
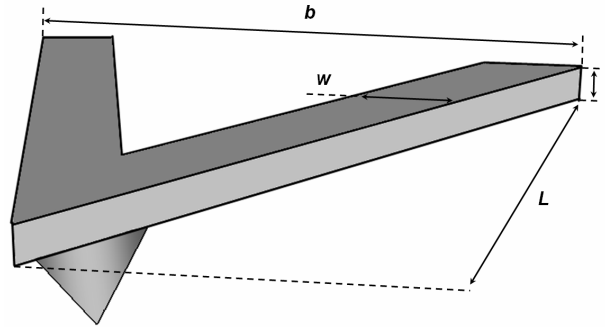
Figure I-8. An atomic force microscopy probe (V-shaped cantilever)

The stiffness of the cantilever determines its resonant frequency and sensitivity. According to the equation (1.15) a stiffer cantilever bends less for the same force and consequently has a reduced sensitivity.

The movement of the cantilever in air or vacuum can be approximated by a point mass on a massless spring and then the resonant frequency can be expressed as [46]:

$$\nu_0 = \frac{1}{2\pi}\sqrt{\frac{k}{m*}}$$ (eq.1.18)

where $m*$ is the effective mass.

A high resonance frequency is responsible for the time resolution of an AFM or in the other words, high resonance frequency makes possible AFM scanning with higher velocity [47]. On the other hand, the resonance frequency should also be as high as possible to avoid the influence of external vibrations and noise [48].

Usually, cantilevers are coated on the reflective side with a metallic layer to increase their reflectivity. This means that any variation of the temperature or chemical environment of the cantilever provokes a bending of the cantilever as for bimorph stacked materials. Slight difference in surface stresses leads to uncontrolled drift of the cantilever deflection which can confuse measurements [49]. To reduce the drift, optimal design of the cantilever should be chosen. In practice, it implies a compromise between dimensions and materials. The cantilever geometry can also play an important role depending on the application, for example V-shaped cantilevers are often chosen to increase lateral stability.

III-1-1 Calibration of the spring constant

Nowadays, commercially available cantilevers are usually calibrated by manufacturer. However, exact values of the stiffness are often required for high precision measurements such as quantitative force experiments.

As it was already shown (equations 1.16, 1.17), the spring constant can be calculated knowing material properties and geometry of the cantilever. However, real characteristics of the cantilever are not perfect. For example, the thickness is not homogeneous and Young's modulus of a thin layer can differ from that of the bulk material [50]. Theoretically calculated spring constants are often different from experimentally determined ones [51, 52] and absolute values of the spring constant should be determined for quantitative measurements.

The most popular methods to measure cantilever spring constant are the Cleveland method [53], the Sader method [54], the thermal noise method [55] and the method of calibration by using a reference cantilever [56].

The Cleveland method consists in adding a known mass at the end of the cantilever and measuring the resulting shift in the resonance frequency [53]. In the Sader method, the spring constant is determined by using the quality factor and the resonance frequency, when knowing the length and width of the cantilever [54]. In the approach proposed by Hutter and Bechhofer [55], the spring constant is calculated by measuring the intensity of the thermal noise induced by thermal fluctuations of the cantilever. The convenient way is to use an already calibrated cantilever as a reference to determine the unknown spring constant of a cantilever [56]. This method is relatively easy but it implies the calibration of the reference cantilever. These three methods give good precision in measurements but they imply some complexity in achievement. The Cleveland method requires to precisely determine the mass of the particle fixed to the cantilever. The Sader method is dependent on geometrical parameters, such as non constant thickness of the cantilever, for example. The thermal noise method is the most common used because it does not require any external manipulation with the cantilever. Nowadays, this method of the cantilever calibration is implemented in many commercial AFMs.

III-1-2 Cantilever deflection measurements

Far from a surface, no force acts on the cantilever. The tip-sample interaction changes the cantilever position which can be measured.

Historically, the first detection method was proposed by Binnig et al [12]. It consists in using *STM probe for deflection measurements* of the AFM cantilever. However, this approach was not widespread because of its limitation to conductive cantilevers, the high contamination sensitivity and its design complexity. For the measurements of small cantilever displacements, an *optical interferometer* can be used. This method provides a high accuracy in the cantilever deflection detection via the wave length [57, 58]. Deflection can directly be registered with *piezoelectric cantilever*. Such instrument does not require external detection mechanism, it is particularly useful for application with limited space [59].

The optical lever method is the commonly used approach for cantilever displacement measurements. Today, most of AFMs are implemented by this inexpensive technique. A collimated beam from a laser diode is focused at the end of the cantilever, on the top side, and the reflected light is registered by a position sensitive detector (PSD) (Figure I-9).
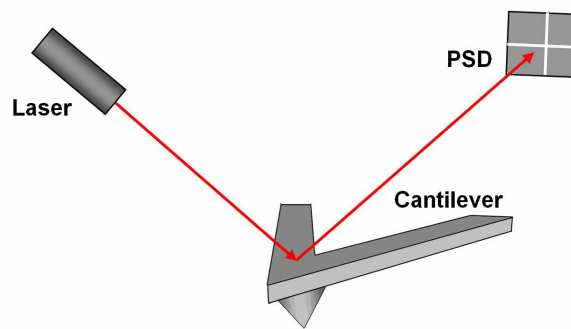
Figure I-9. Optical lever detection technique

The position of the reflected laser beam is usually detected by a four-segment photodetector, allowing the detection of the cantilever movement along vertical and horizontal directions. The bending of the cantilever leads to a shift of the laser spot which changes the signal on the segments proportionally to the cantilever deflection. A lateral shift is caused by the torsion of the cantilever in presence of a frictional force. In both cases, this system assures high sensitivity and sufficient stability, however the cantilever deflection should be relatively small in order to provide the detector operation in linear regime [60].

III-1-3 Resolution and limits of AFM

Topographical AFM image is a 3-dimensional representation of the sample surface which therefore can be characterized by lateral and vertical resolution.

In most cases, the lateral resolution is determined by the tip characteristics, the tip-surface interaction and elastic properties of the sample. Real AFM tips have a finite curvature radius r and angle α, consequently the point of contact is not always at the apex of the tip. It leads to broadening effects which manifest by overestimated lateral dimensions of small surface features (Figure I-10) [61].
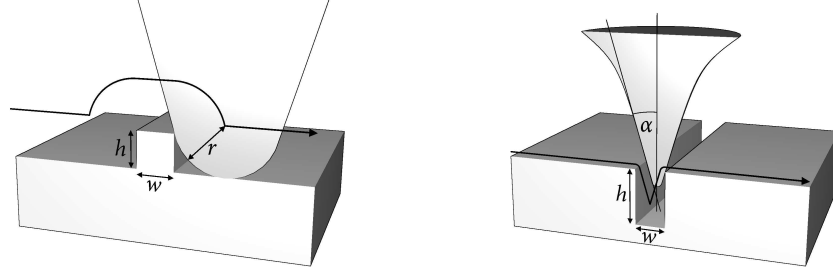
Figure I-10. Influence of a finite tip size in AFM measurements.
The scanning lines are different from the real profile of the feature [61].

For idealized tip and sample geometries, the imaging error can be obtained by geometrical construction. Scanning on a rectangular object of width w and height h by a tip with a curvature radius $r \geq h$, produces a topographical image with an apparent width of the object of:

$$w' = w + 2\sqrt{2rh - h^2}$$

(eq.1.19)

When a cavity is scanned, the apparent depth is given by:

$$h' = \frac{w}{2}\cot\alpha - r(\csc\alpha - 1)$$

(eq.1.20)

The vertical resolution is mostly limited by thermal fluctuations. For the optical-lever detection system, the cantilever thermal noise can be estimated by the expression [62]:

$$z = \sqrt{\frac{4k_B T}{3k}}$$

(eq.1.21)

For example, for a temperature of T=295K and a cantilever spring constant k=40N/m, the thermal fluctuations are of the order of 0.01nm. It means that the AM-AFM may provide vertical resolution of 0.1nm or better [63].

Albrecht et al. have shown that the uncertainty of the frequency caused by the thermal noise is given by the following relation [64]:

$$\left\langle (\delta\omega)^2 \right\rangle = \frac{\omega_0 k_B TB}{kQA^2} \qquad \text{(eq.1.22)}$$

where B is the detection bandwidth, and A is the amplitude of the cantilever oscillation.

The minimal force gradient that can be detected is

$$\delta F_{min} = \left(\frac{4kk_B TB}{\omega_0 QA^2} \right)^{1/2} \qquad \text{(eq.1.23)}$$

For low temperatures of the order of some Kelvins, eqs. (1.22) and (1.23) give $\delta\omega \sim 1.0\times10^{-3}$ s^{-1} and $\delta F_{min} \sim 2.3\times10^{-4}$ N/m. It is remarkable that the sensibility of the cantilever is inversely proportional to the oscillation amplitude. This (eq. (1.23)) shows that optimal conditions correspond to high quality factor, low temperature (thus in UHV, in FM-AFM at 4°K) [65].

III-2 Atomic Force Microscope operation modes

The operating modes of an AFM are often defined as contact or non-contact (NCM) modes, in the literature. In contact mode, AFM operates in a regime of static force measurements in the repulsive part of the surface potential. Non-contact mode is defined by an operation in the attractive part of the potential. This regime provides a higher sensitivity in detecting small attractive forces and prevent the cantilever from jumping-to-contact (unless such regime is not set by the operator). Interaction regimes of both AFM modes are illustrated in Figure I-11.
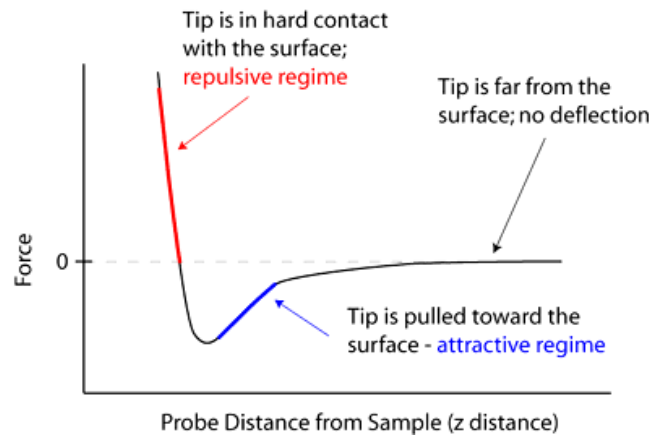

Figure I-11. Interaction regimes of different AFM modes [4]

III-2-1 The contact mode

III-2-1-1 Imaging

In this operation mode, the tip is in continuous contact with a sample surface. At such small separation distances, the interaction potential has a strongly repulsive character resulting from the Pauli exclusion principle, when the electronic orbitals of tip and sample overlap. When the tip is scanned on the surface, the deflection of the cantilever changes with the topography of the sample, leading to a different value of the force. Thanks to the feedback loop, the tip surface distance is adjusted to maintain the applied force at a fixed setpoint value. The adjustment of the distance is performed by applying voltage on the Z piezo ceramic translator. Thus, an image is obtained by scanning the tip at a fixed applied force (setpoint). Variation of the tip-sample distance reflects the topography of the sample. For an analytical description, the cantilever is supposed to be placed horizontally along *x*-axis and the force acting on the probe is applied to the end of the cantilever in vertical direction. It is also assumed that the cantilever deflection is measured by optical lever method.

When the probe is affected by the action of the tip-sample force, the cantilever bends and its deflection is detected by the optical lever. If the force acting on the cantilever changes during a period of time much slower that the period of resonant oscillations of the cantilever, then this force can be considered as a static force. In the static force regime, the elastic response of the cantilever, at a given position *X,* is related to its torque *F(L-X)* according to the following relation:

$$EI \frac{d^2Z}{dX^2} = F(L - X) \qquad \text{(eq.1.24)}$$

where *I* is the moment of inertia.

Resolving this differential equation with the boundary conditions *Z(X=0)=0* and *dZ/dX(X=0)=0* for a rectangular cantilever gives:

$$Z = \frac{F}{2EI}\left(LX^2 - \frac{X^3}{3} \right) \qquad \text{(eq.1.25)}$$

where *E* is the Young's modulus of the cantilever material.

Usually, the laser beam is focused at the end of the cantilever i.e. *X=L.* Substituting it in eq.(1.25) and knowing that for rectangular cantilever *I=wt³/12,* the cantilever deflection can be expressed as:

$$Z_c = \frac{4FL^3}{Ewt^3} \qquad \text{(eq.1.26)}$$

here *L, w* and *t* are the length, width and thickness of the cantilever, respectively.

The inclination at the end of the cantilever (endslope) is then:

$$\frac{dZ_c}{dX} = \frac{6FL^2}{Ewt^3}$$

(eq.1.27)

Hence, the deflection can be rewritten as:

$$Z_c = \frac{2}{3}L\frac{dZ_c}{dX}$$

(eq.1.28)

The equation (1.28) demonstrates that the deflection measured with the optical lever technique is proportional to the inclination of the cantilever.

For *V*-shaped cantilever, the expression is more complicated [66], however often it can be successfully approximated by rectangular geometry that is experimentally confirmed by Sasaki et al. [67]. During the scanning in the repulsive regime the interaction force between the tip and sample surface can be high enough. It means that the elastic deformation of the tip and the sample must be taken into account [68].

III-2-1-2 Force measurements

Another important possibility to investigate the sample or tip properties is the study of interaction between tip and sample. Such measurement is known as *force measurements* or *force spectroscopy*.

In a force spectroscopy experiment, the cantilever deflection is measured while the tip is approached and retracted from a surface by the piezoelectric translator (Figure I-12).
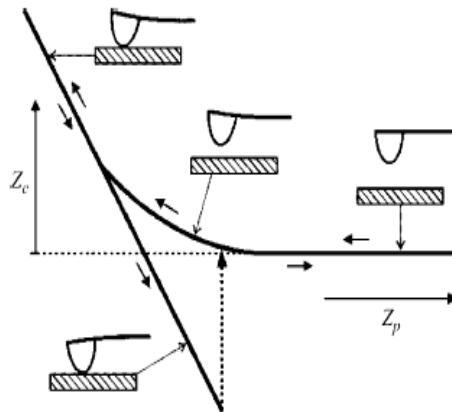

Figure I-12. Different steps of cantilever approach-retracting movement [63]

The result of force measurements is the detection of the cantilever deflection as a function of the Z piezo position. In practice, the deflection is measured as a photodiode current I_{PSD} and should be converted in

a force. It implies that the sensitivity of a "contact regime" curve should be determined, and that the cantilever should be calibrated. Then, the interaction force can be calculated according to the Hook's law $F=kZ$, where k is the spring constant and Z is the deflection of the cantilever. The whole tip-sample distance D consists in the position of the piezo translator Z_p and the deflection Z, so that $D=Z_p+Z$.

The graphical representation of the measured force F in function of the distance D is commonly called *force-versus-distance curve* or simply *force-distance curve* (Figure I-12).

The conversion of the cantilever deflection into a force is crucial in force spectroscopy because it determines the correctness of measurements. However in practice, the previously described method may provide incorrect interpretation, when highly deformable samples are used or in case of strong repulsive force.

For the force measurement, such parameters as the sensitivity and the zero-distance must be obtained directly from the experimental force-distance curve and not indirectly by independent methods.

A force-distance curve consists of approaching and retracting parts and each part corresponds to two regimes: contact and non-contact regime (Figure I-13).
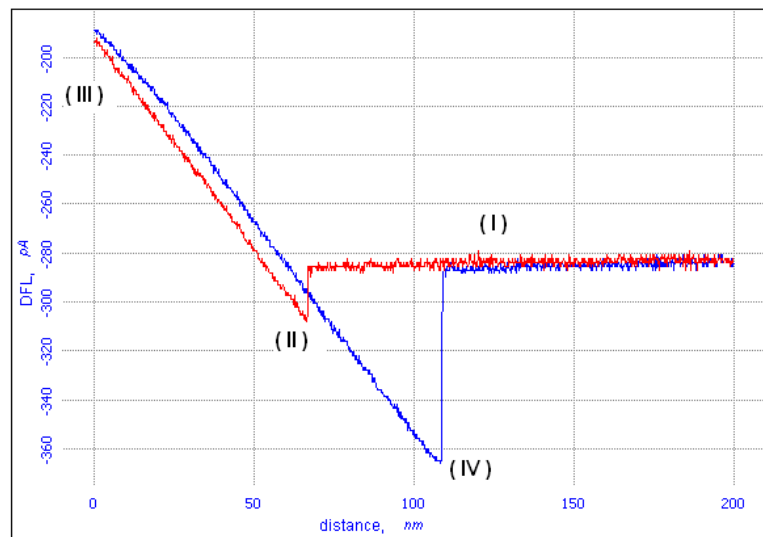
Figure I-13. Schematic representation of a force-versus-distance curve

When the approach begins, the cantilever is far from the sample and any force acts on the tip (in assumption that long-range forces can be neglected). The tip moves toward the sample, the tip-surface distance decreases and the deflection signal remains unchanged ($Z=0$ and distance $D=Z_p$). This phase of approach corresponds to the *non-contact* zero force line which defines the zero deflection of the cantilever (part I in the Figure I-13).

As the tip goes on approaching toward the sample, the gradient of the attractive force becomes sensitive to the surface. When its strength exceeds the spring constant ($dF_{surf}/dD > k$), the cantilever jumps from equilibrium state in contact with the surface (so called "jump-in" point), that corresponds to the part II

in the Figure I-13. This unstable regime is induced by capillary forces acting on the tip due to the presence of a water layer on the surface in ambient conditions [69].

From the "jump-in" point, the tip is in contact with the surface and its movement into the surface induces an increase of the load (linear on stiff surface). It corresponds to the *contact part* of the force-distance curve (part III in the Figure I-13). The slope of the linearly increasing contact part corresponds to the sensitivity $\Delta I_{PSD}/\Delta Z_p$. The cantilever deflection can be calculated from the detector signal according to the following relation: $Z=I_{PSD}/(\Delta I_{PSD}/\Delta Z_p)$. Then, the force can be obtained from the deflection by: $F=kZ$. Because the tip is in contact with the surface, the distance $D=0$, and then $Z_p=-Z$.

The contact regime of the retraction part corresponds to the situation when the cantilever is moved backward from the surface but the tip still remains in contact with the surface by an adhesion force (part IV in the Figure I-13). During retraction, the cantilever bends in the opposite direction compared to the one for the approach until the energy of the cantilever overcomes the adhesion force (also called the *pull-off* force) (part C in the Figure I-13). If the sample deformation can be ignored, this energy can be described as:

$$W_{ad} = \frac{F_{ad}^2}{2k}$$

(eq.1.29)

Then, the cantilever returns from the pull-off point, in the initial starting point passing by the non-contact zero force line (part I in the Figure I-13).

In real situation, all solid materials are deformable. It leads to a nonlinear dependence of the cantilever deflection on the applied force, during approach. It means that the indentation of the sample δ must be taken into account. In most cases, many materials are characterized by small indentation $\delta << Z$ and a change in applied force ΔF corresponds to a change in the cantilever deflection: $\Delta F \approx k \, \Delta Z$. If the sample indentation can not be ignored, for example when indentation is caused by strong adhesion force, an appropriate model should be used for force-distance curve description [70].

The difference between approaching and retracting parts of the contact regime, the *hysteresis,* is usually due to plastic or viscoelastic deformation of the sample [71]. In the case of elastic deformation, lines of contact regime should have identical slope.

The force spectroscopy is widely used for quantitative characterization of plastic and elastic properties of polymers [72, 73] and biological samples [74, 75] in ambient, gas or liquid media.

Another information given by the AFM spectroscopy is the measurement of adhesion and van der Waals forces with a high resolution. Probing these forces offers the possibility to measure the *surface energy* of materials. It is the object of experimental works when the classical method of contact angle measurement is not efficient [76]. This is the case when the sample surface is not homogeneous, chemically reactive or unstable in the environment of the probing liquids and also when samples are small or patterned with microscopic domains [76].

The original possibility to determine surface energy γ by AFM consists in determining the work of adhesion between the tip and the sample from experimental force distance curves knowing the radius of the cantilever tip [77].

During spectroscopy, the contact time between the tip and the sample is short (order of *ms*), consequently, the adhesion is only due to Van der Waals forces and the measurable work of adhesion represents the thermodynamic work of adhesion W_0:

$$W_0 = 2\gamma \qquad\qquad (eq.1.30)$$

On the other hand, the tip-surface contact can be considered as a contact between a sphere and a plane with low deformation and low contact radius. Then, the DMT model (Derjaguin Muller Toporov) can be applied for an approximation of the thermodynamic work of adhesion [78].

Experimental force-distance curves give the force necessary to separate the tip from the surface (during the pull-off – the adhesion force F_{adh}), then the DMT model relates this adhesion force F_{adh} to the thermodynamic work of adhesion as follow:

$$F_{adh}=2\pi R W_0 \qquad\qquad (eq.1.31)$$

where F_{adh} is the adhesion force and R the tip radius.

The expression for the surface energy can be deduced by substituting eq. (1.30) into eq. (1.31):

$$\gamma = \frac{F_{adh}}{4\pi R} \qquad\qquad (eq.1.32)$$

The cantilever bending during the separation obeys to the Hook's law, thus the adhesion force between the tip and the sample is:

$$F_{adh} = k \cdot \Delta Z \qquad\qquad (eq.1.33)$$

where k is the cantilever spring constant and ΔZ is the cantilever bending (*pull-off* on force-distance curve during retraction).

In several cases, measured surface energy differs from theoretically predicted values. This is because analyzed surfaces or more precisely tip-sample systems should be carefully approximated by appropriate elastic continuum models (described in details in section "Interaction forces in atomic

31

force microscopy"). For example, if the system is not quite correctly described by the DMT model, it may be possible to obtain better approximation with JKR model or vice versa. In addition, the origin of the difference between experimental and theoretical data can be related to tip geometry, non homogeneity, morphology and plastic deformation of the sample. However, in several cases the DMT and JKR theories lead to correct results, which are in good accordance with Maugis approximation [79, 80].

III-2-2 Dynamic mode

The AFM technique can be used in another mode: the dynamic mode. The idea of using an oscillating regime was first proposed by Martin et al [81]. The principle of AFM in dynamic mode is based on the dependence of the amplitude, the resonance frequency and the phase shift of the oscillating cantilever on the tip-surface interaction. Depending on the operation regime, some of these signals can be used as feed-back parameters to image the surface topography. The main advantage of dynamic force microscopy is the possibility to probe the sample surface without tip-surface mechanical contact i.e. in *non-contact* mode that is especially important for experiments with polymer and biological materials. AFM imaging in static mode (contact mode) of DNA molecules or of protein membranes was possible due to their relative rigidity and strong adsorption on the substrate. However, weakly attached single macromolecules were often damaged by the tip or pushed away. Non-destructive dynamic AFM modes have enabled high-resolution imaging of individual proteins [82, 83], polymers [84] and DNA [85] in air and liquids.

The excited cantilever is usually considered as a point-mass spring and then the tip motion can be approximated by an equation of harmonic oscillator according to the Newton's equation [86, 87]:

$$m\frac{d^2z}{dt^2} + kz + \frac{m\omega_0}{Q}\frac{dz}{dt} = F_{ts} + F_0\cos(\omega t) \qquad \text{(eq.1.34)}$$

Here $F_0\cos(\omega t)$ is the external periodic excitation force with angular frequency ω; Q, ω_0, m and k are quality factor, angular resonance frequency, mass and spring constant of the cantilever respectively; F_{ts} is the tip-surface interaction force, respectively.

The interaction force F_{ts} contains long-range van der Vaals interactions, short-range repulsive interactions, adhesion and capillary forces, described in details in section "Interaction forces in atomic force microscopy".

The response of a cantilever to a periodic excitation can be obtained by solving eq. (1.34) [88]:

$$z(t) = A\cos(\omega t - \varphi) \qquad \text{(eq.1.35)}$$

where the oscillation amplitude A in function of the excitation frequency is expressed as:

$$A(\omega) = \frac{F_0/m}{[(\omega_0^2 - \omega^2)^2 + (\omega\omega_0/Q)^2]^{1/2}} \qquad \text{(eq.1.36)}$$

The phase shift between the driving force and the cantilever response is then given by:

$$\tan\varphi = \frac{\omega\omega_0/Q}{\omega_0^2 - \omega^2} \qquad \text{(eq.1.37)}$$

The graphical representation of the cantilever response given by equations (1.36) and (1.37) is shown in Figure I-14.
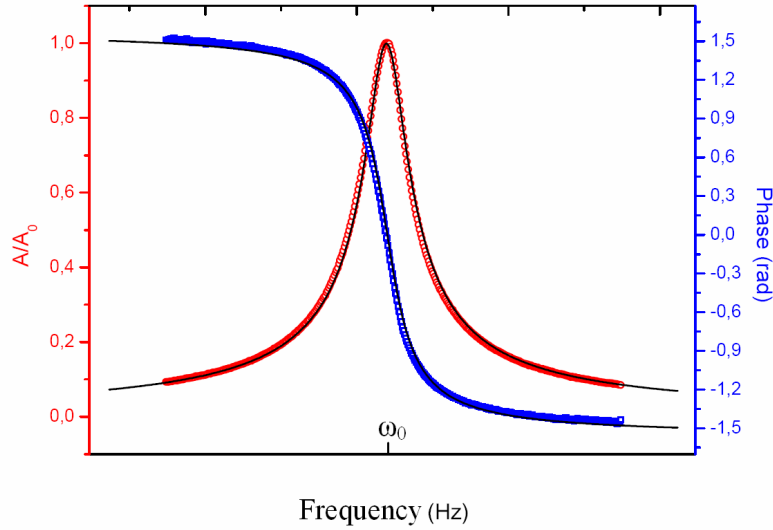
Figure I-14. Amplitude and phase responses of the cantilever to periodic excitation [89]

According to the eq. (1.36), the cantilever oscillation amplitude depends on the magnitude of the exciting force F_0, the discrepancy between the mechanical resonance frequency ω_0 and the excitation frequency ω and the hydrodynamic damping Q. Q can be calculated by the thickness of the peak $Q=\Delta\nu/\nu_0$.

The tip-surface force F_{ts} includes the elastic response and the effective resonance frequency of such harmonic oscillator depends on the gradient of the interaction force dF_{ts}/dz [63]:

$$\omega_e = \left(\frac{k - dF_{ts}/dz}{m}\right)^{1/2} \qquad \text{(eq.1.38)}$$

According to the equation (1.36), a change in the effective resonance frequency ω_e, provokes a shift of the whole resonance curve as it is shown in Figure I-15.
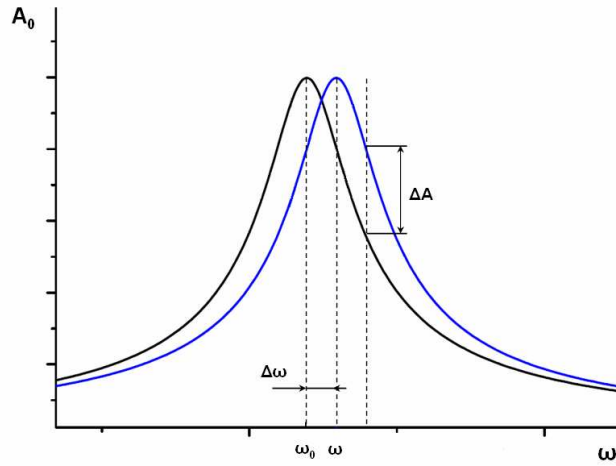
Figure I-15. Shift of the resonance curve under influence of tip-surface interaction gradient

The dependence of the effective resonance frequency and consequently of the oscillating amplitude on the strength of the tip-surface interaction is the principle of the signal detection in dynamic atomic force microscopy. On this basis, two commonly used dynamic AFM modes have been developed for sample surface probing: Amplitude-Modulation AFM (AM-AFM) and Frequency-Modulation AFM (FM-AFM) modes.

In *AM-AFM*, the cantilever is excited at a constant frequency which is equal or close to its resonant frequency. The detection principle consists in measuring the change in the amplitude response ΔA caused by the shift in the resonant frequency $\Delta \omega$ due to the tip-sample interaction (Figure I-15). Thanks to the feedback loop, the system reacts moving the Z piezo translator, to maintain the amplitude to its setpoint value. Once again, variations of the Z piezo movement acting on the tip surface separation are recorded, they reproduce the topographical change of the surface relief [90, 91]. In this mode, mechanical and physico-chemical information about the sample may be obtained by measuring the phase shift between the excitation signal and the cantilever oscillation [63].

In *FM-AFM*, the role played by frequency and amplitude are reversed towards the AM-AFM mode. The cantilever is excited at a constant amplitude which is equal or close to its resonant amplitude. This corresponds to a fixed setpoint frequency. The resonant frequency shift $\Delta \omega$ towards the setpoint frequency is measured (Figure I-15) [92, 93]. The resulting image is formed by scanning the sample surface with a constant frequency shift. The FM-AFM mode allows to image in a real non contact mode at few nm from the surface, and is well-appropriate to high resolution imaging. It is often used in UHV and begins to be used in liquids [94]. The AM-AFM mode is appropriate to imaging in air and in liquids but not in UHV. In fact, the high quality factor Q in vacuum, requires a long relaxation time between two oscillations and then the scanning of a whole image in several hours. [95].

Generally, the AFM modes are named contact mode, non-contact and tapping mode.

The *contact-mode* corresponds to the static mode, where the repulsive part of the surface potential is probed (contact region in Figure I-16). The *non contact mode* operates in the attractive part of the surface

potential (non contact region in Figure I-16) and is often associated to the FM-AFM mode. The *Tapping* or *intermittent mode* refers to the AM-AFM mode. In this last mode, the tip passes from attractive interaction to repulsive interaction during one oscillation cycle. This means that the interaction passes from one force to another one. In the AM-AFM, it can be difficult to distinguish non-contact and tapping modes and detailed understanding of tip-surface interaction is required [63, 96].
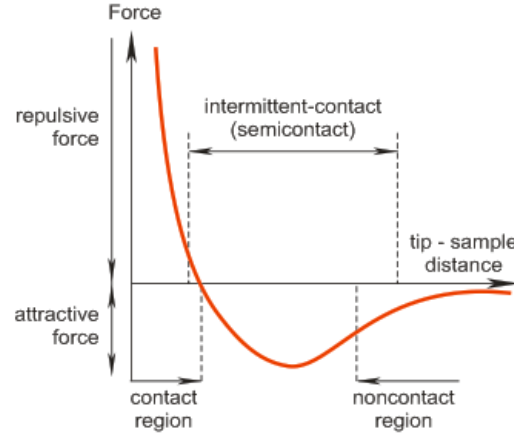
Figure I-16. AFM operation modes with respect to surface potential [4]

The dynamic AFM modes (equations 1.34-1.38) are described above in assumption that the vibrating cantilever can be considered as a harmonic oscillator. The harmonic approach implies that the tip-surface interaction induces a shift in the resonant frequency. However, Garcia et al. showed [63] that tip-surface interaction is also related to an energy transfer. In addition, the force gradient was assumed to be smaller than the cantilever spring constant and independent of the separation. In most experiments, harmonic approximation is not suitable and non-linear dynamic effects appear in the tip motion of dynamic AFM [97].

In its basis, dynamic tip-surface interaction is characterized by non-linear attractive and repulsive forces that give rise to coexistence of two stable oscillation states in AM-AFM [63].

The numerical solution of eq. (1.34) shows that, in certain conditions, the tip motion is described by two different solutions, called a low (*L*) and high (*H*) amplitude solutions:

$$Z_{L(H)} = Z_0 + A_{L(H)} \cos(\omega t - \varphi_{L(H)}) \qquad \text{(eq.1.39)}$$

The oscillation state (low or high amplitude solution) is determined by initial conditions (*z, dz/dt, ωt*) if tip-sample separation and external excitation force parameters (F_0 and ω) are constant.

The existence of single or double stable oscillation state is defined by sample properties and parameters such as the cantilever spring constant and the free oscillation amplitude. For example, low elastic modulus of the sample or large excitation force reduce the difference between the two stable states, in most cases, and both *L* and *H* branches merge into a single branch [63].

The transition from one to another state is characterized by a hysteresis loop on the amplitude versus distance curve (the spectroscopic signature of the AM-AFM mode) (Figure I-17).
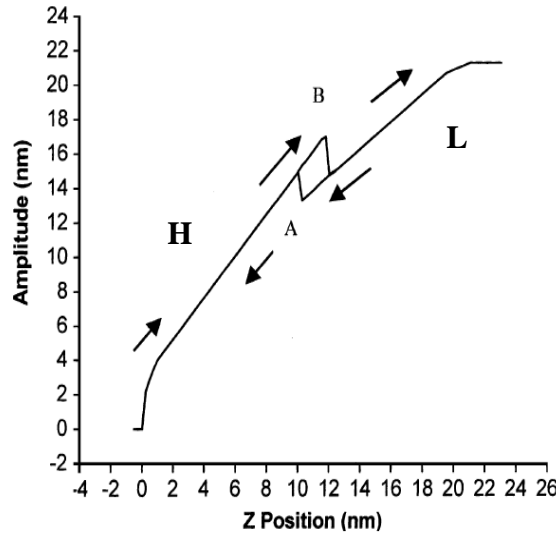
Figure I-17. Hysteresis loop of transitions between L and H oscillation states [63]

Figure I-17 presents two transitions at different values of the tip-surface separation. During the approach of the tip toward the sample, an *L-H* transition occurs (point A in Figure I-17) and an *H-L* transition occurs during the retraction of the tip (point B in Figure I-17). The step-like transition between the *L* and *H* branches implies that for a chosen setpoint amplitude A_{sp} corresponding to the hysteresis position then the AFM operation is possible for two different tip-sample separations. Consequently, imaging occurs in the *L* or *H* state, or in an unstable regime characterized by the switching between the two branches. Then, the choice of all the parameters, working frequency, free oscillation amplitude, setpoint amplitude, is crucial to perform images in a stable regime [63]. An example will be given in paragraph IV.

Another important ability of dynamic AFM is the simultaneous imaging of topography and sample-related properties. As it was shown (eq. 1.37), the phase shift of excited cantilever is related to tip-sample interaction force. However, there are several contributions to phase shift related to material properties such as adhesive, elastic and viscoelastic properties of the sample [98]. Therefore, AM-AFM offers a powerful method for probing sample properties through measuring phase response of the interaction with the surface cantilever.

36

III-2-3 AFM in liquids

In previous sections, AFM experiments have been discussed in ambient conditions, in air. However, in some cases such as for biological or chemical applications, imaging in a liquid media is preferred. AFM in aqueous buffers is crucial to obtain the morphology of biomolecules in physiological conditions or to study chemical and biological reactions in situ [84]. Furthermore, working in liquids eliminates the meniscus and then the capillary forces and can allow to image using short-range chemical forces [99, 100], even with atomic resolution in some cases.

Despite this, performing dynamic AFM experiments in liquids is complex and images are difficult to interpret. The dynamic behaviour of the cantilever in a liquid is more complicated than in air or vacuum. The liquid induces a high hydrodynamic damping of the cantilever which manifests by a significant decrease of the cantilever quality factor Q. Typically, Q range between 1to 20 instead of 10-500 in air and 10^4-10^8 in vacuum. On the other hand, the resonant spectrum of the cantilever is characterized by several resonant peaks that makes difficult the choice of the driving frequency. These numerous peaks are due to acoustical vibrations and also to the coupling of normal vibration modes of the cantilever [63]. Figure I-18 presents a comparison of the resonant peaks in air, vacuum and liquids. The hydrodynamic effects induce an increase in the effective mass of the cantilever leading to the shift of the peak to the low frequencies (according to eq. 1.38) [54].

In other words, surrounding liquid with higher viscosity leads to lower resonant frequency of the cantilever [101, 102].
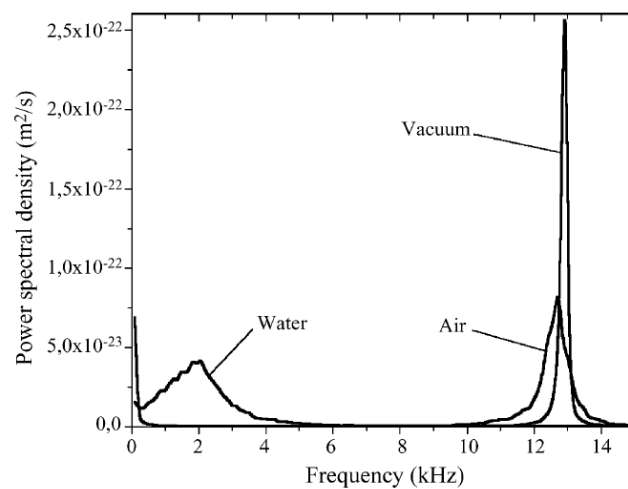
Figure I-18. Comparison of noise power spectra in vacuum, air and water [66]

To understand the tip dynamics in liquid, one should solve the equation of the cantilever motion in a fluid which is not a trivial task. The model, proposed by Sader [102, 103] and Scherer [104] includes contact of the liquid with the cantilever that increases its effective mass. It also considers the effect of the fluid motion excited by external driving force, around the cantilever. The proposed equation is expressed as:

$$EI \frac{\partial^4 w(x,t)}{\partial x^4} + \mu \frac{\partial^2 w}{\partial t^2} + a_0 \frac{\partial w}{\partial t} = F(x,t) \qquad \text{(eq.1.40)}$$

where $w(x,t)$ is the transverse displacement of the cantilever; E, I, μ are the Young's modulus, moment of inertia and the mass per unit of length of the cantilever respectively. The coefficient a_0 describes the hydrodynamic damping of the cantilever in the liquid. The term $F(x, t)$ includes all forces per unit of length acting on the tip. This model also describes the coupling of the oscillation modes of the cantilever.

IV - Illustration of the AM-AFM mode: a DNA – array study

The AM-AFM mode is currently used to observe soft materials such as biological molecules deposited on stiff substrates, because images are relatively easy to obtain even by non- AFM specialist. Moreover, phase imaging can be a versatile tool to characterize compositional contrast variations at the nanoscale, especially on soft materials. Phase shifts are related to the dissipated energy per oscillation [105] and provide information on AFM tip-sample localized interactions. Phase shift imaging was usually applied on heterogeneous materials, to map mechanical properties such as local viscoelasticity or adhesion [106-108].

However, the complexity of the tip-sample interaction with a non linear behaviour of the oscillating cantilever movement makes it difficult to relate the phase shift imaging to material properties [109]. Before imaging, the experimental parameters (free amplitude, amplitude ratio, cantilever characteristics) should be well–defined. In that sense, acquisition of amplitude or phase versus distance curves allows to determine the conditions for a good stability of the cantilever and to get a better knowledge of the interaction nature.

Several studies try to establish the relationship between the quality of the image and the nature of the interaction (mostly attractive or repulsive). They also try to link the phase image to mechanical properties of the surface. In most cases, force spectroscopy is performed on model substrates, phase imaging on multiblock polymers.

This study is related to a DNA-array devoted to biological applications, which is a more complicated system with a thin layer of organic, and then, soft material (few nanometers) on a hard silicon substrate. In a previous work, it was shown that, DNA molecules hybridized on a DNA array could be imaged and that the hybridized region along the molecule could be distinguished (2nm high) from the single non hybridized part (1nm) [110]. This was possible by imaging in the AM-AFM mode with appropriate experimental conditions, in particular with a well defined amplitude ratio $A_{sp}/A_0 \sim 90\%$, where A_{sp} and A_0 are the feedback amplitude or setpoint amplitude value at which imaging is performed, and the free amplitude value when the cantilever is far from the surface where no interaction occurs, respectively.

Herein, we study the effect of reducing the setpoint amplitude, at a fixed free amplitude and working frequency, on topographic height and phase shift AFM images and amplitude-phase curves. Our objective is to link experimental conditions to expected informations: high resolution topographic imaging of DNA, better understanding interaction dissipative processes involved in DNA breaking on our DNA system.

IV-1 Experiment

The sample chosen for this study was a biosensor composed of 25-base oligonucleotides covalently bonded to an oxidized silicon surface by means of a silane molecule layer. This entity was used as a DNA-array and was previously described [110]. On this bio-system, each oligonucleotide acts as a probe molecule with which a long DNA strand target can hybridize. In a previous work, we showed that isolated hybridized DNA molecules lying on an oligo-probe carpet can be observed.

The experiment was carried out on a Smena A AFM (NT-MDT, Russia) operating in air at room temperature and at a relative humidity of 40%. The cantilevers used had nominal spring constants of approximately 4.5 Nm^{-1}, resonance frequencies around 150 kHz (149.626 kHz) and quality factors between 350 and 375. The exciting phase signal was adjusted to obtain phase lags around 90° at the resonance frequency. The drive frequency was slightly below ($\Delta\nu = - 66Hz$) the resonance frequency ($\nu=149.56$ kHz).

This value is close enough to the resonant frequency to consider thereafter a dynamic behaviour of the system in the case of resonant excitation but slightly below to force the system to immediately "jump" into the tapping state and avoid a path to a non contact regime. [111].

The setpoint value A_{sp} was first adjusted at 91.3% of the free amplitude $A_{free} = 22.9$ nm $\pm$ 0.3nm to achieve a stable feedback. Then, A_{sp} is reduced to successive lower values up to 3.1%. For each setpoint value, topographical height and phase shifts images were recorded at a line frequency of 1.8Hz (512x512 pixels). Each image was preceded by spectroscopic measurements: amplitude and phase shift curves. They were obtained by approaching the tip towards the sample from a distance with negligible tip-sample interaction to the distance corresponding to the setpoint amplitude chosen when imaging. Amplitude and phase shifts were recorded on a reduced distance to limit contact with surface and then tip contamination or surface modification before imaging. For the same reasons, curves and images were successively performed from lower interaction 91.3%, to higher interaction 3.1%.

IV-2 Discussion of experimental results

IV-2-1 The surface

Figure I-19 shows simultaneously acquired topographical and phase images focussed on a 500 nm x 500 nm area where one DNA target molecule had hybridized with one DNA probe molecule [110]. The target is lying on the surface extending over the entire imaged zone, with probe molecules also visible on the background. Each probe corresponds to a small island of around 20 nm in diameter. The islands size is higher than expected due to the well-known tip radius dilation effect [112, 113].

These images were performed with the A_{sp}/A_{free} ratio of 91.3%. We observe a clear and noise-free topographic image in Figure I-19a, and a phase image in Figure I-19a' that presents a low phase shift contrast $\Delta\varphi$ of 7.76°. According to literature, we assume that these images are obtained in a light contact intermittent mode of operation, (the setpoint amplitude was chosen in the upper part of the low branch). On the phase image, the low contrast is linked to a weak interaction with the surface and includes only topographic information [114]. To obtain a significant phase contrast, the tip should be in strong interaction with the surface. Then, the phase shift is related to mechanical properties [115].

Ratio values around 90% correspond to optimal values for height images on this system. They allow to obtain optimum topographical information and then a clear interpretation of structures. Stars on Figure I-19a depict the location where spectroscopic measurements were performed for each ratio.
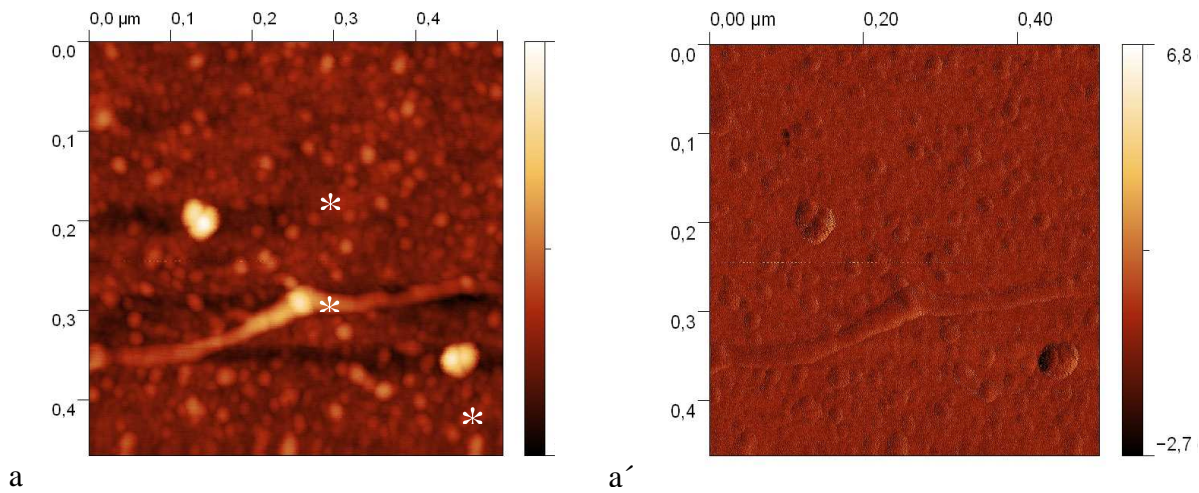

a   a´

Figure I-19. Topography (a) and Phase (a´) AFM images with the A_{sp}/A_{free} ratio of 91.3%.
Spectroscopy points are marked by stars "*".

IV-2-2 Amplitude versus distance and phase versus distance curves

Figure I-20 presents the spectroscopic curves performed before each image. The curves are plotted between two limits which correspond to the free amplitude and a value slightly below the setpoint amplitude. The curves corresponding to the ratio of 91.3% (images on Figure I-19) was not plotted because A_{sp} and A_{free} are too close and the curves are not really significant. The first curves correspond to a ratio of 34.9% and then the ratio was progressively decreased for the following curves up to 3.1%. We, deliberately, chose to successively realize the analysis from a high amplitude ratio, corresponding to a weak interaction, to a low amplitude ratio, corresponding to a strong interaction. Thus, we limit the contact of the tip with the surface and then the degradation of the sample and the contamination of the tip before the acquisition of images at each setpoint.

All the spectroscopic curves were carried out at the same place on the sample. They were recorded on three different points: on the DNA molecule, on the chip and on the structure at the right bottom of the image. These points are depicted by stars in Figure I-19. Similar characteristics were obtained on these three points and thus only the one performed on the DNA strand was reported.

Figure I-20 allows to follow the evolution of the curves, for both amplitude and phase versus tip-sample distance. These characteristics are representative of the non linear dynamic response of the cantilever with 4 different parts:

- A first gradual decrease of the phase and amplitude values versus the distance corresponding to the low branch, (mostly attractive interaction regime) from Figures I-20a, I-20b. Some noise appears on the phase curve near the setpoint value (Figures I-20a' – I-20b').

- A levelling of transition region between the two branches is observed for the amplitude, in Figure I-20c. It corresponds to a moderate fall and a sign inversion of the slope for the phase, in Figure I-20c'.

- A second gradual decrease of the amplitude along the high branch (mostly repulsive interaction regime) in Figures I-20d – I-20f and a sharp rise of the phase slope in Figures I-20d' – I-20f'.

- Finally, the amplitude carries on its decrease in Figure I-20g and the phase slope reaches a plateau beyond the setpoint value, in Figure I-20g'. All the setpoint values corresponding to the different curves were reported by dots on these last curves.

a $A_{sp}/A_{free} = 29.2\%$ SP=5

a´

b $A_{sp}/A_{free} = 22.6\%$ SP=4

b´

c $A_{sp}/A_{free} = 11.7\%$ SP=2

c´

d $A_{sp}/A_{free} = 9.1\%$ SP=1.5

d´

e $A_{sp}/A_{free} = 5.7\%$ SP=1

e´

f $A_{sp}/A_{free} = 4.7\%$ SP=0.75
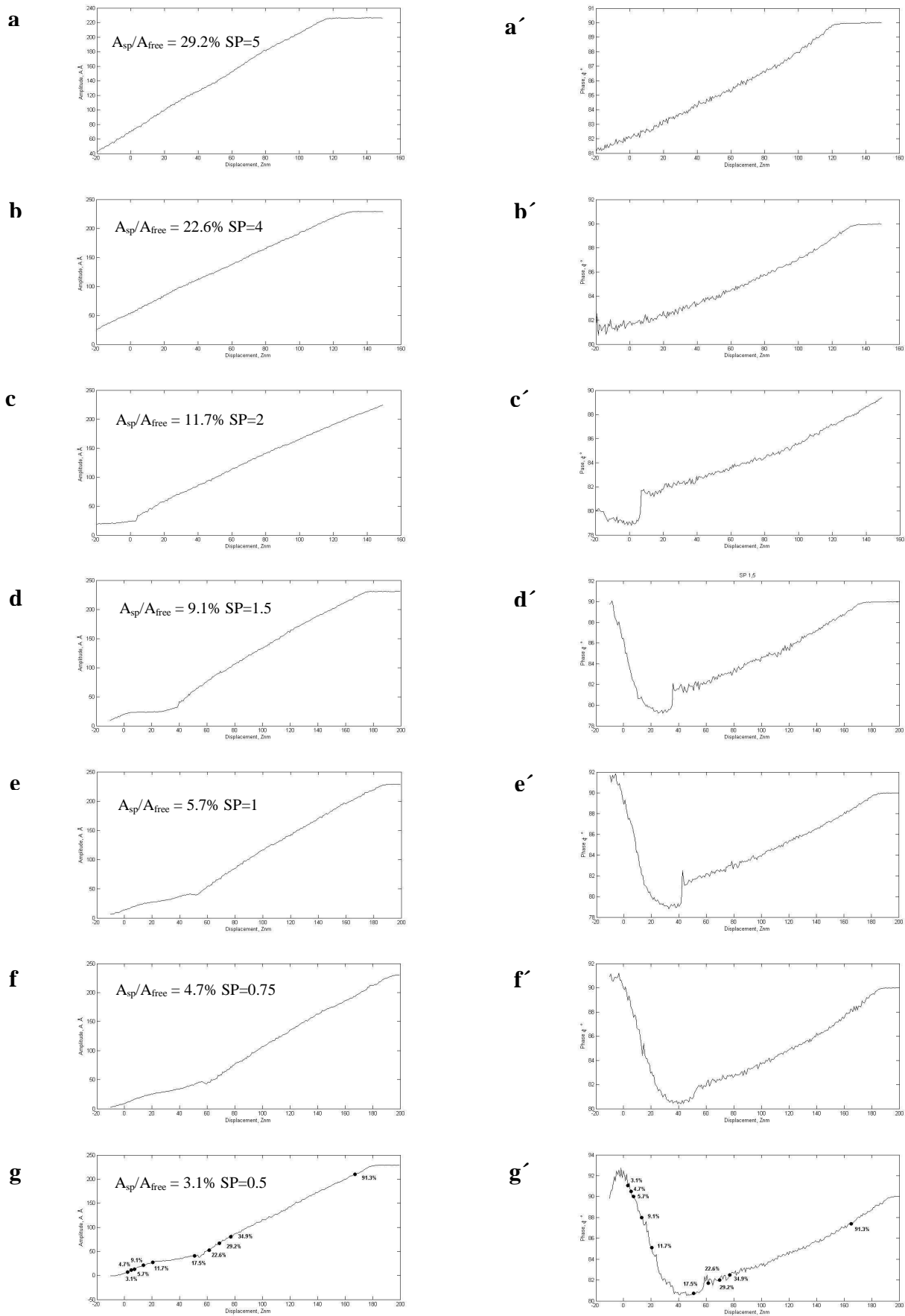
f´

g $A_{sp}/A_{free} = 3.1\%$ SP=0.5

g´

Figure I-20. Amplitude-vs-distance (a-g) and Phase-vs-distance (a´-g´) spectroscopic curves

IV-2-3 Topographic and phase shift images

For a specific ratio, both topographic and phase images were performed after spectroscopic curves. All the images were done on the same area. In order to ease comparison, the original images have been clipped (Figure I-21).

The A_{sp}/A_{free} ratio is successively decreased from 34.9% to 3.1%. Before 34.9%, no particular evolution of the images was observed. They looked similar to the topographic image for a ratio of 91.3% presented in Figure I-19.

Images in Figures I-21a, I-21b and I-21c were acquired at 34.9%, 22.6% and 11.7% respectively, which correspond to the bottom of the low branch on the amplitude versus distance curve (Figures I-20a – I-20c). Compared to Figure I-21a, they appear noisy at some places. The noise manifests also on the phase shift images (Figures I-21a' – I-21c'), at exactly the same location of the corresponding height images, i.e., close to the main features (for example: along the DNA strand). On the phase images, the colour full scale $\Delta\varphi$ extends nearly to the total range of 173.2°, 184.5° and 166.5° for Figure I-21b' and Figure I-21c', respectively. This noise is representative of instability of the tip during scanning. As the tip locally touches the surface, on the elevated features, the phase drastically changed, jumping from repulsive to attractive mode. It appeared in our fixed experimental conditions, because the feedback loop which tries to keep the amplitude constant, responds by re- retracting the probe from the sample, in order to increase the suddenly decreased amplitude to the fixed setpoint value. This instability is also visible on the phase curves (Figures I-20a'– I-20c'), and may correspond to the entry in the zone where the two branches coexist. Lee et al [116] have shown that for large free oscillation amplitude, the coexistence of different solutions gives rise to the presence of two stable states and one bistable state. The phase more sensitive to the repulsive region is noisy for these setpoint amplitudes (Figures I-20a' – I-20c'). The fact that line breaks were observed, at the same places, on both images, height and phase, indicates that the amplitude and the phase are not independent. This phase contrast may be related to phase jumps due to competition between the attractive and repulsive forces and is not due to dissipation [108]. In a remarkable review article, Giessibl estimated that instability can occur when the product of k and A reaches a value of roughly 100nN [117]. In our study, this optimal value is attained with our fixed parameters and can explain these break lines on the image. Obviously, this instability can be avoided by choosing appropriate values of k and A.

Figure I-21d was acquired at the transition region between low and high branches for an A_{sp}/A_{free} of 9.1%. On the topographic image, characteristic fringes show up around the main features whereas the phase image is particularly well-contrasted ($\Delta\varphi =147.1°$) and faithfully reflects the sample features (Figure I-21d'). However, there is a phase inversion on the probe islands: they appear as phase "holes" in Figs I-21a-c and phase "hills" in Figure I-21d. Such observations – fringes and phase inversion – are well-described in literature at the transition region [105, 106].
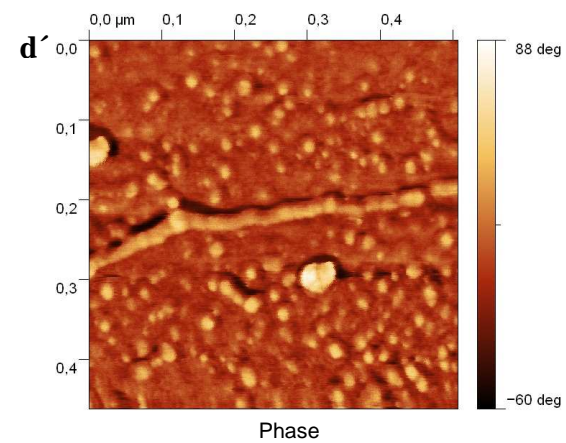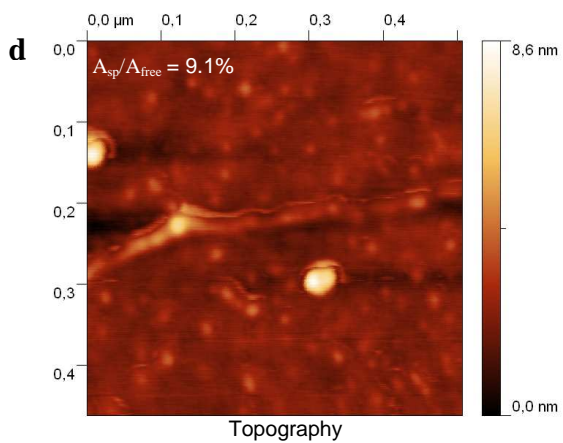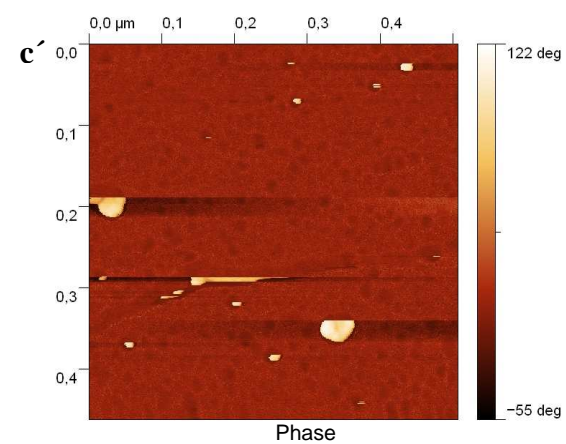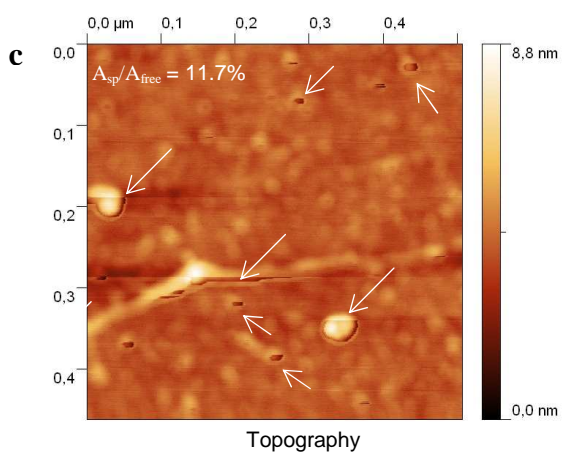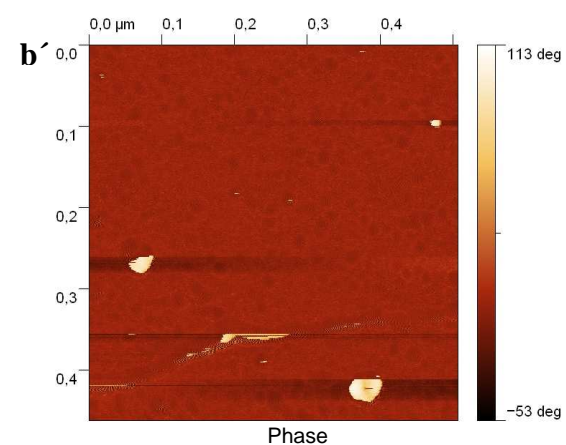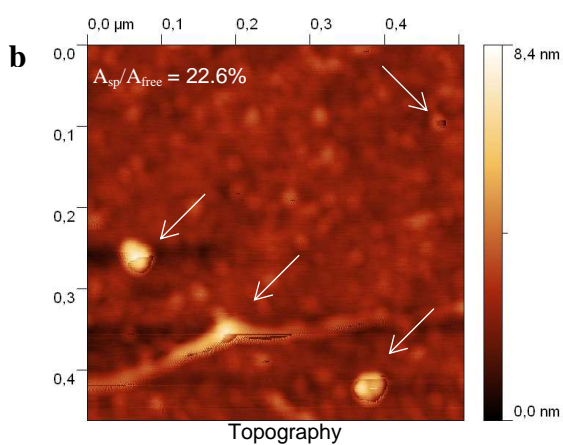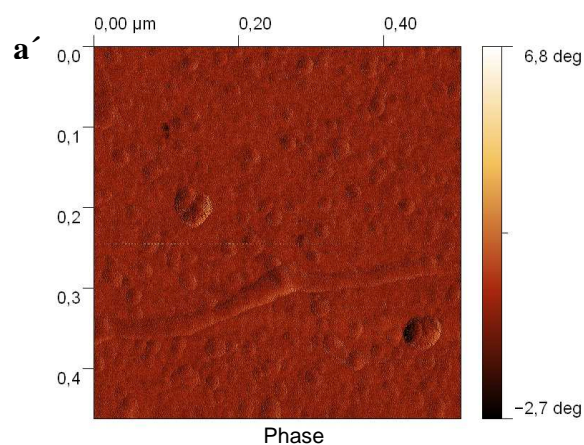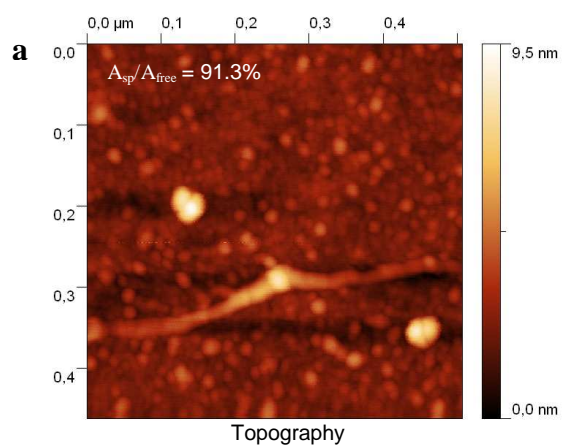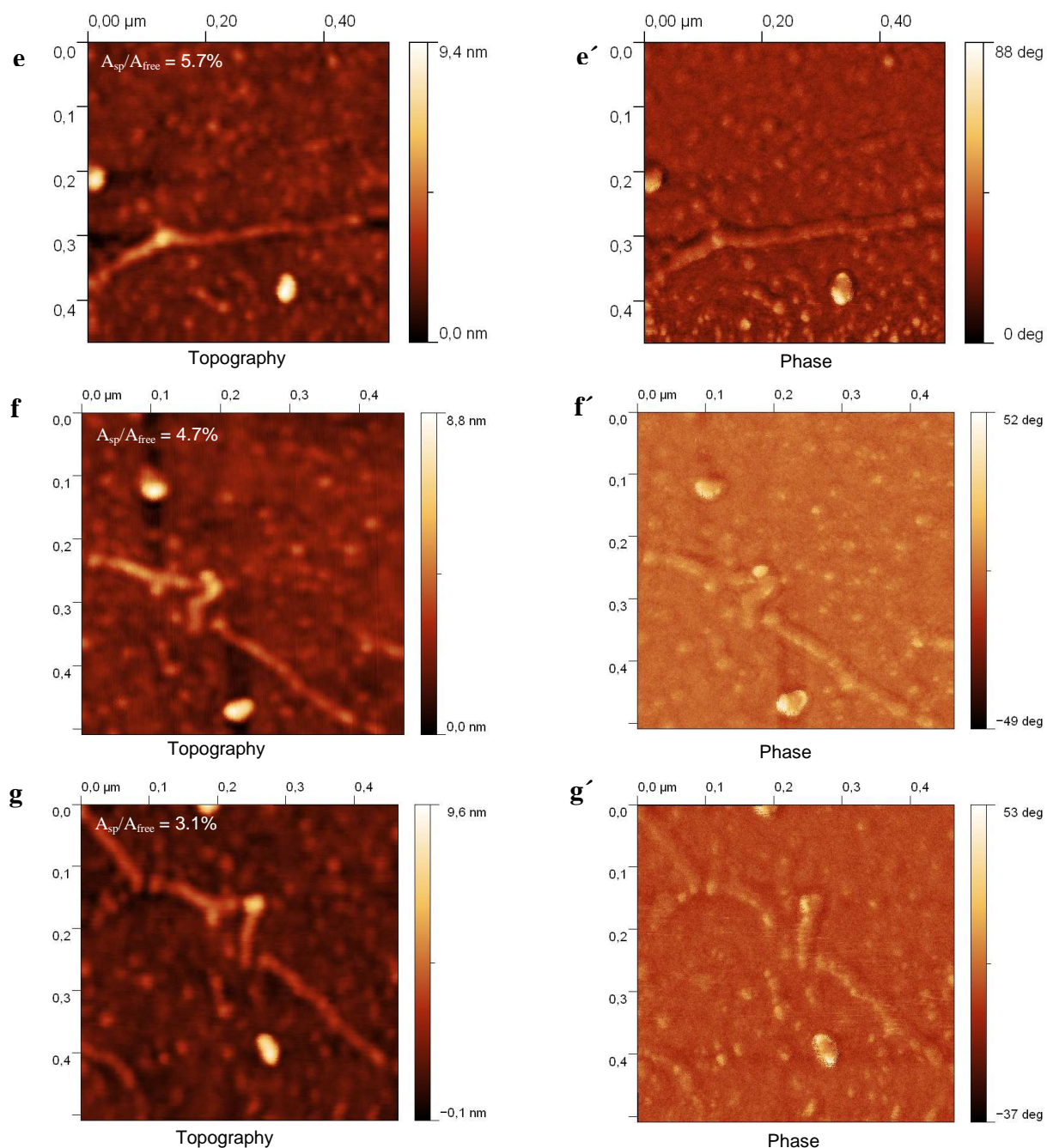
Figure I-21. Topographic (a-g) and Phase shift (a'-g') images

The probe islands have only little topography on top and have a height smaller than the level shift. In that case, the contrast may be reversed, called "reversal contrast". This phenomenon does not appear on the higher DNA features because their heights are globally higher than the level shift [105].

After this turning point, images were acquired in the high branch, mostly repulsive region, with ratio of 5.7%, 4.7%, and 3.1%, respectively (Figures I-21e-g). The system recovered its stability, the noise previously observed in Figures I-21a- I-21c disappeared. Relatively high quality topographic images are obtained without reaching the quality of the 91.3% ratio one. The phase images are still representative of the

surface but with a lower contrast than the one measured in Figure I-21d' ($\Delta\varphi$ = 87.3°, 80.7° and 83°, for Figures I-21e'-I-21g' respectively).

Note that, a too great amplitude reduction could induce the breaking of the DNA strand by the tip as shown in Figure I-21f. However, the tip could still image the surface without broadening features or inducing noise as can be seen in the following image for a ratio as low as 3.1% (Figure I-21g). We only observed the displacement of the disrupted part of the DNA. On the high branch, the tip is touching the surface once each oscillation cycle. The time spent in contact with the surface increases with the decreasing of A_{sp}/A_{free} ratio and is maximal on the largest and elevated part of the DNA where the breaking occurred.

IV-3 The dissipative energy

As the A_{sp}/A_{free} ratio evolves from 91.3% to 3.1%, we observe large variations in the phase shift images, with a maximal contrast for a ratio of 9.1%, in Figure I-21. Different theoretical as experimental studies [107, 108] have established a relationship between the phase shift of the tip motion and the energy dissipated by the tip-surface forces. In these studies, the average energy supplied to the cantilever per period is considered equal to the average energies dissipated either via hydrodynamic viscous interactions with the environment ($E_{med.}$) or by inelastic interactions at the tip-sample interface ($E_{dis.}$). According to the references [108] it leads to the following expression:

$$\sin\varphi = \frac{\omega A_{sp}}{\omega_0 A_{free}} + \frac{QE_{dis}}{\pi k E_{free} A_{sp}}$$ (eq.1.41)

It shows that phase shifts are exclusively associated to inelastic processes (A_{sp}/A_{free} = constant) in amplitude modulation AFM. For $\omega = \omega_0$, the previous equation can be rewritten in a more compact form:

$$E_{dis} = (\sin\varphi - \frac{A_{sp}}{A_{free}})\frac{A_{sp}}{A_{free}} F_e \ ,$$ (eq.1.42)

$$\text{with } F_e = \frac{\pi k A_{free}^2}{Q}$$ (eq.1.43)

In Figure I-22, the dissipative energy curve is deduced by applying equation (1.42) to the data presented in Figure I-20g'.
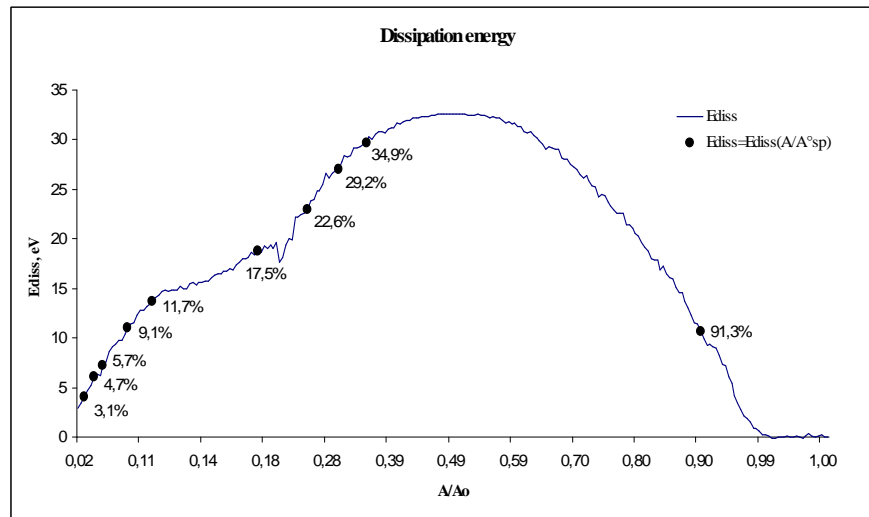
Figure I-22. Dissipation energy calculated for A_{sp}/A_{free} ratios from 91.3% to 3.1%

The particular ratios at which images were performed are depicted by black dots. This curve is in agreement with those presented by Garcia et al [118]. The area enclosed by the loop represents the dissipation. This shape is due to competitive effects [118]:

- The increase of energy dissipated in the sample when the amplitude ratio decreases from one unit to 0.5 because the interaction is increased.

- A reduction of the dissipated energy when the tip–surface separation decreases. A reduction of the tip-surface distance will imply a reduction of the force–distance area enclosed by approaching curves. Thus, in our specific experimental conditions, the maximal value of the dissipative energy, ~ 33eV per cycle, corresponds to A/A_0 ratio of 50%. Curiously, the optimal height image and the optimal phase image were obtained for amplitude ratio 91.3% and 9.1 % respectively, corresponding to roughly the same dissipation energy of 11eV.

Garcia et al [118] performed study of dynamic dissipation on samples with well known mechanical properties. It allows to associate characters of energy dissipation which determine the curve shape to tip-sample interaction regime and mechanical properties of the sample. They used silicon surface and polystyrene in polybutadiene matrix. Simulated (solid line) and experimental (circles) curves shown in Figure I-23a correspond to silicon surface when there is not mechanical contact between tip and surface. The curves in Figure I-23b were also measured on silicon surface where there are surface energy hysteresis and long-range interfacial interactions. The dissipation curve shown in Figure I-23c is made on polystyrene surface and present a quite similar symmetry as the curve in Figure I-23a. As it can be seen, the dissipation processes may considerably differ even on the same surface of silicon (Figures I-23a, b). This can be explained by different tip-sample interaction regimes: long-range attractive regime in the case of Figure I-23a and the transition between attractive and repulsive regimes of interaction for the Figure I-23b. However, obviously different mechanical properties of silicon and polystyrene are not visible on quite similar curves in Figures I-23a and I-23c [14].

47
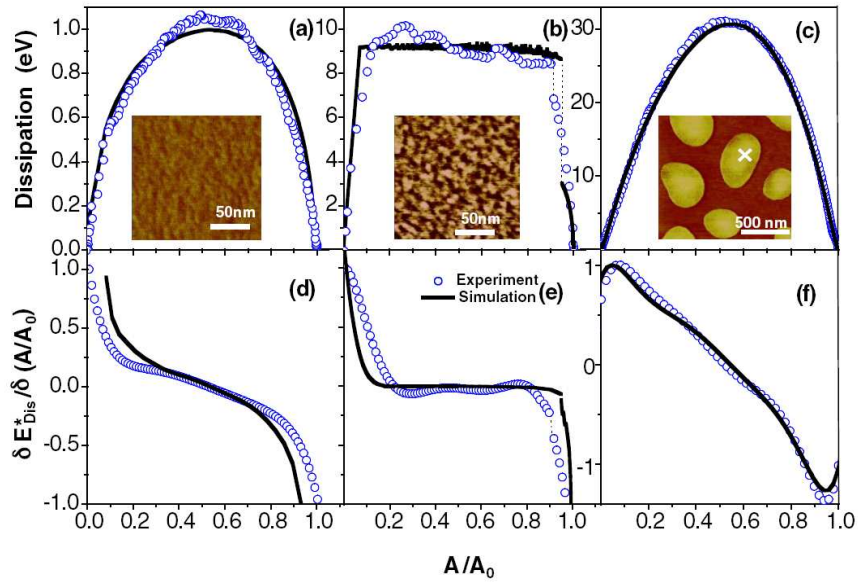
Figure I-23. Energy dissipation curves with their respective derivative curves obtained for silicon surface (images a, d; b, e) and polystyrene in polybutadiene matrix (images c, f) [118]

Actually, these curves in I-23a and I-23c correspond to two different interactions: long-range and viscoelastic interactions respectively. This was determined thanks to the identification method proposed by Garcia et al [118] which consists in the calculation of the derivative of measured dissipation energies. As it can be seen in Figures I-23d, e and f, the derivative unambiguously distinguishes each dissipative process.

In order to determine which interaction regime is responsible for dissipation processes in our experimental system, the derivative of the curve presented in Figure I-22 was calculated using algorithm that takes eight adjacent points. The derivative of dissipated energy $\delta E_{diss}/\delta(A/A_0)$ is plotted versus the amplitude ratio A/A_0 and represented in Figure I-24.
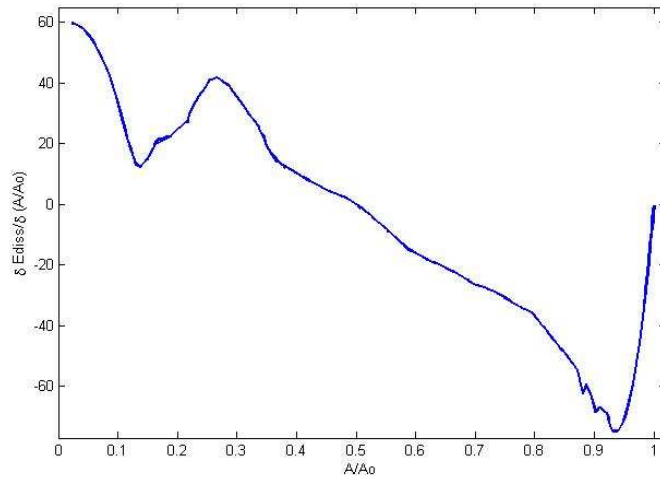
Figure I-24. The derivative of the dissipation energy corresponding to curve shown in Fig. I-22

As one can see, the derivative curve in Figure I-24 looks similar to the curve in Figure I-23f. Consequently, it can be concluded that the dynamic dissipation process of our system is mostly defined by a viscoelastic tip-sample interaction. However, the derivative in Figure I-23f corresponds to a polystyrene

48

sample which can be broadly considered as a perfect sample with given properties. In our experiment, dynamic measurements were performed on a sample composed of some hybridized DNA strands lying on a DNA single strand layer covalently bonded to a silicon surface by means of a silane layer. Then, these conditions are far from ideal model conditions. During one cycle, the tip interacts with a smooth layer (DNA and silane) and can reach the stiff material (silicon).This fact is responsible of the second local minimum in the experimental derivative curve at around $A/A_0 \sim 14\%$ (Figure I-24). Under this point, the change of the dissipation energy $\delta E_{diss}/\delta(A/A_0)$ begins to increase again until the moment when the DNA strand break. Namely, this increase which corresponds to A/A_0 ratios from 11.7% to 3.1% can be explained by the fact that under $A/A_0 \sim 14\%$ the increase of tip-sample interaction force (decrease of A/A_0) leads to a larger DNA indentation. This provokes a larger plastic deformation and consequently, larger dissipation losses. This ultimately causes the rupture of the DNA molecule for a A/A_0 below 4.7%.

The derivative of the dissipation energy (Figure I-24) explains why the breaking of the molecule did not arise for the maximal energy of 33eV but for a value of 6 eV more than five times lower (Figure I-22). The reason is that around $A/A_0 = 50\%$ (which corresponds to maximal energy of 33eV) the energy losses δE_{diss} per one oscillation cycle are not significant ($\delta E_{diss}/\delta(A/A_0) \sim 0$). However, for $A/A_0 = 4\%$ (which corresponds to maximal energy of 6eV, the energy losses become considerable ($\delta E_{diss}/\delta(A/A_0) \sim 60$).

Since the sample can appreciably be deformed during repulsive tapping, it is interesting to see if any compression of the DNA can be observed, when decreasing the A/A_0 ratio. A dependence has been observed by Round et al [119] in particular demonstrating a decrease of DNA height from 1nm to 0.46nm for DNA adsorbed on mica.

In Figure I-25, we reported the DNA height measured at three different locations (on hybridized zones).
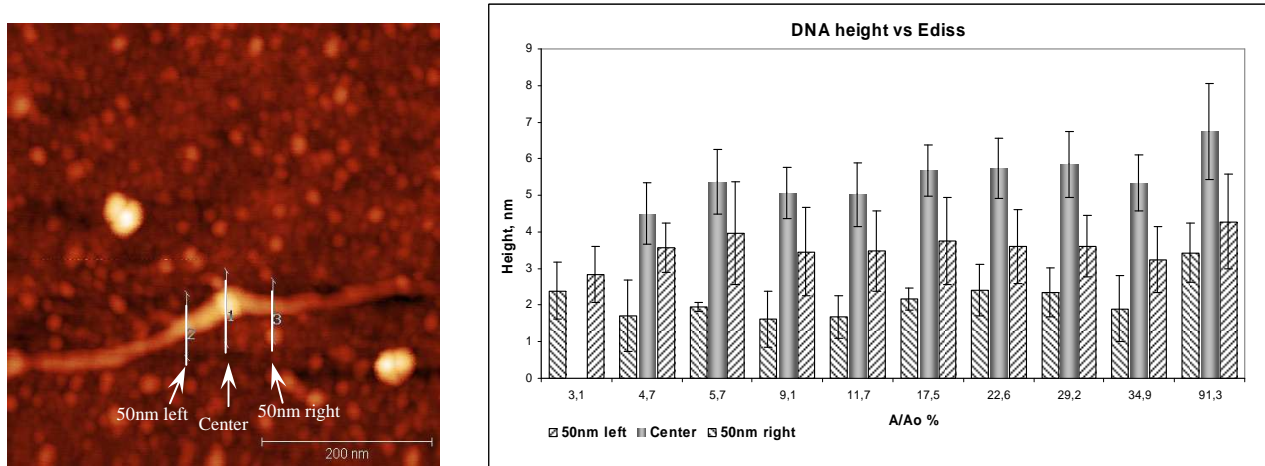
Figure I-25. Measured DNA heights as a function of setpoint value. b) experimental sample, zones of measurements are marked by arrows; b) measured heights in corresponding zones

In our case, there is almost no difference in the observed height of the structures on the left and on the right from the central part which corresponds to hybridized zone of two DNA molecules. The reason is probably due to the fact that the substrate material and the DNA structure are deformed equally much. One should remember that the hybridized DNA is lying on a DNA- silane layer and not directly on a stiff

substrate such as silicon or mica. However, the central part (marked as "center" in Figure I-25a) is affected by increased load for corresponding A/A_0 ratios from 91.3% to 4.7%. This deformation corresponds to 33% in comparison to initial height of 6.74nm (decrease from 6.74 nm to 4.5nm). For the $A/A_0 = 3.1\%$ the hybridized zone was almost totally broken and that is because for this ratio only the heights of single DNA strands ("left" and "right" markers in Figure I-25b) were measured. It is worth to note that the measured heights in Figure I-25b (it relates more to the central and located on the right zones) are larger than 2nm. This indicates that the hybridized zone involves more than 1 double-stranded DNA molecules.

IV-4 Conclusion

We have studied the dependence of the phase shift on the tip-surface separation, interaction regime, cantilever properties and excitation force. Phase shift data depend on the sign of the average value of the interaction force. Consequently, they can be used to characterize the interaction regime controlling the tip motion. Using intermediate oscillation amplitudes, and relatively soft cantilevers, we showed that, the system could present instabilities that induce noise on the images and contrast artifacts. This noise is present on a large part of the high branch. The setpoint amplitude should be chosen carefully towards the free amplitude to obtain noiseless height image and characteristic phase image. As expected, a setpoint close to the free amplitude gives the optimal height image, and close to the phase slope change gives the optimal phase image. We also showed that the phase shift images are not always correlated to energy dissipation. In fact, the energy dissipation is very low in our system of DNA strands lying on a DNA chip, and the maximal phase contrast is obtained for a setpoint corresponding to the start of the low branch where the repulsive interaction appeared.

We demonstrated that by converting phase shifts into the dissipation energy it is possible to follow the dynamics of dissipation processes during scanning, and from the derivative of dissipation energy, information about the tip-surface interaction regime. Compositional contrast of images is illustrated by imaging conjugated molecular islands deposited on silicon surfaces. Because the maximum in the energy dissipation curves is about 30eV per cycle, material contrast may be achieved without introducing irreversible tip-surface modifications.

V - Statistical analysis of the AFM images

Scanning probe microscopy such as STM or AFM give information of the surface topography and this information have to be quantify by parameters. Surface roughness is one of the most important characteristic of a surface and plays an important role in the functional performance of many engineering components. The importance of the relationship between surface microstructure of a thin film and its functionality will be discussed for pentacene based OFETs in Chapter 2.

The term "topography" represents all spatial structure of irregularities that exist on a surface. The roughness consists of the closely spaced peaks and valleys with a typical roughness height and a typical roughness spacing. Roughness is usually produced by the basic forming process of a surface and, therefore, has characteristic structure related to this process. Often, the terms surface roughness, surface topography and surface texture can be used interchangeably. Usually, if we talk about topography we principally refer to the roughness itself.

In general, surface topographies are highly complex and statistical by nature, because the characterization of such a surface requires a statistical description.

Surface roughness can be described by variety of techniques based on different physical principles of measurements. In addition, measured data may be processed and presented by various ways. There are basically two general methods of description:

- Parameters that quantify some aspects of the surface statistic with a single number (such as root mean square RMS roughness),
- Surface statistical functions (such as power spectral density PSD).

Many of these statistical parameters and functions have been developed previously for the characterization of random processes.

V-1 Surface statistical parameters

Roughness is often described as the variation of heights in regards to a reference surface plane. A convenient way of describing the roughness is in terms of profile height $h(x, y)$ in each point of coordinates x and y of the surface.

The roughness of surfaces carried out with AFM is often expressed by commonly used statistical parameters such as peak-to-valley roughness (R_{pv}), average roughness (R_a) and RMS roughness σ (R_q), which represents the root-mean-square deviation of the height of a surface relative to its mean value. For a digitized image of NxM pixels with a given height h, in each point x_n and y_n , these parameters are defined as follow:

$$R_{pv} = h_{\max} - h_{\min} \qquad (eq.1.44)$$

$$R_a = \frac{1}{NM} \sum_{n=1}^{N-1} \sum_{m=1}^{M-1} \left| h(x_n, y_m) - \overline{h} \right| \qquad (eq.1.45)$$

$$R_q = \left(\frac{1}{NM} \sum_{n=1}^{N-1} \sum_{m=1}^{M-1} [h(x_n, y_m) - \overline{h}]^2 \right)^{\frac{1}{2}} \qquad (eq.1.46)$$

where $\overline{h}$ is the average height defined as

$$\overline{h} = \frac{1}{NM} \sum_{n=1}^{N-1} \sum_{m=1}^{M-1} h(x_n, y_m) \qquad (eq.1.47)$$

Parameters R_a and R_q are both useful for describing the average height of the surface profile and are widely used for general morphology control.

However, these statistical representations provide information only on the vertical deviation of the roughness profile and do not take into account the lateral distribution of the surface features. In general, these parameters are insensitive to small changes in profile geometry and also to intrinsic properties of the profile. In these cases, the information about roughness properties is represented by a single number and can not be considered as complete. For example, two images of different surface morphologies may exhibit exactly the same RMS values [120, 121].

V-2 Surface statistical Function:PSD

V-2-1 General description

Both vertical and lateral information can be reached by spectral and correlation techniques based on Fourier transformation. In particular, a more complete description can be provided by the power spectral density (PSD) of the surface topography. PSD function performs decomposition of the surface profile into its spatial wavelengths and allows comparison of roughness data taken over various spatial frequency ranges. Such methodology also offers a representation of the direct space periodicity and roughness amplitude. In

this way, PSD functions contain information about two general aspects of the surface roughness such as the variations of height from a mean plane, and the lateral distance over which this variation occurs [122]. Therefore, PSD describes a surface much better than the RMS roughness.

To determine the power spectral density of the surface roughness, the variations of height $h(x,y)$ in real space of AFM image can be transformed in reciprocal frequency space by the Fourier transform (FT) [123]:

$$F(k_x, k_y) = (\frac{L}{N})^2 \sum_{n=1}^{N-1} \sum_{m=1}^{N-1} h(n,m) \times \exp\left\{ (\frac{-i2\pi}{N})(k_x n + k_y m) \right\} \qquad \text{(eq.1.48)}$$

where L is the scan size, N is the number of pixels per line, k_x and k_y are the reciprocal position vectors for each point in real space.

Then, the two-dimensional power spectral density of the Fourier transform of the topography $h(x,y)$ is defined as

$$PSD(k_x, k_y) = \frac{1}{L^2} \left| F(k_x, k_y) \right|^2 \qquad \text{(eq.1.49)}$$

However, this two-dimensional information is complex and for the interpretation of the measurements difficult to reach [124]. In order to facilitate the analysis concepts, we will take into account only the surface profiles measured along the AFM fast-scan direction. This goal can be reached by extracting a 1D magnitude of the 2D transform. As a result 1D PSD can be plotted in function of the spatial frequencies:

$$PSD(k_x) = \frac{1}{L} \left(\sum_{n=1}^{N-1} h(n) \times \exp(\frac{-i2\pi}{N} k_x n) \right)^2 = \frac{1}{L} \left(F(k_x) \right)^2 \qquad \text{(eq.1.50)}$$

This one-dimensional spectral analysis provides a good representative description of the overall surface roughness.

Another useful representation of the 2D reciprocal space is the radial PSD (rPSD). In the rPSD description, the angular average of the 2D power spectrum is taken, using the radius, k_θ. In the reciprocal space, k_θ is the spatial frequency, normalized by the number of pixels used to define the radius. The resulting 1D PSD is expressed as a function of radial frequencies k_θ (eq. 1.51):

$$PSD(k_\theta) = \frac{1}{L^2} \left| F(k_x, k_y) \right|^2 \qquad \text{(eq.1.51)}$$

where $\quad k_\theta^2 = k_x^2 + k_y^2$.

The radial PSD (eq. 1.51) is a more rigorous tool for the analysis of anisotropic surfaces than the two-dimensional PSD because it takes into account the correlation heights for all angles and not only one direction (eq. 1.49) [125].

As it was mentioned above, real surface roughness is random and statistically disordered [126]. A surface profile can be considered as a superposition of spatial waves with increasing frequencies in regard to the multi-scale nature of roughness. In terms of fractal geometry, it has been demonstrated recently that the fractal geometry and scaling concepts can describe the rough surface morphology [127, 128]. The surface morphology at different scales is believed to be self-similar and related in the fractal geometry, or in another words, the symmetry of the surface is unchanged at different scales. The ability of fractal analyses to extract many different types of information from measured textures compared to common, conventional analyses makes this approach very useful in describing surface characteristics of thin films. Several studies have demonstrated that the complexity of thin film morphology were fractal in nature, and can be characterized quantitatively by the fractal strengths and their dimensions as well [127, 128].

Therefore, the PSD is useful for studying the strength of various periodic components in the surface profile.

The PSD spectra calculated from AFM images include roughness values in a limited bandwidth of spatial frequencies. This range is determined by length scale and sampling rate in general case. It also can be additionally restricted by the influence of measurements artefacts.

The spatial frequency range lies between the inverse image size *(1/L)* and the high-frequency limit f_{max} $= N/(2L)$ (the Nyquist frequency), where N is the number of pixels per scan line.

Figure I-26 presents a typical PSD spectrum of a thin film deposited on a bulk substrate.

All power spectra exhibit three distinct regions, represented as parts I, II and III.

– The region I includes the low spatial frequencies which correspond to a nearly constant value of the roughness. This low-frequency plateau means an absence of correlation (it does not change with the scale) and indicates an absence of any characteristic length.

– The next region II involves intermediate frequencies. For this high-frequency range the PSD is strongly frequency dependent and represents the power-law decay. This region characterizes the mechanism of surface formation and indicates the surface self-affine behaviour [129].

– The region III corresponds to the highest frequencies of the spectrum. This range of spatial frequencies correlates with physical dimensions of the AFM tip. Therefore, the convolution of the tip and surface features occurs and consequently, PSD is highly affected by AFM tip artefacts and can not be considered for further surface analysis.
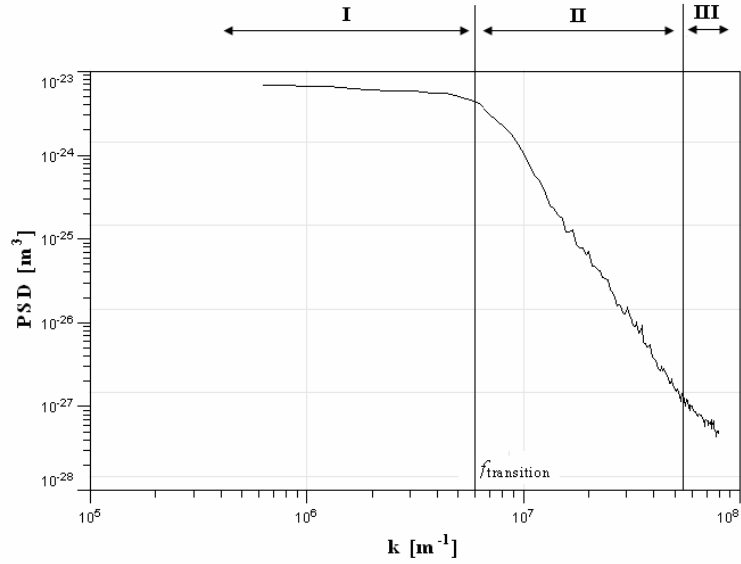
Figure I-26. Typical *PSD* spectrum of a thin film deposited on a bulk substrate.

Consequently, we can summarize that the experimental PSD curves are constant at low frequencies and exhibit an exponential dependence at high frequencies. This statistical function is well adapted to characterize the roughness of polycrystalline films with self-affine properties and will be used in chapter 2 for the study of the pentacene growth on two isolating polymers.

The scaling laws can be applied to describe the surface topography [130].

$$\text{PSD}(f) = \begin{cases} Kf^{-\gamma}, & 1/f < \xi \\ A, & 1/f > \xi \end{cases}$$

(eq.1.52)

where *K* and *A* are constants, γ is the roughness related exponent and ξ is the correlation length.

The transition between the low-frequency plateau and the high-frequency self-affine region (transition between regions *A* and *B*) is related to some spatial frequency $f_{\text{transition}}$ that determines the characteristic length (ξ). The characteristic length (ξ) is defined as the *correlation length* and can be calculated as the inverse of the transition frequency between two regions ($\xi = 1/f_{\text{transition}}$).

The correlation length represents the minimum distance between two points at the surface which are not affected by each other. In another words, the correlation length corresponds to the mean distance between two grains in the case of nanocrystalline films. In case of dense surface features, the parameter (ξ) defines the mean grain diameter. Therefore, in general case, the correlation length describes transitions between physical processes involved in the surface evolution.

The classical way to calculate the correlation length consists in determining the transition frequency $f_{\text{transition}}$ in the intersection point of the two fitting curves of regions *A* and *B* in the PSD spectra.

The slope (γ) of the region II is related to the scaling exponent of the surface. This scaling exponent (α) describes the processes controlling the surface morphology during the growth and the mechanism

55

responsible for the films deposition [130, 131]. Firstly, the scaling approach was introduced for studying self-assembled surfaces. In such surfaces, the PSD can be described by power-law function $PSD(f) \approx f^{-\gamma}$, where $\gamma = 2(1+\alpha)$, for distances inferior to the correlation length (ξ). This power-low decay indicates a self-affine behaviour, i.e., the RMS roughness $\sigma \approx L^{\alpha}$.

In order to determine the slope of the high-frequency region II, the exponential part of the PSD was fitted using the expression (1.52), which gives for asymptotic range ($f \rightarrow \infty$):

$$PSD(f) = Kf^{-\gamma} \qquad \text{(eq.1.53)}$$

The scaling exponent is equal to 1 ($\alpha = 1$) if a single slope is selected, which in most cases corresponds to circular shapes of grains. If the grains are not regular (not circular), the slope is not uniform and α becomes smaller than 1 ($\alpha < 1$).

However, a real sample is composed of the superposition of surface profiles which results in the superposition of Fourier transformations. Consequently, in the frequency domain, the influence of some dominant sample characteristics can be separated. One can consider two dominant characteristics: the substrate surface and the superstructure of the film [132].

The separation of each contribution is strongly affected by the magnitude of the difference between film features and substrate which is determined by a relation between the corresponding correlation lengths (ξ) (as shown in Figure I-27)
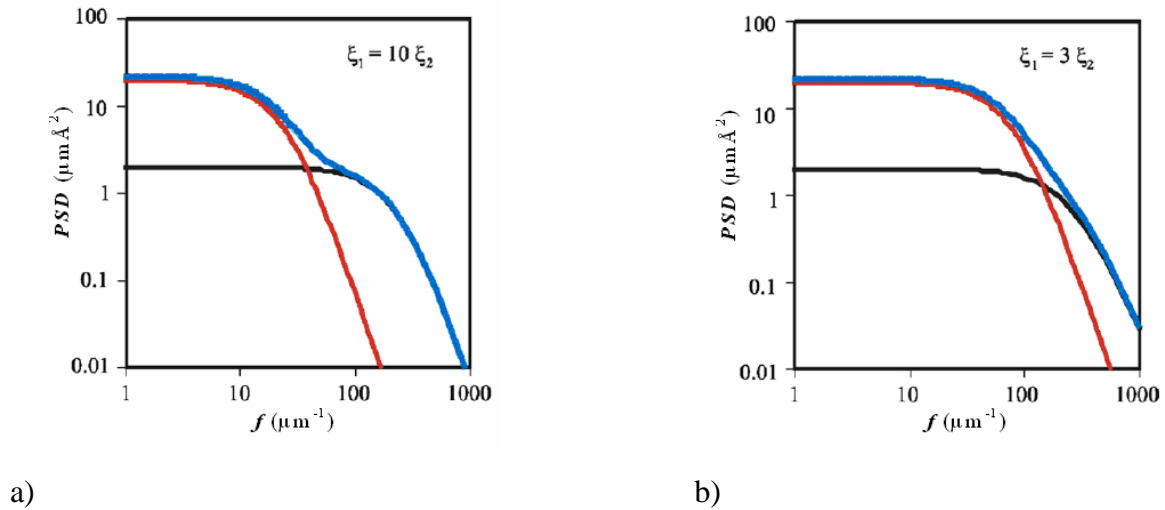
Figure I-27. Superposition in blue of the PSD of the thin film (black) and the substrate (red) a) ξ_1, ξ_2 corresponds to the correlation length of substrate and thin-film respectively (adapted from [13]).

Figure I-27a shows that if the correlation length of the substrate is ten times higher than the correlation length of the thin-film, a well-defined separation of each contribution can be observed. However, real surfaces usually exhibit a graded superposition with unapparent separation region that is the case for a correlation length ratio of 3 in Figure I-27b.

In general, the direct application of the k-correlation model gives an approximation of the sum of the pure film PSD and the substrate PSD [133] and consequently only effective parameters of sample roughness can be obtained.

In order to describe all surface roughness contributions, the analytical models should include the mathematical terms describing the properties of the substrate, pure film and superstructures (aggregates).

V-2-2 Analytical description of PSD

However, to interpret an experimental PSD function more qualitatively, an appropriate analytical approach is highly essential. Several models have been introduced to describe the specificities of surface morphologies. Basically, these models consist of approximation functions (or their combinations) of an experimental PSD curve and their using is often limited by some specific application areas.

For example, one of the wide used models appropriate for PSD of a thin film is the sum of Henkel transforms of Gaussian and exponential autocorrelation functions [134-136]. However, this model is not efficient for large spatial frequencies range.

In order to describe the PSD over a large spatial frequency bandwidth, the model should take into account the roughness contribution from all features of the surface.

In this study, we will focus on three analytical models which will be used to fit the experimental PSD curves:

- the k-correlation model (PSD_{ABC}).
- the fractal analytical model ($PSD_{fractal}$),
- the superstructures (PSD_{sh})

V-2-2-1 The k-correlation model

The PSD function of a random rough surface can be conveniently characterized over a large length scale by the *k-correlation model*, also called the *ABC model* [137]. In fact, it gives an appropriate analytical description of the PSD of a pure film by its functional parameters *A*, *B* and *C*. In this model, the PSD function is described as follow:

$$PSD_{ABC} = \frac{A}{(1 + B^2 f^2)^{(C+1)/2}}$$
(eq.1.54)

where *A, B, C* are the functional parameters.

57

A is the magnitude at low spatial frequency, which relates to the height of the rough surface.

B determines the position of the 'knee', which is related to correlation length representing the mean grain size.

C is the inverse slope at high spatial frequency range, which gives the nature of the roughness and can be related to different growth mechanisms [138] (Figure I-28).

Typically, C=1 relates to a viscous flow

C=2 to an evaporation and condensation mechanism

C=3 to bulk diffusion, and finally

C=4 to surface diffusion.
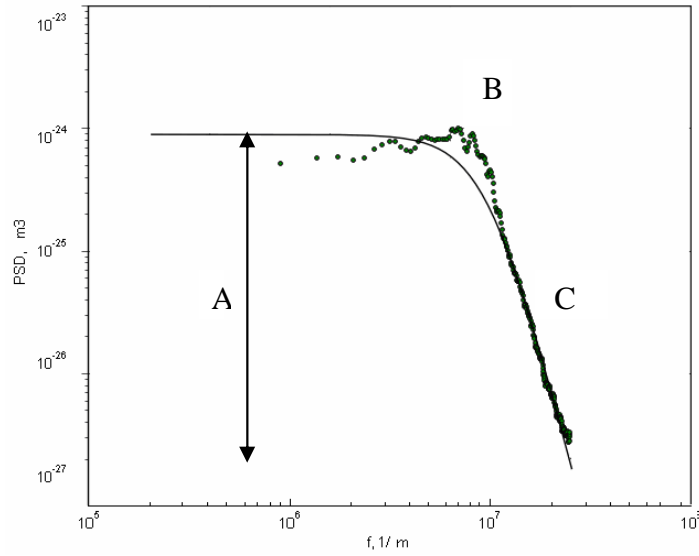
Figure I-28. Fitting of PSD function by the *k*-correlation model:

identification of the 3 functional parameters A, B, C

In addition, intrinsic roughness parameters σ_{ABC} and τ_{ABC} which represent respectively the equivalent RMS roughness and the correlation length can be calculated from the functional parameters using the following equations:

$$\sigma^2_{ABC} = \frac{2\pi A}{B^2(C-1)} \qquad\qquad \tau^2_{ABC} = \frac{B^2(C-1)^2}{2\pi^2 C} \qquad\qquad \text{(eq.1.55)}$$

The σ_{ABC} value can be compared to the RMS roughness value calculated on the whole image in the direct space. This would allow the comparison of different methods of measuring of the same morphological parameter. The correlation length τ_{ABC} gives a more precise description of the features size than the simple expression of *B* in this model.

V-2-2-2 The fractal model

Most of deposition processes (including chemical and physical vapour deposition CVD and PVD) are random in nature, that produces not perfectly packed and disordered thin film surfaces. The appropriate methods of analysis of such complex surfaces make it possible to relate their structure with morphology evolution. One of the more effective methods is the analysis of fractal geometry of rough surface morphology, which takes into account its scaling concepts and elements of symmetry. For surfaces with fractal geometry, the symmetry means that thin film morphology at different scales is characterized by self-affinity [139]. Thin film morphology can be quantitatively characterized by fractal strengths and fractal dimensions that allow to obtain many useful information about the thin film structure. It makes this approach very suitable comparing to common conventional analyses.

The PSD of the substrates generally follows a fractal model which can be described by the inversed power law [140]:

$$PSD_{fractal}(f, K, v) = \frac{K}{f^{v+1}}$$ (eq.1.56)

where f is the spatial frequency, K is the spectral strength and v is the spectral index.

The fractal dimension D_f can be obtained from the assumption that the substrate is self-affine (that is the case for the majority of substrates [140]) and is given by:

$$D_f = \frac{1}{2}(7 - (v+1)) = \frac{1}{2}(6 - v)$$ (eq.1.57)

To determine the fractal components, the high-frequency region (region II) of the PSD curves (Figure I-26) were fitted with the $PSD_{fractal}$ model given by eq. (1.56).

The fractal dimension takes into account the substrate influence and provides the information about the relative amounts of the surface irregularities at different scales.

Three fractal dimension values are significant [139]:

- The marginal fractal which corresponds to $D_f = 2$;
- The brownian fractal: $D_f = 2.5$;
- The extreme fractal: $D_f = 3$.

More precisely, the fractal dimensions $D_f = 2$ ($\nu=2$) and $D_f = 3$ ($\nu=0$) correspond to three dimensional thin film growth. Both marginal and extreme fractal geometries can be explained by the modified ballistic deposition model which takes into account the thin film sticking probability factor (The ballistic deposition model is the model of low-temperature thin film growth. This model considers that particles randomly fall on initially flat surface and thus they became part of the substrate [141]. The sticking probability defines the probability of each deposited particle to stick to the surface in the point of first contact). Namely, the case of $D_f = 2$ corresponds to flat surfaces with low sticking probability, whereas the $D_f = 3$ is associated with high sticking probability factor [141]. The case of $D_f = 2.5$ ($\nu=1$) indicates the presence of Brownian fractals in surface morphology and is related to strong dependence of microstructure nature on deposition parameters [139].

V-2-2-3 The superstructure model

The real experimental thin films are often characterized by the formation of superstructures (aggregates) on the surface. Such complexity of the sample morphology manifests by the presence of local maxima in the low-frequency region of the PSD curve. However, all the above models are monotonically decreasing functions of spatial frequency and can not explain these additional morphological features.

To characterize the superstructures on the surface the superstructure PSD model, PSD_{sh} can be used. This model is a Gaussian function with its peak shifted to a non-zero spatial frequency [142, 143]:

$$PSD_{sh}(f;\sigma_{sh},\tau_{sh},f_{sh}) = \pi\sigma_{sh}^2\tau_{sh}^2 \exp[-\pi^2\tau_{sh}^2(f-f_{sh})^2] \qquad \text{(eq.1.58)}$$

More precisely, the superstructure model corresponds to a Gaussian function multiplied by a cosine, the frequency of which corresponds to the spatial frequency f_{sh} of the superstructures on the surface. This frequency is determined as the shift of the PSD maximum to the frequency f_{sh} (from this implies the origin of model name PSD_{sh} i.e. "*sh*" – "*shift*"). The other model parameters τ_{sh} and σ_{sh} are related to size and height of the superstructures respectively.

An example of fitting an experimental PSD curve with the superstructure model, in comparison with already discussed approaches (fractal and ABC-model), is shown in Figure I-29.
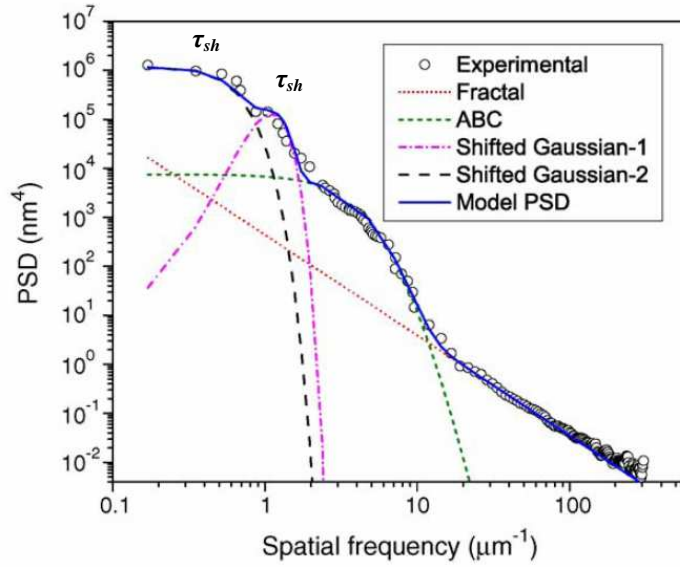
Figure I-29. Fitting of a PSD curve by the superstructure model together with fractal and ABC-models [143]

Most of the thin-films obtained by deposition from vapor phase are usually characterized by the presence of more than one local maximum in the low-frequency range of PSD curve. Each of these peaks is related to superstructures with different τ_{sh} and σ_{sh}. Inaccessible to the k-correlation and fractal models (chapters V-2-2-1 and V-2-2-2), the mean superstructure size τ_{sh} and height σ_{sh} can be calculated through the fitting of experimental PSD curve by a Gaussian function with a shifted peak (eq. 1.58).

VI - Conclusion

Information that can be achieved from experimental AFM images depends on method used for their analysis. Commonly used methods of surface analysis give information on sample properties in normal to its surface direction. However, described in PSD-method gives access to the surface properties in two dimensions i.e. in vertical and lateral directions.

The application of this method to AFM images is possible thanks to their high spatial resolution. It allows their transformation into 2D reciprocal Fourier space and then representation in 1D graph (PSD curve). Analysis of experimental PSD-curves was performed with fractal and nonlinear parametrical models which provides exhaustive information not only on the accessible surface of the sample but also on its inner structural properties.

Actually, the fractal model describes self-affine properties of the surface providing its fractal dimension which is for example related to mechanism of deposition for thin films obtained by CVD method. Whereas k-correlation (or ABC) and superstructures models provide information about growth mechanisms of thin films and give quantitative description of vertical and lateral dimensions of the surface features and their aggregates.

All these methods complete each other and provide exhaustive description not only of the accessible surface of the sample but also of its inner structural properties.

VII - References:

[1] W. Demtröder, Springer Berlin, 1988.

[2] V. V. Ngo, M. Hernandez, B. Roth, D. C. Joy, Microscopy Today 15(2), 12-16 (2007).

[3] G. D. Danilatos, Advances in Electronics and Electron Physics 71, 109-250 (1988).

[4] http://www.ntmdt.com/

[5] G. Binnig, H. Rohrer, C. Gerber, and E.Weibel. Physical Review Letters, 49(1):57–61, July 1982.

[6] G. Schmalz. Zeitschri des Verbandes Deutscher Ingenieure, 73:144–161, October 1929.

[7] R. Young, J. Ward, and F. Scire. Physical Review Letters, 27(14):922–924, October 1971.

[8] G. Binnig and H. Rohrer. Reviews of Modern Physics, 59(3):615–625, July 1987. Nobel Lecture.

[9] R. Young, J. Ward, and F. Scire. Review of Scientific Instruments, 43(7):999–1011, July 1972.

[10] D. Drakova. Reports on Progress in Physics, 64:205–290, 2001.

[11] W. A. Hofer, A. S. Foster, and A. L. Shluger. Reviews of Modern Physics, 75:1287–1331, October 2003.

[12] G. Binnig, C. F. Quate, and C. Gerber, Physical Review Letters 56(9), 1986, 930–933.

[13] J.Israelachvili, Academic Press, London, 1992

[14] F. London, Faraday Soc. 33 (1937) 8.

[15] A.D. McLachlan, Proc. R. Soc. London A 202 (1963) 224.

[16] B.V. Derjaguin, Kolloid Zeitschrift 69 (1934) 155.

[17] H. Hertz, J. Reine Angew. Math. 92 (1882) 156.

[18] K.L. Johnson, K. Kendall, A.D. Roberts, Proc. R. Soc. London A 324 (1971) 301.

[19] B.V. Derjaguin, V.M. Muller, Y.P. Toporov, J. Colloid Interf. Sci. 53 (1975) 314.

[20] H.-J. Butt, P. Siedle, K. Seifert, K. Fendler, T. Seeger, E. Bamberg, A.L. Weisenhorn, K. Goldie, A. Engel, J. Microsc.169 (1993) 75.

[21] D. Maugis, J. Colloid Interf. Sci. 150 (1992) 243.

[22] J.A. Greenwood, K.L. Johnson, Phil. Mag. 43 (1981) 697.

[23] M.A. Lantz, S.J. O'Shea, M.E. Welland, K.L. Johnson, Phys. Rev. B 55 (1997) 10776.

[24] W.J. O'Brien, J.J. Hermann, J. Adhes. 5 (1973) 91.

[25] L. Bocquet, J.L. Barrat, Phys. Rev. Lett. 70 (1993) 2726.

[26] M. Fuji, K. Machida, T. Takei, T. Watanabe, M. Chikazawa, Langmuir 15 (1999) 4584.

[27] X. Xiao, L. Qian, Langmuir 16 (2000) 8153.

[28] R. Jones, H.M. Pollock, J.A.S. Cleaver, C.S. Hodges, Langmuir 18 (2002) 8045.

[29] L. Sirghi, M. Nakamura, Y. Hatanaka, O. Takai, Langmuir 17 (2001) 8199.

[30] T. Stifter, O. Marti, B. Bhushan, Physical Review B 62 (2000) 13667.

[31] Q. Ouyang, K. Ishida, K. Okada, Appl. Surf. Sci. 169 (2001) 644.

[32] B.V. Derjaguin, L. Landau, Acta Physicochim. URSS 14 (1941) 633.

[33] E.J.W. Verwey, J.T.G. Overbeek, Elsevier Publishing Inc., New York, 1948.

[34] P. Debye, E. Huckel, Physikalische Zeitschrift 24 (1923) 185.

[35] M. Gouy, J. Phys. (Paris) 9 (1910) 457.

[36] D.L. Chapman, Phil. Mag. (London) 25 (1913) 475.

[37] R. Hogg, T.W. Healy, D.W. Fuerstenau, Trans. Faraday Soc. 62 (1966) 1638.

[38] H.J. Butt, Nanotechnology 3 (1992) 60.

[39] V.A. Parsegian, D. Gingell, Biophys. J. 12 (1972) 1192.

[40] D.E. Yates, S. Levine, T.W. Healy, J. Chem. Soc., Faraday Trans. I 70 (1974) 1807.

[41] P. Attard, Adv. Colloid Interf. Sci. 104 (2003) 75.

[42] J.N. Israelachvili, R. Pashley, J. Colloid Interf. Sci. 98 (1984) 500.

[43] P.M. Claesson, H.K. Christenson, J. Phys. Chem. 92 (1988) 1650.

[44] Q. Lin, E.E. Meyer, M. Tadmor, J.N. Israelachvili, T.L. Kuhl, Langmuir 21 (2005) 251.

[45] J. E. Sader. Review of Scientific Instruments, 74(4):2438–2443, April 2003.

[46] J.P. Cleveland, S. Manne, D. Bocek, P.K. Hansma, Rev. Sci. Instrum. 64 (1993) 403.

[47] T.R. Albrecht, S. Akamine, T.E. Carver, C.F. Quate, J. Vac. Sci. Technol. A 8 (1990) 3386.

[48] G.Y. Chen, R.J. Warmack, T. Thundat, D.P. Allison, A. Huang, Rev. Sci. Instrum. 65 (1994) 2532.

[49] T. Thundat, R.J. Warmack, G.Y. Chen, D.P. Allison, Appl. Phys. Lett. 64 (1994) 2894.

[50] A. Khan, J. Philip, P. Hess, J. Appl. Phys. 95 (2004) 1667.

[51] J.E. Sader, I. Larson, P. Mulvaney, L.R. White, Rev. Sci. Instrum. 66 (1995) 3789.

[52] H.-J. Butt, P. Siedle, K. Seifert, K. Fendler, T. Seeger, E. Bamberg, A.L. Weisenhorn, K. Goldie, A. Engel, J. Microsc.169 (1993) 75.

[53] J.P. Cleveland, S. Manne, D. Bocek, P.K. Hansma, Rev. Sci. Instrum. 64 (1993) 403.

[54] J.E. Sader, J.W.M. Chou, P. Mulvaney, Rev. Sci. Instrum. 70 (1999) 3967.

[55] J.L. Hutter, J. Bechhoefer, Rev. Sci. Instrum. 64 (1993) 1868.

[56] C.T. Gibson, G.S. Watson, S. Myhra, Nanotechnology 7 (1996) 259.

[57] Y.Martin, C.C.Williams, and H.K.Wickramasinghe. Journal of Applied Physics, 61(10):4723–4729, May 1987.

[58] R. Erlandsson, G.M.McClelland, C.M.Mate, and S. Chiang. Journal of Vacuum Science and Technology A, 6(2):266–270, March/April 1988.

[59] T. Akiyama, S.Gautsch, N. F. de Rooij,U. Staufer, P.Niedermann, L.Howald,D.Muller,

A. Tonin, H.-R. Hidber, W. T. Pike, and M. H. Hecht. Sensors and Actuators A, 91:321–325, 2001.

[60] S. Alexander, L. Hellemans, O.Marti, J. Schneir, V. Elings, P. K. Hansma,M. Longmire, and J. Gurley. Journal of Applied Physics, 65(1):164–167, January 1989.

[61] T. Stadelmann. PhD Thesis. the University of Oxford, 2006.

[62] H.J. Butt, M. Jaschke, Nanotechnology 6 (1995) 1.

[63] R. García, R. Pérez, Surface science reports. 47 (2002) 197-301.

[64] T. Albrecht, P. Grütter, D. Horne and D. Rugar. J. Appl. Phys 69. 668 (1991).

[65] F. J. Giessbl. Rev. Mod. Phys. 75. 949 (2003).

[66] H.-J. Butt, P. Siedle, K. Seifert, K. Fendler, T. Seeger, E. Bamberg, A. L.Weisenhorn, K. Goldie, and A. Engel, J. Microsc. 169, 75 ~1993.

[67] M. Sasaki, K. Hane, S. Okuma, Y. Bessho, Rev. Sci. Instrum. 65 (1994) 1930.

[68] B. Cappella and G. Dietler. Surface Science Reports, 34:1–104, 1999.

[69] N.A. Burnham, R.J. Colton, H.M. Pollock, J. Vac. Sci. Technol. A 9 (1991) 2548.

[70] J.B. Pethica, A.P. Sutton, J. Vac. Sci. Technol. A 6 (1988) 2490.

[71] E. Boschung, M. Heuberger, G. Dietler, Appl. Phys. Lett. 64 (1994) 1794.

[72] G. Gillies, C.A. Prestidge, P. Attard, Langmuir 18 (2002) 1674.

[73] M. Reitsma, V. Craig, S. Biggs, Int. J. Adhes. Adhes. 20 (2000) 445.

[74] J. Domke, S. Dannohl, W.J. Parak, O. Muller, W.K. Aicher, M. Radmacher, Colloids Surf. B 19 (2000) 367.

[75] T. Yamada, H. Arakawa, T. Okajima, T. Shimada, A. Ikai, Ultramicroscopy 91 (2002) 261.

[76] J. Drelich, G. W. Tormoen, E. R. Beach. J. Colloid Interf. Sci. 2004; 280(2): 484.

[77] B. Capella, G. Dielter. Surf. Sci. Rep. 1999; 34: 1.

[78] B.V. Derjaguin, V.M. Muller, Yu.P Toporov. J. Colloid Interf. Sci. 1975; 53: 314.

[79] J. Drelich, G.W. Tormoen, E.R. Beach, J. Colloid Interf. Sci. 280 (2004) 484.

[80] M.A. Rixman, D. Dean, C.E. Macias, C. Ortiz, Langmuir 19 (2003) 6202.

[81] Y.Martin, C.C.Williams, H.K.Wickramasingher, J.Appl.Phys.61 (1987) 4723.

[82] A. San Paulo, R. García, Biophys. J. 78 (2000) 1599.

[83] C. Möller, M. Alle, V. Elings, A. Engel, D. Müller, Biophys. J. 77 (1999) 1150.

[84] G. Reiter, G. Castelein, P. Hoerner, G. Riess, J.-U. Sommer, G. Floudas, Eur. Phys. J. E 2 (2000) 319.

[85] C.Bustamante, D.Keller, Phys. Today 48 (1995) 33.

[86] N.A.Burham, O.P.Behrend, F.Oulevey, G.Gremaud, P.-J.Gallo, D.Gourdon, E.Dupas, A.J. Kulik, H.M. Pollok, G.A.D. Briggs, Nanotechnology 8 (1997) 67.

[87] R. García, A. San Paulo, Phys. Rev. B. 60 (1999) 4961.

[88] W.A. Ducker, R.F. Cook, Appl. Phys. Lett. 56 (1990) 2408.

[89] J. Senzier. Thèse préparée à l'Institut Néel / CNRS – Grenoble. 2007.

[90] M.A. Lantz, S.J. O'Shea, M.E. Welland, Appl. Phys. Lett. 65 (1994) 409.

[91] M.C. Friedenberg, C.M. Mate, Langmuir 12 (1996) 6138.

[92] T.R. Albrecht, P. Grütter, D. Horne, D. Rugar, J. Appl. Phys. 69 (1991) 668.

[93] H. Ueyama, Y. Sugawara, S. Morita, Appl. Phys. A 66 (1998) S295.

[94] Bart W. Hoogenboom. Volume 8, Issue 3, pages 50–51, September 2006.

[95] R. Bennewitz, M. Bammerlin, M. Guggisberg, C. Loppacher, A. Barato, E. Meyer, and H.-J. Guntherodt. Surface and Interface Analysis, 27:462–466, 1999.

[96] G. Couturier, R. Boisgard, L. Nony, and J. P. Aime. Review of Scientific Instruments, 74(5):2726–2734, 2003.

[97] H. Hölscher, U.D.Schwarz, R.Weisendager, Appl. Surf. Sci. 140 (1999) 344.

[98] A. San Paulo, R. García. Phys. Rev. B, V. 64 (2001) 193411.

[99] F. M. Ohnesorge. Surface and Interface Analysis, 27:179–385, 1999.

[100] F. M. Ohnesorge and G. Binnig. Science, 360(5113):1451–1456, June 1993.

[101] F.J. Elmer, M. Dreier, J. Appl. Phys. 81 (1997) 7709.

[102] J.E. Sader, J. Appl. Phys. 84 (1998) 64.

[103] J.W.M. Chon, P. Mulvaney, J.E. Sader, J. Appl. Phys. 87 (2000) 3978.

[104] M.P. Scherer, G. Frank, A.W. Gummer, J. Appl. Phys. 88 (2000) 2912.

[105] A. Kuhle, A.H. Sorensen, J.B. Zandbergen, J. Bohr, Appl. Phys. A 66, S329-S332, (1998)

[106] R. Garcia and R. Perez, Surf Sci Rep. 47, 197, (2002)

[107] N. F. Martınez,W. Kaminski, C. JGomez, C. Albonetti, F. Biscarini, R. Perez, R. Garcıa. Nanotechnology 20 (2009) 434021 (7pp)

[108] J. P. Cleveland, B. Anczykowski, A. E. Schmid,V. Elings, 1998 Appl. Phys. Lett. 72 2613

[109] R. Garcia, C. J. Gómez, N. F. Martinez, S. Patil, C. Dietz, R. Magerle. Phys. Rev. Lett, 97, 016103 (2006)

[110] M. H. Rouillat, V. Dugas, J. R. Martin, M. Phaner-Goutorbe. Applied Surface Science, 252, 1765-1771 (2005).

[111] B. Anczykowski, D. Kruger, K.L. Babcock, H.Fuchs, Ultramicroscopy 66 (1996) 251-259

[112] D. Keller, Surf. Science, 294 (1993), pp. 409–419.

[113] P. E. Mazeran, J. L. Loubet, Tribol. Lett. 3 125 (1997)

[114] K. Schroter, A. Petzold, T. Henze, T. Thurn-Albrecht. Macromolecules 2009, 42, 1114-1124

[115] Y. Zhao, Q. Cheng, M. Qian, J. H. Cantrell. J. of Appl. Phys. 108, 094311 (2010)

[116] M. Lee and W.Jhe, Phys. Rev. Lett. 97, 036104 (2006)

[117] F. J. Giessibl, M. Tortonese, Appl. Phys. Lett. 70, 2529 (1997)

[118] R. Garcia, C. J. Gómez, N. F. Martinez, S. Patil, C. Dietz, R. Magerle. Phys. Rev. Lett, 97, 016103 (2006)

[119] A.N. Round and M.J. Miles, Nanotechnology 4 (15) (2004), pp. S176–S183

[120] S. D. Halepete, H. C. Lin, S. J. Fang, and C. R. Helms, Mater. Res. Soc. Symp. Proc. 386, 383 (1995)

[121] S. J. Fang, W. Chen, T. Yamanaka, and C. R. Helms, Appl. Phys. Lett. 68, 2837 (1996).

[122] J.M. Elson, J.M. Bennett, Appl. Opt. 34 (1995) 201.

[123] D. F. Elliott and K. R. Rao New York: Academic (1982)

[124] S. J. Fang, S. Haplepete, W. Chen, C. R. Helms and H. Edwards (1997) J. Appl. Phys. 82 5891–8

[125] P.Dumas, B.Bouffakhreddine, C.Amra, O.Vatel, E.Andre, R.Galindo, F.Salvan, Europhys. Lett. (1993), 22, 717.

[126] J. Kondev, C.L. Henley, D.G. Salinas, Phys. Rev. E 61 (2000) 104.

[127] A.J. Perry, Surf. Coat. Technol. 132 (2000) 21.

[128] W.Kwasny, L.A.Dobrzanski, M.Pawlyta, W.Gulbinski, J.Mater. Process. Technol. 157–158 (2004) 188–193.

[129] A. E.Lita, J. E. Sanchez, J. Phys. ReV. B (2000), 61, 7692–7699.

[130] A.L. Barabasi, H.E. Stanley, Cambridge University Press, 1995.

[131] S. Das Sarma and S. V. Ghaisas, Phys. Rev. Lett. 69, 3762 (1992); 71, 2510 (1993).

[132] V. Cimalla, T. Machleidt, L. Spiess, M. Gubisch, I. Hotovy, H. Romanus and O. AmbacherUltramicroscopy 107 989–94 (2007)

[133] S. Jakops, A. Duparre, H. Truckenbrodt, Appl. Opt. 37 (1998) 1180.

[134] J.M. Elson, J.M. Bennett, J. Opt. Soc. Am. 69 (1979) 31.

[135] J.M. Elson, J.P. Rahn, J.M. Bennett, Appl. Opt. 19 (1980) 669.

[136] J.M. Elson, J.P. Rahn, J.M. Bennett, Appl. Opt. 22 (1983) 3207.

[137] J.F. Borrull, A. Duparre, E. Quesnel, Appl. Opt. 40 (13) (2001) 2190–2199.

[138] D.G. Stearns, P.B. Mirkarim, E. Spiller, Thin Solid Films 446 (2004) 37–49.

[139] N.K. Sahoo, S. Thakur, R.B. Tokas, Thin Solid Films 503 (2006) 85–95.

[140] E.L. Church, Appl. Opt. 22 (1988) 1518.

[141] J. Yu, J.G. Amar, Phys. Rev., E 65 (2002) 060601.

[142] G. Rasigni, F. Varnier, M. Rasigni, J. Palmari, A. Llebaria, Phys. Rev. B 27 (1983) 819.

[143] M. Senthilkumar, N. K. Sahoo, S. Thakur, R. B. Tokas. Applied surface science, vol.252 n.5 pp:1608-1619 (2005)

Chapter II

AFM studies of pentacene thin films for organic field effect transistors

I - Organic Thin Film Field effect Transistors

I-1 History of Organic semiconductors

After the invention of the first transistor, in 1947, by John Bardeen and Walter Brattain, inorganic semiconductors such as Si or Ge became the dominant materials in electronics. This led to the replacement of vacuum tube based electronics by solid state devices that initiated the development of semiconductor microelectronics, especially at the end of the 20th Century.

Nowadays, in the first decade of the 21st Century we are contemporaries of a new breakthrough in electronics that has become possible due to the understanding of a new class of materials generally named as *organic semiconductors*. The progress in this field has been driven by the perspective of their application in large area flexible displays and light sources, low cost printed circuits and plastic solar cells [1] (Figure II-1).
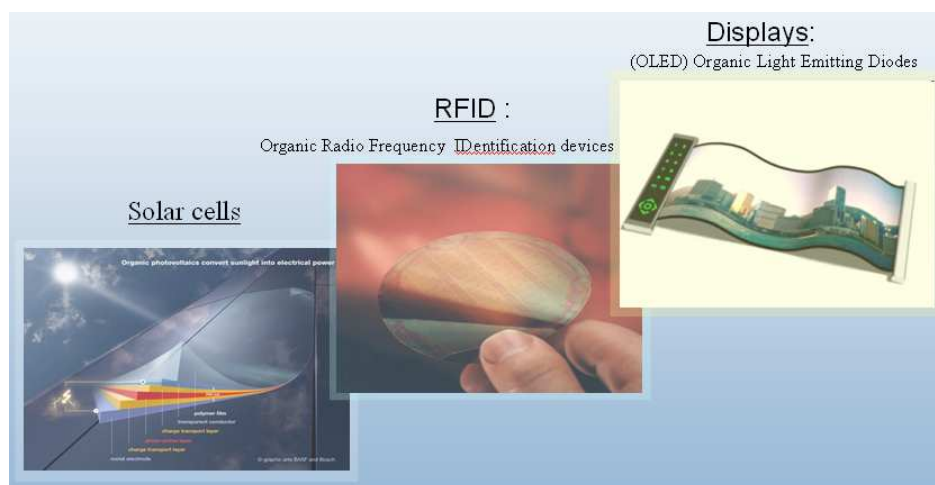

Figure II-1. Different applications of organic semiconductors

The organic materials were firstly discovered and studied for their fluorescence properties when Stokes discovered this phenomenon in 1852. The intensive study of charge-carrier phenomena in organic crystals started with the experimental works on dark conductivity of phtalocyanines, in the late 1940s [2]. At the same time, the first prototypes of organic semiconductor diodes were made in anthracene crystals [2]. More intensively in the 1960s, the basic processes involved in charge carrier and optical excitation of the molecular crystals were investigated [3, 4]. These organic electroluminescent diodes were made in crystals of some hundred micrometers to several millimeters in thickness and thus, needed a high operating voltage. Moreover, no satisfying operating stability was achieved. Until recently, these difficulties prevented the practical use of these early devices.

The first successful applications of conducting polymers for conducting coatings [5] or photoreceptors in electrophotography [6] were realized in the 1970s. It became possible due to achievements in the synthesis and to the controlled doping of conjugated polymers.

In the 1980s, a fresh boost of organic semiconductor electronics was given by the first successful fabrication of organic thin film transistor (OTFT) [7-9] and the creation of high-performance electroluminescent diodes from conjugated polymers [10] and the elaboration of vacuum-evaporated molecular films [11]. Recently, organic semiconductor materials have displayed their potential as a new class of materials opening low-cost/disposable applications in microelectronics and optoelectronics [12]. Today, organic light-emitting devices (OLEDs) have progressed rapidly; they have commercial applications incorporating OLED displays, due to efforts of academic and industrial researches. Further applications of organic semiconductors as organic photovoltaic cells (OPVCs) or circuits based on organic field-effect transistors (OFETs) are expected in the near future.

I-2 Basic properties of organic semiconductors

The fundamental difference between organic and inorganic semiconductors is in the nature of their crystal bonds. In comparison to covalently bonded inorganic semiconductors such as GaAs or Si, the solid state of organic molecular crystals is possible due to van der Waals bonds. These intermolecular forces are significantly weaker than covalent bonds, they provoke weak delocalization of electronic wave-functions between molecules and directly affect charge carrier transport and optical properties.

Molecules of organic semiconductors consist in neighboring carbon atoms linked to each other by single and double bonds. As shown in Figure II-2, p_z-orbitals of sp^2-hybridized carbon atoms orient perpendicularly to the backbone plane. As the distance between carbons is close enough, the overlap of neighboring p_z-orbitals is possible and leads to the creation of the so-called π bonds. These π bonds, constituted of delocalized electrons are present above and bellow the backbone plane.
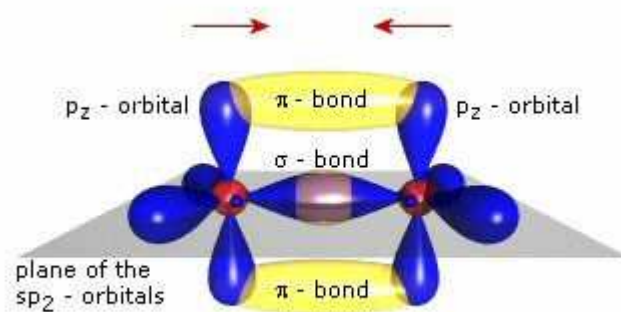
Figure II-2. π-bonding in ethene as an example for the simplest conjugated π-electron system

In comparison to the σ bonds which constitute the backbone of the molecules, the π bonds are much weaker. That is because the electrons from p_z-orbitals have a high probability to be delocalized along the overlapped π-orbitals. This delocalization is responsible of the optoelectronic properties of organic semiconductor materials. Strictly speaking, the electronic properties of a molecule depend on the conjugation length and on the presence of donor-acceptor groups [13].

In organic semiconductors, interaction between molecules occurs thanks to the delocalization of electronic states in the molecule and to a good inter-molecular orbital overlapping. In other words, sufficient structural ordering defines the formation of extended electronic states and consequently governs charge transport properties of organic semiconductors.

Molecules involving π-conjugations have in their p_z-orbitals unpaired electrons that form bonding and anti-bonding levels, also called highest occupied molecular level (HOMO) and lowest unoccupied molecular level (LUMO). Unlike traditional inorganic semiconductors, organic materials exhibit natural p-type or n-type conducting behaviours with dominating hole or electron carriers, respectively. They don't need to be doped by the addition of doping impurities. The charge transport for semiconductors with high HOMO levels exhibit *p*-type conductivity and *n*-type conductivity occurs through low LUMO levels [14].

Organic semiconductors can be divided in two major classes: low molecular weight semiconductors (short chain oligomers) and high molecular weight semiconductors (long chain polymers) [15].

Typical *p*-type semiconductors can be categorized, according to their molecular structure, as follow [13]:

- *acenes* such as picene, tetracene, rubrene, pentacene etc…
- *heterocyclic oligomers* such as thiophene, phenylene, polythiophenes, phenanthrene etc…
- *tetrathiafulvalenes* (TTFs) such as naphthalene-fused derivatives, quinoxaline containing TTF, benzene and thiophene-fused derivatives, pyrrol-fused TTFs …

Some molecular structures are presented on Figure II-3.
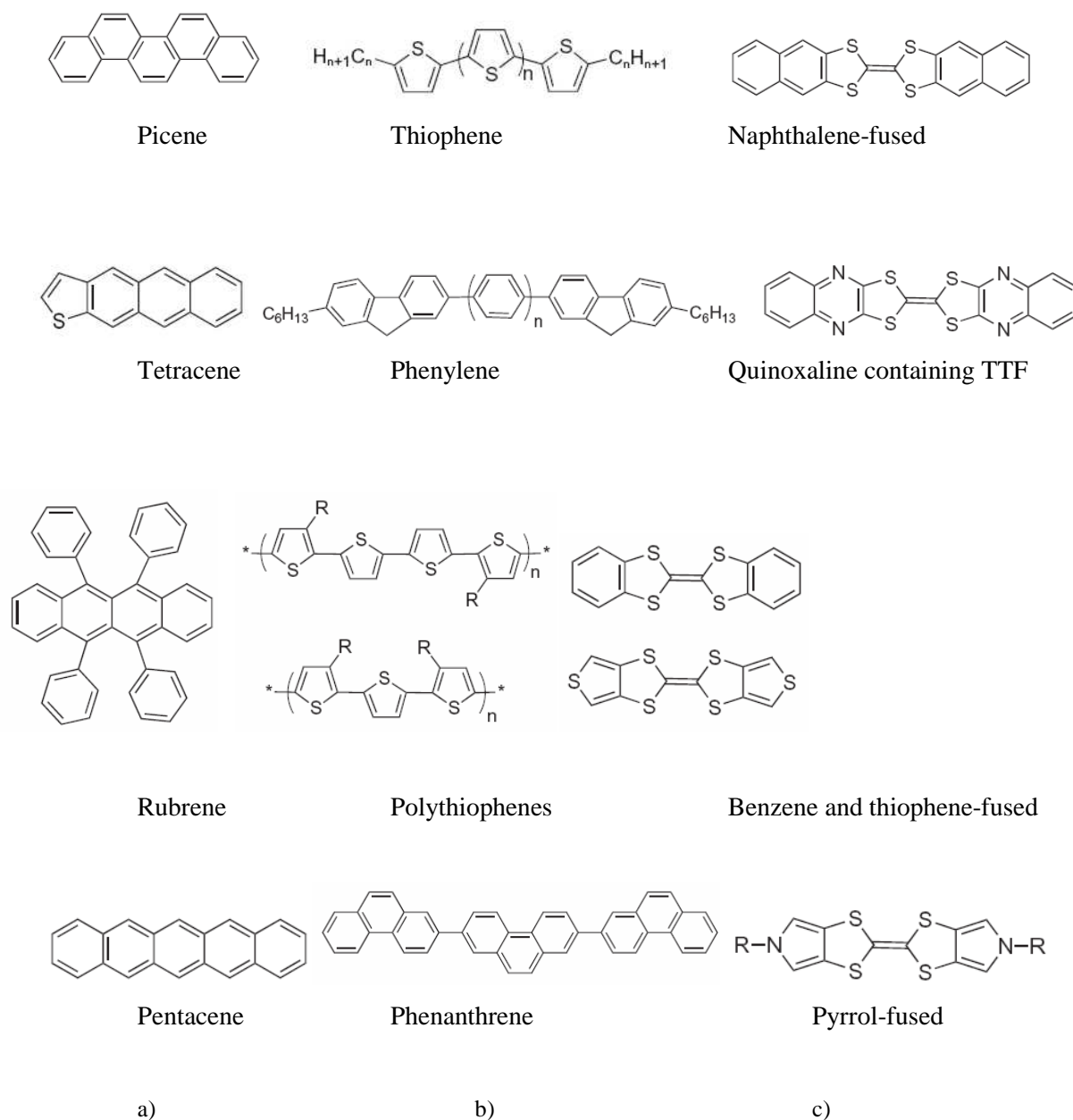
Figure II-3. Examples of *p*-type organic semiconductors: a) *acenes*, b) *heterocyclic oligomers,*
c) *tetrathiafulvalenes* [13]

The highest mobilities of oligomers do not exceed the values of 0.50 – 0.60 cm²/Vs [16, 17] and the tetrathiafulvalenes mobilities are reported to be of around 0.40 cm²/Vs [18, 19]. However, acenes present hole mobilities between 1.6 – 3.0 cm²/Vs [20, 21], that is greater than the mobility of amorphous silicon ($\sim$1cm²Vs⁻¹). The best mobility is obtained with the crystalline pentacene for which measured mobilies range between 0.3 and 12.3 cm²/Vs [22, 23].

N-type semiconductors are not fully developed and their performances are lower comparing to those of *p*-type organic semiconductors [13]. Some typical *n*-type semiconductors are shown in Figure II-4.

Perylenediimides   Perfluoronated pentacene   Fullerene

Thiophene oligomers with perfluorohexyl groups   Bisthiazole
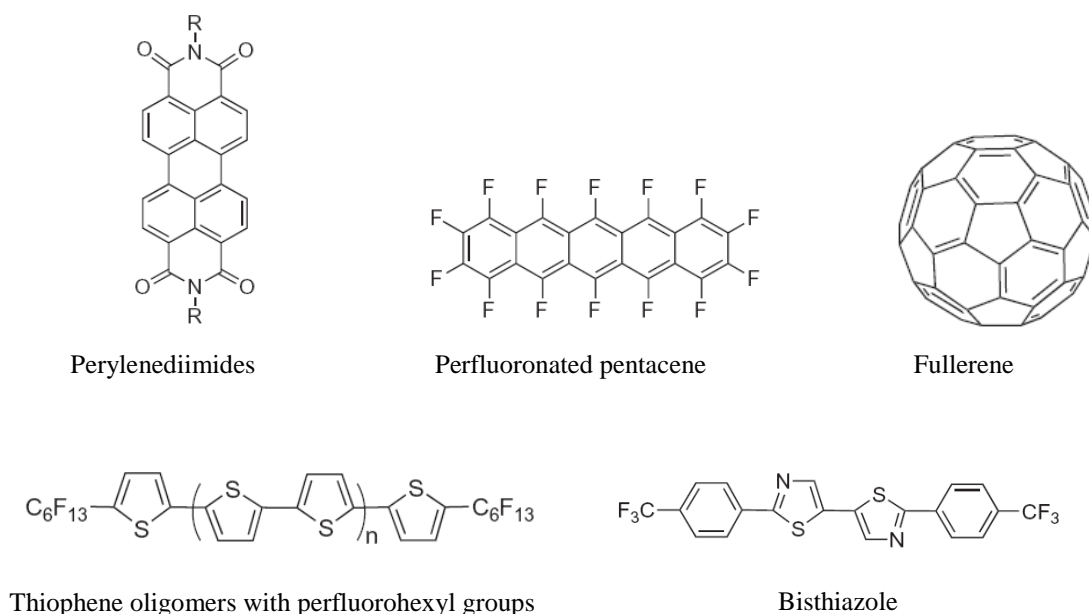
Figure II-4. Examples of *n*-type organic semiconductors [13]

Perylenediimides are known as ones of the famous *n*-type semiconductors and the highest electron mobility of 0.6 cm^2/Vs was achieved on their octyl derivative [24].

One possibility to create *n*-type semiconductor consists in introducing electron acceptor groups to *p*-type semiconductors. By such a method, perfluoronated pentacene was obtained, with a charge mobility of 0.11 cm^2/Vs under high vacuum conditions [25]. Novel *n*-type compounds are fullerenes. C$_{60}$ has a high electron affinity and presents a mobility of 0.56 cm^2/Vs [26]. The highest electron mobility among *n*-type semiconductors is 1.83 cm^2/Vs [27]. It was reported for bisthiazole derivative of compound with trifluoromethylphenyl groups.

Both *p*- and *n*-type organic semiconductors consisting of small molecules such as acenes or oligomers tend to arrange into a π-π stacking (like rubrene) or a herringbone (like pentacene) systems when they are deposited by vacuum evaporation. Molecular arrangement occurs through Van der Waals intermolecular forces that induced a high ordered packing and consequently a high charge carrier mobility [28-30]. On the other hand, molecular ordering of polymer-based organic semiconductors (like polythiophenes) is less efficient, that is related to cross-linking between molecules during polymerization process. It results in a significantly lower mobility comparing to short conjugated oligomers [31]. Thienothiophene-containing polymer showed a mobility of 0.6 cm^2 /Vs, which is the highest among FETs polymers [17].

The electrical performance of organic semiconductors, typically determined by high charge mobility, has been significantly improved by researches in materials and processes. A wide range of organic materials has been explored, from semiconducting polymers such as polythiophene and polyacetylene, to short conjugated oligomers such as tetracene and pentacene [32].

I - 3 OTFT operation principle

I-3-1 The structure of the transistor

Field effect transistor is an electronic device that uses electric field to govern a current in the channel of a semiconductor. Organic field effect transistors have a similar configuration as inorganic thin film transistors. The FET principle was firstly proposed by Lilienfeld in 1925, when he patented a device similar to a field effect transistor [33].

There are two general configurations in OTFTs: the top-contact bottom gate (TB) and the bottom-contact bottom gate (BB) [34]. The BB transistor geometry is frequently used although OTFTs with TB geometry demonstrate higher electrical characteristics [35].

Typical geometry of the TB OTFT is illustrated in Figure II-5. The conductive channel is placed between the source and drain electrodes and is separated from the gate electrode by an insulator layer. In the channel, the density of charge carriers can be modulated by the applied gate voltage across the insulator. The basic operating regimes will be described for the p-type OTFT.
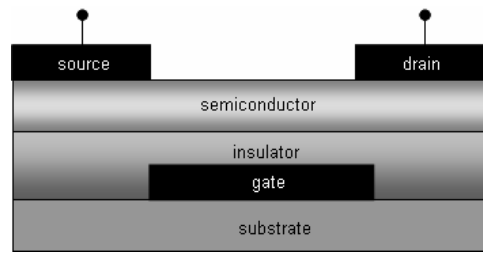
Figure II-5. Schematic representation of a top-contact bottom gate OTFT

If the electrical field induced by the gate voltage is higher than the electrical field induced by the drain voltage ($V_g \gg V_d$), a gradual channel approximation would be considered. Then an analytical approach can by applied for the description of the OTFT operation [36, 37].

In the working regime, the source electrode is grounded (V_s=0V) and voltages are applied to the gate and the drain electrodes, leading to a gate voltage (V_g) between gate and source and a source-drain voltage (V_{sd}).

Applying a negative voltage to the gate electrode and a zero bias to the drain electrode ($V_s = V_d = 0$, $V_g < 0$) provides the accumulation of a high density of positive charge carriers (holes) at the interface between the semiconductor and the insulator leading to an electrical charge noted (q):

$$q = C_i \cdot V_g \qquad \text{(eq.2.1)}$$

where q is the induced charge density and C_i is the capacitance per unit area.

Due to the natural presence of structural defects and chemical impurities, some of the accumulated carriers are trapped and do not contribute to the current until the applied voltage V_g exceeds a certain offset called threshold voltage (V_t). As a result, V_g is reduced to the effective gate voltage ($V_g - V_t$) and the charge density q_c which contributed to the current is given by:

$$q_c = C_i \left(V_g - V_t \right)$$

(eq.2.2)

In the assumption that a small negative bias V_d is applied ($V_d < 0$, $V_d > (V_g - V_t)$), the linear gradient of charge in the channel produces a current flow which is proportional to the source-drain voltage (V_{sd}). The applied drain voltage V_d produces the variation of the potential difference between the gate and the channel. Therefore, the charge density changes along the transistor channel in:

$$q_c = C_i \left(V_g - V_t - V(x) \right)$$

(eq.2.3)

Assuming that only the charge carriers induced by V_g participate to the current (I_d), that flows in the transistor channel, I_d can be expressed as:

$$I_d = W \mu q_c E_x$$

(eq.2.4)

Where W is the channel width, μ is the charge carrier mobility and E_x is the electric field between source and drain contacts.

Taking into account that $E_x = \dfrac{dV}{dx}$ and substituting eq. 2.3 into eq. 2.4 the latter can be presented as:

$$I_d dx = W \mu C_i (V_g - V_t - V(x)) dV$$

(eq.2.5)

Integrating eq. (2.5) gives the relation for I_d:

$$I_d = \frac{W}{L} C_i \mu \left[(V_g - V_t) V_{sd} - \frac{1}{2} V_{sd}^2 \right]$$

(eq.2.6)

(at the source contact $x = 0$ and $V(x) = 0$, at the drain contact $x = L$ and $V(x) = V_{sd}$, $V_{sd} = V_d$ when the source electrode is grounded).

The second term in eq. (2.6) can be neglected because $\left|V_{sd}\right| << \left|(V_g - V_t)\right|$, then eq. (2.6) can be rewritten as:

$$I_d = \frac{W}{L} C_i \mu (V_g - V_t) V_{sd} \qquad (eq.2.7)$$

This equation describes the "linear regime" of the transistor operation. In this case, the channel resistance is low and the transistor operates in the linear regime up to the point $V_d \sim (V_g - V_t)$.

As soon as gate voltage reaches the value $V_d \approx (V_g - V_t)$, the depletion region appears inside the channel. This depletion region is formed near the drain contact by electric potential that exceeds the threshold value (V_t). Therefore, just a limited current can flow through the saturated region. If drain voltage continues to decrease ($V_d < (V_g - V_t)$), the depletion region expanses toward the source electrode, although the current flow does not increase. Such behaviour describes the "saturation regime" of the transistor operation.

This mode can be described by eq. (2.7) in assumption that $\left|V_{sd}\right| > \left|(V_g - V_t)\right|$, therefore V_{sd} is replaced by ($V_g - V_t$) leading to:

$$I_d = \frac{W}{2L} C_i \mu (V_g - V_t)^2 \qquad (eq.2.8)$$

Obtained relations (2.7) and (2.8) are valid if the insulator thickness d is much smaller than the channel length L, and the charge mobility μ is not field-dependent. The operation principle for n-type OFET is similar, but the gate voltage is inverted [38].

I-3-2 The field-effect mobility

The charge carrier mobility of an OTFT can be obtained by measuring the current-voltage (I-V) characteristics in the linear or saturation regime of the transistor operation [39].

In order to calculated the field-effect mobility in the linear regime, the (I-V) characteristics can be extracted by maintaining $V_g = $ const or $V_{sd} = $ const. In other words, eq. (2.7) must be derived with respect to V_g or V_{sd}:

$$g_m = \left(\frac{\partial I_d}{\partial V_g}\right)_{V_{sd}=const} = \frac{W}{L} C_i \mu_{lin} V_{sd} \qquad (eq.2.9)$$

$$g_d = \left(\frac{\partial I_d}{\partial V_{sd}}\right)_{V_g=const} = \frac{W}{L} C_i \mu_{lin} (V_g - V_t) \qquad (eq.2.10)$$

Expressions of g_m and g_d channel transconductivity and conductivity are respectively obtained. The value of g_m is calculated from the linear part of the transfer curve. Extracted from eq. (2.9), the mobility can be presented as:

$$\mu_{lin} = g_m \cdot \frac{L}{W} \frac{1}{C_i V_{sd}} \qquad \text{(eq.2.11)}$$

And eq. (2.10) gives:

$$\mu_{lin} = g_d \cdot \frac{L}{W} \frac{1}{C_i(V_g - V_t)} \qquad \text{(eq.2.12)}$$

Equation (2.11) is more general than eq. (2.12) because it is also valid for gate-voltage-dependent field-effect mobility. In addition, the value of V_t should be determined to describe the charge transfer in eq. (2.12)

In the saturation regime, field-effect mobility can be directly derived from eq. (2.8):

$$\mu_{sat} = I_{d,sat} \cdot \frac{2L}{W} \frac{1}{C_i(V_g - V_t)^2} \qquad \text{(eq.2.13)}$$

Where μ_{sat} and $I_{d,sat}$ are field-effect mobility and drain source-current in the saturation regime, respectively. Here, the value of $I_{d,sat}$ is obtained from (I-V) characteristics in saturation regime for a given V_g.

Another way to determine μ_{sat} is by deriving eq. (2.8) with respect to V_g:

$$\mu_{sat}(V_g) = \frac{\partial I_{d,sat}}{\partial V_g} \cdot \frac{L}{W} \frac{1}{C_i(V_g - V_t)} \qquad \text{(eq.2.14)}$$

Where derivative $\frac{\partial I_{d,sat}}{\partial V_g}$ is experimentally determined from the transfer curve in saturation regime.

For different organic semiconductors, typical values of field-effect mobility vary from 10^{-6} cm^2/Vs to 20 cm^2/Vs [1, 23, 40].

Due to their relatively low charge carrier mobility, OTFTs can not be used in high switching electronics. However, the main advantage of organic FETs over inorganic FETs is their compatibility with light-weight plastic substrates. In addition, organic semiconductors have a low processing temperature whereas higher temperatures are required for Si-based FETs fabrication [41]. These advantages make them very competitive towards traditional thin film transistors for applications, especially requiring low cost large area coverage [1].

I-3-3 The gate dielectric

A crucial criterion in the fabrication of organic TFTs is the choice of the gate dielectric material. Until now, the best electrical performance has been reported for OTFTs processed on high-quality inorganic gate dielectrics, such as ion-beam sputtered silicon dioxide SiO_2 [42 - 44], chemically vapor deposited silicon nitride Si_3N_4 [45 - 47], radio-frequency sputtered aluminium oxide Al_2O_3 [48] and silicon dioxide thermally grown on single-crystalline silicon [49]. The ability to process inexpensive and disposable organic TFTs induces the necessity to use alternative gate dielectrics and low-cost fabrication methods. For large area applications, the use of inorganic dielectrics grown at high temperatures is not of particular interest. For example, thermally grown SiO_2 has a high breakdown voltage, a low gate leakage and a high quality interface. However, it is not suitable for flexible polymer substrates, because it requires high processing temperatures (800º - 1200ºC) that destroy the polymer. Then, several requirements are expected for new materials to replace inorganic dielectrics such as low dielectric constant ($k < 2.5$), thermal stability (400°C or higher), electrical insulating behaviour, high mechanical strength and good adhesion to neighboring layers. These strict requirements eliminate several candidates such as porous silica and carbon-based materials. Several organic dielectrics have been studied so far, including polyvinyl phenol (PVP), polyimide, poly methyl methacrylate (PPMA) etc… Among appropriate candidates, the solution-processable polymers and the self assembled monolayers (as a buffer gate dielectric and semiconductor film) show great promise for the growth of pentacene thin film in transistor fabrication. In addition, these materials can be easily deposited by spin coating, spray coating or printing rather than by vacuum deposition [50].

II - Experimental System: Pentacene-based thin film transistor

II-1 Choice of polymers

Pentacene is known to be one of the most promising candidate in organic electronic applications because of its high field-effect mobility comparable to that of amorphous silicon [51, 52]. Nonetheless, the difficulty to determine and control key properties of the organic layer, such as structure, morphology, and interfaces, is a major factor restricting its electronic applications.

The further progress in pentacene based electronic devices requires the creation of high-ordered and large size molecular crystals [53]. As it has been shown, OTFTs charge mobility is very sensitive to crystalline properties of thin film, i.e. to the grain size [54, 55], defect density [56] and crystal polymorph [57, 58]. However, the pentacene film quality can be modulated by two ways: changing the deposition parameters (deposition rate, controlling the energy of incident molecules) [59, 61] and varying the substrate properties (substrate temperature and surface chemistry) [62-67].

In order to improve pentacene growth, hydrophobic polymers can be used as substrates to favour a better packing of pentacene molecules. Furthermore, it was reported that the hydrophobic dielectric layers have a tendency to give higher field-effect mobility for both amorphous polymer semiconductors and crystalline organic semiconductors [68]. One of the largest carrier mobility reported for pentacene-based OTFT with a polymer gate dielectric (cross-linked polyvinylphenol and a polyvinylphenol-based copolymer) is more than 3cm²/Vs [41].

The goal of this work is to study growth mechanisms of the pentacene thin films deposited onto two dielectric polymers: parylene and benzocyclobutene (BCB).

II-1-1 Crystalline structure of pentacene

The creation of the first pentacene based thin film field effect transistor by Horowitz et al., in 1992 [38], stimulated intensive studies of pentacene thin film growth and pentacene based electronic devices. Presently, pentacene is considered as a research model for the fundamental studies of semiconducting oligomers.

Pentacene is a p-type organic semiconductor: its molecule ($C_{22}H_{14}$) consists of five fused benzene rings and presents a planar configuration (Figure II-6), its energy gap between HOMO and LUMO levels is 2.6eV [69].
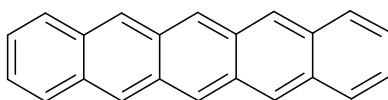
Figure II-6: Structure of the pentacene molecule ($C_{22}H_{14}$)

It was shown that a pentacene monolayer has crystalline structure [70] (Figure II-7). Two main crystalline phases of pentacene are known to sublimate in pentacene layers in vacuum: thin-film phase and bulk phase.
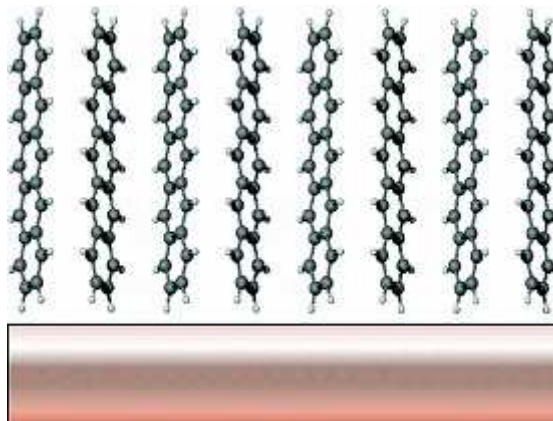
Figure II-7. Crystalline structures of pentacene thin films [70]

In the thin film phase, pentacene has an orthorhombic crystal structure [70, 71] whereas the bulk phase shows a triclinic structure [72]. In both cases, pentacene molecules are arranged in an herringbone configuration due to the interaction between π-orbitals which favours face-to-face π-stacking of molecules and the quadrupolar interaction which governs edge-to-face packing [73, 74].

The morphology of pentacene films is characterized by inter-layer spacing of 1.54 nm for thin film phase and 1.44 nm for bulk phases. Experimental results show that the thin-film phase favours the charge carrier transport with respect to the bulk phase. This can be explained by a better overlap of π-orbitals at the grain boundaries [75]. Moreover, it has been shown that, thin film and bulk structure can coexist in the early pentacene nucleation period [76]. In fact, the formation of pentacene polymorphs is dependent on factors such as the nature of the substrate surface, the substrate temperature and the thin film thickness [77- 80].

II-1-2 Charge carrier transport in pentacene-based OTFT

The charge carrier transport in organic semiconductors depends on the degree of molecular order and is based on two mechanisms: band or hopping transport [32].

In the band transport, the charge carriers are described by a Bloch formalism and their motion is represented as the propagation of delocalized plane waves [81]. In this case, the charge carrier mobility is $\mu \gg 1 \text{cm}^2\text{Vs}^{-1}$ and the temperature dependence obeys to a law: $\mu \sim T^{-n}$, $n > 1$.

In the hopping mechanism, the charge carrier transport occurs by hopping between localized states [82].

The temperature dependence of the mobility follows a Boltzmann law and is described as $\mu \sim \exp(-E/kT)$. In that case, the mobility is $\mu < 1 cm^2/Vs$. Band transport manifests in highly purified and highly ordered organic molecular crystals, constituted of small molecules. For oligomers, achievable charge mobility can reach the values of $400 cm^2 Vs^{-1}$ at low temperatures [83, 84].

In the case of conjugated polymers, the film structure is disordered and carrier transport is possible by charge hopping from site to site. In such structures, the hopping is phonon-assisted and the charge mobility increases with temperature, but mobility remains relatively low ($\mu < 1 cm^2/Vs$) [85, 86].

According to reported data for pentacene-based OTFTs [18, 87], the values of field-effect mobility are in intermediate range ($\mu \sim 1$-$3 \ cm^2/Vs$) because the charge transport mechanism can not be strongly determined (can be related to both hopping and band transport). In addition, Nelson et al. [88] have shown that the temperature dependence of charge mobility in pentacene films is not reproducible and varies from sample to sample even if OTFTs were fabricated under the same conditions. Furthermore, they also noticed that, the charge mobilities have demonstrated temperature independent behaviours, in some experiments.

The charge mobility in organic semiconductors is strongly depended on molecular ordering and thus can be improved by the quality of the thin film structure. Especially, spatial orientation of the pentacene molecules is directly affected by the chemical properties of the substrate on which they are deposited. On a chemical inert surface, pentacene molecules normally present a standing-up orientation [89, 90]. In the contrary, the standing-up orientation changes to a lying-down orientation, in the case of chemically reactive surfaces such as cleaned silicon surface [91, 92] or metallic surfaces like Au or Cu, due to the presence of unsaturated bonds [93, 94].

Substrate dependent arrangement of pentacene films and resulting electrical performances were studied experimentally and are schematically represented in Figure II-8 [1]. Figure II-8 shows that highly ordered structure and increased intermolecular packing, significantly favour OTFTs electrical performances [95- 97].
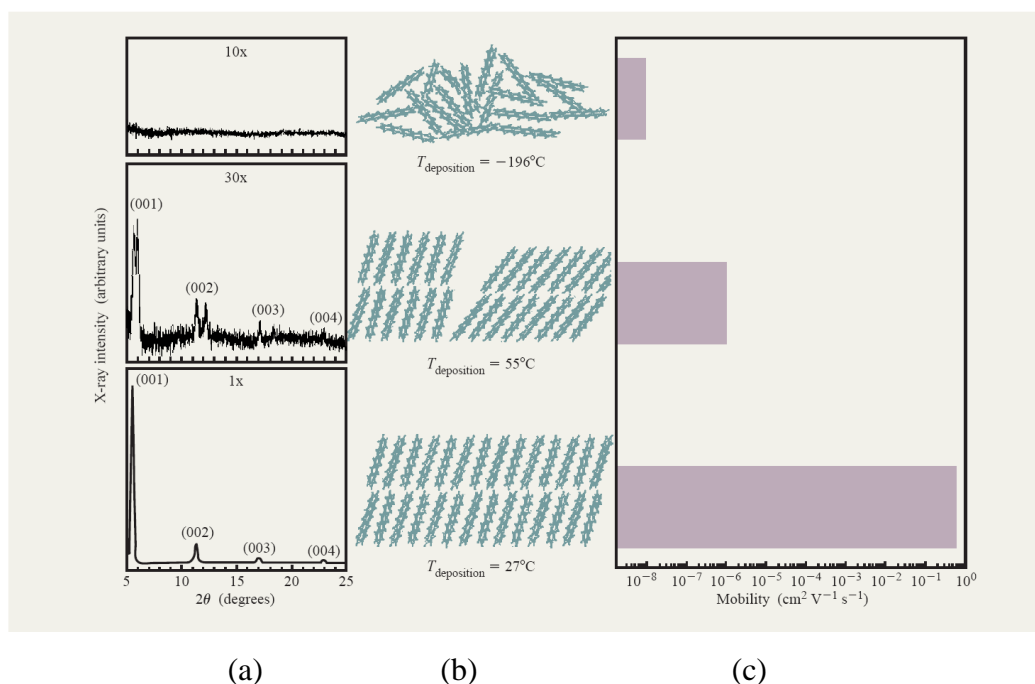

(a)　　　　(b)　　　　(c)

Figure II-8. Dependence of field-effect mobility of pentacene on thin film structural order [1]

(a) X-ray diffraction graphs, corresponding structural models (b) and mobilities (c)

Another important factor that affects pentacene film growth is the roughness of a dielectric surface. The increased roughness of the gate dielectric provokes dramatically decreasing of pentacene grain size and results in the decrease of carrier mobility. It was shown that the hole mobility decreased from 0.49 cm²/Vs to 0.11 cm²/Vs when the dielectric roughness increased from 0.24 to 1.15 nm in pentacene based OTFTs with SiO_2 gate dielectrics. In another work, it decreased from 0.31 to 0.02 cm²/Vs with a roughness increase from 0.2 to 1.5 nm [98, 99].

Therefore, the properties of the interface between the pentacene active layer and the gate dielectric play a very important role in determining the molecular orientation, the adsorption probability, the surface diffusivity and consequently the OFETs charge mobility.

II-1-3 The gate polymers: parylene and benzocyclobutene

In our study, we focussed on parylene (poly-p-xylylene) and BCB (divinyltetramethyldisiloxane-bis or benzocyclobutene) (Figure II-9).

a)   b)
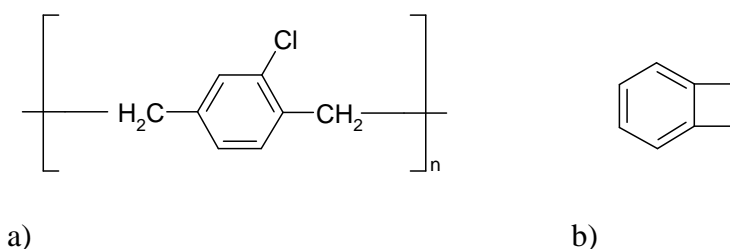
Figure II-9. Molecular structure of parylene-C (a) and benzocyclobutene (BCB) (b)

There are many types of parylene including parylene-D, parylene-N and parylene-C. However, Yasuda et al have reported that, the best FET performances were obtained when parylene-C has been used as a gate dielectric [100]. Gas phase polymerization makes parylene layers absolutely uniform and conformal on all surfaces. Another experimental results show improvement of the OFETs operating performance when a thin parylene dielectric layer has been introduced between the SiO_2 and the pentacene active layer [101].

On the other hand, the molecules of BCB constitute thin and defect-free films by simple solution casting. Knipp et al. have reported the use of benzocyclobutene as gate dielectric to fabricate pentacene FETs with charge mobilities and on/off ratios similar to those obtained using inorganic dielectrics [102]. Namely, on thermal oxide and silicon nitride the mobilities are of 0.2 - 0.6 cm^2/(Vs) and on/off ratio larger than 10^8. Whereas for transistor with BCB gate the mobility and the on/off ratio are of 0.3 cm^2/(Vs) and 10^7, respectively [102].

Both parylene-C and BCB are hydrophobic in polymerized state and possess most of the required gate dielectric properties: high mechanical strength, thermal stability and good electrical insulation [103, 104]. They have very close dielectric constants ($k = 3.10$ for parylene and $k = 2.65$ for BCB [105, 106]) which can

be comparable with that of SiO_2 as a reference (k = 3.9). Higher dielectric constant induces higher capacitance and consequently higher electric field at the surface of the dielectric. This dependence strongly affects charge mobility because a stronger electric field increases the carrier concentration at the surface [107].

Furthermore, they present high electrical insulation characteristics, even for thin layers. That is very important, not only for passivation in organic electronic devices, but also, for the gate dielectric of organic field effect transistors [108 - 110]. This makes parylene and BCB layers extremely suitable in technologies requiring high quality dielectric coatings.

II-2 Samples preparation

The detailed description of the sample preparation is presented in the PhD manuscript of Karim Diallo [111].

Pentacene thin films were deposited by Vacuum Evaporation method at 70ºC and with velocities between 0.2 and 0.4 Å/s to favour a better organisation of the molecules. Thermally sublimated pentacene molecules are adsorbed on chemical inert surfaces through van der Waals force interaction [98]. After adsorption, the pentacene molecules aggregate into the solid condensed phase via the surface diffusion. Further molecule ordering is determined by surface chemistry and roughness of the dielectric [99].

Both parylene and BCB were deposited on a cleaned glass surface through CVD and spin coating techniques as shown in Figure II-10.

Gas injection ring   Wafers

Pump

a)   b)
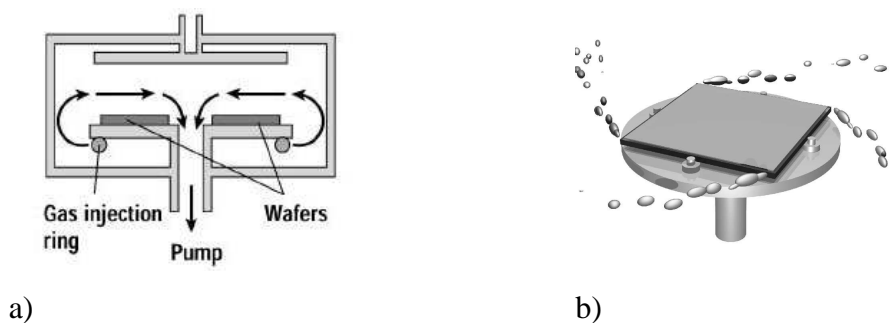
Figure II-10. Deposition of gate dielectrics: a) parylene by CVD, b) BCB by spin coating

The Parylene deposition followed three stages: first, the powder was vaporized in an oven with a temperature maintained at 175ºC and a pressure of 0.1 Torr. This leads to the formation of dimers. Then, dimers were crashed into monomers, in a second oven at 690ºC and a pressure of 0.5 Torr. During the last step, the monomers of parylene were condensed and polymerised on the substrate in the deposition chamber, at ambient temperature (25ºC).

Deposition of the benzocyclobutene was performed from a liquid phase by a spreading method. At the beginning, the substrate was covered by an adhesion promoter (Dow Chemical, AP3000) at 500 rpm during 5s, then at 3500 rpm during 5s. After that, the solution of BCB T1100 (1:1) was deposited at 500 rpm during 5s, then 3500 rpm during 30s. BCB was polymerised by an annealing process during 72h at 170°C in air.

Thicknesses of 690 nm for parylene and 500 nm for BCB were experimentally determined as more accurate in previous studies and were chosen for all the experiments [111].

II-3 Atomic Force Microscopy experimental conditions

Both static (contact) and dynamic (non or intermittent contact) modes have been employed in order to determine the most appropriate operating mode for pentacene films studying (cf Chapter I).

The AFM system used in these studies was a Solver P-7 (stand alone Smena-B) scanning probe microscope, designed by NT-MDT company, Russia and a DI (Veeco) microscope. Samples scanning was performed with cantilevers Nanosensors PPP-contact (k = 0.002N/m) and Nanosensors SSS-NCLR (k = 0.3N/m) for static and dynamic modes, in order to obtain high sensitivity or high Q-factor, respectively. Scanning rate was 1Hz for both modes.

As a test sample, we used the pentacene thin film, with a 30 nm thickness, deposited on BCB.

II-3-1 Contact mode

The cantilever deflection was measured by the intensity of the reflected laser beam on the photodetector (in pA). When the tip reached the surface, the intensity varied from -450 pA to -200pA (setpoint value), leading to an applied tip-surface interaction force corresponding to an intensity of 250pA. The resulting image presented on Figure II-11a, is rather noisy: several line jumps can be seen and the pentacene surface appears blurred with not well contrasted morphological details. This noise is representative of a large contact pressure induced by a large applied force and /or a sharp probing tip.

To improve the resolution and avoid pentacene surface damages, the lowest tip-sample interaction force should be applied. The minimal force value at which the scanning in contact mode can still be realized was determined by the force spectroscopy method.

The principle is based on the analysis of the force-distance curve, namely on its "backward" part. Figure II-12 presents the characteristic obtained on the same surface, with the tip (red curve – approach, blue curve – retract). At the start of the cycle, a large distance separates the fixed part of the cantilever and the sample (around 130 nm) and the cantilever is not deflected (I). The cantilever and the tip are moved close to the sample, at a constant velocity. Once the force acting on the tip exceeds the stiffness of the cantilever, the tip jumps into contact to the sample surface (II) leading to a deflection of the cantilever. If the movement of

the cantilever towards the sample goes on, the cantilever deflection reverses (red curve) until a pre-set maximum load on the tip is reached (III). At this point, the cantilever is moved away from the surface (blue curve) and the tip and sample are separated. Interactions between the tip and sample cause the tip to remain attached to the surface as the cantilever retracts, until a "snap out" point where the tip detaches from the surface (IV).

a)   b)
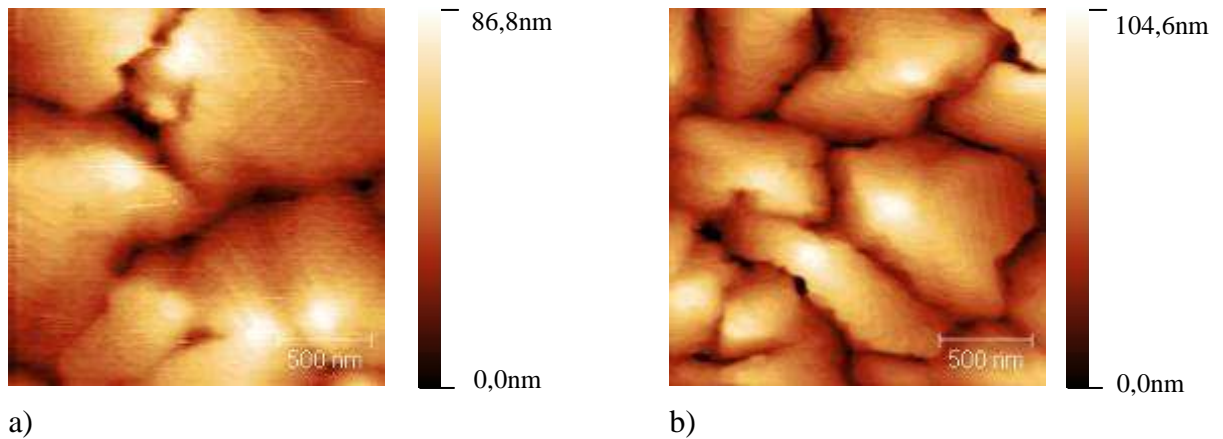
Figure II-11. Pentacene 30nm on BCB. Contact mode images 2x2µm

Once the cycle of data acquisition is completed, the DFL axis (deflection of the cantilever (DFL) is proportional to the interaction force see Chapter I) is correctly scaled relative to the non deflected cantilever position. It makes possible to determine a deflection value when the cantilever is just "snap out" from the pentacene surface. This value represents the limit of the influence of adhesion forces on the tip. In other words, contact AFM imaging is impossible when tip-surface interaction force (setpoint value) is less than this adhesion limit value.
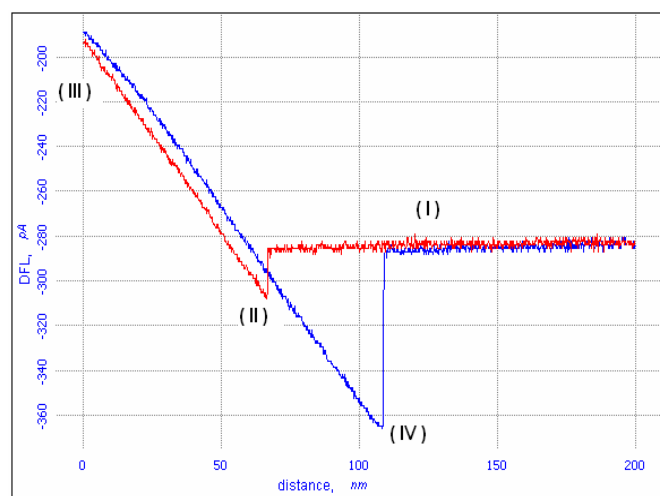
Figure II-12. Typical force-distance curve

The "snap out" for 30nm pentacene film, corresponds to a DFL = -285pA that was determined from force-distance curves presented on Figure II-12. So, the adhesion limit is 165pA if we take into account the initial deflection $DFL_0 = - 0.45nA$.

Scanning in contact mode with an applied load force equal to the adhesion limit value, leads to an image without defects (Figure II-11b). This soft contact regime induces low surface deformation and provides a better visibility of nano-scale patterned pentacene shapes. This analysis demonstrates the ability of AFM contact mode for studying polymers surface morphology and pentacene surfaces, in particular.

II-3-2 Dynamic mode

We used AFM dynamic mode (amplitude modulation), in order to confront the performances of both dynamic and static modes applied to the same type of pentacene surfaces. The scanning of the sample was realized using rectangular cantilever with spring constant of 22N/m and tip radius of 10nm. The most appropriated value of the free oscillation amplitude has been found experimentally and was determined to be around 15 nm at the resonance frequency of 150-160kHz.

Typical high quality images presented in Figure II-13, demonstrate the advantages of the dynamic mode over the contact mode. As the tip touches the sample surface just one time per oscillation period, the dissipated energy is much lower than when the tip is constantly close to the surface as in the contact mode. This fact makes possible the accurate reproducing of exact pentacene morphology. The high resolution image of heights (Figure II-13a) excludes any possible artifact and has a better contrast on the characteristic edges of pentacene than the best image of pentacene in contact mode (Figure II-11b).

a)   b)   c)
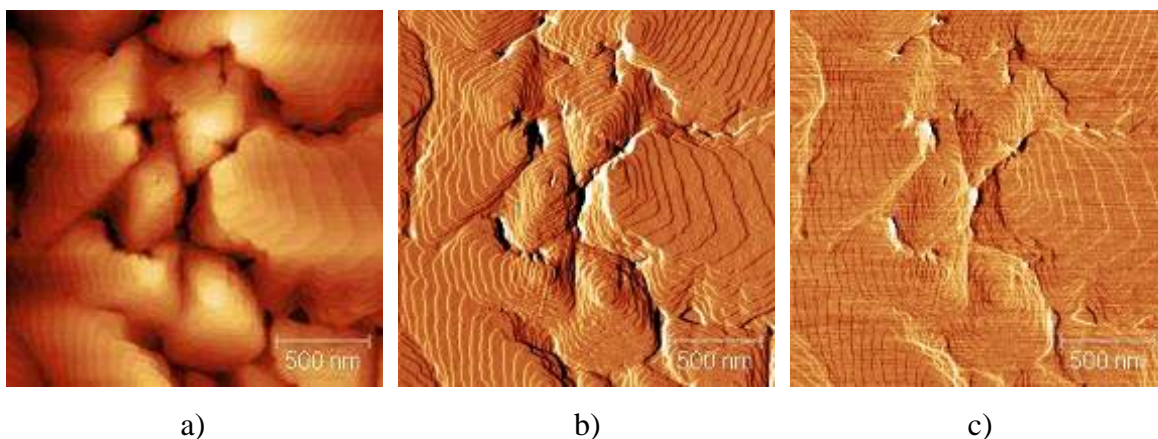
Figure II-13. Pentacene on BCB (30nm thick). Dynamic mode, AM-AFM images on a $2x2\mu m^2$ area
a) height image, b)amplitude image, c) phase image

Furthermore, during the same scanning cycle, amplitude and phase signals can be collected. The amplitude image (Figure II-13b), presents a more detailed surface structure than the height image (Figure II-13a) because it is not affected by the large surface height difference. Hence, this data is helpful for observing the detailed structure of a surface with a complex topography. The phase image from the scanned sample (Figure II-13c) can also be obtained in parallel with the height image. At fixed oscillating amplitude, the phase signal is derived from the phase shift between the excited cantilever and the input drive signal. Phase imaging is an efficient tool that can complete morphological data with information about the structure and the chemical composition of the surface on the nanometer scale.

So, even if it was shown that under specific conditions, the contact mode can be suitable for pentacene surface morphology studies, the dynamic mode will be used in the whole following experiences, because it offers a better noise-free high resolution imaging.

II-3-3 Surface energy measured by AFM Spectroscopy

An original mean to determine the surface energy γ consists in using the atomic force microscope. The work of adhesion between tip and sample can be deduced from experimental force distance curves [112], knowing the tip radius value.

During the spectroscopic measurement, the contact time between tip and sample is short (order of *ms*), consequently the adhesion is only due to Van der Waals forces and the measured work of adhesion represents the thermodynamic work of adhesion W_0:

$$W_0 = 2\gamma \qquad \text{(eq 2.15)}$$

In addition, the tip-surface contact can be considered as a contact between a sphere and a plane with low deformation and low contact radius. Then, the DMT model (Derjaguin Muller Toporov) can be applied for approximation of the thermodynamic work of adhesion [113] (Cf chapter I).

The DMT model relates this adhesion force F_{adh} to the thermodynamic work of adhesion as follow:

$$F_{adh} = 2\pi R W_0 \qquad \text{(eq 2.16)}$$

where F_{adh} is the separation force and R is the tip radius.

The expression for surface energy can be deduced by substituting eq. (2.15) into eq.(2.16):

$$\gamma = \frac{F_{adh}}{4\pi R} \qquad \text{(eq 2.17)}$$

From experimental force-distance curves, the adhesion force F_{adh} can be deduced. It corresponds to the force needed to separate tip and surface and it is related to the cantilever bending by the Hook's law:

$$F_{adh} = k \cdot \Delta Z \qquad \text{(eq 2.18)}$$

where k is the cantilever spring constant and ΔZ is the cantilever bending on the "snap out" point of the curve (point IV on Figure II-12).

Measurements of adhesion forces were performed using AFM force spectroscopy technique in contact mode in air. In our study, we used cantilevers with tip radius of R=10nm and spring constant of k = 0.3N/m, these parameters allow to avoid the sticky effect in our experimental conditions. On the curve, the F_{adh} is given in pA, one should realize a curve on a hard surface (Silicon for example) and determine the slope. The curve gives the value of the spring constant in pA/nm: $k(pA/nm)=\Delta y/\Delta x$. Knowing the value of k in nN/nm one can obtain the value of F_{adh} in nN:

$$F_{adh} \text{ [nN]} = \Delta y \text{ [pA] x } k \text{ [nN/nm] / } k \text{ [pA/nm]} \qquad \text{(eq. 2.19)}$$

For example, for the backward curve shown in Figure II-12, the value of the "snap-out" is ΔY = 0.688-0.482 = 0.206nA, which corresponds to the piezo displacement ΔZ = 173-80 = 93nm. According to eq.2.19, the corresponding adhesion force with k = 0.3N/m, k(pA/nm) = 0.206/93 and F_{adh} = 0.206[pA] · 0.3 [N/m] / (0.206/93) [pA/nm] = 27.9 nN.

In the contact mode spectroscopy, the cantilever tip penetrates in the layer of water adsorbed on the surface. As a result, the measured adhesion force represents the sum of the capillary force between water adsorbed on the tip and sample surfaces, and the adhesion force due to the Van der Waals interaction. Then, the total force of adhesion is expressed as follows:

$$F_{adh} = F_{VdW} + F_{cap} \qquad \text{(eq. 2.20)}$$

The strength of the capillary force is determined by the meniscus between the two surfaces and depends on their geometry. In our experiments, interacting surfaces can be considered as sphere-plane contact. In this case, the capillary force, given by Israelachvili [114], is expressed as:

$$F_{cap} = 2\pi R \gamma (\cos\theta_1 + \cos\theta_2) = 4\pi R \gamma \cos\theta \qquad \text{(eq. 2.21)}$$

where R is the tip curvature, γ is the surface energy of the liquid, θ_1 and θ_2 are water contact angles (if non-identical) and θ is water contact angle for symmetric drop.

III - AFM study of the pentacene growth

III-1 AFM imaging

III-1-1 The dielectric surfaces

First of all, the morphologies of the gate dielectric surfaces were studied. Figure II-14 presents typical AFM images of both dielectric surfaces, the parylene (Figure II-14a) and the BCB (Figure II-14b). Images are representative of a $2x2\mu m^2$ area with a RMS (Root mean square) value of 3.47nm on the parylene and 0.42nm on the BCB.

This difference in the RMS roughness relates to different structure specificities of each surface. In the BCB case, we observe a flat and homogeneous surface with a "peak to valley" value ΔZ_{BCB} = 4.39nm. In the parylene case, the surface is rougher and presents an island-like morphology with ΔZ_{Par} = 28.1nm. Both ΔZ_{BCB} and ΔZ_{Par} are approximately proportional to their RMS-values that indicate a good homogeneity of the observed films. The difference in the roughness between the two dielectric surfaces leads to different initial conditions for the pentacene growth.
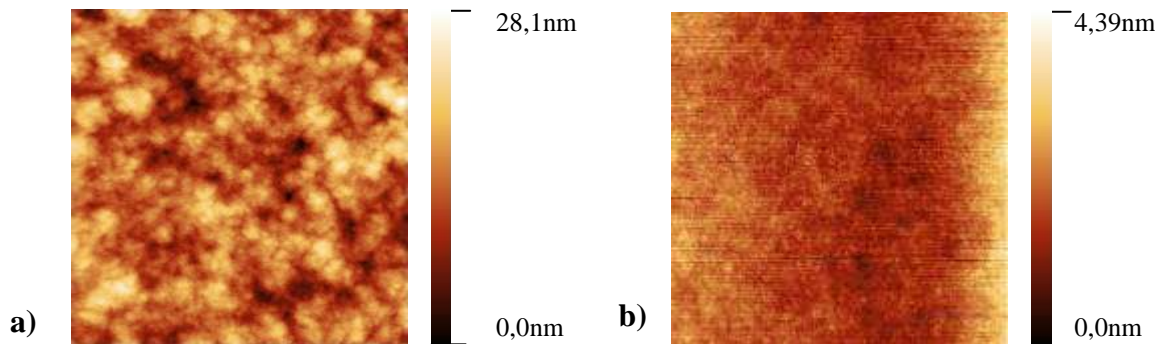
Figure II-14. AM-AFM Images of the (a) parylene-C (thickness 630nm; RMS=3,47nm) and (b) BCB (thickness 500nm; RMS=0,42nm) surfaces. Scan area: 2 x 2µm^2

III-1-2 The pentacene films

III-1-2-1 A grain structure

Pentacene films were deposited onto the gate dielectrics over a large scale range of equivalent thicknesses: 6, 10, 15, 20, 30, 35, 40 and 60 nm. The objective was to explore the pentacene growth evolution from early initial stages to well formed surface structures. Figure II-15 and Figure II-16 illustrate the evolution of the growth for some specific thicknesses on both BCB and parylene substrates on a 10x10µm^2, and 2x2µm^2 scan areas, respectively.

h=6nm ΔZ=83.6nm RMS=8.7nm   h=10nm ΔZ=45.6nm RMS=6.4nm   h=15nm ΔZ=62.0nm RMS=7.0nm   h=20nm ΔZ=78.3nm RMS=6.4nm

h=30nm ΔZ=62.5nm RMS=8.1nm   h=35nm ΔZ=74.0nm RMS=8.5nm   h=40nm ΔZ=64.3nm RMS=6.7nm   h=60nm ΔZ=63.8nm RMS=8.6nm

a)

h=6nm ΔZ=48.2nm RMS=5.6nm   h=10nm ΔZ=28.3nm RMS=3.6nm   h=15nm ΔZ=29nm RMS=3.8nm   h=20nm ΔZ=44.6nm RMS=4.9nm

h=30nm ΔZ=45.9nm RMS=5.6nm   h=35nm ΔZ=62.8nm RMS=6.6nm   h=40nm ΔZ=44.3nm RMS=6.4nm   h=60nm ΔZ=48.6nm RMS=7.2nm

b)

Figure II-15. Height AM-AFM images of pentacene surface for different pentacene thicknesses deposited on the parylene (a) and on the BCB (b) surfaces. Scan area: $10 \times 10 \mu m^2$.

h=0nm ΔZ=28.3nm RMS=3.47nm   h=6nm ΔZ=30.06nm RMS=4.43nm   h=10nm ΔZ=50.1nm RMS=6.33nm

a)   h=15nm ΔZ=47.6nm RMS=7.77nm   h=30nm ΔZ=55.1nm RMS=7.88nm   h=60nm ΔZ=51.3nm RMS=8.60nm

h=0nm ΔZ=4.39nm RMS=0.42nm   h=6nm ΔZ=41.8nm RMS=5.25nm   h=10nm ΔZ=24.2nm RMS=3.51nm

b)   h=15nm ΔZ=26.6nm RMS=3.69nm   h=30nm ΔZ=42.7nm RMS=5.38nm   h=60nm ΔZ=45.0nm RMS=7.28nm

Figure II-16. AFM images representative of a 2 x 2 μm^2, for some selected thicknesses of pentacene deposited on (a) parylene and (b) BCB.

Clearly, three general specificities can be seen among them:

1) A change in size of the grains with increasing the pentacene film thickness for both substrates

2) A different type of structuration before and after the thickness of 15nm for both substrates BCB and Parylene;

3) A sharp distinction in size and shape of the grains between layers deposited on the different dielectrics

From 6nm to 15nm pentacene equivalent thicknesses, a lateral growth of the islands with an evolution in shape is observed. The characteristic evolution of pentacene-on-BCB growth manifests by a shape transition of the islands from random shape at 6nm to compact pyramidal shape at 15nm. Otherwise, the pentacene-on-parylene growth begins from early small initial islands that form a quasi-layer at 6nm, difficult to separate from the parylene surface, and transforms to compact bulk shapes at 15nm (Figure II-16).

The film at10nm corresponds to an intermediate stage of semiconductor growth: deposited islands are larger and better developed than at 6nm but they are not already so compactly packed than at 15nm. The dielectric substrate is visible at some places (Figures II-15, II-16). Analysis of this first three films shows that the equivalent thickness of 15nm corresponds to a certain quantity of pentacene matter for which a new mode of surface growth begins. At this critical mass, the islands are well packed and their lateral growth can be limited by the close presence of the boundaries of neighbouring islands. Further 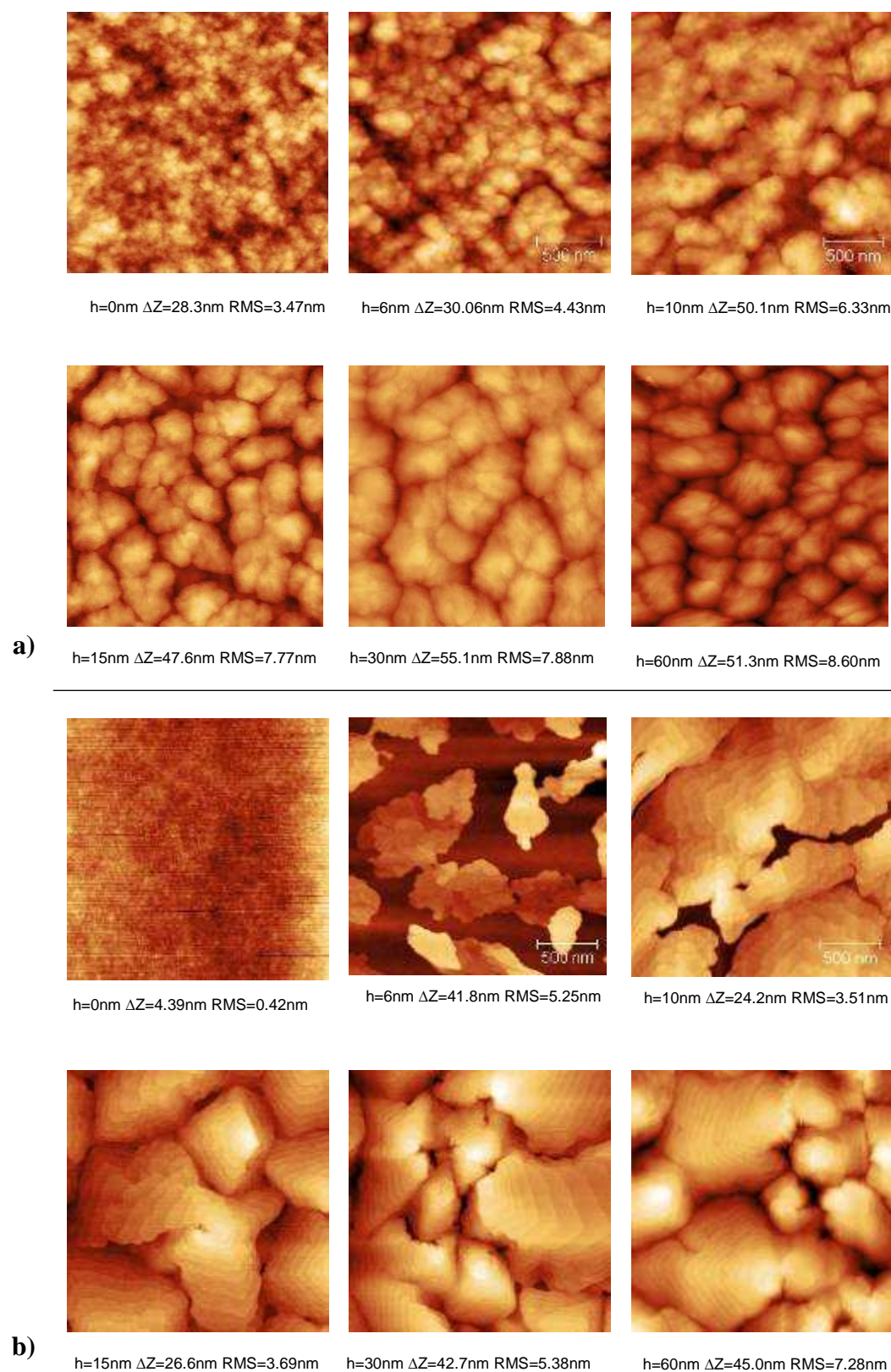increasing of coverage just induces an island size evolution with any significant changes in lateral shape: between 15nm and 60nm thicknesses, pentacene-on-BCB exhibits pyramidal structures and pentacene-on-parylene presented bulk-like shapes (Figures II-15, II-16).

III-1-2-2 Terraces in the grains

Distinctions between pentacene-on-BCB and pentacene-on-parylene, can be observed not only in grains shape. As an illustration, let's focus on one of the pentacene films with an equivalent thickness of 60nm. Figure II-17 shows AFM topography and amplitude error images of the pentacene surface on both substrates. Error images have a higher spatial resolution than topographic images (it represents a differential of the topography image, since it accentuates sharp turning points in the sample topography (high frequency information) at the expense of smooth slowly undulating areas (low frequency information)). On BCB, all islands have rectilinear accurate boundaries and grow narrowing to the peak that gives them a pyramid-like shape. Each pyramid is composed of a terrace stacking less and less larger in the vertical direction. The islands on parylene are smaller and present bulk-like shape with rounded boundaries. The islands have a granular rounded structure and they are not terminated by the presence of a single clear-defined peak. Basically, these bulks consist of small fragments of pentacene layer at least not well-ordered.

The surface structure of the islands is followed by performing cross sections on several images. On typical images of Figure II-17, cross sections were realized and the black (red) line on each image represents one typical cross section.

For pentacene-on-parylene, islands are presented with an irregular shape structure (Figure II-17e). The cross sections show a step height which approximately relates to two or three molecule lengths (3.42 nm and 4.54 nm ± 0.13). In achieved experiment, it was shown by RDS that molecules tilt differently on PMMA and Ta_2O_5 [115].
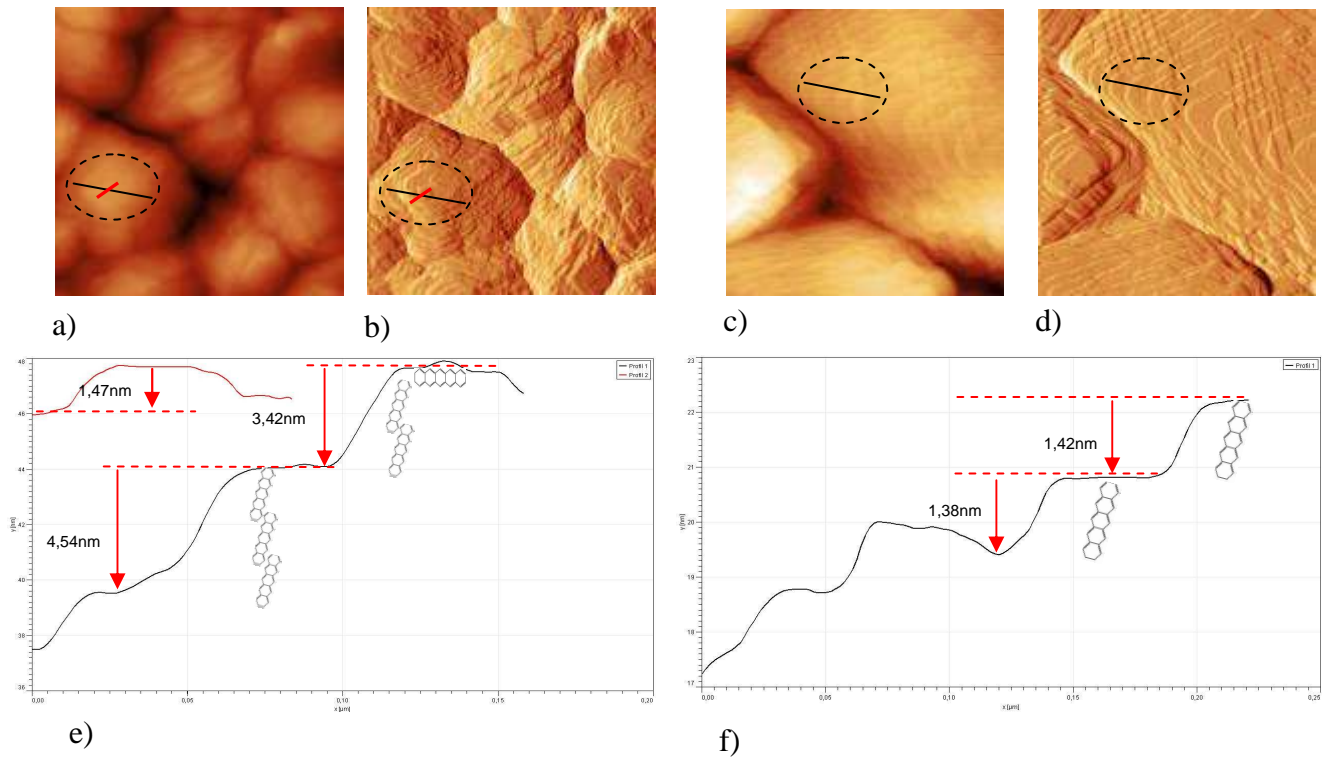
Figure II-17. Grain structure of Pentacene (thickness 60nm) on (a, b) Parylene and on (c, d) BCB. Topography (a, c) and error (b, d) images of 1x1µm. Cross sections (e) black and red lines on the images (a, b) and (f) black line on the images (c, d).

Besides, for pentacene-on-BCB, the height of each terrace step is about 1.4nm ± 0.07 that approximately corresponds to the length of the pentacene molecule (Figure II-17f). Moreover, judging from the continuity of the terraces borders and the homogeneity of the large edges, we can establish that each terrace corresponds to a pentacene monomolecular layer. Then, the pyramidal islands are composed of flat homogenous monolayers of standing up pentacene molecules, deposited vertically one to each other.

According to the deviation standard error in the measurement, it is impossible to conclude on a possible tilt of the pentacene molecule on the terraces. However, it is clear that the shape of the islands for the low coverage influences the mean height of the terraces, one monolayer for pentacene on BCB and 2 or 3 monolayers for pentacene on parylene.

III-2 Statistical grain analysis

The knowledge of the structural composition of pentacene islands, their geometry and their ordering allows us to understand how the pentacene films form. In order to study the influence of film thicknesses on these parameters, a statistical analysis of the geometrical size of the islands was performed.

III-2-1 Width and height of grains

The RMS distribution of the grain heights represents quantitative information about the surface irregularity. Figure II-18 shows the roughness of the pentacene films surfaces for all deposited thicknesses.
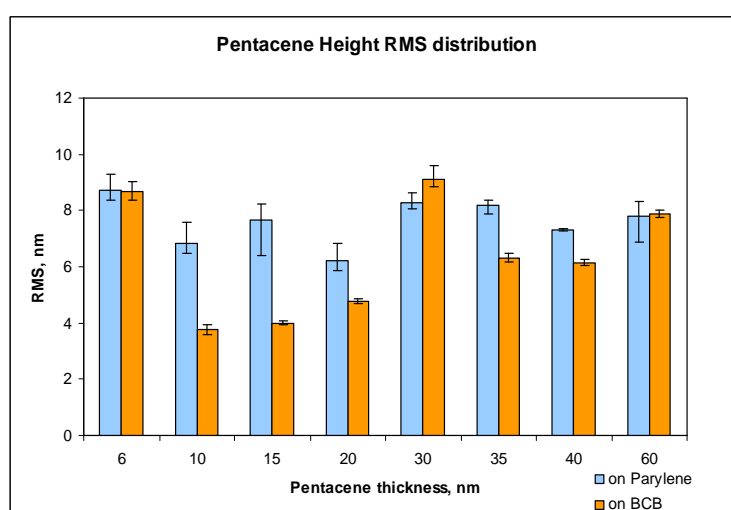
Figure II-18. RMS distribution of Pentacene islands heights deposed on BCB and Parylene
(for an area of 10 µm x 10µm)

By comparing data on Figure II-18, we can establish two general tendencies:

1) the RMS values of pentacene surface on BCB and parylene (RMS Pen/BCB and RMS Pen/Par) present two peaks for the same film thicknesses for 6nm and 30nm (30 - 35nm for parylene).

2) the RMS Pen/Par values are greater than the corresponding RMS Pen/BCB excepted for the 30nm pentacene thickness.

The similarity between the RMS values of both samples for 6nm and 30nm can be explained in the following way. The thickness of 6nm pentacene relates to a situation where the islands on both BCB and Parylene substrates are not already connected. Consequently, the RMS was calculated for the real island heights – between a substrate surface (bottom of island) and top of island.

At the same time, RMS calculations for the following stages of growth (thicknesses greater than 10nm) can be performed just for accessible surface of pentacene. In other words, beginning at 15nm film thickness, the islands are well-packed and the lowest point of deposed layer corresponds to the level of border juxtapositions. In this case, the substrate surface is well covered and is not accessible to the SPM probe.

92

Despite the case at 6nm, RMS values could then be compared for higher coverages and the increase at 30nm for both substrates is significant of a roughening of the surface for this peculiar thickness.

To interpret this behaviour, RMS analysis can be completed by additional statistical investigations necessary to define the size and volume occupied by the islands. In order to establish the variation of the islands lateral dimensions, calculation of grains size distribution was performed. RMS, grain sizes and grain volumes were calculated with Gwyddion modular program for SPM data visualization and analysis [116]. Grain size and volume calculations were performed by using the segmentation algorithm implemented in Gwyddion. This algorithm is based on surface area triangulation scheme and an example of it application is shown in Figure II-19 (c) and (d) for pentacene 30nm thickness on BCB. More precisely, knowing the pixel dimension it becomes possible to calculate the size and volume for each one marked by a mask area (blue color on Fig. 19(d)), that corresponds to the shape of a grain.
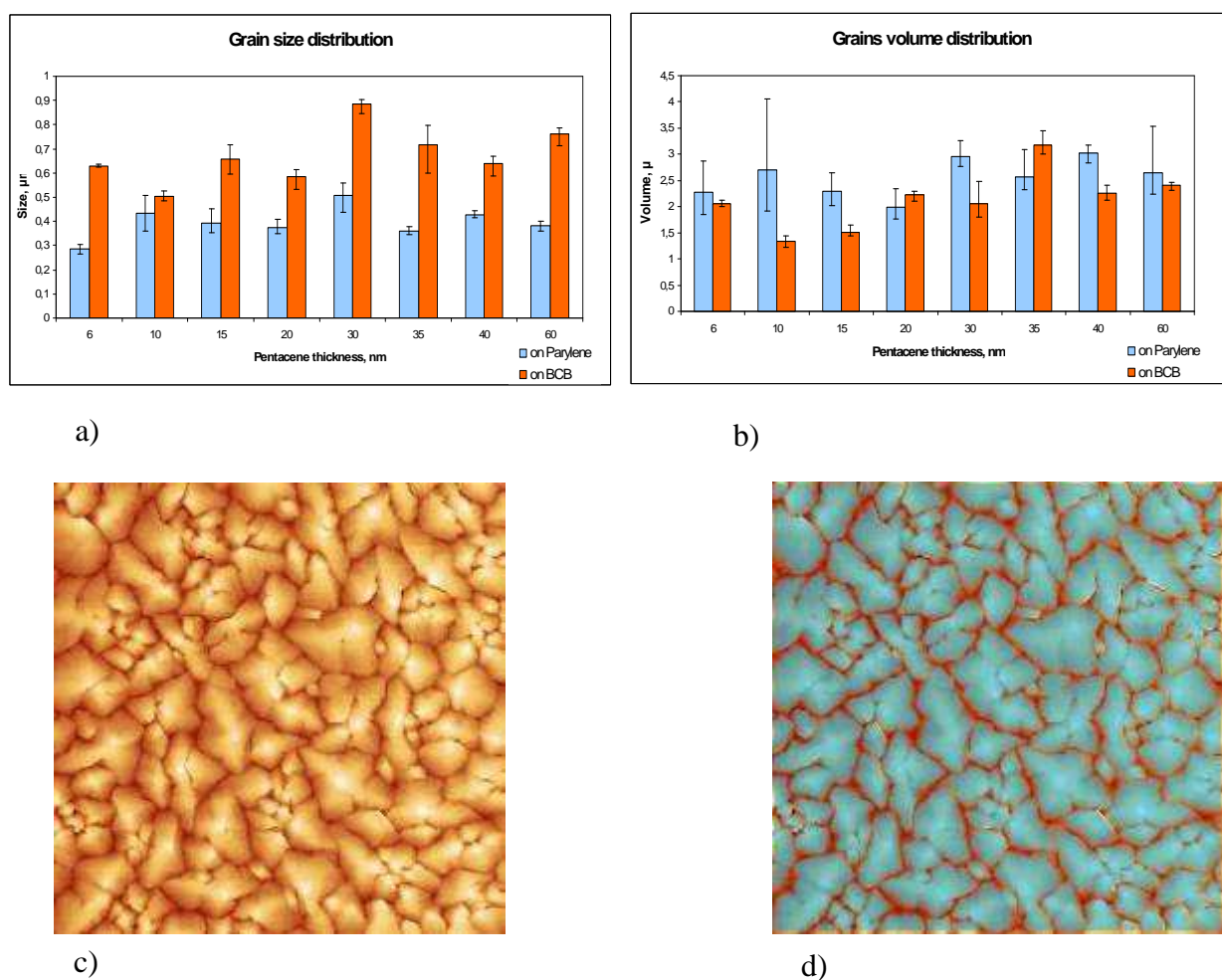

a)

b)

c)

d)

Figure II-19. Distribution of the grain size (a) and grain volume (b) of Pentacene deposed on BCB and Parylene. Figures (c) and (d) represent an example of application of segmentation algorithm (Gwyddion) for pentacene 30nm on BCB (10µm x 10µm). Figure II-(c) – before segmentation (without mask), and Figure II-(d) – after segmentation (with blue color mask).

The results of the analysis are obtained for both pentacene-on-BCB and pentacene-on-Parylene films for each coverage and are presented on Figure II-19a. We can see that the pentacene islands on BCB are noticeably larger than on parylene. This difference in size is especially expressed for 30nm of the film thickness both on BCB and Parylene. In addition, the size distribution presents the same evolution than the RMS distribution: an increase from 6nm to 30nm followed by a decrease from 30nm to 60nm.

This size parameter is not sufficient to give a complete information about a shape structure so the total volume covered by the islands was also evaluated (Figure II-19b). The peak at 30 nm is not so marked than for the grain size distribution, a maximal volume value is obtained for coverage of 30nm and 40nm for pentacene on parylene and for a coverage of 35 nm for pentacene on BCB.

In addition, the grain volume distribution is often inversed compared to the grain size distribution at 30 nm. In another words, it means that the largest pyramids on BCB occupy a smaller total volume than the small islands on parylene for the majority of thicknesses. This seems to indicate that the growth follows more a 3D mode on parylene than on BCB.

III-2-2 The PSD analysis

In order to complete the grain size analysis, PSD spectra were measured on typical images of 10µm x10µm for coverage from 15 to 60nm on both systems. The theory of the PSD spectra has been developed in details, in chapter I. The PSD analysis was performed on our AFM images to quantify both the evolution of the average grain size and the surface roughness as a function of the thickness of the films and also to provide information on the growth mechanism.

Figure II-20 presents topographic AFM images over $10 \times 10µm^2$ scanned areas for a 40nm thickness and their respective PSD spectra for both systems. The bandwidth of the spatial frequencies extends between the minimal and the maximal spatial frequencies.

Because the length scale (L) is 10µm, the minimal spatial frequency is given by f_{min}=1/10µm=0.1µm^{-1} and the maximal spatial frequency by $f_{max} = 1/(2\Delta) = (25.6µm^{-1})/2 = 12.8$ µm^{-1}, where Δ is the sampling rate, given by: $\Delta = 10µm/256 = 39nm$.

As mentioned in chapter I, all power spectra exhibit three distinct regions, represented as parts I, II and III.

– The region I includes the low spatial frequencies with a $k < 10^7$ m^{-1} for pentacene on parylene and a k $< 7.10^6$ m^{-1} for pentacene on BCB which correspond to a nearly constant value of the roughness σ_{PSD} (magnitude of PSD). This low-frequency plateau means an absence of correlation (it does not change with the scale) and indicates an absence of any characteristic length.

– The region II involves intermediate frequencies between approximately 10^7m^{-1} and $6·10^7$m^{-1}. For this high-frequency range the PSD is strongly frequency dependent and represents the power-law decay. This region characterizes the mechanism of surface formation and indicates the surface self-affine behaviour [117].

– The region III corresponds to the highest frequencies of the spectra ($k > 6.10^7 m^{-1}$). As we mentioned in chapter I, the PSD in this region is tip size dependent and should not be taken into account.

a)   b)
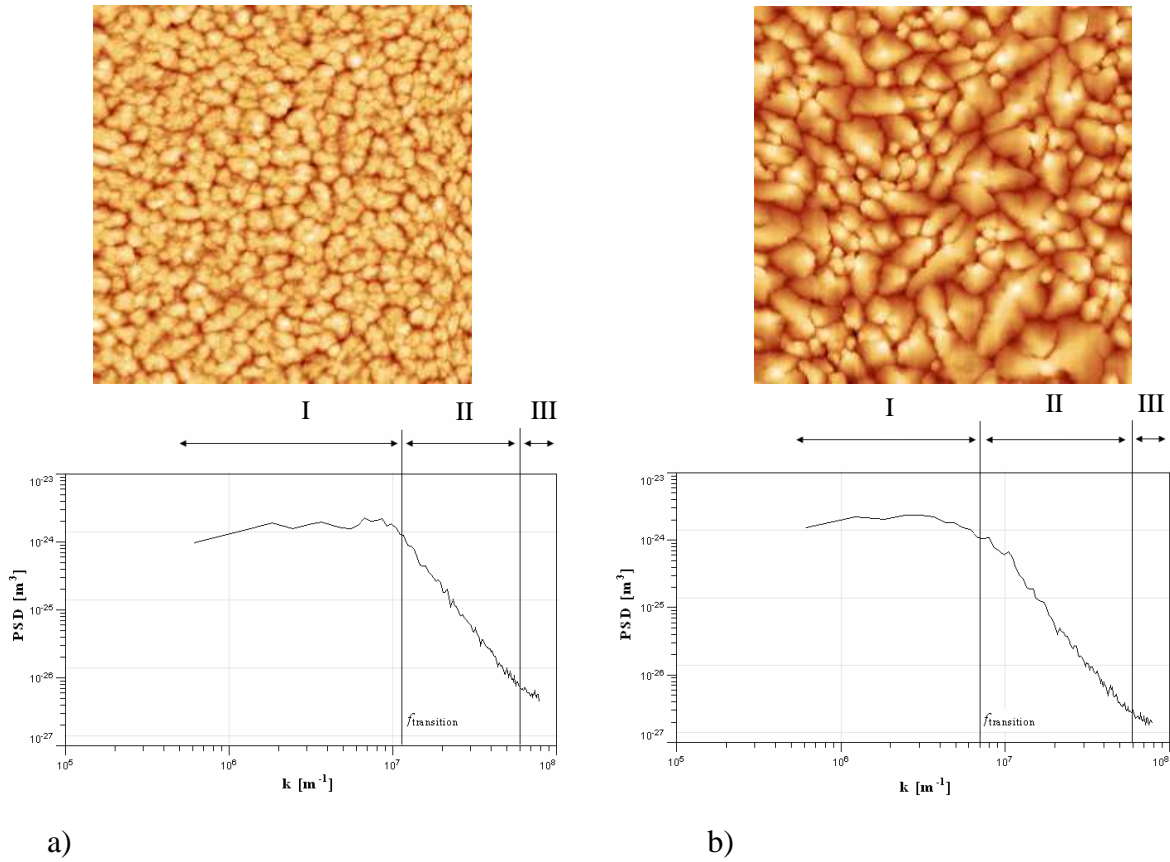
Figure II-20. Topographic image and typical PSD spectra of the pentacene
deposited on parylene (a) and BCB (b) for a coverage of 40 nm

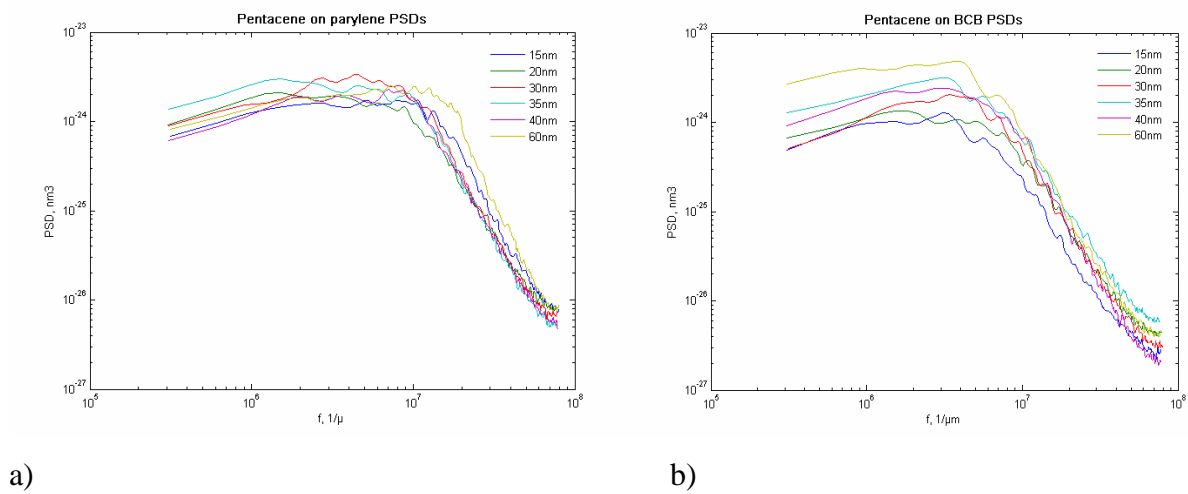a)   b)

Figure II-21. PSD spectra of the pentacene films deposited on parylene a) and BCB b)

Figure II-21 shows in details two sets of PSD spectra for different thicknesses of pentacene upon both substrates, reflecting different stages of the surface morphologies formation.
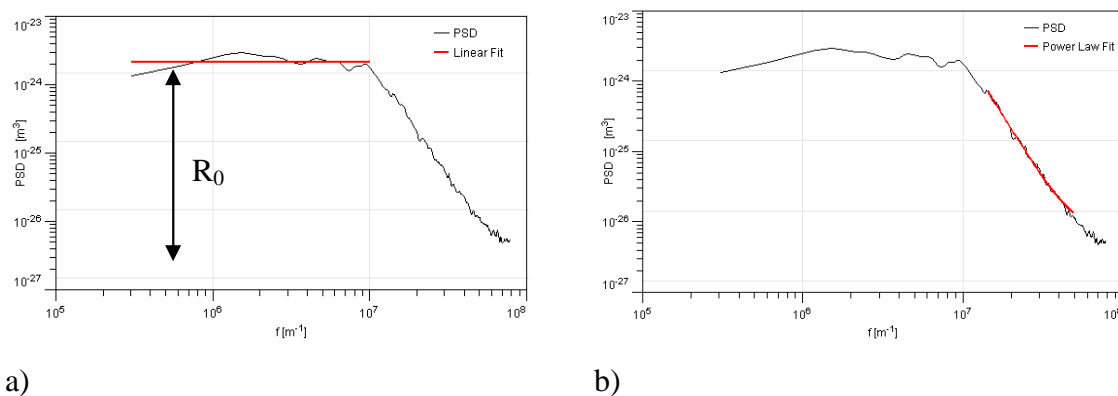
Figure II-22. Calculation of PSD magnitude R_0 for low spatial frequencies region using linear fitting

For region I, the magnitude of the PSD spectra R_0 increases from 15nm up to the 30 – 35nm and then starts to decrease, for pentacene on parylene. Such behaviour is less pronounced for pentacene on BCB. The plateau heights (R_0) were measured using the linear fitting of the low spatial frequencies region I of spectra as shown in Figure II-22a. However, this fitting is not really appropriate because we can see that the PSD magnitude is not at a constant value in region I on experimental curves (Figure II-21). The PSD magnitude increases with the frequency in this region. The slope is more pronounced for the 30nm thickness, it means that small features (contributing to higher PSD magnitude near $f_{transition}$) are more numerous than large features (contributing to lower PSD magnitude in the region I).

Table 1 summarizes the PSD magnitudes R_0 identified from experimental curves in Figure II-21, in comparison with RMS roughness σ which corresponds to the integral of the PSD curve, theoretically. R_0 is a peculiar parameter corresponding to the low frequency, thus the large features.

These two parameters could not be compared directly but they present the same evolution trend toward thickness for our experimental systems (table 1). This means that large features mostly govern the total roughness. These results are in a good agreement with the evolution of values of the RMS roughness σ (eq. 3 for R_q) which were previously calculated over the same sample areas.

film thickness, (nm)	pentacene on parylene		pentacene on BCB	
	σ, (nm)	R_0, (m^3)	σ, (nm)	R_0, (m^3)
15	7.80 ± 0.93	$1.71 \times 10^{-24} \pm 4.5 \times 10^{-26}$	4.03 ± 0.05	$0.91 \times 10^{-25} \pm 5.8 \times 10^{-26}$
20	6.20 ± 0.49	$1.63 \times 10^{-24} \pm 5.0 \times 10^{-26}$	4.71 ± 0.08	$1.06 \times 10^{-24} \pm 3.9 \times 10^{-26}$
30	8.32 ± 0.28	$2.27 \times 10^{-24} \pm 1.1 \times 10^{-25}$	9.96 ± 0.37	$1.39 \times 10^{-24} \pm 9.6 \times 10^{-26}$
35	8.07 ± 0.25	$2.22 \times 10^{-24} \pm 7.2 \times 10^{-26}$	6.26 ± 0.15	$1.76 \times 10^{-24} \pm 1.5 \times 10^{-25}$
40	7.43 ± 0.06	$1.75 \times 10^{-24} \pm 4.0 \times 10^{-26}$	6.09 ± 0.12	$1.95 \times 10^{-24} \pm 7.8 \times 10^{-26}$
60	7.11 ± 0.72	$1.47 \times 10^{-24} \pm 4.2 \times 10^{-26}$	8.03 ± 0.14	$3.35 \times 10^{-24} \pm 1.9 \times 10^{-25}$

Table 1. PSD magnitudes R_0 obtained from the PSD curves (Figure II-2)

and RMS roughness σ corresponding to Figure II-21.

The classical way to calculate the correlation length consists in determining the transition frequency $f_{transition}$ in the intersection point of the two fitting curves of regions I and II in the PSD spectra (Figure II-22 a, b). Such an approach gives the order of magnitude of $f_{transition}$ about $10^7 m^{-1}$, for the experimental PSD curves, in Figure II-20, which corresponds to a mean grain diameter $\xi \sim 100nm$. But the real grain size varies between 360-508nm for pentacene on parylene and between 504-866nm for pentacene on BCB (Figure II-19 a). So, this method does not provide a complete description of a whole grain but is just sensitive to the details of the high spatial scales. Another approach that provides more adequate grain description will be discussed below.

In order to determine the slope of the high-frequency region II the exponential part of PSD was fitted using the expression (9) (see Figure II-22b), which gives for asymptotic range ($f \rightarrow \infty$):

$$PSD(f) = K f^{-\gamma} \qquad \text{(eq 2.22)}$$

Resulting values of the slope (γ) are reported in the table 2 with related values of scaling exponent (α). where $\gamma = 2(1+\alpha)$, for distances inferior to the correlation length (ξ) (Figure II-25 b).

film thickness, (nm)	pentacene on parylene		pentacene on BCB	
	γ	α	γ	α
15	2.94 ± 0.10	0.47	2.66 ± 0.11	0.33
20	3.07 ± 0.06	0.49	2.88 ± 0.07	0.43
30	3.14 ± 0.12	0.91	2.95 ± 0.12	0.49
35	3.27 ± 0.07	0.89	3.05 ± 0.08	0.54
40	3.15 ± 0.07	0.58	2.82 ± 0.14	0.46
60	3.13 ± 0.10	0.56	2.69 ± 0.09	0.34

Table 2. PSD slope (γ) and scaling exponent (α)

The calculated α for both pentacene on parylene and on BCB exhibit nonlinear evolution: the scaling exponents increase up to their maximum values at 30-35nm and then decrease for higher coverages. It means that grains become more circular or compact at these thicknesses. The pentacene grown on parylene showed a grain morphology approaching the ideal circular shape ($\alpha=1$) with a related α of 0.91 and 0.89, for thicknesses of 30nm and 35nm, respectively. For pentacene on BCB, the same increase of the α value is observed at the same thicknesses. However, the values reached are not high enough to reveal a particular change in the grains shape (respectively 0.49 and 0.54).

Using the fractal model, we can calculate the spectral strength (K) the spectral index (ν) parameters and the fractal dimension D_f. Values are reported in Table 3.

film thickness, (nm)	pentacene on parylene			pentacene on BCB		
	K	v	D_f	K	v	D_f
15	4.04×10^{-3}	1.94 ± 0.10	2.49	1.49×10^{-6}	$1.66 \pm 0,11$	2.42
20	6.32×10^{-3}	1.98 ± 0.07	2.50	8.22×10^{-5}	$1.86 \pm 0,11$	2.47
30	2.67×10^{-2}	2.81 ± 0.19	2.70	2.34×10^{-4}	$1.98 \pm 0,09$	2.50
35	1.74×10^{-1}	2.78 ± 0.08	2.69	1.28×10^{-3}	$2.08 \pm 0,16$	2.52
40	2.15×10^{-2}	2.16 ± 0.15	2.54	4.33×10^{-5}	$1.92 \pm 0,09$	2.48
60	1.45×10^{-2}	2.12 ± 0.06	2.53	5.44×10^{-6}	$1.67 \pm 0,10$	2.42

Table 3. Fractal contribution components (PSD$_{fractal}$): spectral strength (K), spectral index (v) and fractal dimension D_f

The fractal dimension takes into account the substrate influence and provides the information about the relative amounts of the surface irregularities at different scales.

In our case, it means that it can be influenced by the parylene or BCB surface, respectively. Table 3 shows that all D_f values are around ~ 2.5, which indicates the presence of Brownian fractals in surface morphology and is related to a strong dependence of the microstructural nature of pentacene surfaces on the deposition parameters. One can notice that the D_f values for pentacene on parylene are slightly larger than the corresponding values for pentacene on BCB, meaning a higher sticking probability of pentacene molecules while deposition on the parylene than on the BCB (see paragraph V-2-2-2 for more details). The maximal fractal dimensions are obtained for film thicknesses of 30 and 35nm in both cases, that can be explained by an increase of the sticking probability for these coverages. The fractal strength K is stronger for pentacene on parylene surfaces than on BCB that can be related to the respective roughness of the surfaces..

Using the k correlation model, we can extract the 3 functional parameters A, B, C. They are presented in Table 4.

film thickness, (nm)	pentacene on parylene			pentacene on BCB		
	A (m^3)	B (m^{-1})	C	A (m^3)	B (m^{-1})	C
15	2.34×10^{-24}	3.51×10^7	3.14	1.04×10^{-24}	1.38×10^7	1.26
20	1.99×10^{-24}	5.63×10^7	2.12	1.24×10^{-24}	9.47×10^6	1.64
30	2.25×10^{-24}	4.99×10^7	2.54	1.31×10^{-24}	1.03×10^7	1.43
35	2.89×10^{-24}	5.67×10^7	2.53	2.60×10^{-24}	1.07×10^7	1.52
40	1.60×10^{-24}	4.44×10^7	2.63	2.13×10^{-24}	9.22×10^6	2.03
60	2.90×10^{-24}	3.75×10^7	2.85	4.24×10^{-24}	1.55×10^7	1.38

Table 4. Parameters of k-correlation model for PSD plots of pentacene films

The A parameter has the same physical sense than R_0 but they are calculated differently. Obtained values for A and R_0 look similar (tables 1 and 3). The inverse value of the parameter B represents the mean grain size. According to ABC-model, the maximum grain sizes of $1/B_{parylene} = 1/3.51 \times 107 = 28.49$nm (for thickness of 15nm) and $1/B_{BCB} = 1/1.03 \times 107 = 108.46$nm (for thickness of 30nm). However, these values are not in agreement with the mean size of the grains measured on Figure II-19 a): 508nm for pentacene on parylene and 866nm for pentacene on BCB. These lower values of 28.49nm (on parylene) and 108.46nm (on BCB) are due to the high sensitivity of the k-correlation model to small morphological features. In fact, this measurement allows to identify a subjacent structure inside the grains, which can be related to size of small terrasses on the top of grains (see Figure II-17 b, d).

Values of the C parameter are in the interval between 2.12 to 3.14 for pentacene on parylene and between 1.26 to 2.03 for pentacene on BCB. It was shown in Chapter I that these values inform to the growth mechanisms. In our study, it means that the growth of the pentacene films on parylene begins by an evaporation and condensation mechanism ($C = 2$) and evoluates in a bulk diffusion mechanism ($C = 3$) for thicknesses higher than 30nm. For the pentacene on BCB, the growth begins by a viscous flow mode until a thickness of 35nm and changes in an evaporation and condensation mechanism for higher thicknesses.

In addition, the equivalent RMS roughness σ_{ABC} and the correlation length τ_{ABC} can also be calculated and are reported in Table 5.

film thickness, (nm)	pentacene on parylene		pentacene on BCB	
	σ_{ABC} (nm)	τ_{ABC} (nm)	σ_{ABC} (nm)	τ_{ABC} (nm)
15	0.57	239.88	4.32	46.96
20	1.18	64.31	2.06	192.16
30	0.94	109.21	2.82	110.84
35	1.22	95.30	3.75	133.03
40	0.69	132.19	2.08	353.40
60	0.74	184.92	8.11	63.94

Table 5. Intrinsic contribution components σ_{ABC} and τ_{ABC} (equivalent RMS roughness and correlation length)

For both substrates, σ_{ABC} values are lower than those calculated from root-mean-square deviation of the height (σ values in Table 1). Unfortunately, the general trend of a singular value for 30 or 35 nm thicknesses is not observed. This can be explained by the fact that the expression of σ_{ABC} implies a well-defined value of the A parameter, thus in our spectra, we don't have a uniform plateau but a decaying function toward lower frequencies. This induces a high uncertainty on the A value and then on the σ_{ABC}.

The k-correlation model is more suitable in the domain of spatial frequencies corresponding to the B and C parameters. Then the correlation length τ_{ABC} describes more precisely the size of the features. τ_{ABC} values are larger than B-values, however they are still smaller than real grains size. This can be interpreted

by the fact that the position of the "knee" describes a structure corresponding to the irregularities of the grain surface.

Applying the superstructure model, gives parameters presented in table 6. The parameters τ_{sh1} and τ_{sh2} correspond to the size of aggregates and single grains with their respective height parameters σ_{sh1} and σ_{sh2}. This model is appropriate to our system, because the deposition rate of pentacene was constant and the formation of aggregates has been influenced by the variation of the film thickness (see Chapter I).

film thickness, (nm)	pentacene on parylene				pentacene on BCB			
	$\tau_{sh1,nm}$	$\sigma_{sh1,nm}$	$\tau_{sh2,nm}$	$\sigma_{sh2,nm}$	$\tau_{sh1,\mu m}$	$\sigma_{sh1,nm}$	$\tau_{sh2,nm}$	σ_{sh2}
15	780.78 $\pm$ 82	2.47 $\pm$ 0.17	285.23 $\pm$ 11	3.91 $\pm$ 0.08	1.27 $\pm$ 0.14	1.46 $\pm$ 0.10	386.31 $\pm$ 45	2.54 $\pm$ 0.19
20	813.58 $\pm$ 99	2.54 $\pm$ 0.21	296.56 $\pm$ 19	4.19 $\pm$ 0.19	1.39 $\pm$ 0.16	1.41 $\pm$ 0.10	410.89 $\pm$ 34	3.89 $\pm$ 0.22
30	1100 $\pm$ 110	2.09 $\pm$ 0.13	292.66 $\pm$ 6.2	4.35 $\pm$ 0.06	1.56 $\pm$ 0.21	1.44 $\pm$ 0.13	511.96 $\pm$ 41	3.01 $\pm$ 0.17
35	831.7 $\pm$ 40	2.98 $\pm$ 0.09	292.40 $\pm$ 11	4.34 $\pm$ 0.08	1.35 $\pm$ 0.14	1.97 $\pm$ 0.14	428.89 $\pm$ 28	3.77 $\pm$ 0.16
40	672.72 $\pm$ 61	2.51 $\pm$ 0.17	360.95 $\pm$ 14	3.51 $\pm$ 0.08	1.18 $\pm$ 0.12	2.17 $\pm$ 0.16	502.90 $\pm$ 29	3.58 $\pm$ 0.13
60	596.55 $\pm$ 41	2.40 $\pm$ 0.11	201.90 $\pm$ 5.5	4.36 $\pm$ 0.08	1.03 $\pm$ 0.12	3.28 $\pm$ 0.25	399.70 $\pm$ 12	5.28 $\pm$ 0.09

Table 6. Superstructure contribution components (PSD$_{sh}$). Parameters τ_{sh1} and τ_{sh2} describe mean size of aggregates (superstructures) and grains respectively with their height parameters σ_{sh1} and σ_{sh2}

Figure II-23 shows an AFM image of both systems for a 40nm thickness; Morphological features (grains and aggregates of grains) are reported with their characteristic parameters τ_{sh1} and τ_{sh2} for pentacene deposited on parylene (Figure II-23a) and on BCB (Figure II-23b). The mean sizes of aggregates are described by the τ_{sh1} parameter. Inside the aggregates, smaller grains are presented with a mean size described by the τ_{sh2} parameter. On the image, blue contours surround aggregates with their constituent grains and scale bares represent the real values of τ_{sh1} and τ_{sh2}.

These two kinds of grains, small and large are easy to observe on the pentacene on BCB surface (Figure II-23b), they correspond to the two size τ_{sh1} and τ_{sh2}. For the pentacene on parylene the τ_{sh1} parameter describes the size of large grains composed by the small ones characterized by the τ_{sh2} parameter (aggregates).

τ_{sh1}
τ_{sh2}

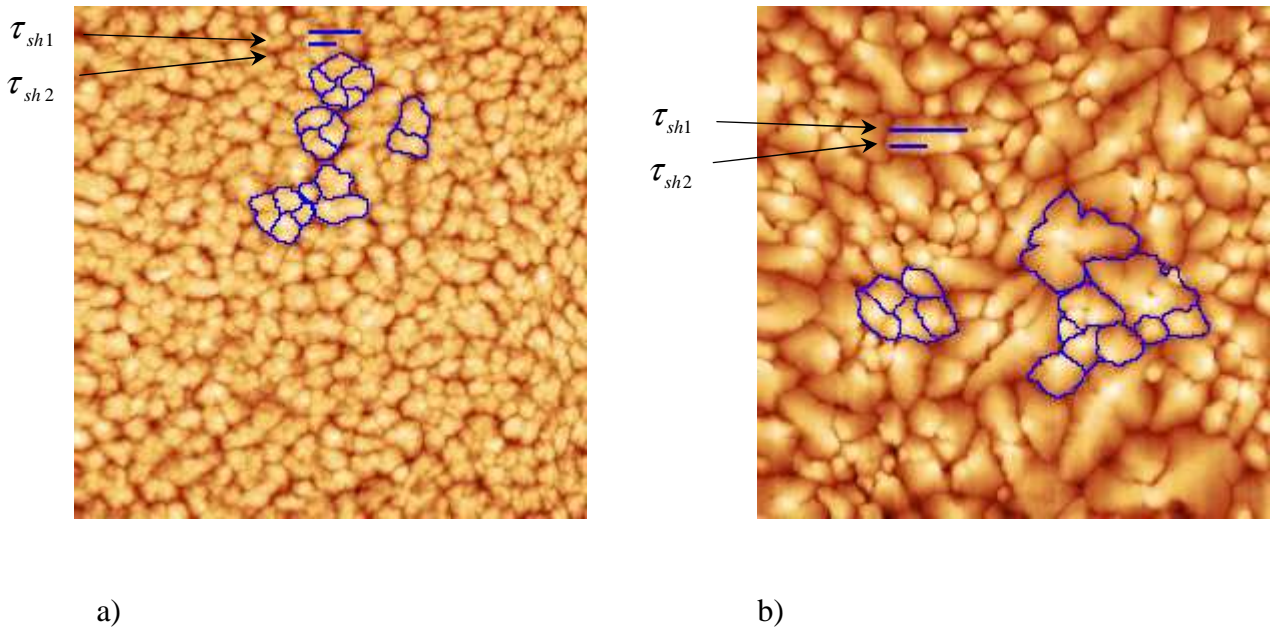a)   b)

Figure II-23. Correspondence between aggregate sizes and grain size on AFM images 10µm x 10µm for a
40nm thickness deposited on parylene (a) and BCB (b)

Table 3 shows that aggregate and grain sizes, τ_{sh1} and τ_{sh}, are both 60% smaller for pentacene on parylene than for pentacene on BCB. It is in agreement with results obtained by the segmentation method (Figure II-19 (c), (d)).

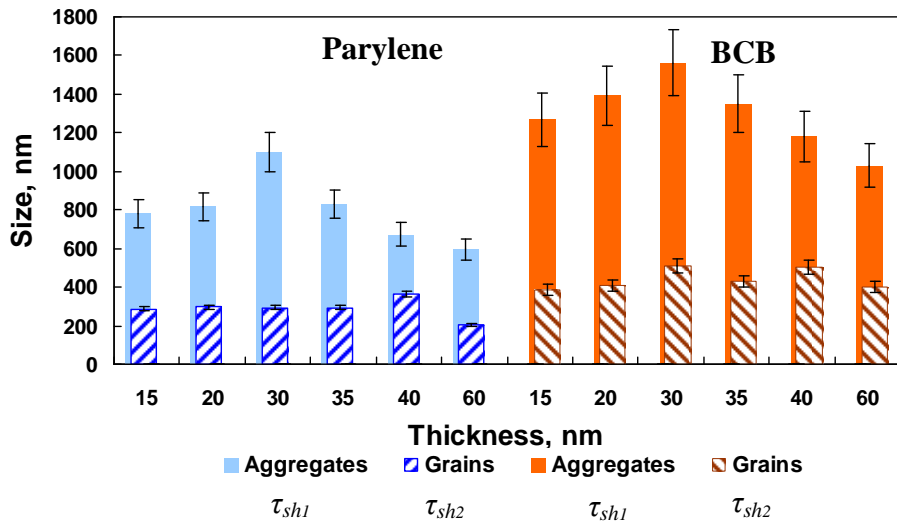For more convenience, the τ_{sh1} and τ_{sh2} values are presented in Figure II-24.

Figure II-24. Grain and aggregate sizes, τ_{sh1} and τ_{sh2} obtained with the superstructure PSD_{sh} model

101

As shown in Figure II-24, the variation of film thickness has caused the formation of superstructures with sizes ranging from 596nm to 1100nm, for pentacene on parylene. More precisely, by increasing the film thickness, the size of this superstructure increases from 780nm to a maximal value of 1100nm for a thickness of 30nm and then decreases progressively to a value of 596nm. At the same time, the τ_{sh2} parameter characteristic of the grain size remains around the same value of 288 +/– 50.7nm independently from the deposited thickness.

The same behaviour is also observed for the pentacene on BCB system. The superstructure size evolves from a τ_{sh1} value of 1.27µm to 1.56 µm for a 30 nm thickness and then falls linearly down to 1.03µm. Similarly, the τ_{sh2} parameter remains around a value of 440 +/– 54.1nm, for all thicknesses.

An important conclusion is that the size evolution of the aggregates is not due to an evolution of the size of the grains that form them but is mostly influenced by the quantity of these grains.

On both substrates, the height parameters σ_{sh1} and σ_{sh2} reflect the relation between superstructure and grain heights for different film thicknesses but not their absolute values. For both substrates, calculation of the height parameters lead to $\sigma_{sh2} > \sigma_{sh1}$. This means that individual grains are higher than their aggregates. This erroneous result can be understood by the shape of the PSD curve at low frequency, a decreasing tendency (Figure II-21). Consequently, lower spatial frequencies representative of aggregates (larger features), have lower PSD magnitude values, leading to lower heights than smaller grains. It means that σ_{sh1} and σ_{sh2} absolute values can not be compared directly between them.

The surface analysis of the morphological structure during growth was done by classical parameters measurements and by using the PSD spectral method with different models. Several informations were obtained and particularly, the specificity of the 30-35 nm thickness was demonstrated by many parameters. According to the k-correlation model, this thickness corresponds to an evolution in the growth mechanisms: rrom evaporation and condensation modes to a bulk diffusion mode, for pentacene on parylene, and from a viscous flow to an evaporation condensation mode for pentacene on BCB.

The α value shows that a more regular shape of the grains is obtained at this thickness, it tends to a circular shape for pentacene on parylene. Three different feature sizes were identified, the terrace length around 30nm and 100nm for pentacene on parylene and on BCB respectively, given by the B parameter, the grain size and the superstructure, aggregate, size obtained by the superstructure model. It was shown that the grain size is roughly constant during growth and that the aggregates enlarge by adding grains reaching the largest size for the 30nm thickness.

The surface analysis is not sufficient to answer to the issue "Why is there a specific 30nm thickness?" We should take into account, surface energy considerations, and experimental conditions of the film deposition.

III - 3 Surface free energy of pentacene: one of the driving factors in films patterning

Hence, we can establish two general stages in pentacene film growth: one is substrate-induced and the other one is a thickness-driven stage.

Substrate-induced pentacene growth mode can be explained by the dependence of the diffusion length of the deposited molecules on the roughness and the free energy of the surfaces.

To interpret the mechanism driving the enhancement of the pentacene grains size, we propose to follow the pentacene surface free energies for corresponding thicknesses 15nm, 30nm and 40nm.

III-3-1 Contact-angle measurements

The surface energies for different pentacene samples were calculated by measuring contact angles with various test liquids. Two types of contact angle-meters were used: a PG-3 Measuring Head (FIBRO System AB, Sweden) and a GBX Instrumentation Scientifique (France).

First experiments were realized with the PG-3 Measuring Head at a temperature $T = 23\text{-}24°C$ and a relative humidity of 33%. The algorithm ASTM D5946 (Standard Test Method for Corona-Treated Polymer Films using Water Contact Angle Measurements) allows to perform free surface energy calculations and only requires deionised water (copyright ASTM International)In our calculation, we will take the value of $\gamma=72.8$ mJ/m^2 for the surface tension of the deionised water [114]

The liquid deposition was realized in automatic regimes with microsyringe that pulled the liquid into the teflon capillary to prevent the wetting of the liquid. The volume of the water drop was 1.5µl that provided stable conditions of deposition. However, a relaxation after deposition was observed when the drop was brought in contact with the surface. The relaxation process was studied in dynamic regime of contact angle measurements. Results showed that a stabilization time of 60s is necessary to obtain a stable geometry of the water drop (Figure II-25).
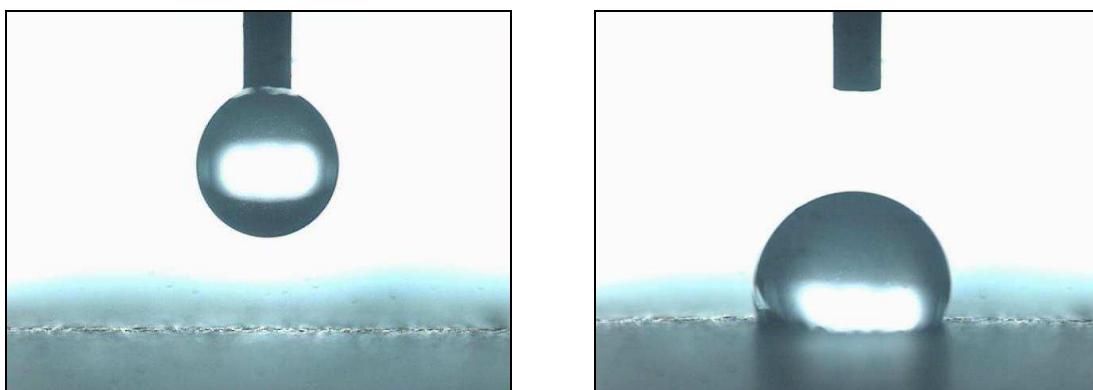

Figure II-25. Liquid drop (distilled water) deposition with the PG-3 Measuring Head on pentacene surface

After the instrument calibration, the contact angle measurements were realized with five equivalent drops for each pentacene sample. Each measurement was started 60s after the drop deposition. The contact angle measurements were performed for pentacene on parylene and on BCB with equivalent thicknesses of 15, 30 and 40nm. Experimental angles and their corresponding pentacene surface energies are shown in Table 7.

P15Par		P30Par		P40Par		P15BCB		P30BCB		P40BCB	
$\theta °$	γ_s mJ/m²	$\theta °$	γ_s mJ/m²	$\theta °$	γ_s mJ/m²	$\theta °$	γ_s mJ/m²	$\theta °$	γ_s mJ/m²	$\theta °$	γ_s mJ/m²
78.9	36.5	73	38.6	74.2	38.2	71.5	39.2	76.7	37.3	75.5	37.7
80	36.1	68.6	40.2	78.1	36.8	75.1	37.9	80.2	36	74.9	38
78.8	36.5	68.5	40.3	74.2	38.2	75.3	37.8	80.8	35.8	63.7	42
70	39.7	61.9	42.7	64.9	41.6	72.8	38.7	79.6	36.3	57.9	44.1
76.6	37.3	70.4	39.4	68.6	40.2	70.1	39.7	80.8	35.8	62.2	42.6
$<\theta>$	$<\gamma_s>$	$<\theta>$	$<\gamma_s>$	$<\theta>$	$<\gamma_s>$	$<\theta>$	$<\gamma_s>$	$<\theta>$	$<\gamma_s>$	$<\theta>$	$<\gamma_s>$
76.86	37.22	68.48	40.24	72.00	39.00	72.96	38.66	79.62	36.24	66.84	40.88

Table 7. $\theta °$ – water contact angle, γ_s – surface free energy of pentacene on parylene (blue columns) and on BCB (orange columns)

Figure II-26 presents the average values of the pentacene surface energies γ_s for both substrates. The variation of the surface energy towards thickness is not really marked. We can observe that both systems reach their extremum for the 30nm thickness: a maximal value for pentacene on parylene, $\gamma_{s\ Pen30/Par} = 40.24$mJ/m², and a minimal value for pentacene on BCB, $\gamma_{s\ Pen30/BCB} = 36.24$mJ/m². Because these values are largely dispersed, this variation seems to be not really significant.
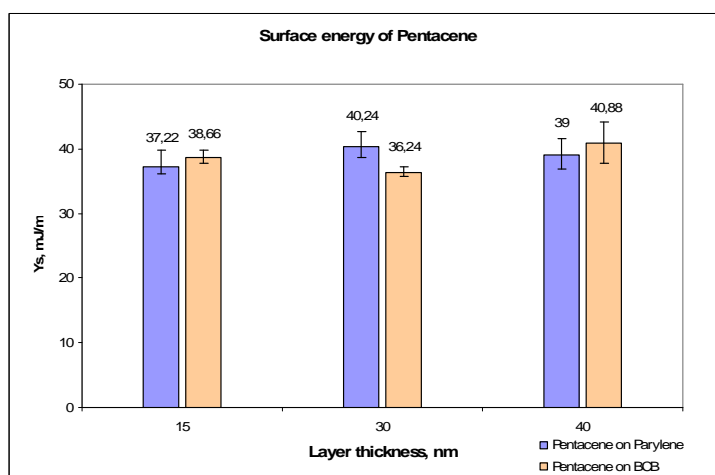

Figure II-26. Pentacene surface free energy as a function of pentacene film thickness calculated using the model ASTM D5946.

Therefore, a second set of experiments was performed using different liquids: formamide (surface tension γ = 58.2 mJ/m²), diiodomethane (γ = 50.8 mJ/m²) and ethyleneglycol (γ = 47.7 mJ/m²) [118]. They were realized with the GBX Instrumentation Scientifique at a temperature T = 22-23°C and a relative humidity of 40%. Surface free energy was calculated by the integrated software using the Owens & Wendt model and the average values of the contact angle (See Annexe I):

	P15Par	P30Par	P40Par	P15BCB	P30BCB	P40BCB
	θ °	θ °	θ °	θ °	θ °	θ °
Diiodomethane	37.4	40.2	41.2	34.7	36.8	38.1
	37.5	39.2	40.5	33.8	36.8	40.7
	37.5	38.6	40.5	31.4	36.3	40.7
Average	37.4 $\pm$ 0.34	39.2 $\pm$ 0.86	41.2 $\pm$ 0.50	33.8 $\pm$ 1.73	36.8 $\pm$ 1.14	40.7 $\pm$ 1.56
Ethyleneglycol	60.3	58.3	58	51.9	55.8	52.2
	60.5	58.8	58	51.7	55.3	49.8
	60	59.2	58.9	51	55.2	52.7
Average	60.3 $\pm$ 0.84	58.8 $\pm$ 0.50	58 $\pm$ 1.55	51 $\pm$ 0.89	54.1 $\pm$ 1.18	49.9 $\pm$ 1.54
Formamide	42.3	45.1	53.2	40	32	53.6
	43.8	44.9	53.3	40.3	29.9	52.6
	43.3	44.1	53.8	39.5	29.8	49.8
Average	43.3 $\pm$ 0.71	44.9 $\pm$ 0.80	53.2 $\pm$ 0.95	40 $\pm$ 0.40	29.9 $\pm$ 1.26	52.6 $\pm$ 2.17
γ_s mJ/m² Total	**43.4 $\pm$ 2.08**	**42.6 $\pm$ 2.04**	**40.8 $\pm$ 1.96**	**45.7 $\pm$ 2.15**	**45,7 $\pm$ 2.15**	**41.7 $\pm$ 1.96**

Table 8.Contact angles θ° of diiodomethane, ethyleneglycol and formamide and corresponding pentacene surface free energies γ_s (measured with the GBX Instrumentation Scientifique)

Contact angles presented in Table 8, for all liquids, were measured in a dynamic mode. The stable part of the relaxation period was used to calculate the free energy. Each liquid was deposed 3 times upon the pentacene samples.

As we can see on Figure II-27, the pentacene free energy gradually decreases from $\gamma_{s\ Pen15/Par}$ = 43.4mJ/m² to $\gamma_{s\ Pen40/Par}$ = 40.8mJ/m² in case of pentacene on parylene and from $\gamma_{s\ Pen15/BCB}$ = 45.7mJ/m² to $\gamma_{s\ Pen40/BCB}$ = 41.7mJ/m² in the case of pentacene on BCB. No extreme values for the thickness of 30nm were observed. Furthermore, the obtained free energy values are greater than those calculated by the ASTM D5946 model.
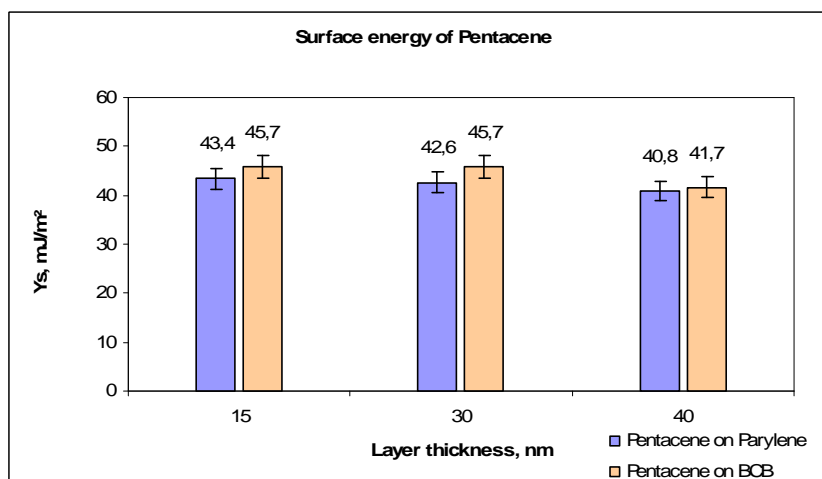
Figure II-27. Pentacene surface free energy as a function of pentacene film thickness
calculated using the model of Owens and Wendt (see in annexe 1)

Hence, it is difficult to interpret these results according to the different free energy values obtained for identical samples. The analysis with three liquids is more convenient for hydrophobic surfaces like pentacene. However, we did not observe large variation of the surface energy towards thickness. In fact, the contact angle method is an efficient technique for investigating the surface energy flat, homogeneous and chemically inert surfaces. Uncertainties on surface energy appear for small sample surfaces or patterned surfaces with microscopic domains [119].

It seems that the contact angle technique is not enough sensitive to make a difference between various thicknesses of pentacene and both substrates. The drop size is larger than the superstructure observed on the pentacene and only global measurements are obtained.

III-3-2 AFM spectroscopy

An alternative method consists in performing the surface free energy measurements using force spectroscopy in the contact mode AFM. The objective is to obtain direct and local information on the pentacene surface properties by the measurement of adhesion forces.

This method consists in performing force-distance curves at some point of the surface [112]. To obtain sufficient set of measured data, several force-distance curves are required. However, measurements at the same place may provoke damages of the sample or contamination of the cantilever tip. It may introduce significant inaccuracy in experimentally measured results. For this reason, spectroscopic data were collected from well predefined areas of corresponding pentacene surfaces. This approach also allows to avoid the influence of a *bad* positioning of the tip on the surface i.e. positioning in contaminated zones or in zones with structural defects.

Each scanned area represents a square grid of 10x10 points corresponding to a 200x200nm area (Figure II-28). Thus, the distance between neighboring nodes of the grid is 20nm, which is larger than the typical diameter of the tip (R_{tip} = 10nm). By this way, the pentacene surface was probed just one time, on points separated by a step of 20nm. The grid size of 10x10 points was chosen experimentally and was a good compromise between the necessary number of measurements and the time needed to perform measurements of the whole grid. In this experiment, the duration of one cycle of force-distance measurement was 1s. Increasing the grid dimension increases (more than 100 points), induces a raise of the total time of data acquisition. Thus, the thermal drift becomes significant and already indented areas can be repeatedly rescanned.
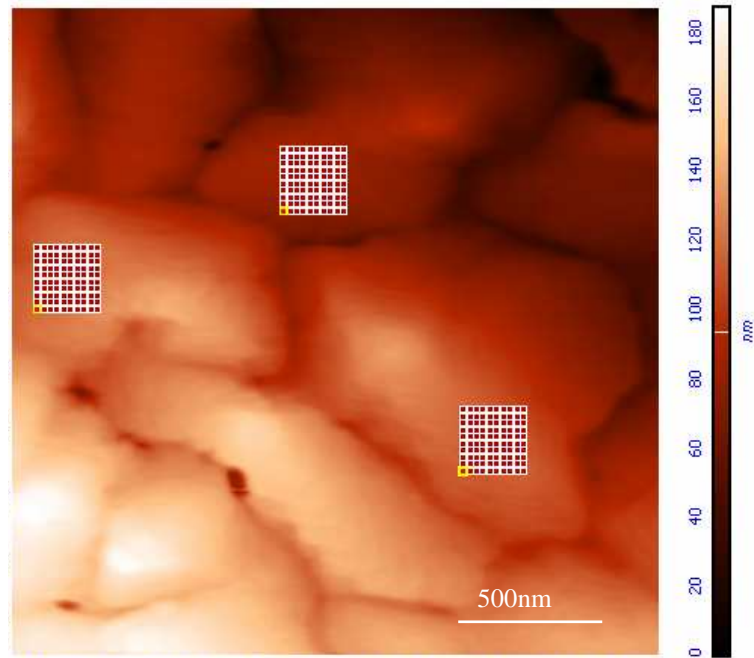

Figure II-28. Adhesion measurements by grid scanning method
(AFM image 2x2µm of pentacene 35nm deposited on BCB)

Each pentacene sample was scanned at three different places, as shown on the example in Figure II-28. The grids were located on different grains, in such way that one grid covered the surface of only one grain.

The same samples that have already been studied by AFM were analysed. Unfortunately, the samples corresponding to the thicknesses of 15nm and 40nm were contaminated by the contact angle measurements. Then, for this AFM spectroscopy experiment, samples corresponding to 20, 30 and 35nm thicknesses were analysed. We deliberately chose to remain on exactly the same deposition conditions.

On each point, a spectroscopic curve was done such as the one in Figure II-29. The F_{adh} value (in pA) was calculated by NOVA (NT-MDT) software and was presented with the other one in a diagram of 100

points. Diagrams from grid 1 to grid 3 are presented in Figure II-29 (a). In order to show the dispersion of the F_{adh}, histograms were presented in Figure II-30b.

Figure II-29 and 30 present raw data measured on the pentacene surface of 35nm thickness on BCB, described by the AFM image in Figure II-28.
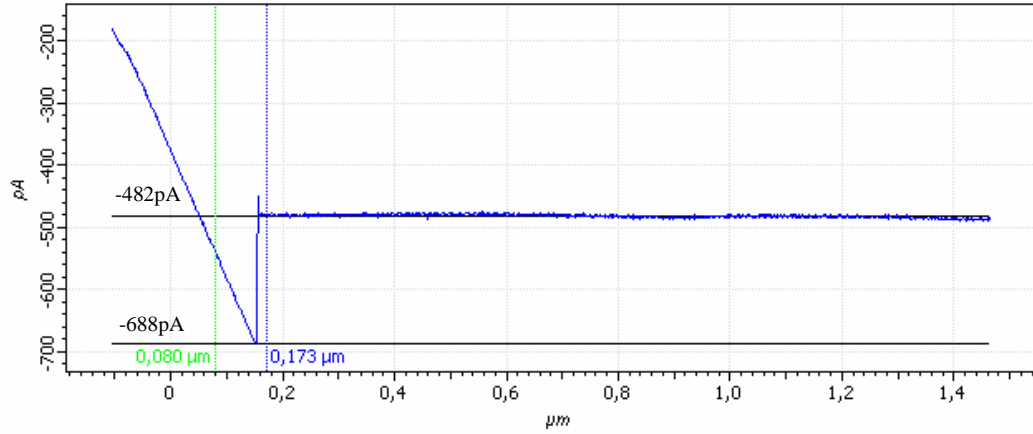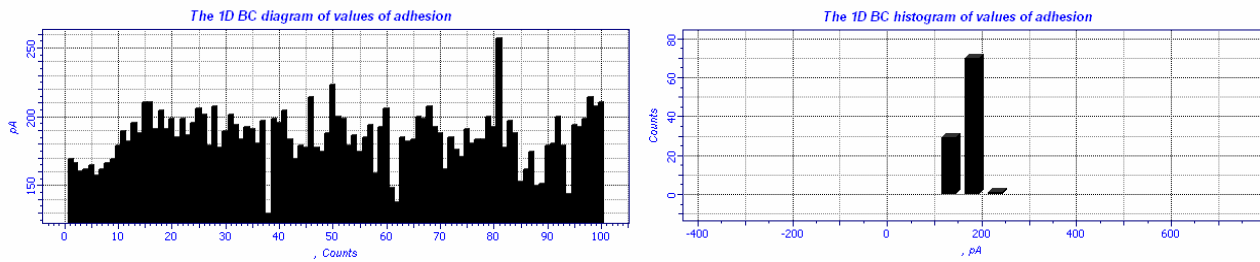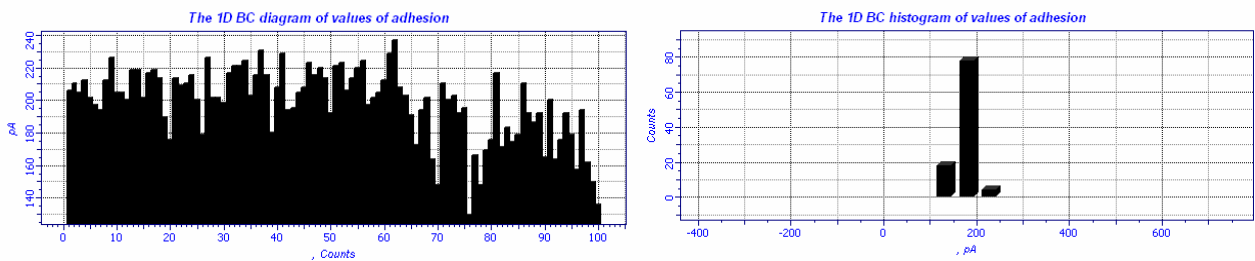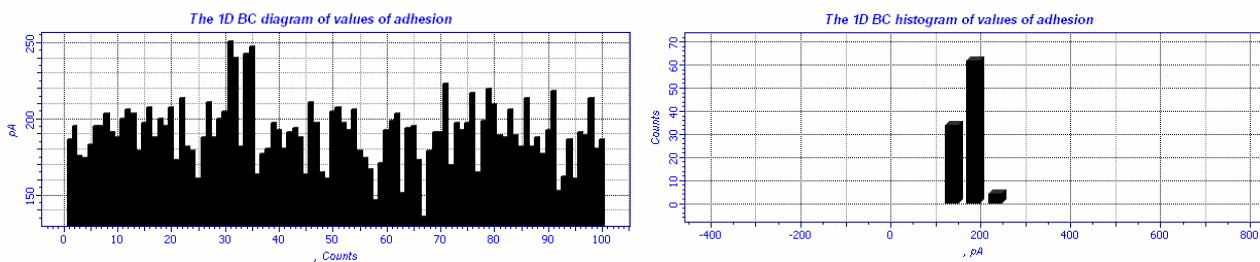

Figure II-29. Measurements of the displacement ΔZ on the backward part of the force-distance curve for pentacene 35nm on BCB.

Grid 1

Grid 2

Grid 3

a) **b)**

Figure II-30. Diagrams (a) and histograms (b) of raw data of adhesion forces for pentacene 35nm on BCB on the 3 different places of the surface.

108

Adhesion forces were calculated from histograms of achieved data. As shown in Figure II-30 b), the number of points of the scanning grid (number of force-distance cycles) is enough to obtain clearly pronounced peaks which correspond to adhesion between the tip and surface during separation (300 points). The three grids show that the F_{adh} corresponding to 200pA is statistically the most probable (70%, 80%, 62% on grids 1, 2, 3 respectively). Histograms give cantilever deflection values in "pA", knowing the spring constant of the cantilever, 0.3N/m, and using equations 2.18 and 2.19, one can obtain the adhesion force value in nanoNewtons.

With the assumption that the force acting on the cantilever is a linear function of the piezo displacement, the adhesion force can be calculated according to the Hook's law using displacement ΔZ corresponding to the "snap-out" value on the backward curve (Figure II-29).

Calculated adhesion forces F_{adh} of pentacene (eq. 2.18) and corresponding surface energies (eq. 2.17) are presented in Table 9.

	P20Par	P30Par	P35Par	P20BCB	P30BCB	P35BCB
F_{adh} nN	9.44 ± 0.47	6.84 ± 0.72	12.98 ± 1.19	11.45 ± 1.19	10.84 ± 0.71	13.65 ± 2.60
γ mJ/m²	75.12 ± 2.62	54.46 ± 3.43	103.30 ± 7.44	91.12 ± 7.26	86.31 ± 4.25	108.68 ± 16.67

Table 9. Adhesion forces F_{adh} of pentacene with corresponding surface energies γ

For technical reasons, the AFM spectroscopic measurements were performed in air at a temperature of 24°C and a relative humidity of 33%. Under these conditions, the contribution of the capillary forces should be taken into account. The capillarity can be neglected only if relative humidity is below 20%. In this case, a water meniscus can not be formed between the tip and the surface [121, 122].

In the contact mode spectroscopy, the cantilever tip penetrates in the layer of water adsorbed on the surface. As a result, the measured adhesion force represents the sum of the capillary force between water adsorbed on the tip and sample surfaces, and the adhesion force due to the Van der Waals interaction.

For capillary estimation, we used the average contact angle values obtained for both systems in deionised water (table 7). These mean values are: $\theta_{parylene}$ = 72.45° for pentacene on parylene and θ_{BCB}=73.14° for pentacene on BCB. For a water surface energy of γ = 72.6mJ/m² and a tip curvature of R=10nm, capillary forces F_{cap}, roughly around 2.75nN and 2.64nN, were calculated for pentacene on parylene and pentacene on BCB, respectively. Thus, the adhesion force only due to the Van der Waals interaction can be expressed as $F_{VdW} = F_{adh} - F_{cap}$, and the corresponding surface energy γ_{VdW} takes the following form:

$$\gamma_{VdW} = \frac{F_{adh} - F_{cap}}{4\pi R} \qquad \text{(eq. 2.23)}$$
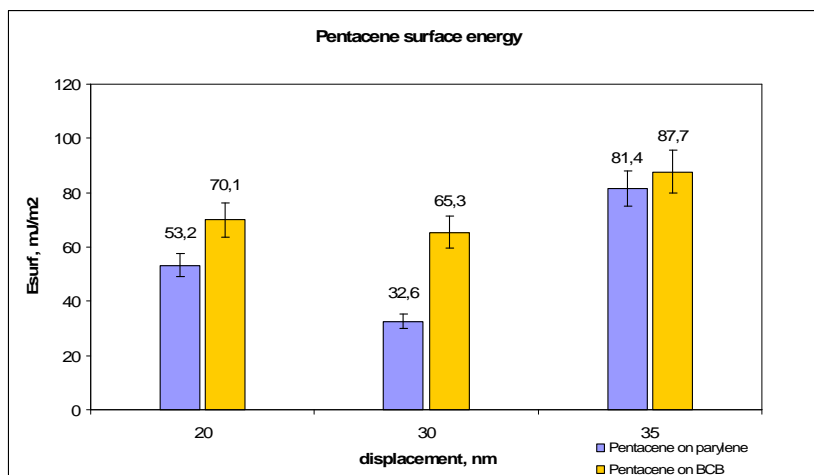
Figure II-31. Van der Waals contribution to the pentacene surface energy γ_{VdW} after correction of the capillary effect

Figure II-31 presents the γ_{VdW} pentacene surface energy. The comparison of the surface energy values with and without the capillary contribution is important (E_{surf} in Table 9 and γ_{VdW} in Figure II-31). For a 30nm pentacene thickness, the value decreases from 54 mJ/m^2 to 33 mJ/m^2 for pentacene on parylene, and from 86 to 65 mJ/m^2, for pentacene on BCB. The contribution of the capillary force to the total energy is around 26%, thus not negligible. However, even after the correction of the capillarity effect the surface energy measured by AFM is globally higher than the one measured by contact angle method. The difference can be explained by the presence of two models representative of the contact area of drops on micro-patterned surfaces as shown in Figure II-32 [123]:

-   A Wenzel regime, where the solid/liquid interface exactly follows the solid roughness
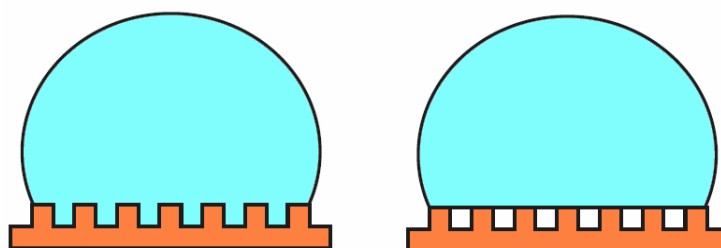-   An air-pocket (AP) or Cassie regime, where air patches are confined below the drop.

Figure II-32. Regimes of contact: a) Wenzel and b) aire-pocket regimes

Hydrophobic pentacene surface in contact with polar liquids (such as water or formamide) is favourable to an air-pocket contact regime. In that case, only a part of the force acting on the drop is measured, leading to undervalued surface energy values.

In addition, transitions from Wenzel to air-pocket regime and from air-pocket to Wenzel regime are possible indicating that a metastable state of deposited drop may occur [124]. Such transitions from stable to metastable drop states (and *vice versa)* can dramatically change the contact angles leading to a large divergence of measured contact angles on pentacene.

These spectroscopic measurements are qualitatively different from those obtained by the contact angle method. They are obtained by a local probe, *in situ,* and represent a direct method of measurements. One can see that the surface energies measured for pentacene on both substrates (parylene and BCB) show a similar dependence on the pentacene thickness. For all film thicknesses, the surface energy of pentacene on BCB is higher than of the energy of pentacene on parylene. The same tendency has also been observed using contact angle method (Table 8, Figure II-27). This is in good agreement with our results of morphological analysis: pentacene on the BCB exhibits a well ordered molecular crystal structure whereas on the parylene it is more disordered (Figure II-11). Disorder implies a decrease in the surface energy. It is important to note that for both substrates, the surface energy reaches its minimal value for the pentacene thickness of 30nm. Taking into account that the surface energy of pentacene 35nm is higher than those of the pentacene 20nm, we can assume that pentacene thickness of 30nm seems to be a critical thickness between different crystal organizations.

Based on these results, it can be concluded that the contact angle measurement technique is not applicable to patterned heterogeneous solid surfaces, like pentacene. In addition, the interfacial tension between a surface and a liquid can not be easily deduced from contact angle measurements [125]. In comparison with the AFM approach, the contact angle technique provides "average" properties of heterogeneous surfaces, whereas the AFM, probing at local scale, is able to identify the discrete nature of such surfaces at microscopic and submicroscopic levels allowing a direct surface characterization.

IV - Discussion

IV-1 the growth mechanisms and the critical thickness

The growth of pentacene on parylene and BCB followed from equivalent thicknesses of 6nm to 60nm was studied by AFM. AFM images and their grain analysis, contact angle and AFM spectroscopy measurements, have revealed several information about the growth mechanism of pentacene and the resulting morphology on both substrates.

The growth manifests by the presence of grains which grow laterally and vertically and are connected to each other at a thickness of 30 nm (Figures II-15-II-16). The size of the grains on parylene varies from 780nm to a maximal value of 1100nm for a thickness of 30nm and then decreases progressively to a value of 596nm. On BCB, it increases from 1.27µm to 1.56 µm for a 30nm thickness and then decreases to 1.03µm. Their shape is also different, bulk-like shape on parylene and pyramidal structure on BCB.

As the deposition process of pentacene on the two substrates was identical, it was shown that the nature of the substrate influences the size of the grains, even for high coverage. The morphology of the film at early growth stages (6-15nm) is directly influenced by substrate properties. However, following growth for thicknesses between 15 and 60nm is also dependent on the initial growth at 6 nm and then on the substrate even if the substrate is totally covered, at this thickness.

Difference in the size and the shape of grains, for the same equivalent thickness of pentacene, can be explained by the difference in chemical and physical properties of these insulators. More precisely, the free energy and the roughness of the substrate are responsible of two phenomena:

- the distribution of the first deposited pentacene molecules on the surface
- the length of the free motion of the molecules during initial stages of the grain formation. This mode of thin film growth is also called Diffusion Limited Growth (DLG) [79].

The influence of the insulator surface on the initial pentacene growth can be clearly seen on Figure II-33. These AFM images show the morphology of the pentacene film for an equivalent thickness of 6nm.

- 3D small rounded grains are formed yet, on parylene.
- Well- separated 2D pentacene islands are visible on BCB.

The study of the surface energy by contact angle measurements has shown that the variation in energy, between the two substrates, are not significant. Thus, the main parameter which influence the size and shape of the grains, is the roughness of the substrate. On AFM images of 2 x 2µm^2, a RMS of 3.47nm and a RMS of 0.42nm are obtained on parylene and BCB, respectively. This difference, more than 8 times higher for parylene than for BCB is determinant in the initial growth. Reduction in grain size of an organic semiconductor with increasing of roughness of the dielectric was reported [54, 55]. For rougher dielectrics, the film exhibits a distinctly reduced crystal size [64, 68].

For pentacene on parylene, it seems that the growth begins from small rounded grains which cover the rough surface of parylene, they coalesce in more or less rounded grains of around 300 nm at a 10nm coverage. These grains are always present on images independently of the coverage beyond this thickness. Their size corresponds to the τ_{sh2} value of 288 ± 51nm calculated by the superstructure model.

We assume that the deposition of the pentacene on parylene is a 3D growth mode, droplets of pentacene adsorb on the parylene, and they grow laterally, reach their maximum size of around 300nm and join to each other forming a larger superstructure for the thickness of 30nm. Beyond 30nm, they go on growing vertically, maintaining their 300nm size, they appear more separated to each other because of their vertical extension.

It is clear on the images (Figure II-16) that the grains are closer to each other for the thickness 30nm. It corresponds to the highest value of the superstructure parameter $\tau_{sh1} = 1100\pm110$nm (τ_{sh1} corresponds to mean size of aggregated grains) and the lowest value of the surface energy measured by AFM (55 mJ/m^2 or 33 mJ/m^2 without capillarity), thus the best organization on the surface.
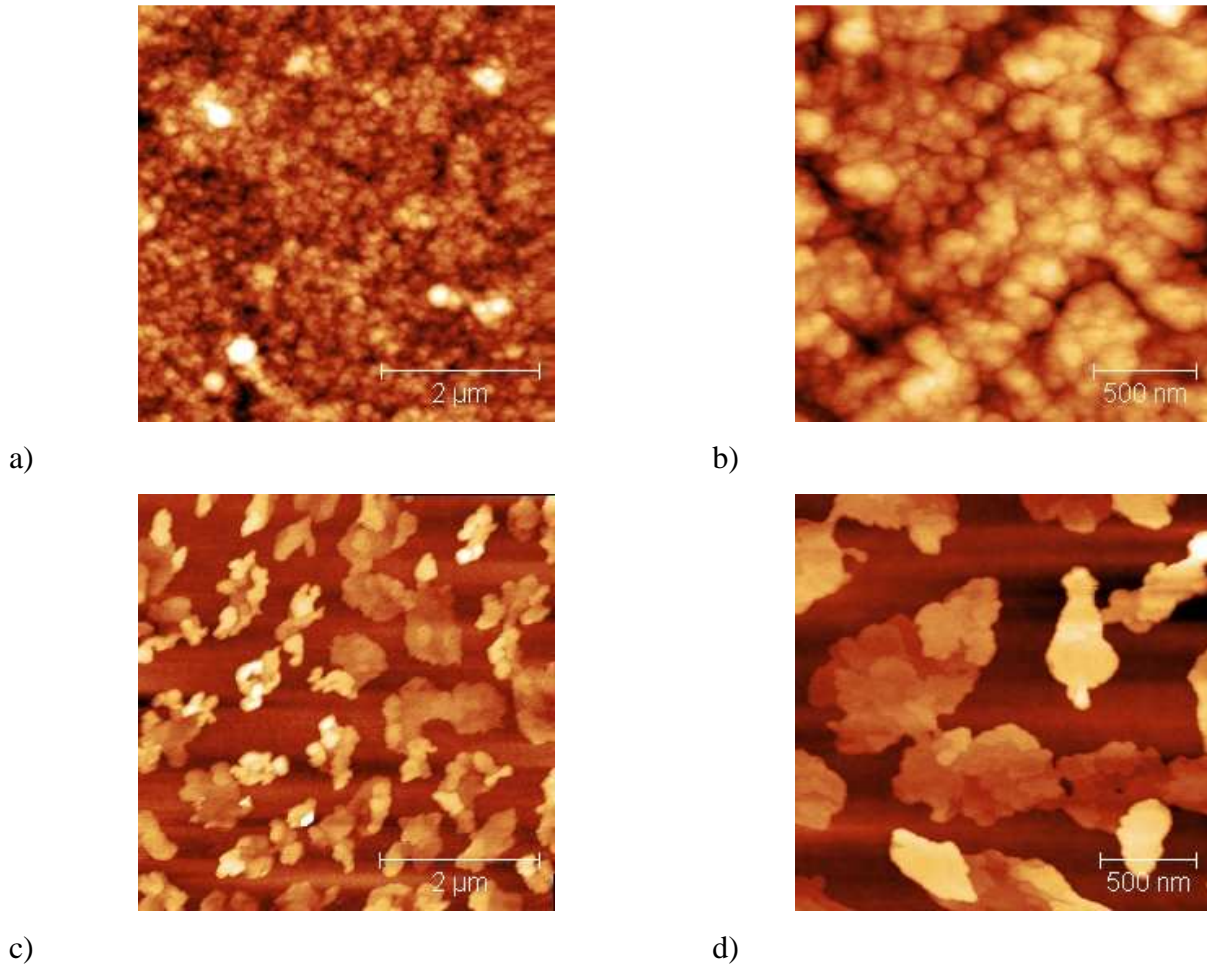

a)

b)

c)

d)

Figure II-33. Pentacene 6nm deposited (a) (b) on parylene (RMS=6.75nm) and (c) (d) on BCB (RMS=6.01nm) Topography AFM images of 5x5µm^2 on (a), (c) and 2x2µm^2 on (b), (d).

According to the k-correlation model, the growth mechanism of pentacene on parylene begins by an evaporation – condensation phase (the droplets forming 3D grains) and changes to bulk diffusion from 30nm (the vertical growth). 3D grain formation in the early deposits is not in favor of the creation of large monomolecular terraces. That's why, multimolecular layers are observed (Figure II-17).

For pentacene on BCB, the growth is different. Well-separated 2D pentacene islands are visible on BCB for a thickness of 6 nm. On some islands, a second, third or forth layers begin to grow. One can notice that these supplementary layers never grow in the center of the island; they need a step edge to form and extend. In this growth mode, there is some kind of competition between the deposition of species on BCB and on pentacene. In both cases, molecules seem to diffuse on the surface and stop at a step edge of pentacene: on the bottom or on the top. This suggests that the interaction pentacene /pentacene is favored over the interaction pentacene / BCB. The islands grow laterally and extend vertically through a stack of successive terraces of monolayer height, which decrease in size gradually as one approaches the summit. This pyramidal shape reaches its maximal width for the thickness of 30nm. It corresponds to the maximal value of the τsh_1 parameter 1.56 ± 0.26 μm and the minimal value of the surface energy calculated with the AFM measurements (86 mJ/m^2 or 65 mJ/m^2 without capillarity).

Close relationship of pentacene morphology with the substrate properties was also revealed by the fractal model. The fractal strength was determined to be stronger for pentacene films on the parylene than on the BCB, indicating larger roughness of parylene in comparison with BCB. In the same time, the fractal dimension corresponds to Brownian fractal structure of pentacene morphology. In the framework of modified ballistic deposition model, it means that pentacene molecules during deposition are not in strong interaction with the substrate and have some probability to move. This probability (sticking probability) is strongly dependent on the microstructural nature of substrates and the deposition conditions. Really, the mean fractal dimension of pentacene on parylene of 2.6 ± 0.09 is slightly higher than those on BCB which is of 2.47 ± 0.04. That is because the probability of free motion of the pentacene molecules on BCB is higher than on parylene which is one of the factors responsible for more regular pentacene grain structure on BCB.

IV-2 Pentacene molecular organization

More precisely, pentacene morphologies are related to the structure of pentacene molecular crystals. So, the relationship between pentacene growth mechanisms, microstructural film characteristic and as a result OTFT performance could be understood.

It was already shown by X-ray diffraction (XRD) method that evaporated pentacene thin films exhibit two different phases – "thin film" and "bulk" phases, which are characterized by d-spacing 1.54 and 1.45nm, respectively [126]. The dominant pentacene film phase depends on film deposition parameters such as substrate temperature and deposition rate, and for certain grain conditions there is a critical film thickness d_c which separates these two phases [126, 127]. The thin-film phase normally takes a place for faster growth rates, at lower growth temperatures, and for smaller film thicknesses compared to the bulk-phase.

Drummy and Martin reported [126] that the critical thickness d_c where transition from thin-film to bulk phase mode occurs is related to interfacial surface energy mismatches. These mismatches related to the difference between the pentacene surface energy and the bulk energies of the two different phases.

For the thin-film phase, pentacene has an orthorhombic crystal structure [128, 129] and bulk phase is characterized by a triclinic crystal structure [127].

In the same work [126], the authors have performed the thermodynamic calculations of the surface energy for these two pentacene polymorphs. According to reported data, surface energy for triclinic phase is of 76mJm^{-2} and 38 mJm^{-2} for orthorhombic phase. These theoretical predictions are in good agreement with the results determined by AFM. In fact, for pentacene on parylene, the surface energy values are 81.4 mJm^{-2} (pentacene 35nm) and 32.6 mJm^{-2} (pentacene 30nm) as it is shown in Figure II-31. For the pentacene on BCB, the higher values of surface energy are induced by other mechanisms of thin film growth (Table 4).

Our experimental results are in many ways similar to data reported by Cheng et al. [129], where the pentacene films were deposited on two types of dielectric substrates – SiO$_2$ and polymeric dielectrics (polyimide and polymethylmethacrylate). They observed a thickness-dependent evolution of polymorphs of pentacene thin-films with a transition from orthorhombic thin-film phases to triclinic bulk phase.

As it was discussed above, the transition from orthorhombic to triclinic phases for pentacene growth on BCB and parylene occur with respect to film thicknesses close to 30-35nm, for pentacene on BCB and parylene. In the work of Cheng et al., the authors observed a polymorph transition for the thickness of 16nm, on both polymeric substrates and 30nm on SiO$_2$ [129]. However, their proposed growth model [129] is relevant for a description of the thickness-dependent morphology evolution of pentacene on our systems (Figure II-34):
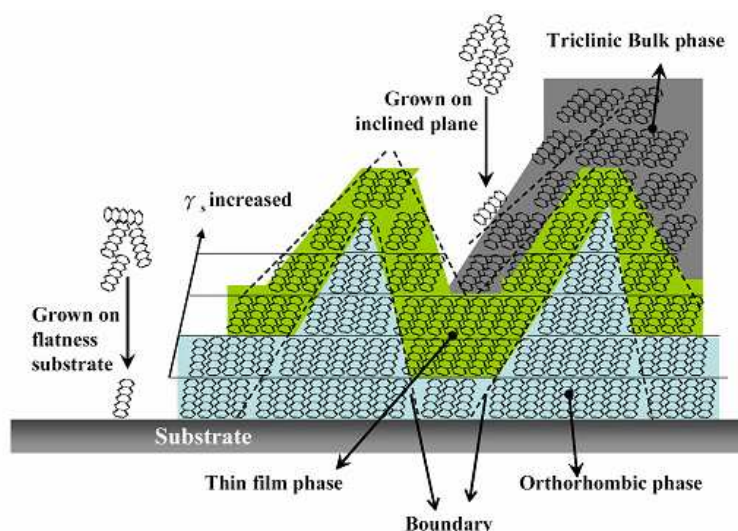

Figure II-34. Thickness-driven pentacene thin-film polymorphs [129]

The pentacene molecules have a tendency to stand vertically on a flat surface forming the orthorhombic crystalline structure, on both polymeric substrates. Further increasing of film thickness leads to a pentacene growth on a gradually formed surface of grain hillsides. This causes an additional inclination of the pentacene molecules and as a result the thin film phase and triclinic bulk phase are formed at higher film

thicknesses. This effect is more marked for the pentacene on BCB, because the substrate is flatter and the first deposited pentacene molecules line up next to each other. For pentacene on parylene, an ordering of the first deposited molecules on the substrate is not as obvious. It is possible that the triclinic bulk phase is present since the first deposits.

IV-3 Critical thickness and mobility of charges

In order to follow the thickness-dependent carrier transport properties of pentacene films, three series of electrical characteristics were performed, for the thicknesses of 30nm, 60nm and 100nm. Measurements were realized for a top-gate OTFT with a BCB gate dielectric [111].
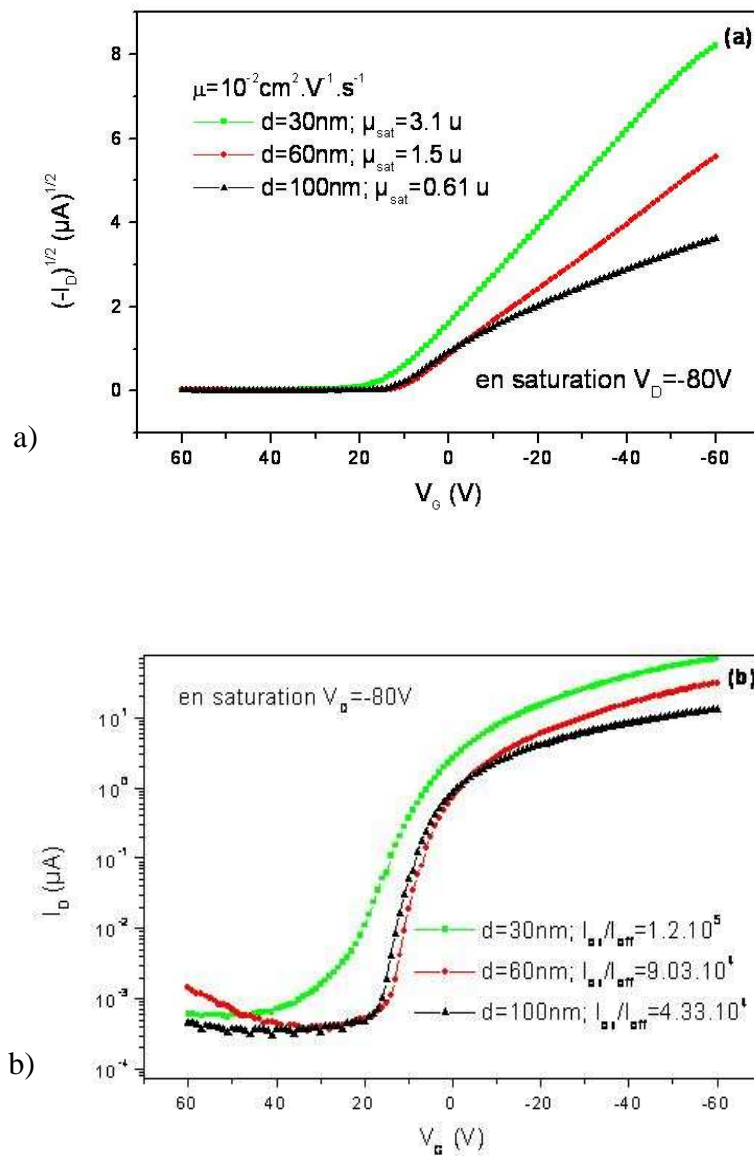

Figure II-35. Output characteristics of pentacene/BCB top gate transistors; a) $(-I_D)^{1/2}$ vs. gate voltage, b) drain current vs. gate voltage with switch on/of characteristics. Adapted from [111]

Figure II-(385 a) presents the pentacene hole mobility versus applied gate voltage with a saturation of the drain voltage V_D at -80V. The mobility decreases from $\mu = 3.1\times10^{-2}$ cm²/Vs, for the thickness of 30nm down to $\mu = 0.61\times10^{-2}$ cm²/Vs, for 100nm. Similar tendency was obtained for I_{on}/I_{off} characteristics (Figure II-35 b). The OTFT speed performance decreases from $I_{on}/I_{off} = 1.2\times10^{5}$, for 30nm, to $I_{on}/I_{off} = 4.33\times10^{4}$, for 100nm [111].

Hence, the best electrical performances were obtained for pentacene thickness of 30nm, which corresponds to the thickness of the film with the largest grain size. Thickness-driven carrier properties can be explained by the dependence of pentacene mobility on the crystal polymorph and the molecular order which can be affected by various crystal defects (Figure II-36).
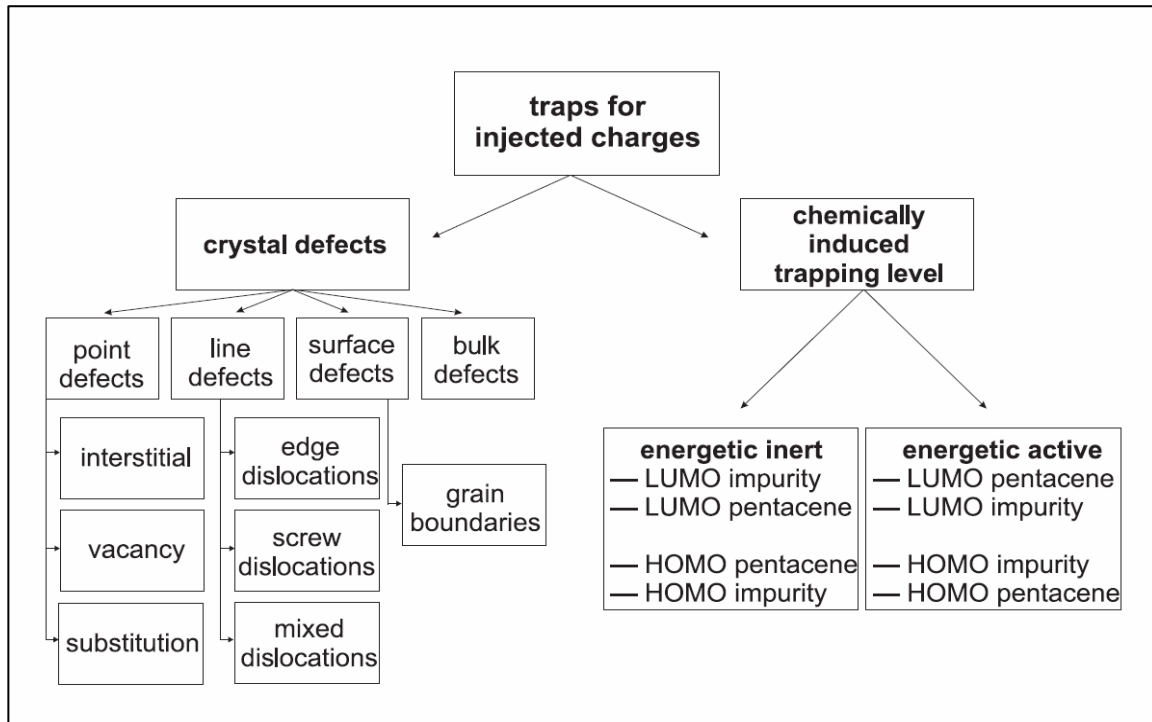

Figure II-36. Origin of charge traps in pentacene thin-film. Adapted from [130]

The charge traps in the channel region considerably limit the channel mobility and the threshold voltage. The traps in the pentacene crystals are partially caused by structural imperfections and chemical impurities. In addition extended defects, such as edge dislocations or screw dislocations modify the available energy level corresponding to the appearance of accessible vacant orbitals in the band gap [131]. So, on the one hand, the observed sensitivity of measured mobility on the film thickness is related to polymorph structure of pentacene. However, on the other hand, most traps are located at the grain boundaries and at the semiconductor/substrate interface [132]. This is confirmed by our experimental results which show that higher mobility corresponds to films with the largest grains (Figure II-35 a). It is due to the fact that larger grains lead to smaller boundary perimeter between grains and consequently to smaller density of grain boundary traps.

V - Conclusion

This work present an AFM study of the growth of pentcene on two different substrates: parylene and BCB.

It was shown that under AM-AFM mode, it was possible to perform high-quality mapping of pentacene surfaces with sub-molecular resolution. Several deposits of pentacene were studied from an equivalent thickness of 6 nm to 60 nm. A precise analysis of the grain dimensions (lateral size, height, volume) was performed by classical grain analysis techniques but also by the spectral methods of surface analysis in reciprocal space. The Power Spectrum Density (PSD) was applied on the AFM images and 3 different models were used: k-correlation, fractal and superstructures models to get the maximum information on the growth mode of pentacene. In parallel, contact angle and AFM spectroscopy measurements were performed to get information on the surface energy of pentacene on parylene and BCB. A lower surface energy was obtained for the pentacene on parylene than on BCB and for both substrate the lower value was obtained for a thickness of 30nm.

It was shown a substrate-induced effect on the growth of pentacene, where the roughness of the substrate influence more the morphology than the surface energy.

As expected, the rougher substrate pentacene induces the formation of smaller 3D grain than the flatter substrate. The 3D grains seem to appear for the first deposit, for the pentacene on parylene. For pentacene on BCB, the islands grow laterally and extend vertically through a stack of successive terraces of monolayer height, which decrease in size gradually as one approaches the summit.

A growth mode mechanism was proposed in accordance with the measurements obtained by the PSD models and with literature [129].

The presence of a critical thickness of 30-35 nm was demonstrated by statistical grain analysis and by surface energy measurements. It corresponds to the largest size of the structures and the lower surface energy. In addition, in our electrical measurements, it also corresponds to the optimal electrical performance of the OTFT.

VI - References

[1] C. D. Dimitracopoulos and D.J. Mascaro, IBM J. Res. & Dev., vol. 45, no. 1, Jan. 2001.

[2] M. Pope and C. E. Swenberg. Oxford University Press, Oxford 1999, 2nd ed., p. 337–340.

[3] N. Karl, O. Madelung, M. Schulz, and H. Weiss. Landolt-Boernstein (New Series), Group III, Vol. 17, Semicondcuctors, Subvolume 17i, p. 106. Springer, Berlin, 1985.

[4] E. A. Silinsh, Organic Molecular Crystals. Springer, Berlin 1980.

[5] T. A. Skotheim, R. L. Elsembaumer, and J. R. Reynolds, Marcel Dekker, New York 1998.

[6] P. M. Borsenberger and D. S. Weiss. Marcel Dekker, New York 1993.

[7] H. Koezuka, A. Tsumara, and T. Ando, Synth. Met. 18, 699 (1987).

[8] J. H. Burroughes, C. A. Jones, and R. H. Friend, Nature 335, 137 (1988).

[9] G. Horowitz, D. Fichou, X. Z. Peng, Z. Xu, and F. Garnier, Solid State Commun. 72, 381 (1989).

[10] J. H. Burroughes, D. D. C. Bradley, A. R. Brown, R. N. Marks, K. Mackay, R. H. Friend, P. L. Burn, and A. B. Holmes, Nature 347, 539 (1990).

[11] C. W. Tang and S. A. VanSlyke, Appl. Phys. Lett. 51, 913 (1987).

[12] a) L. Zhou, A. Wanga, S.-C. Wu, J. Sun, S. Park, T. N. Jackson, Appl.Phys. Lett. 2006, 88, 083 502. b) R. A. Street, W. S. Wong, S. E.Ready, M. L. Chabinyc, A. C. Arias, S. Limb, A. Salleo, R. Lujan, Mater. Today 2006, 9, 32. c) P. Mach, S. J. Rodriguez, R. Nortrup, P. Wiltzius, J. A. Rogers, Appl. Phys. Lett. 2001, 78, 3592.

[13] Yoshiro Yamashita (2009). Sci. Technol. Adv. Mater. 10: 024313.

[14] Y. Shirota and H. Kageyama, Chem. Rev. 107, 953 (2007).

[15] R. Farchioni, G. Grosso (eds.). Springer, Berlin, 2001.

[16] Meng H, Sun F, Goldfinger M B, Jaycox G.D, Li Z, Marshall W.J, Blackman G.S. 2005 J.Am.Chem.Soc.127 2406

[17] Mcculloch I et al 2006 Nat. Mater. 5 328

[18] Gao X et al 2007 Adv. Mater. 19 3037

[19] Naraso, Nishida J, Tada H, Inoue Y, Tokito S and Yamashita Y 2005 J. Am. Chem. Soc. 127 10142

[20] Moon H, Zeis R, Borkent E-J, Besnard C, Lovinger A.J, Siegrist T, Kloc C, Bao Z 2004 J. Am.Chem.Soc.126 15322

[21] Takimiya K, Ebata H, Sakamoto K, Izawa T, Otsubo T and Kunugi Y 2007 J. Am. Chem. Soc. 128 12604

[22] Klauk H, Halik M, Zschieschang U, Eder F, Schmid G and Dehm C 2003 Appl. Phys. Lett. 82 4175

[23] Lin, C.-S., Lin, Y.-J. Journal of Non-Crystalline Solids, 2010, 356 (50-51), pp. 2820-2823

[24] Malenfant P R L, Dimitrakopoulos C D, Gelorme J D, Kosbar L L, Graham T O, Curioni A and Andreoni W 2002 Appl. Phys. Lett. 80 2517

[25] Sakamoto Y, Suzuki T, Kobayashi M, Gao Y, Fukai Y, Inoue Y, Sato F and Tokito S 2004 J. Am. Chem. Soc. 126 8138

[26] Kobayashi S, Takenobu T, Mori S, Fujiwara A and Iwasa Y 2003 Appl. Phys. Lett. 82 4581

[27] Ando S, Murakami R, Nishida J, Tada H, Inoue Y, Tokito S and Yamashita Y 2005 J. Am. Chem. Soc. 127 14996

[28] M. M. Ling and Z. Bao, Chem. Mater. 16, 4824 (2004).

[29] E. A. Silinsh and V. Capek, AIP press, New York, 1994.

[30] C. R. Newman, C. D. Frisbie, D. A. da Silva Filfo, J.-L. Bredas, P. C. Ewbank, and K. R. Mann, Chem. Mater. 16, 4436 (2004).

[31] A. Salleo, Mat. Today 10, 38 (2007).

[32] P. M. Borsenberger and D. S. Weiss. Marcel Dekker, New York 1993.

[33] Lilienfeld, Julius Edgar, U.S. Patent 1,745,175 1930-01-28 (filed in Canada 1925-10-22, in US 1926-10-08).

[34] A. Facchetti, Mat. Today 10, 28 (2007).

[35] I. Kymissis, C. D. Dimitrakopoulos, and S. Purushothaman, IEEE Trans. Elect. Dev. 48, 1060 (2001).

[36] K. Seeger, Springer, Berlin, 7th ed. 1999

[37] M. Koehler and I. Biaggio, Phys. Rev. B 70, 045314 (2004)

[38] G. Horowitz, X. Peng, D. Fichou and F. Garnier, Synth. Met. 51, 419 (1992).

[39] S. M. Sze, (John Wiley and Sons, New York, 1981), 2nd ed.

[40] A. R. Brown, C. P. Jarrett, D. M. de Leeuw, and M. Matters, Syn.Met. 88, 37 (1997).

[41] H. Klauk, M. Halik, U. Zschieschang, G. Schmid, and W. Radlik, J. Appl. Phys. 92, 5259, 2002.

[42] C.D. Sheraw, J.A. Nichols, D.J. Gundlach, J.R. Huang, C.C. Kuo, H. Klauk et al.. Int Electron Dev Meeting Tech Dig, pp. 619–622, 2000.

[43] C. D. Sheraw et al., Appl. Phys. Lett. 80, 1088, 2002.

[44] D. J. Gundlach, H. Klauk, C. D. Sheraw, C. C. Kuo, J. R. Huang, and T.N. Jackson, Tech. Dig. - Int. Electron Devices Meet. 1999, 111.

[45] B. K. Crone, A. Dodabalapur, R. Sarpeshkar, R. W. Filas, Y. Y. Lin, Z. Bao, J. H. O'Neill, W. Li, and H. E. Katz, J. Appl. Phys. 89, 5125, 2001.

[46] H. E. A. Huitema, G. H. Gelinck, J. B. P. H. van der Putten, K. E. Kuijk, K. M. Hart, E. Cantatore, and D. M. de Leeuw, Adv. Mater 14, 1201, 2002.

[47] D. Knipp, R. A. Street, B. S. Krusor, and R. B. Apte, Proceedings of the Fall 2001 Materials Research Society Meeting, 2001, p. 553.

[48] J. H. Schon and C. Kloc, Appl. Phys. Lett. 79, 4043, 2001.

[49] Y. Y. Lin, D. J. Gundlach, S. F. Nelson, and T. N. Jackson, IEEE Electron Device Lett. 18, 606, 1997.

[50] C. D. Sheraw, D. J. Gundlach, and T. N. Jackson, Mater. Res. Soc. Symp. Proc. 558, 403, 1999.

[51] C. D. Dimitrakopoulos and P. R. L. Malenfant, Adv. Mater. 14, 99 (2002).

[52] S. Lee et al., Appl. Phys. Lett. 88, 162109 (2006).

[53]A. C. Mayer, R. Ruiz, R. L. Headrick, A. Kazimirovc and G. G. Malliaras, Organ. Electr. 5, 257 (2004).

[54] A. Di Carlo, F. Piacenza, A. Bolognesi, B. Stadlober and H. Maresch, Appl. Phys. Lett. 86, 263501 (2005).

[55] a) R.A.Street, D. Knipp and A.R. Volkel, Appl. Phys. Lett. 80, 1658 (2002). b) Lee, Wen-Hsi; Wang, C. C. J. Vac. Sci. Technol. B **27**, 1116 (2009).

[56] B. Nickel, R. Barabash, R. Ruiz, N. Koch, A. Kahn, L. C. Feldman, R.F. Haglund and G. Scoles, Phys. Rev. B, 70 125401 (2004).

[57] A. C. Mayer, A. Kazimirov and G. G. Malliaras, Phys. Rev. Lett. 97, 105503 (2006).

[58] S. Schiefer, M. Huth, A. Dobrinevski and B. Nickel, J. Am. Chem. Soc. 129, 10316 (2007).

[59] S. Iannotta, T. Toccoli, J. Polymer Sci. B, 41, 2501 (2003).

[60] L. Casalis, M. F. Danisman, B. Nickel, G. Bracco, T. Toccoli, S. Iannotta and G. Scoles, Phys. Rev. Lett. 90, 206101 (2003).

[61] F. De Angelis, T. Toccoli, A. Pallaoro, N. Coppedè, L. Mariucci, G. Fortunato and S. Iannotta, Synth. Met. 146, 291 (2004).

[62] S. Pratontep, F. Nuesch, L. Zuppiroli and M. Brinkmann, Phys. Rev. B 72, 085211 (2005).

[63] M. Kitamura and Y. Arakawa, J. Phys Condens. Matter 20,124011 (2008).

[64] F.-J. Meyer zu Heringdorf, M.C. Reuter and R.M.Tromp, Nature 412, 517, (2002).

[65] B. Stadlober, U. Haas, H. Maresch and A. Haase, Phys. Rev. B 74, 165302, (2006).

[66] R. Ruiz, B. Nickel, N. Koch, L.C. Feldman, R.F. Haglund, A. Kahn and G. Scoles, Phys. Rev. B 67, 125406, (2003).

[67]. G. Yoshikawa, T. Miyadera, R. Onoki, K. Ueno, I. Nakai, S. Entani, S. Ikeda, D. Guo, M. Kiguchi, H. Kondoh, T. Ohta and K. Saiki, Surf. Sci. 600, 2518 (2006).

[68] S. Steudel, S. De Vusser, S. De Jonge, D. Janssen, S. Verlaak, J. Genoe, P. Heremans, Appl. Phys. Lett. 85 (2004) 4400–4402.

[69] F. Amy, C. Chan, and A. Kahn, Org. Elect. 6, 85 (2005).

[70] S. E. Fritz, S. M. Martin, C. D. Frisbie, M. D. Ward and M. F. Toney, J. Am. Chem. Soc. 126, 4084 (2004).

[71] L. F. Drummy and D. C. Martin, Adv. Mater. 17 (2005) 903.

[72] R. B. Campbell, J. M. Robertson and J. Trotter, Acta Crystallogr. 15, 289 (1962).

[73] C. R. Newman, C. D. Frisbie, D. A. da Silva Filfo, J.-L. Bredas, P. C. Ewbank, and K. R. Mann, Chem. Mater. 16, 4436 (2004).

[74] G. A. de Wijs, C. C. Mattheus, R. A. de Groot, and T. T. M. Palstra, Syn. Met. 139, 109 (2003).

[75] H. Yanagisawa, T. Tamaki, M. Nakamura, and K. Kudo, Thin Solid Films 464-465, 398 (2004).

[76] C. D. Dimitrakopoulos, A.R. Brown and A. Pomp, J. Appl. Phys. 80, 2501(1996).

[77] L. F. Drummy and D. C. Martin, Adv. Mater. 17 (2005) 903.

[78] C. C. Mattheus, A. B. Dros, J. Baas, G. T. Oostergetel, A. Meetsma, J. L. de Boer, T. T. M. Palstra, Synth. Met. 138, 475 (2003).

[79] S. Schiefer, M. Huth, A. Dobrinevski and B. Nickel, J. Am. Chem. Soc. 129, 10316 (2007).

[80] T. Kakudate, N. Yoshimoto and Y. Saito, Appl. Phys. Lett. 90, 081903 (2007).

[81] M. W. Ashcroft and N. D. Mermin, (Saunders col-lege Publishing, Fort Worth, 1976).

[82] M. Pope and C. E. Swenberg, Oxford University Press, New York, 1999, 2nd ed.

[83] W. Warta and N. Karl, Phys. Rev. B 32, 1172 (1985).

[84] N. Karl, J. Marktanner, R. Stehle, and W. Warta, Syn. Met. 41-43, 2473 (1991).

[85] B. Hartenstein, H. BÄassler, S. Heun, P. Borsenberger, M. V. der Auw-eraer, and F. C. D. Schryyer, Chem. Phys. 191, 321 (1995).

[86] L. Dennany, E. J. O. Reilly, P. C. Innis, G. G. Wallace, and R. J. Forster, Electroc. Acta 53, 4599 (2008).

[87] D. Knipp, R. A. Street, A. VÄolkel, and J. Ho, J. Appl. Phys. 93, 347 (2003).

[88] S. F. Nelson, Y. Y. Lin, D. J. Gundlach, and T. N. Jackson, Appl. Phys. Lett. 72, 1854 (1997).

[89] C. E. Thayer, J.T. Sadowski, F. M. zu Heringdorf, T. Sakurai and R. M. Tromp, Phys. Rev. Lett. 95, 256106 (2005).

[90] J. E. Northrup, M. L. Tiago and S. G. Louie, Phys. Rev. B 66, 121404 (2002).

[91] R. J. Hamers, Nature 412, 489 (2001).

[92] F. J. M. Heringdorf, M. C. Reuter and R. M. Tromp, Appl. Phys. A 78, 787 (2004).

[93] P. G. Schroeder, C.B. France, J.B. Parkinson, J. Appl. Phys. 91, 3010 (2002).

[94] M. G. Betti, A. Kanjilal and C. Mariani, J. Phys. Chem. A 111, 12454 (2007).

[95] C. D. Dimitracopoulos, A. R. Brown, and A. Pomp. J. Appl. Phys., vol. 80, no. 4, pp. 2501 – 2508, Aug. 1996.

[96] I. Kymissis, C. D. Dimitracopoulos, and S. Purushothaman, J. Vac. Sci. Technology B, vol. 20, no. 3, pp. 956 – 959, May/June 2002.

[97] Y.-Y. Lin, D. J. Gundlach, S. F. Nelson, and T. N. Jackson, IEEE Electron Device Lett., vol. 18, no. 12, pp. 606 – 608, Dec. 1997.

[98] S. Steudel, S. D. Vusser, S. D. Jonge, D. Janssen, S. Verlaak, J. Genoe and P. Heremans, Appl. Phys. Lett. 85, 4400 (2004)

[99] S. E. Fritz, T. W. Kelley and C. D. Frisbie, J. Phys. Chem. B, 109, 10574 (2005).

[100] T. Yasuda, K. Fujita, H. Nakashima, and T. Tsutsui, Japan. J. Appl. Phys. Part 1, vol. 42, no. 10, pp, 6614-6618, Oct. 2003.

[101] J. Jakabovic, J. Kovac, M. Weis, D. Hasko, R. Srnanek, P.Valent, R.Resel, Microelectronics Journal 40 (2009) 595– 597

[102] D. Knipp, P. Kumar, A.R. Volkel, R.A. Street, Synthetic Metals 155 (2005) 485–489

[103] V. Podzorov, V.M. Pudalov, M.E. Gershenson, Appl. Phys. Lett. 82 (2003) 1739–1741.

[104] D. Knipp, R.A. Street, B. Krusor, R. Apte, J. Ho, J. Non-Cryst. Solids 299–302 (2002) 1042.

[105] Specialty Coating Systems, Cookson Electronics. http://www.scscookson.com/parylene/properties.cfm

[106] Th.B.Singh, N.Marjanović, G.J.Matt, S.Günes, N.S.Sariciftci, A.Montaigne Ramil, A. Andreev, H.Sitter, R.Schwödiauer and S.Bauer, Mater. Res. Soc. Symp. Proc. Vol. 871E 2005

[107] P. Richman, New York: McGraw-Hill, 1967.

[108] Ch Kim, A. Facchetti, T.J. Marks, Science 318 (2007) 76–80.

[109] K.N.N. Unni, S. Dabos-Seignon, J.M. Nunzi, J. Mater. Sci. 41 (2006) 317–322.

[110] Lay-Lay Chua, Peter K. H. Ho, Henning Sirringhaus, and Richard H. Friend, Appl. Phys. Lett. 2004, 84, 3400.

[111] A. K. Diallo, Transistors organiques pour des applications biocapteurs. Thèse de doctorat de l'Ecole Centrale de Lyon. 2008.

[112] Capella B, Dielter G. Surf. Sci. Rep. 1999; 34: 1.

[113] Derjaguin BV, Muller VM, Toporov YuP. J. Colloid Interf. Sci. 1975; 53: 314.

[114] Israelachvili J. (2nd edn).Academic Press: London, 1992.

[115] Deman A.-L., Erouel M., Lallemand D., Phaner-Goutorbe M., Lang P., Tardy J., Journal of Non-Crystalline Solids 354 (15-16), pp. 1598-1607

[116] http://gwyddion.net

[117] Lita, A. E.; Sanchez, J. E., Jr. Phys. ReV. B 2000, 61, 7692–7699.

[118] A. Carré. J. Adhesion Sci. Technol., Vol. 21, No. 10, pp. 961–981 (2007)

[119] Drelich J, Tormoen GW, Beach ER. J. Colloid Interf. Sci. 2004; 280(2): 484.

[120] Xiao X, Oian L. Langmuir 2000; 16: 8153.

[121] Sedin DL, Rowlen KL. Anal. Chem. 2000; 72: 2183.

[122] De Gennes P.-G., Brochard-Wyart F. and Quéré D., Gouttes, Bulles, Perles et Ondes (Belin, Paris) 2002.

[123] C. Ishino, K. Okumura and D. Quéré, Europhys. Lett., 68 (3), pp. 419–425 (2004)

[124] Drelich J, Tormoen GW, Beach ER. J. Colloid Interf. Sci. 2004; 280(2): 484.

[125] D. Knipp, R. A. Street, A. Volkel, A. Ho, J. Appl. Phys. 2003, 93, 347.

[126] L. F. Drummy, D. C. Martin, Adv. Mater. 2005, 17, 903.

[127] D.Holmes, S.Kumaraswamy, A.J.Matzger, K.P.C.Vollhardt, Chem.Eur. J. 2001, 7, 933

[128] C.C.M.Palstra, Acta Crystallogr., Sect. C: Cryst.Struct.Comm.2001, 57, 939

[129] H.-L. Cheng, Y.-S. Mai, W.-Y. Chou, L-R. Chang, X.-W. Liang, Adv. Func. Mat., Vol. 17, pp. 3639-3649 (2007)

[130] A. V. Dzyabchenko, V. E. Zavodnik and V. K. Belsky. Acta Cryst. (1979). B35, 2250-2253.

[131] O.D. Jurchescu, J. Baas and T.T.M. Palstra, Appl. Phys. Lett. 84 (2004), pp. 3061–3063.

[132] S. D. Wang, T. Miyadera, T. Minari, Y. Aoyagi, K. Tsukagoshi. Applied Physics Letters, Vol. 93, No. 4. (2008)

Chapter III

AFM study of DNA-arrays assembling from X- and Y-shaped DNA strands

I - Introduction

I-1 DNA-array assembling in the literature

Nowadays, bio-nanotechnology plays an important role in the development of new materials and devices. The use of DNA molecules is motivated by their unique ability for self-organization, their extremely high length-to-width ratio of 10^7, and their appropriate chemical structure for electric charge transport.

Highly specific intermolecular interactions between DNA molecules are programmed by Watson-Crick complementarities which leads to the formation of double helices from single strands [1]. Based on highly precise recognition between DNA molecules, Seeman proposed to use DNA as a building block for the construction of new nanometer scale architectures that gave rise to the development of structural DNA nanotechnology, in 1982 [2]. Thanks to controlled arrangement of interacting molecules, DNA-based nano-structures have attracted much attention for nanoscale applications. Particular interest is due to the possibility to create more complex intermolecular patterns than double helices. The range of programmable self-assembled architectures includes linear one-dimensional (1D) structures [3-6], more complex assembly of two-dimensional (2D) DNA arrays [3, 7-10], and even three-dimensional (3D) DNA nano-objects [3, 11-13].

A fundamental property of DNA-based structures is that the final association has a predictable local geometry. This important feature of self-assembled nano-arrays has stimulated rapid progress in nanomedicine and molecular electronics. Concerning nanomedicine, DNA-based materials show enormous potential applications in tissue engineering, protein engineering and drug delivery systems [14a]. Another important strategy of DNA nanoarrays is their use for DNA-based fluorescent nano-barcodes for single cell and molecular sensing [14b, 15]. On the other hand, algorithmic self-assembly could also be used for DNA-based computation [16-18]. For example, simple computations such as commutative XOR and binary counting were performed in some works [19, 20]. More detailed descriptions of novel DNA-based materials and their applications are discussed in reviews of Yan et al. and Luo et al. [21, 22].

Future applications of DNA-based nanostructures in molecular diagnostics and therapeutics can be potentially coupled with molecular computers. Molecular computers can be programmed for targeting and

drugs delivery in the cellular environment. Together with DNA-based detection systems, it will allow autonomous detection and disease diagnostic [21].

Biophysical functions of DNA macromolecules are strongly dependent on their surroundings, thus, a good understanding of self-assembly properties and of changes in DNA conformation at a molecular scale is crucial for structural DNA-nanotechnology. In addition, the arrangement of DNA molecules often occurs through self-assembly surfaces. It has considerably motivated studies on the DNA behaviour on solid surfaces, in recent years [3-13, 21, 22].

Much progress in understanding controlled assembly of DNA molecules on solid surfaces has been made by using AFM. AFM is an appropriate technique for DNA molecules and DNA-based complexes on flat surfaces, especially due to its high spatial resolution and ability to operate in liquid environment, making it possible to image DNA under physiological conditions [23, 24]. The choice of appropriate substrates is very important in DNA imaging because DNA-substrate interactions could affect the conformation and the biophysical function of the macromolecule [25]. Reproducible AFM imaging depends on deposition conditions of DNA molecules. at the same time, to obtain a high resolution AFM image at a molecular scale, a completely flat surface should be used [25, 26].

Furthermore, in some cases, it is very important to preserve biophysical activity of DNA. This implies that on one hand, molecules should weakly interact with the substrate to be able to move, but on the other hand, they should be relatively strongly attached to guarantee stable imaging [25].

Several substrates have been used and many protocols were developed for appropriate deposition of DNA-samples onto the surface [27-30]. In this respect, the preferred substrate is *mica* thanks to its atomically flat surface over a large area [31, 32]. In recent years, mica was frequently used to study DNA-DNA and DNA-protein interactions and conformational changes by AFM [33-36].

The binding of DNA molecules to mica is mainly obtained by weak electrostatic interactions through multivalent cations [37, 38].The strength of the DNA adsorption can be changed by an adjustment of the cations concentration [39]. For example, the attraction between negatively charged DNA molecules and the mica surface is often referred as a "*salt bridge*" effect, by means of divalent or multivalent cations [40]. The mica pre-treatment by ions and the respective role of monovalent and divalent ions concentration have been recently established [31, 41]. However, the correct principle of DNA adsorption on the mica surface is not clearly understood yet. Fortunately, the origin of several forces that help to bind DNA molecules on mica surface was elucidated in the work of Zozime et al. [25].

In fact, to study the DNA assembling, it is important to understand how DNA interacts with mica surface. For this purpose, physical and chemical properties of both DNA and mica should be considered in details.

I-2 Deposition of DNA molecules onto the mica surface

I-2-1 Physic of adsorption

I-2-1-1 Mica as substrate for DNA imaging by AFM

Mica has become a standard substrate for AFM biotechnology even if surfaces of silicon, glass, graphite or lipid bilayer and silanised substrates can also be used [42, 43]. There are several types of mica which slightly differ from each other, in chemical nature. Mica represents a group of minerals that includes muscovite, biotite, phlogophite, lepidolite and other one [44, 45]. One of the most common used mineral surfaces is the *muscovite mica* because its perfect cleavage along the {001} planes ensures atomically flat and chemically inert surface that makes it suitable for deposition of many biological materials like DNA and proteins [46]. The control of the adsorption and biophysical reactions of biological materials on the mica surface requires deep understanding of the structure of cleaved mica on the atomic scale.

A crystalline structure of muscovite mica $KAl_2(Si_3Al)O_{10}(OH)_2$ includes aluminosilicate layers which are negatively charged due to a substitution of Si^{4+} ions by Al^{3+} ions. These layers are electrostatically bound with each other by interlayer potassium ions K^+ as shown in Figure III-1a).
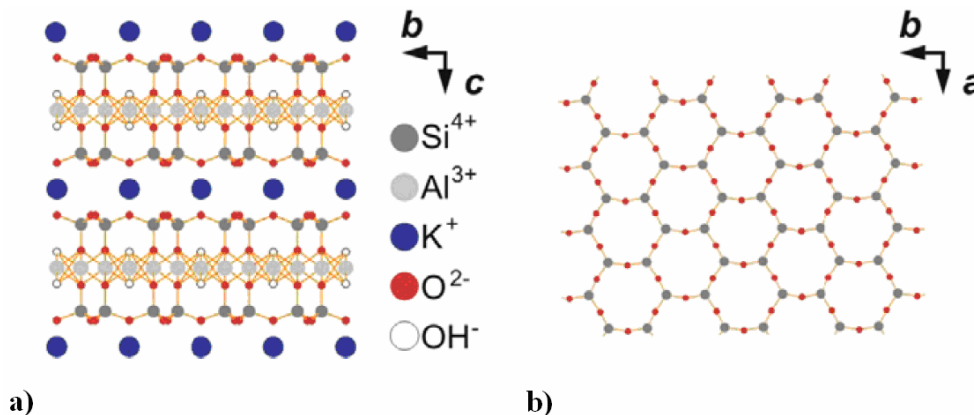

Figure III-1.Crystalline structure of the muscovite mica. a) Side view (projection onto the a-axis). b) Top view (projection onto the b-axis). Vectors a and b define {001} plane, residual potassium ions are not shown [48].

During the cleavage, the separation occurs through interlayer of potassium ions. This separation is possible due to the weak bonds between the potassium ions and the adjacent aluminosilicate layers. It was established that the potassium layer breaks during the cleavage whereas the atomic structure of the aluminosilicate layers remains undisrupted [47]. A cleaved mica surface consists in a {001} plane with a hexagonal arrangement of silicon Si (partly Al) and oxygen O atoms, as shown in Figure III-1b). In turn, the K^+ ions are generally distributed in an equal manner between two surfaces. In totality, the electric charge of

the mica surface is negative, but the local distribution of this charge is not homogenous [48]. In addition, the deposition of a liquid on the cleaved mica produces heterogeneous exchanges between the K$^+$ ions of the surface and the cations of the solution [49].

The binding forces between the negatively charged DNA and the negatively charged surface of mica change inevitably the conformation of molecules during deposition [50]. In the case of a weak DNA-surface binding, the molecules can move on the substrate and their final conformation corresponds to the lowest energy state. If the molecules adhere strongly to the surface, they can not equilibrate and their resulting conformation reflects the process of adsorption. Therefore, it is difficult to distinguish the native DNA conformation from those induced by the surface adsorption [51].

Consequently, a quantitative interpretation of adsorption mechanisms is required to understand the processes which affect the DNA arrangement and the resulting changes in size and conformation.

I-2-1-2 Double-layer interaction between DNA and mica

The electrical double-layer model is an analytical model to describe qualitatively the binding of DNA to the mica surface [52]. The corresponding force includes the electrostatic repulsion between the counterion clouds and the thermal pressure [52, 53].

This model is applied in assumption that only divalent counterions interact with DNA and mica.

For relatively high ionic strength, between 0.1 and 1M, the highly charged DNA molecule can be considered as a charged plane surface [54]. In this case, for low DNA concentration (lower that 1µg/ml), DNA molecules are covered by a thin layer of counterions with a thickness λ_Z [55]:

$$\lambda_Z = \frac{e}{4\pi\sigma l_b z} \qquad \text{(eq.3.1)}$$

Where e is the electron charge, σ the surface charge density, z the ions valence and lb the Bjerrum length (the separation at which the electrostatic interaction between two elementary charges is comparable in magnitude to the thermal energy) given by:

$$l_b = \frac{e^2}{\varepsilon k_B T} \qquad \text{(eq.3.2)}$$

where ε is the dielectric constant, k_B the Boltzmann constant, and T is the temperature.

Equation (3.1) shows that the thickness λ_Z is only dependent on the surface charge density and on the valence of the counterions.

The double-layer force can be derived in assumption that the double-layer potential is situated outside the adsorbed ion layer and that the surface charge densities of the two planes are different. Then according to Lau et al. [56], the pressure $P(d)$ between DNA and mica is:

$$P(d) = \frac{k_B T}{dl_b} \int_0^d dx \left(\frac{1}{2} \left(\frac{d\varphi}{dx} \right)^2 - \frac{d}{dx} \left(\frac{d\varphi}{dx} \right) \right) \qquad \text{(eq.3.3)}$$

where d is the distance between adsorbed ion layers and $d\varphi/dx$ is the gradient of electrostatic potential.

In equation (3.3), the first term corresponds to the thermal pressure of the counterions and the second one represents the electrostatic interaction of the counterion clouds.

The electric potential can be calculated by using the Poisson-Boltzmann equation for the case of mobile ions between two charged surfaces [52, 56]:

$$\frac{d^2\varphi(x)}{dx^2} + k^2 e^{-\varphi(x)} = \frac{l_b}{z} n(x) \qquad \text{(eq.3.4)}$$

with boundary conditions:

$$\left. \frac{d\varphi(x)}{dx} \right|_{x=0} = -\frac{\sigma_a l_b}{ze} \; ; \qquad \left. \frac{d\varphi(x)}{dx} \right|_{x=d} = -\frac{\sigma_b l_b}{ze} \qquad \text{(eq.3.5)}$$

where $\varphi(x)$ is the normalized electrostatic potential, $n(x)$ the external charge density, k is a constant depending on boundary conditions, σ_a and σ_b are the surface charge densities of mica and DNA, respectively.

It is worth to note that, from boundary conditions, equation (3.5) follows that electric potential only depends on σ_a for $x = 0$ and on σ_b for $x = d$.

Substitution of eq. (3.5) into the eq. (3.3) gives the next system of transcendental equations for pressure $P(d)$ [57]:

$$|P(d)| = \frac{k_B T}{2l_b} \left[\sigma_a \sigma_b \left(\frac{l_b}{ze} \right)^2 + \frac{l_b(\sigma_a + \sigma_b)}{ze} \sqrt{\frac{2l_b|P(d)|}{k_B T}} \coth\left(\sqrt{\frac{2l_b|P(d)|}{k_B T}} d \right) \right] \quad \text{if } P(d) < 0, \qquad \text{(eq.3.6)}$$

$$P(d) = \frac{k_B T}{2l_b} \left[\sigma_a \sigma_b \left(\frac{l_b}{ze} \right)^2 + \frac{l_b(\sigma_a + \sigma_b)}{ze} \sqrt{\frac{2l_b P(d)}{k_B T}} \cot an\left(\sqrt{\frac{2l_b P(d)}{k_B T}} d \right) \right] \quad \text{if } P(d) > 0. \qquad \text{(eq.3.7)}$$

As it follows from equations (3.6) and (3.7), the pressure between DNA and mica depends on their surface charge densities, but does not depend on the bulk concentration of divalent ions. It obviously means that the charge density of the double-layer profile is not dependent on the bulk salt concentration. Also, the negative pressure $P(d)$ corresponds to the attractive interaction force and the positive to the repulsive force.

The pressure between two planes can by obtained by solving numerically the equations (3.6) and (3.7) [57]. The results of theoretical calculation are shown in Figure III-2, where pressure between DNA and mica surfaces is represented versus the distance d for different charges of mica surface.
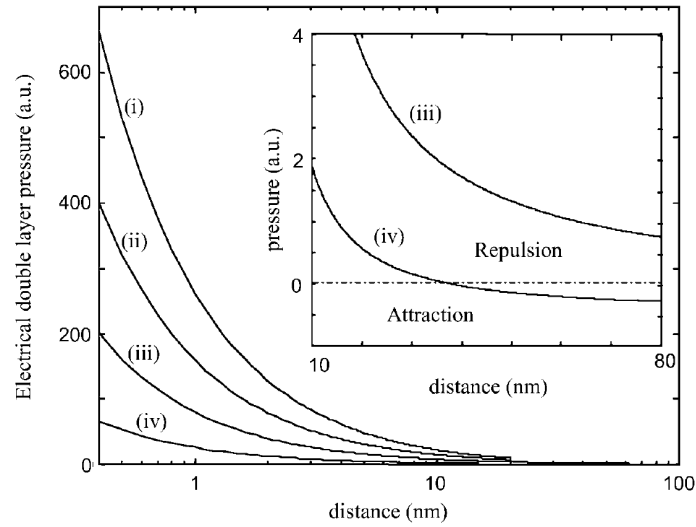

Figure III-2. Electrical double-layer pressure between DNA and mica surfaces for different σ_a/σ_b ratios, where σ_a and σ_b are surface charge densities of mica and DNA respectively: (i) $\sigma_a/\sigma_b=4$; (ii) $\sigma_a/\sigma_b=2$; (iii) $\sigma_a/\sigma_b=0.5$; (iv) $\sigma_a/\sigma_b= - 0.5$[53].

The density of the net surface charge is the sum of the native surface charge density (for DNA $\sigma_b =$ $- 10^{18}e/m^2$ and for mica $\sigma_a = - 2 \cdot 10^{18}e/m^2$, where e is the electron charge) and the adsorbed density of ions. According to Figure III-2, for a net surface charge of DNA $\sigma_b = 0.15e/nm^2$, the repulsion pressure decreases for small surface charge of mica (decrease from (i) to (iv)).

Furthermore, if the DNA and the mica are oppositely charged $\sigma_a/\sigma_b= - 0.5$, the pressure between them becomes attractive for large separation distance. Namely, if the separation $d \geq d_0$ then the attractive pressure exceeds the thermal repulsion. The characteristic distance d_0 can be obtained from eq. (3) at the condition $P(d_0) = 0$, thereby:

$$d_0 = 2\left(\frac{ze}{l_b}\right)\left|\left(\frac{1}{\sigma_a}+\frac{1}{\sigma_b}\right)\right|$$

(eq.3.8)

However, the repulsive force between DNA and mica becomes stronger, for short distances. It can be explained by the fact that the entropy of the counterion clouds decreases near the surface [56].

Obviously, the double-layer approximation does not describe all forces involved in DNA-mica interactions; short-range attraction implies another type of electrostatic force.

I-2-1-3 Counterion correlation

In solution, an electrostatic attractive force between DNA and mica can appear due to the counterion correlation on their surfaces. This mechanism was proposed by Arenzon et al. [58] and it considers that DNA and mica surfaces can be represented as two parallel charged lines. According to the proposed model, the attractive correlation force is expressed by:

$$F_c(d) = \frac{e^2 d}{\varepsilon} \sum_{i,j} \frac{(1 - z_i \phi_i)(1 - z_j \phi_j)}{(x_{i,j}^2 + d^2)^{3/2}}$$

(eq.3.9)

where indexes i and j correspond to the mica and DNA sites respectively; z_i and z_j are the valences of ith and j^{th} ions; d is the distance between DNA and mica charged layers; $(x_{i,j}^2 + d^2)^{1/2}$ is the distance between the ith mica site and j^{th} DNA site. The variables ϕ_i and ϕ_j describe the occupation of the corresponding sites so that $\phi = 0$ if the site is unoccupied and $\phi = 1$ if the site is occupied.

The repartition between occupied and unoccupied sites is determined through the process of energy minimization and it also depends on the system geometry. The optimum repartition of counterions between the DNA line and the mica surface corresponds to a staggered configuration [58] (Figure III-3).
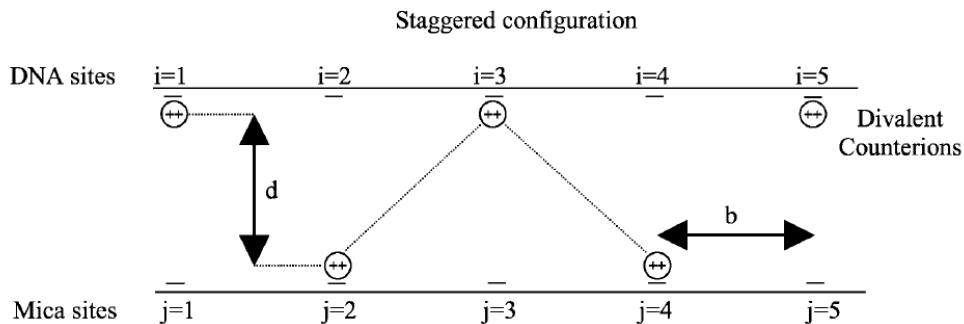

Figure III-3. Staggered configuration of counterions for the line shape of DNA and mica. Indexes i and j correspond to charged sites, d is the distance between interacting layers, b the distance between the counterion sites [58].

In assumption that only the bivalent counterions participate in the interaction between two lines, a numerical solving of the eq. (3.9) shows that the attractive short-range force appears if the interlayer distance d is smaller than the site separation b ($d < b$) [53].

According to the counterion correlation approximation it can be concluded that the range of attraction between DNA and mica is determined by the separation distance between neighboring sites of interacting lines. In other words, short-range attraction is possible if DNA and mica are highly charged. However, this model does not take into account the influence of the temperature on the occupancy of the sites.

I-2-1-4 Influence of temperature on attractive force

The counterion correlation force was assumed to be no temperature dependent. However, in real conditions, thermal motion may considerably affect the attraction of DNA onto mica which, is also dependent on the ionic strength of the solution. More precisely, the ionic strength determines the screening length of the electrostatic potential (Debye length) which together with the temperature defines the probability of the counterions to be placed in staggered position [53]. This probability is qualitatively different for different separation distances.

The separation can be considered as a short separation, if the distance between DNA and mica is much smaller than the Bjerrum length ($d << l_b$). Bjerrum length defines the distance between charges for which their thermal energy equals the electrostatic energy, so for distances $<< l_b$ the average electrostatic energy between two cons-ions is larger than the thermal energy. This leads to a probability of the staggered position significantly higher than unstaggered, and, therefore, the DNA and mica attract each other [53].

At intermediate separations $0.1 \cdot l_b < d < b$ the probability of unstaggered position depends on ionic strength of solution.

– For low ionic strength ($I < 100\text{mM}$), the Debye length is larger than the Bjerrum length ($\lambda_D > l_b$). In this case, the Bjerrum length is of order of the intersite distance b ($l_b \sim b$) that leads to a stable staggered position of counterions. Consequently, the thermal motion weakly affects attraction of the DNA to the mica, and the probability of occupancy in staggered position is high and insignificantly dependent on the ionic strength of the solution [53].

– For high ionic strength ($I \geq 100\text{mM}$), the Debye length is smaller than the intersite separation b ($\lambda_D < b$). In such conditions, the correlation force between counterions is greatly screened and the probability of staggered position is low. So, at high ionic strength, the thermal motion reduces the correlation force between charges that leads to weak the DNA attraction [53].

– For large separations, where the distance between DNA and mica exceeds l_b, the thermal energy of the counterions is larger than their electrostatic energy whatever the ionic strength of solution.

The electrostatic attraction between DNA and mica has been explained by using the model of correlation force between divalent or higher valence cations. However, the mechanism of attraction can be greatly influenced by the presence of monovalent cations.

I-2-1-5 Influence of monovalent cations on attraction force

The valence of cations involved in the DNA-mica interaction determines the attraction force, namely, the monovalent cations enter into the competition with the divalent cations to neutralize negatively charged surfaces of DNA and mica. Hence, the surface density of monovalent and divalent cations on both surfaces is a determinant factor for the attractive force. In fact, the correlation of monovalent cations does not contribute to the attraction, but a high surface density of them may completely inhibit DNA adsorption onto the mica surface [55].

To study the competitive interactions of the mono- and divalent cations with DNA and mica surfaces, their surface charge densities should be associated with their bulk concentrations. For this purpose, the Poisson-Boltzmann theory can be used [55]. According to this theory, the surface concentrations of monovalent (n_{s1}) and divalent (n_{s2}) cations can be presented as follows:

$$n_{s1} = n_{b1} \cdot e^{e\psi/k_BT} \qquad \text{(eq.3.10)}$$

$$n_{s2} = n_{b2} \cdot e^{2e\psi/k_BT} \qquad \text{(eq.3.11)}$$

where n_{b1} and n_{b2} are mono- and divalent cations bulk concentrations, respectively, and ψ is the surface electrostatic potential.

The surface concentration of divalent cations n_{s2} with respect to the bulk concentration of the monovalent n_{b1} and divalent n_{b2} cations can be obtained from the following equation [53]:

$$Yn_{s2}^2 - (2Y+1)n_{s2} + Y = 0 \qquad \text{(eq.3.12)}$$

where
$$Y = \frac{n_{b2}(n_{s1} + n_{s2})}{n_{b1}^2} \qquad \text{(eq.3.13)}$$

In the context of this model, the surface concentrations of cations n_{s1} and n_{s2} are constant if bulk concentrations n_{b1} and n_{b2} vary in such way that the ratio n_{b2}/n_{b1} is constant. It implies that the DNA to mica attraction force remains unchangeable for a given ratio n_{b2}/n_{b1}.

Theoretical calculations show that the attraction force is very sensitive to changes of the concentration of divalent cations n_{s2} on the DNA surface in the case of negligible electrostatic screening, i.e. if $I < 100$mM [53].

Another important aspect in the DNA-mica interaction that should be mentioned is the influence of the chemical functionalizing of mica surface on the adsorption properties. The double-layer and the correlation force models of adsorption, previously discussed, have been considered for clean mica surface

that binds DNA molecule through divalent or higher valence cations. However, for AFM imaging of DNA and DNA-based complexes, the divalent cations are generally used together with chemically pretreated mica surface. On pretreated mica, a competition between mono- and divalent cations occurs only on the DNA surface because of the high binding of Ni^{2+} ions with mica sites.

Generally added to the buffer, the Mg^{2+} counterions for DNA binding to mica do not have a great affinity with the mica surface. As a result, the correlation force of the Mg^{2+} counterions can be affected by thermal agitation. On the contrary, the Ni^{2+} cations contribute to a very strong interaction between DNA and the mica surface. Indeed, Ni^{2+} such as Mg^{2+} can easily interact with the phosphate groups of DNA bases, but Mg^{2+} does not form so strong bonds with mica than Ni^{2+} [59]. This different affinity with the mica surface is explained by the difference in relationship between enthalpy of hydration and ionic radius of Ni^{2+} and Mg^{2+}. For both, ionic radii are very close (0.65 Å), but the enthalpy of hydration of Ni^{2+} is larger than for Mg^{2+} [37]. As a consequence, adsorbed Ni^{2+} counterions can be hardly removed by thermal motion.

I-2-2 The object of study: DNA-based structures

I-2-2-1 Description

In this work, we study self-assembly architectures, of new DNA-based structures at the nanometric scale. The synthesis of these structures was realized under "click" chemistry conditions activated by microwaves. This experimental protocol was developed in the team of F. Morvan [60]. Using this strategy, five different oligonucleotide structures were synthesized, namely: two X structures (X1 and X2 molecules), two Y structures (Y1 and Y2 molecules) and a 20 base molecule. With these structures, three sets of mixtures were prepared: X1+X2, Y1+Y2 and X1+20bases mixtures in order to study their ability to create self-assembled architectures in different conditions.

The X and Y structures are so called due to their X- and Y-like molecular shapes. At a molecular level, both X and Y structures are composed of the pentaerythrityl [60] core and a certain number of single DNA strands (4 for X structures, 3 for Y structures and 2 strands for 20 bases-molecules that is illustrated in details in Annexe II). This core plays the role of a linker between the oligonucleotides and determines the spatial structure of a molecule i.e. the shape of the X or Y structures.

Synthesized X structures are composed of four single strands (each contains 10 oligonucleotide bases) exhibiting twice the same sequence for both X1 and X2 molecules. More precisely, as it is shown in Figure III-4 (a), two sequences of X1 ($X1_1$) are complementary to two sequences of X2 (X2c1) and the other two sequences of X1 ($X1_2$) are complementary to two sequences of X2 (X2c2). Governed by complementary recognition, the molecules of X1+X2 mixture can be arranged in linear double double-stranded chains or more complex two dimensional squared double-stranded net architectures. Expected patterns are schematically illustrated in Figure III-4 (a) and (b).
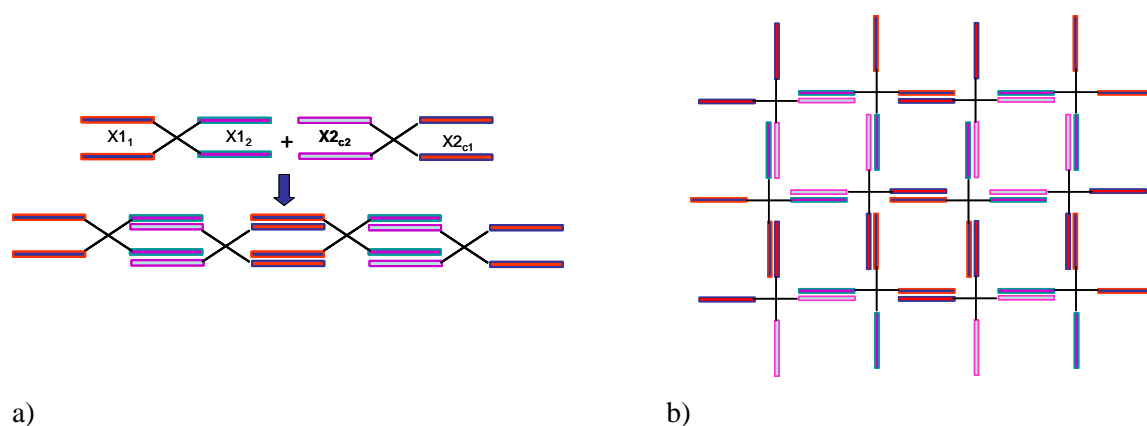
Figure III-4. (a) Linear double double-stranded and (b) mesh of double double-stranded
X structures expected for X1 and X2 shaped molecules.

Using the similar strategy, the Y-shaped structures were synthesized (see Annexe II). Each molecule has three single strands (each composed from 10 bases) connected by Y-like linker between them. Moreover two among these strands are the same for Y1 and Y2 molecules. More precisely, two identical sequences of Y1 ($Y1_1$) are complementary to two sequences of Y2 ($Y2_{c1}$) and another one sequence of Y1 ($Y1_2$) is complementary to one sequence of Y2 ($Y2_{c2}$) (Figure III-5(a)). Two possible arrangements of the Y1 and Y2 are expected. Similarly to X1+X2, the Y1+Y2 can be patterned in a linear chain or a two dimensional mesh architectures, but with different topologies. In this case, the conformation of the chain should be an alternation of double double-stranded and single double-stranded, that is defined by the shape of Y structures (Figure III-5(a)). The Y1+Y2 mixture should also provide the creation of a 2D mesh with a periodical change in the density of double-stranded oligonucleotides, as shown in Figure III-5(b).
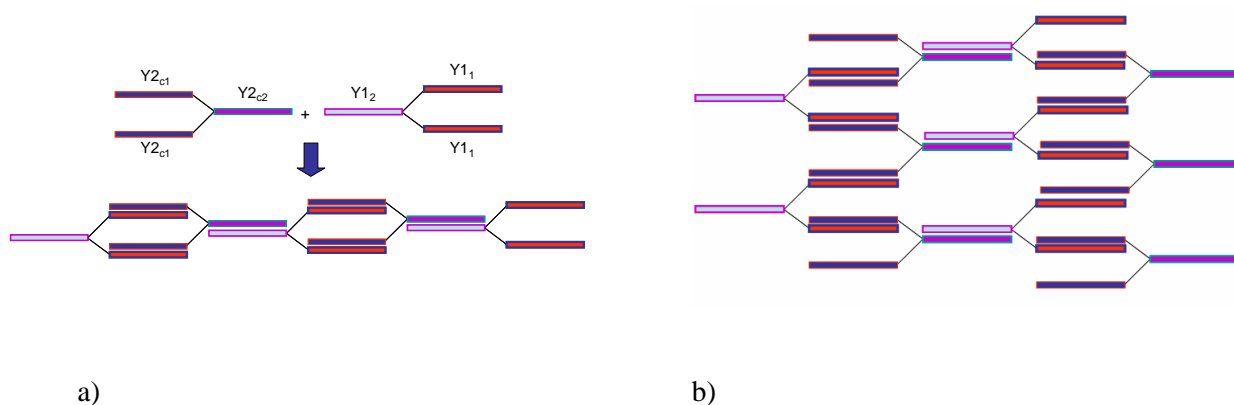

Figure III-5. (a) Linear double/single double-stranded and (b) mesh of double/single double-stranded
structures expected for Y1 and Y2 shaped molecules.

The third mixture includes the previously described X1 structure and the 20 base molecule. The 20 base molecule is a single-stranded oligonucleotide sequence composed of 20 bases. One half of the 20bases is complementary to one sequence of X1 and the other half – to another X1 sequence. Namely, the first part

133

of the 20 base molecule (10mers$_{C2}$ sequence) is complementary to one sequence of X1$_2$ and the second part (10mers$_{C1}$ sequence) is complementary to one sequence of X1$_1$. Molecules of the X1+20 bases mixture are also expected to be able to form linear and 2D architectures, which can be obtained, through the fixation with the 20 base molecules, by the end-to-end stacked X1 molecules, as it is shown in Figure III-6 (a) and (b).
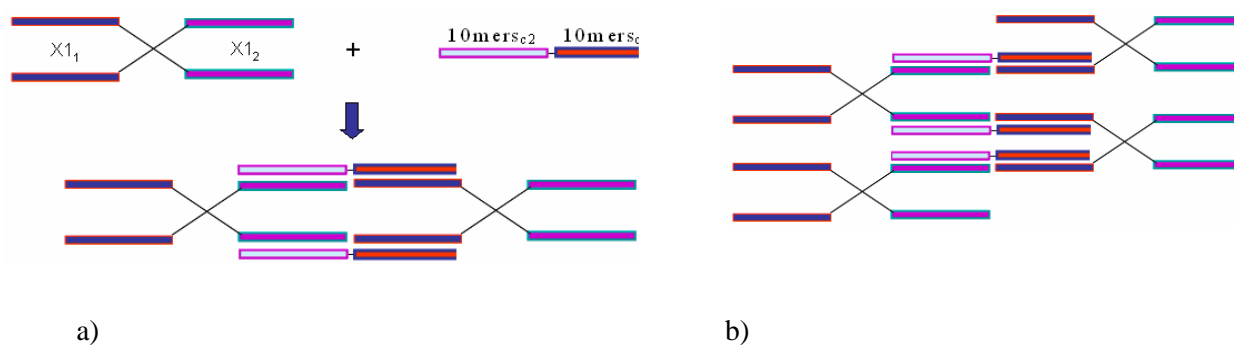

Figure III-6. (a) Linear double double-stranded and (b) mesh of double double-stranded structures expected for X1-shaped and 20 base shaped molecules.

I-2-2-2 Experimental verification of molecular assembly

In order to study the association of the X1+X2, Y1+Y2 and X1+20bases structures, UV-thermal dissociation experiments were realized for each mixture. Thermal dissociation study gives information about fusion and hybridization of nucleotides as a function of the temperature. An example of such study is presented for X1 and X2 structures and their mixture X1+X2 in Figure III-7.
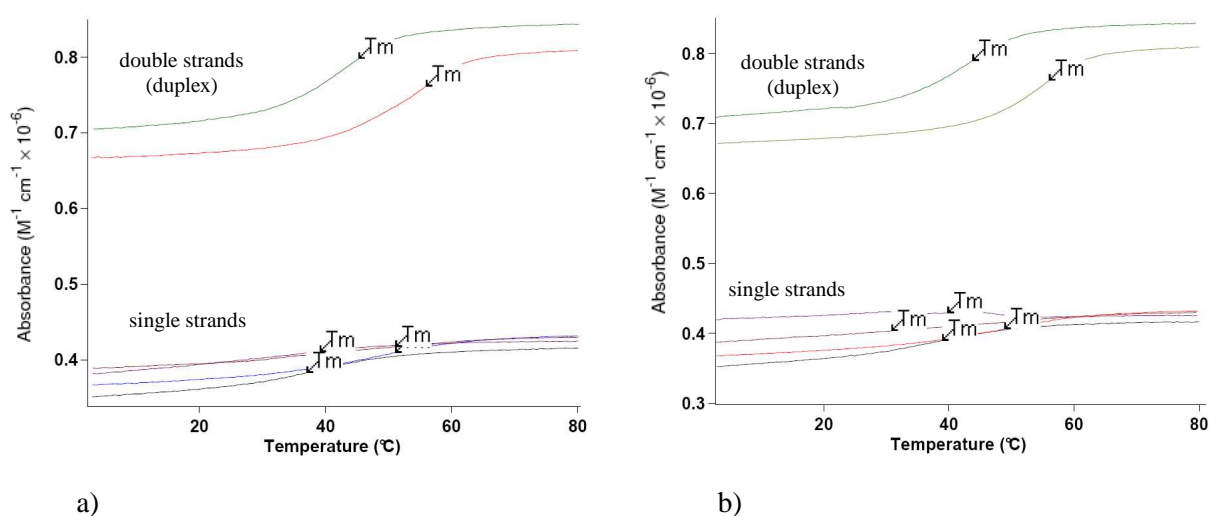

Figure III-7. (a) Experimental fusion and (b) hybridization curves obtained for X1, X2 and X1+X2 structures
Upper curves correspond to X1+X2c1 and X2+X1c2 duplexes, bottom curves –
to single stranded DNA of corresponding structures.

Experimental study of thermal dissociation for X-shaped structures was performed at the concentration of 1μM, for each molecule, in a phosphate buffer solution PBS (at a concentration of 0.01M and pH=7), in which 0.1M or 1M of NaCl was added. Figure III-7 represents the fusion (a) and the hybridization (b) curves for the corresponding concentrations of NaCl, arrows indicates the corresponding melting temperatures (Tm). The values of the melting temperatures, measured from the curves in Figure III-7 (a) and (b), are presented in table 1. Just to recall, melting temperature is defined as the temperature at which half of the DNA strands are in the double-stranded state and half are in the single-strand state [61].

Sample / concentration	Fusion, °C	Hybridization, °C
X1 / 0.1M	37.02	38.92
X1 / 1M	51.07	48.87
X2 / 0.1M	39.08	39.82
X2 / 1M	51.12	30.82
X1+X2 / 0.1M	45.22	43.78
X1+X2 / 1M	55.92	56.02

Table 1. Melting temperatures for X1, X2 and X1+X2 structures
determined from curves in Figure III-7 (a) and (b).

For Y1+Y2 structures, the study of thermal dissociation has been performed in the same conditions as for X1+X2 structure. Corresponding TM values are represented in the summary table together with TM of X1+X2 structures (Table 2). The TMs of X1+20bases structure are believed to be equal to that of X1+X2, because both structures have exactly the same sets of oligonucleotide sequences.

Sample	TM of X1+X2 °C		TM of Y1+Y2 °C	
Denaturation [NaCl]	Fusion	Hybridization	Fusion	Hybridization
0.1 M	45	44	45	46
1 M	56	56	55	58

Table 2. Experimentally determined TM for X1+X2 and Y1+Y2 mixtures.

As it can be clearly seen from fusion and hybridization curves in Figure III-7 (a) and (b), the X1+X2 mixture presents higher absorbance values than isolated X1 or X2 structures. It indicates a high affinity of hybridized double-stranded structures in comparison with non hybridized single strands suggesting that X1 and X2 interact together with more than one sequence. In addition, a higher concentration of NaCl favours stronger interaction between nucleotides. This leads to higher values of melting temperatures measured during fusion and hybridization, meaning a better thermal stability of DNA double strands as a part of X1+X2 structure. The similar tendency was observed for Y1+Y2 structures.

In order to determine which pair of complementary strands (duplex) ($X1_1/X2_{C1}$ or $X1_2/X2_{C2}$ for X1+X2 etc) participates the most to the experimentally measured TM, theoretical prediction of TM values for each duplex was performed using the Zuker's model, "mfold" software [62]. Results are presented in the Table3.

Sample	TM of X1+X2 °C		TM of Y1+Y2 °C	
Duplex [NaCl]	5'-GAC GCT GTG G-3'(X11) 3'-CTA CGA CAC C-5'(X2c1)	5'-GAC GCT AAT C-3' (X12) 3'-CTG CGA TTA G-3' (X2c2)	5'-GAC GCT GTT GG-3' (Y11) 3'-CTA CGA CAA CC5'-(Y2C1)	5'-GAC GCT AAT C-3' (Y12) 3'-CTG CGA TTA G-3' (Y2c2)
0.1 M	43.9	34.0	42.9	34.0
1 M	54.5	44.8	57.2	44.8

Table 3. Theoretically calculated TM for X1+X2 and Y1+Y2 structures in presence of NaCl.

On Table 3, the calculated TM values of the $X1_1/X2_{C1}$ duplex, i.e. ~ 44°C and 55°C for NaCl concentration of 0.1M and 1M, respectively, are very close to the experimental TM values of 45°C and 56°C (fusion) and 44°C and 56°C, (hybridization) presented on Table 2. Calculated values for the $X1_2/X2_{C2}$ duplex, 10°C lower (34°C and 45°C) demonstrate the low contribution of this duplex in the experimental TM. These results are also entirely applicable to X1+20bases structures.

Using similar considerations to Y1+Y2 structure, one can also conclude that experimentally measured TMs corresponds to the $Y1_1/Y2_{C1}$ duplex and not to the $Y1_2/Y2_{C2}$. Experimental TMs for $Y1_1/Y2_{C1}$ are 45°C and 55°C (fusion), and 46°C and 58°C (hybridization) for NaCl concentration of 0.1M and 1M, respectively (Table 2) and predicted values are ~ 43°C and 57°C (Table3). Calculated TMs of $Y1_2/Y2_{C2}$ are ~ 34°C and 45°C for respective NaCl concentrations which is approximately 11°C lower than calculated TMs for $Y1_1/Y2_{C1}$ duplex.

This study of the duplex thermal dissociation leads to an important conclusion: The duplexes, elements of X1+X2, Y1+Y2 and X1+20bases structures are characterized by different thermal stabilities. This indicates that the denaturation starts for $X1_2/X2_{C2}$ duplex while the other duplex $X1_1/X2_{C1}$ remains stable. The same behaviour, also occurs for the Y1+Y2 and X1+20base structures.

Concerning these specific structures, our first hypothesis is that they will form linear double-stranded structures rather than two-dimensional networks. In order to obtain any insights of the global arrangement, an AFM study of the different structures was performed. Our objective is not only to observe but also to determine the influence of the medium (air or different buffers) on the arrangement.

I-2-3 Preparation of samples for AFM studies

I-2-3-1 The salt solution

After the synthesis of X-, Y-shaped and 20bases molecules, their mixtures X1+X2, Y1+Y2 and X1+20bases were prepared in water and thereafter lyophilised and packed in eppendorfs containing 1nmole of each molecule. Then, each mixture was hybridized in a Tris acetate buffer at a concentration of 20mM, containing 10mM of $MgCl_2$ salt.

The thermal dissociation of mixtures has not been studied experimentally for $MgCl_2$ containing solution. However, based on a very good agreement between theoretically predicted and experimentally measured TMs in NaCl containing solution (Tables 2 and 3), the same Zuker's model [62] was used to calculate the melting temperatures in $MgCl_2$ containing solution (Table 4).

As shown in Table 4, the TM values for $MgCl_2$ concentration of 0.01M are between the respective TM values for concentrations of 0.1 and 1M of NaCl, for X1+X2 and Y1+Y2 structures. Furthermore, the relations between TMs of the different duplexes are the same than for NaCl containing solution. Namely, the TM of $X1_1/X2_{C1}$ is 49.5°C, 39.7°C for $X1_2/X2_{C2}$, and the TM of $Y1_1/Y2_{C1}$ is 52.2°C, 39.7°C for $Y1_2/Y2_{C2}$. Once again, the duplexes present considerable difference in their thermal stability (Table 4).

Sample	TM of X1+X2 °C		TM of Y1+Y2 °C	
Duplex [MgCl2]	5'-GAC GCT GTG G-3' (X11) 3'-CTA CGA CAC C-5'(X2c1)	5'-GAC GCT AAT C-3' (X12) 3'-CTG CGA TTA G-3' (X2c2)	5'-GAC GCT GTT GG-3' (Y11) 3'-CTA CGA CAA CC5'-(Y2C1)	5'-GAC GCT AAT C-3' (Y12) 3'-CTG CGA TTA G-3' (Y2c2)
0.01 M	49.5	39.7	52.2	39.7

Table 4. Theoretically calculated TM for X1+X2 and Y1+Y2 structures in presence of $MgCl_2$.

I-2-3-2 The hybridization of oligonucleotides

Since duplexes of mixtures X1+X2, Y1+Y2 and X1+20bases have different melting temperatures, they can not be synthesised at a constant temperature. It implies that the hybridization conditions should ensure the assembly of some duplexes without affecting the assembly of other duplexes. This goal can be achieved by changing the temperature gradient during hybridization.

However, a question arises: how long should continue the hybridization process? The answer to this question can be obtained by an estimation of the duration of the hybridization time of nucleotide sequences.

The hybridization time $t_{1/2}$ is the time required to reach half of the equilibrium (after this value half of all possible duplexes should be already formed) [63]:

$$t_{1/2} = \frac{\sqrt{L}\ln 2}{3.5\cdot 10^5 \cdot C_N} \qquad\qquad\qquad\text{(eq.3.14)}$$

where L is the nucleotide length in nt (nt is the common used abbreviation for nucleotide length measurement; here equal to the total number of base pairs) and C_N is the nucleotide concentration in *mol/liter*.

The total time of hybridization " t " is estimated to be 5 times the $t_{1/2}$, that is sufficient to reach about 90% of the equilibrium [63]. In our case $L = 10$ and $C_N = 10^{-6}$M, then we obtain that $t_{1/2} = 6.3$s and $t = 31.3$s, according to eq. (3.14).

In our experiment, all the duplexes are not totally isolated, but they can form complex structures which are able to create linear or 2D architectures. It implies that the real hybridization time t may exceed the estimated time of 31.3s. Consequently, the cooling velocity should not be too high in order to ensure a sufficient relaxation time for a successful assembly of DNA-based complexes.

Taking into account the above requirements for hybridization of nucleotides, we followed the experimental protocol proposed by Labean et al. [64]. The eppendorfs containing each mixture were put in boiling water and then left to cool in a polystyrene box during 40h.

The change of water temperature, in the box, during hybridization was recorded and is presented in Figure III-8. The temperature which corresponds to the highest TM (52°C for Y1+Y2) is marked by a red circle and the lowest TM (~40°C for both X1+X2 and Y1+Y2) by a blue circle.
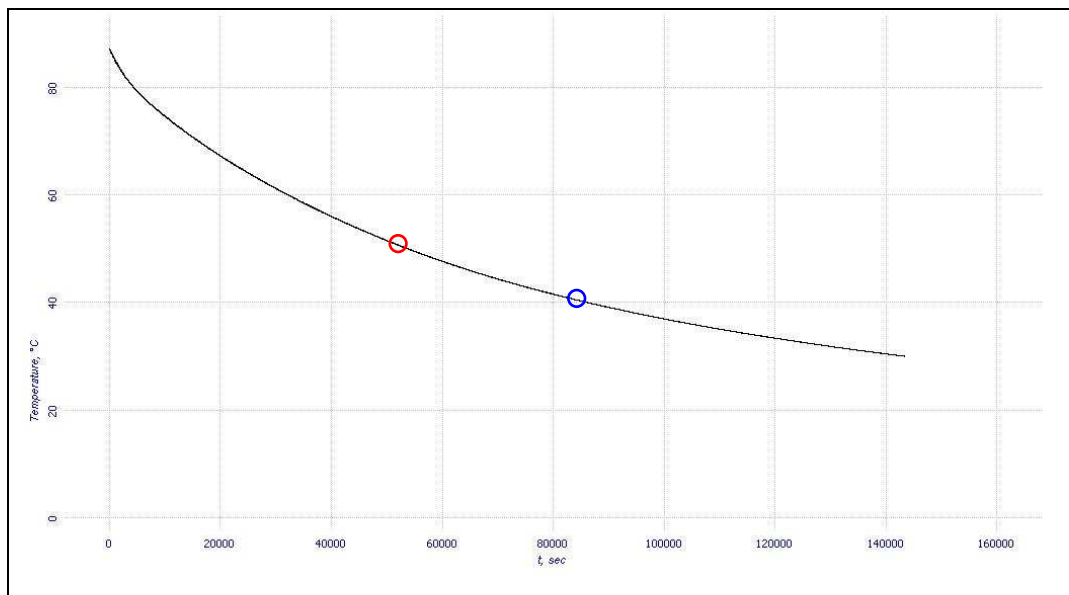

Figure III-8. Temperature gradient during hybridization.

The temperature gradient curve allows to estimate the duration of the change in temperature of 1°C (Figure III-8). The temperature change from 52°C to 40°C takes about ~ 580min, it corresponds to a change of 1°C in around 48min, in assumption that the temperature versus time dependence between the highest and the lowest TMs (between circles) is linear. Thus, during the theoretical hybridization time $t = 31.3s$, we obtain a change of temperature around 0.007°C, which can be considered as constant. One can then conclude that the temperature decreases slowly enough ensuring sufficient time for duplexes formation.

II - AFM studies

AFM imaging was realised in air and in two liquid media: Tris and HEPES buffers.

Each mixture before hybridization, has had the concentration of 1µM of each molecules diluted in 20µL of Tris acetate buffer (see paragraph I-2-3- Hybridization of oligonucleotides). After hybridization, all mixtures were remained intact. In other words, all mixtures were deposited on the substrate from the same solution in which they were hybridized and neither the chemical composition of the solution or the concentration of molecules has not been changed.

The muscovite mica was used as a substrate for the samples deposition according to the reasons discussed in paragraph I-2-1. An appropriate protocol for the deposition of hybridized molecules was used which depends on the chemical properties of the mica surface, namely, chemically pre-treated or simple freshly cleaved mica. All the experiments were realized in dynamic mode AFM (AM-AFM), a detailed description is given below.

II - 1 Observation of the different structures in air

II-1-1 Experimental AFM conditions

AFM imaging in air was carried out with a Smena NT-MDT Microscope Stand Alone P-47 in AM-AFM mode. We deliberately worked in a "light tapping" mode (the high part of the Low branch) where A_{SP}/A_0 ratio was of 67% for a given experimental free amplitude $A_0 = 18nm$ and a working amplitude $A_{SP} \sim 12nm$ in order to be sure to create no damage on the DNA structures. The scanning of samples was performed with rectangular silicon cantilever with the spring constant $k = 11.5N/m$ and a typical tip curvature of 10nm. The cantilever was excited at its resonant frequency of 224.7kHz allowing thus a quality factor of $Q = 488$. Determined experimentally optimal scanning rate was between 0.7-0.9Hz. Scanning was realized in ambient condition, at a temperature T of 23°C and a relative humidity $H = 33\%$.

Values of widths of DNA molecules indicated in all cross-sections of the current chapter represent values after substracting of the convolution effect with the AFM tip. Detailed description of used deconvolution method is explained in the Annexe III.

II-1-2 Deposition on mica substrates

In air, the arrangement was studied on chemically pre-treated and non treated mica surfaces. First of all we will focus on the study of the DNA structures on non pretreated mica.

II-1-2-1 Deposition on non pretreated mica surface

It was known that, smooth and clean mica sheets can be easily obtained by simple cleavage. In our experiments, a mica plate was cleaved with scotch tape until a plane and step-free surface was obtained. Immediately, samples were deposited on this freshly cleaved substrate.

The deposition process follows these different steps:

- deposition from a drop of 2μL of the corresponding solution, using a micropipette,
- incubation in air during 5 or 10 min,
- rinsing with deionised water,
- drying by nitrogen gas.

For such small volume, the deposition period should not exceed a certain time because, the deposited drop can be completely evaporated, that inevitably leads to the desiccation of the deposited molecules, their juxtaposition and an undesirable salt aggregation. It was experimentally determined that deposition time should not be larger than 10-12 min in our experimental conditions. Once the samples were deposited during a sufficient time, the rinsing was performed in order to remove from the surface non adsorbed molecules. We used 0.5mL of deionised water, which was accurately deposited on vertically placed mica surface in order to let the water flow down under gravitational force.

After rinsing, samples were dried in a weak flow of nitrogen in order to minimize the risk to damage deposited molecules.

II-1-2-2 Deposition on pretreated mica surface

The same deposition protocol was performed on pretreated mica.

Chemical pretreatment of the mica surface was performed with divalent cations of $NiCl^{2+}$ in solution. In order to obtain a uniform distribution of divalent cations on the surface, mica was completely immersed in a $NiCl^{2+}$ solution, before deposition of the samples. More precisely, the pretreatment protocol included the following stages:

- diving of the freshly cleaved mica in 10mM $NiCl^{2+}$ solution during 1min.
- rinsing of the treated mica with deionised water.
- drying by nitrogen gas

Immediately, the samples were deposited on this pretreated mica, following the protocol previously described.

II-1-3 AFM imaging

II-1-3-1 Study on non treated mica surface

<u>X1+X2 structures</u>

For a deposit during 5min, AFM images typically show X1+X2 structures randomly distributed on the mica surface in small fragments with lengths ranging between 10 and 160nm and heights between 1.4 and 1.6 nm (Figure III-9a).
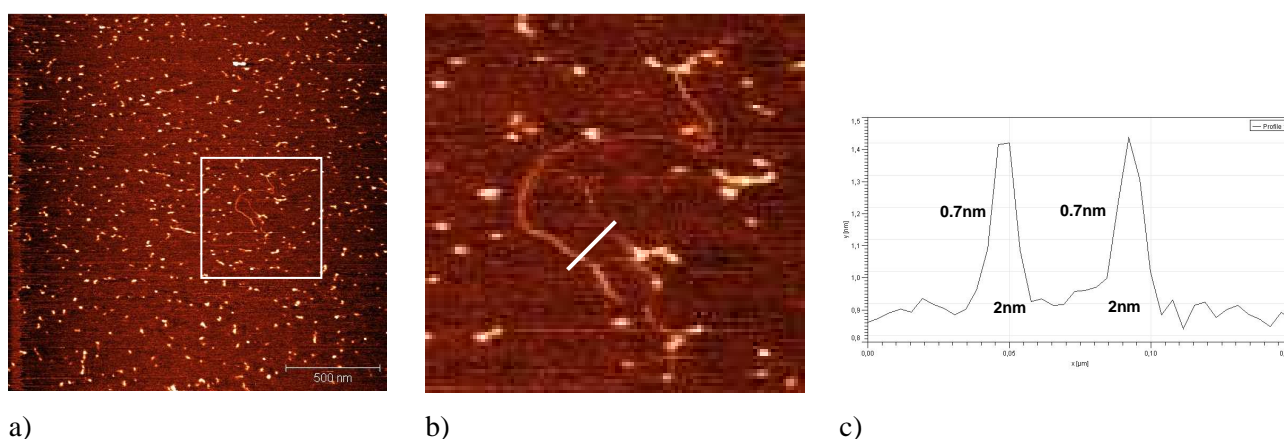

a)   b)   c)

Figure III-9. Arrangement of X1 + X2 mixture in air on non pretreated mica, deposition time t = 5min.

a) Topography image of 2x2µm; b) zoom on the insert area from image (a) 0.5x0.5µm;

c) Cross-section of the filament visible on image (b).

Furthermore, a more complex X1+X2 association was found, among the small linear structures. This molecule is shown in Figure III-9(b), which is a zoom of the area marked by the white rectangle in Figure III-9 (a). This is a 1D structure of ~ 200nm long with four bifurcation points at which branches of the X1+X2 molecule are created. Formed in such a way, branches define loop-like structure of the assembly indicating that there are mismatches between hybridized X1 and X2 molecules. As it can be seen in the Figure III-9 (b), three from four bifurcations are "three-branched" and one point is "four-branched". This is possible thanks to the X-shaped structure of molecules which potentially allows a connection of one molecule with four other molecules (i.e. by forming single double-stranded interaction instead of double double-stranded).

Another interesting point is that the average height of the small fragments (1.5±0.1nm) is higher than the height of the long loop-like macromolecule around 0.7nm (Figure III-9(c)). In addition, fragments are thicker than the macromolecule ~4nm and ~2nm, respectively. This fact indicates that X1 and X2 molecules form long macromolecule by single double-stranded linkage with each other, whereas small fragments are double double-stranded structures.

However, even more complex structures were formed on a base of X1+X2 molecules. For exactly the same deposition condition, a "fishhook-like" structure was observed as shown in Figure III-10(a). This

complex structure presents a symmetrical geometry and involves two types of molecular assembling: a linear (1D) double double-stranded branches (both have a length of ~200nm) and a 2D array assembling in the centre of the structure and at the end of the upper branch. It is worth to note that areas with 2D assembling are higher (1.3-1.4nm) than areas with 1D assembling (0.8-0.9nm) (Figure III-10(c). This can be explained by a larger deformation of 1D structures by the AFM tip during scanning.

Another example of X1+X2 assembling is shown in Figure III-10(b). This structure obtained after 10min of deposition exhibits three types of molecular assembling. Namely, a 1D linear assembling with single double-stranded linkage for upper part of the loop and for a long "tail"; a 1D linear assembling with double double-stranded linkage for the area between the loop and the central perpendicular part and, a 2D-array assembling for the central part.
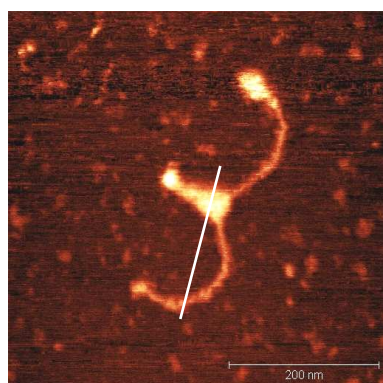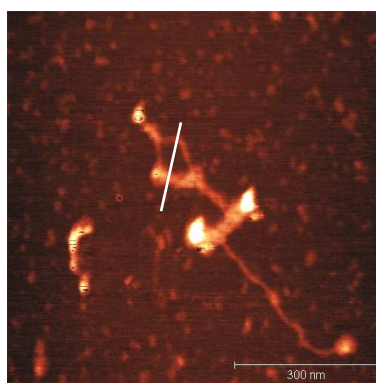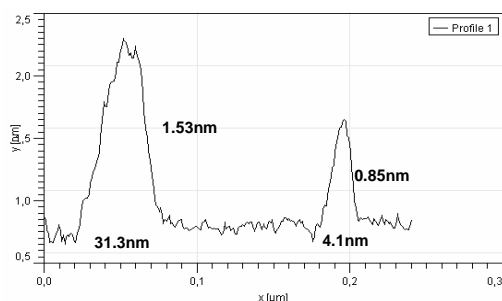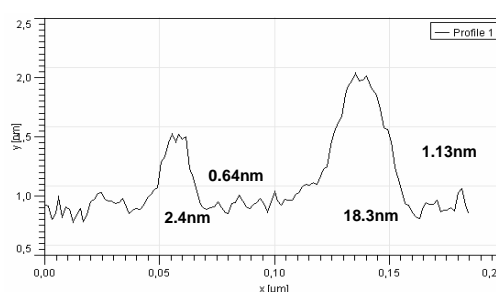

Figure III-10. Arrangement of X1+X2 mixture in air on non pretreated mica. a) deposition time t = 10min; b) deposition time t = 5min; c) and d) are cross-section of structures in images (a) and (b) respectively.

<u>Y1+Y2 structures</u>

As for the X1+X2 structures, the Y1+Y2 structures deposited during 10min manifest generally, by small dispersed fragments on AFM images (Figure III-11(a), (b)). However, the length of these fragments is larger than the length of the X1+X2 fragments. It varies between 30 to 240nm in comparison with 10 to 160nm for the X1+X2 fragments. The typical height of these observed structures is 1.2-1.3nm (Figure III-11(c)).
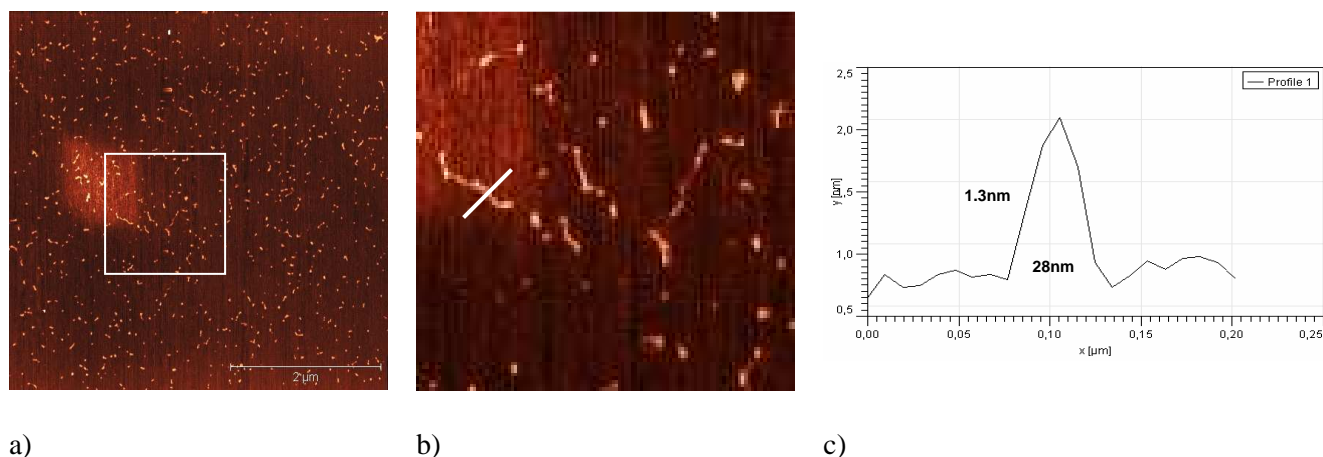

a)   b)   c)

Figure III-11. Arrangement of Y1+Y2 mixture in air on non pretreated mica, deposition time t = 10min; a) Topography image of 5x5µm; b) zoom in the marked area of image (a) 1x1µm; c) cross-section of the filament of image (b).

At the same deposition condition, a large structure with a length of ~3µm was observed (Figure III-12a). This 1D macromolecule has three bifurcation points, two of which create a loop at the upper part of the molecule (Figure III-12b). Homogenous height (0.77nm) and thickness (2nm) along the whole structure indicate that only one type of molecular assembling is presented – single double-stranded linear structure (III-Figure 12c).
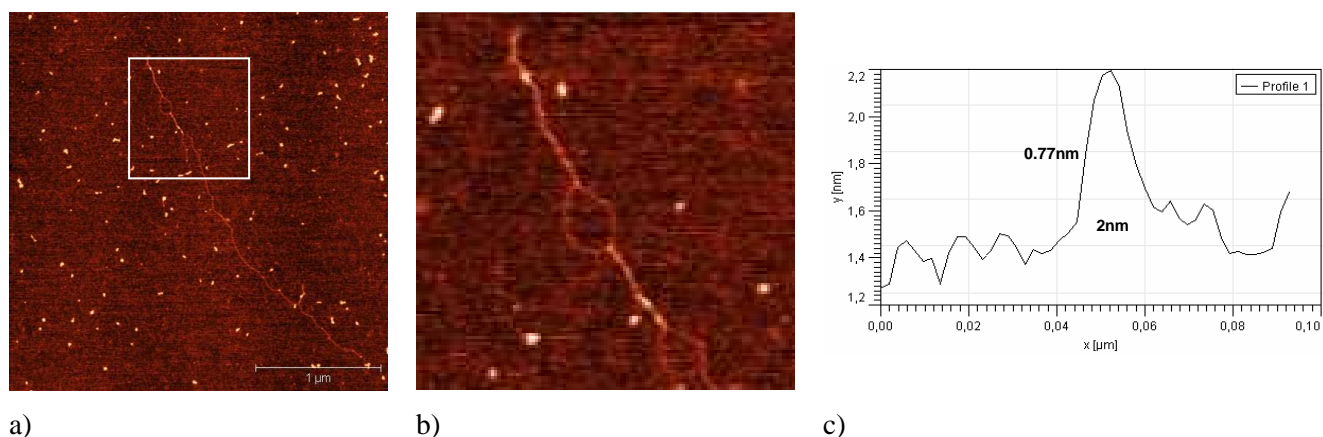

a)   b)   c)

Figure III-12. Arrangement of Y1+Y2 mixture in air on non pretreated mica, deposition time t = 10min; a) Topography image of 2x2µm; b) zoom in the marked area of image (a) 1x1µm; c) cross-section of the macromolecule inthe marked area of image (b).

In comparison with the previously described X1+X2 and Y1+Y2 structures, the X1+20bases mixture did not provide the formation of small fragments on the mica surface (Figure III-13a). Observed linear structure (Figure III-13b) with length of ~260nm and thickness of ~15nm indicate the formation of array which exactly corresponds to the structure shown in Figure III-6 (b).

a)   b)   c)
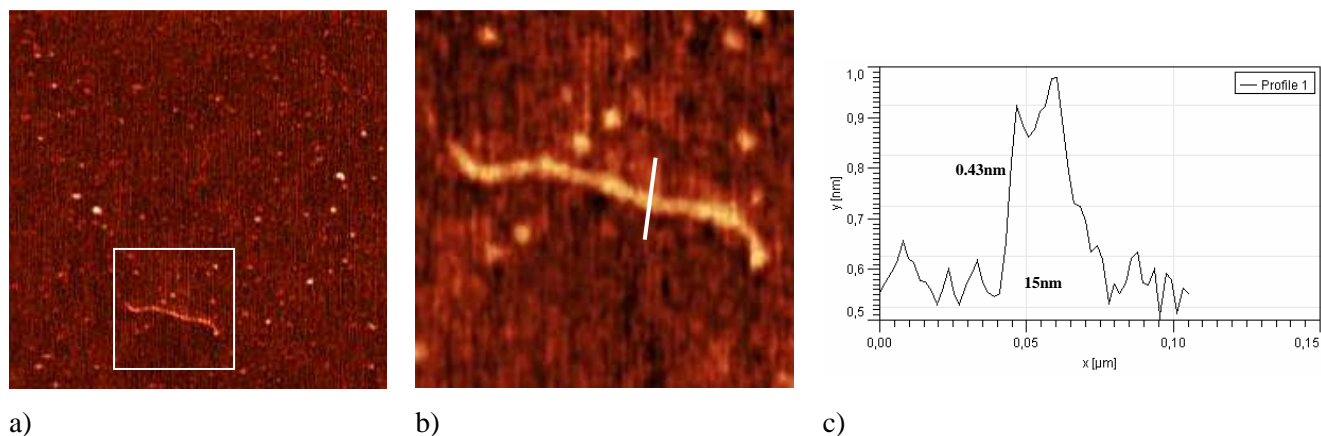
Figure III-13. Arrangement of X1+20 bases mixture in air on non pretreated mica, deposition time t = 10min; a) Topography image of 2x2µm; b) zoom in the marked area of image (a) 0.3x0.3µm; c) cross-section of the macromolecule in the marked area of image (b).

Further observation of deposited X1+20 bases structures gave the same results. No filament and no branched structures were observed with the X1+20bases mixture on non-pretreated surface of mica (Figure III-14a). Macromolecule with similar parameters (length of 140nm, height and thickness of 0.68nm and 13.8nm respectively) was observed (Figure III-14b, c) which indicates a molecular assembling in a small network as shown in Figure III-6(b). In addition, the surface density of the deposited X1+20bases was really low in comparison with that of X1+X2 and Y1+Y2 structures.
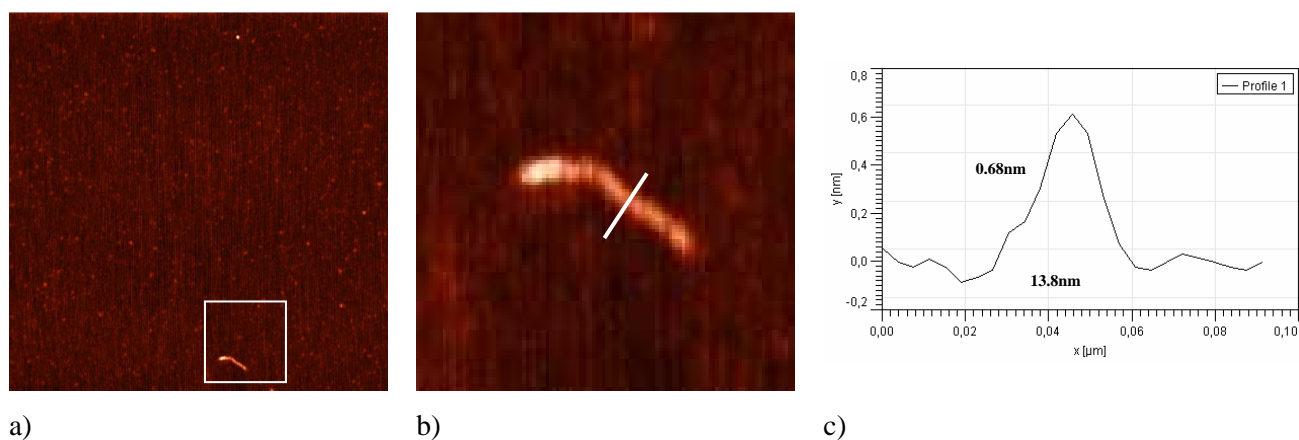

a)   b)   c)

Figure III-14. Arrangement of X1+20 bases mixture in air on non pretreated mica, deposition time t = 10min; a) Topography image of 2x2µm; zoom in the marked area of image (a) 0.3x0.3µm; c) cross-section of the macromolecule in the marked area of image (b).

II-1-3-2 Study on NiCl^{2+} pretreated mica surface

<u>X1+X2 structures</u>

The pretreatment of the mica surface with NiCl^{2+} cations changes drastically the molecular arrangement of the deposited mixtures. As can be seen in Figure III-15(a), the density of the deposited structure is considerably higher than on non pretreated mica, for the same time of deposit 10min (Figure III-9a). Furthermore, the chemical pretreatment leads to the juxtaposition of a large number of deposited molecules, which suggests that the electrostatic interaction between molecules and substrate was increased limiting the diffusion of molecules on the surface.
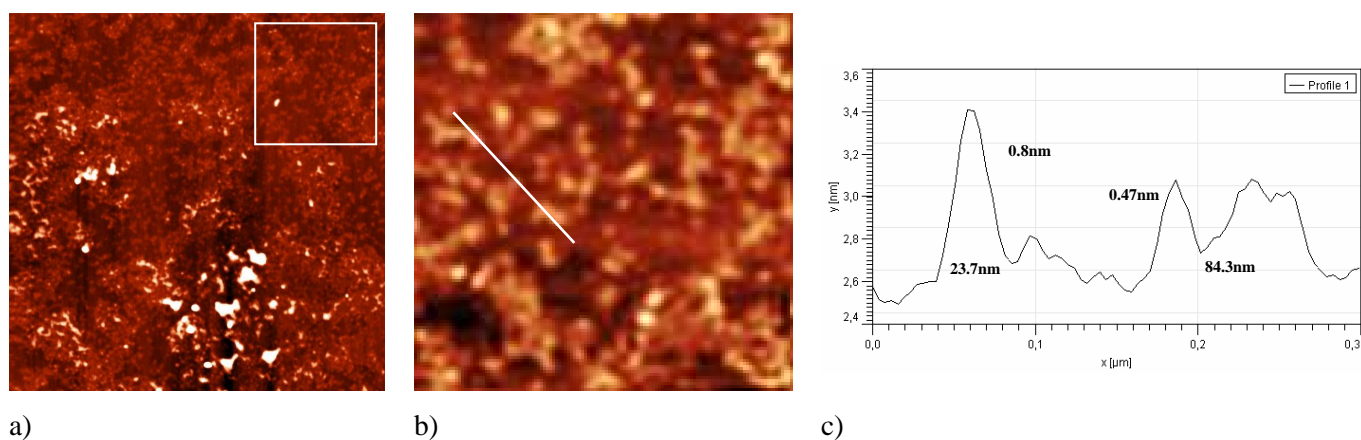

a)   b)   c)

Figure III-15. Arrangement of X1+X2 mixture in air on pretreated mica, deposition time t = 10min; a) Topography image of 2 µm x2µm; Zoom in the marked area of image (a) 0.5µm x0.5µm; c) cross-section of the macromolecule in the marked area of image (b).

A close look at the arrangement of the deposited structures in Figure III-15(a) reveals that among overlapped structures there is large number of small fragments with branched geometry. In addition, it is clearly shown that the strong DNA/substrate interaction also leads to the formation of molecular dendritic aggregates on the surface as can be seen in Figure III-15(b).

<u>Y1+Y2 structures</u>

As in the case of non pretreated surface (Figure III-11a), Y1+Y2 structures are generally assembled in small fragments (Figure III-16a) with comparable surface density, on chemically modified mica. However, these fragments have complex geometry with several branches and do not have a linear structure as observed in Figure III-11(a). Their typical dimensions are 65nm of length and they are homogenous in height ~1.4±0.1nm. This indicates that they arrange in linear structures with double double-stranded linkages between Y1 and Y2 molecules.

Rarely, among the small fragments, large macromolecule with branched structure can be observed (Figure III-16b). This assembly of molecules contains several bifurcation points which make large loop in

the central part of the structure and some smaller loops at its periphery. The macromolecule has a lateral dimension of ~500nm, and a vertical dimension of ~400nm. The height is quite homogenous and is around 1.5 nm, whereas the thickness varies from 4 nm to 30nm indicating the presence of 1D and 2D types of molecular assembling (Figure III-16c).
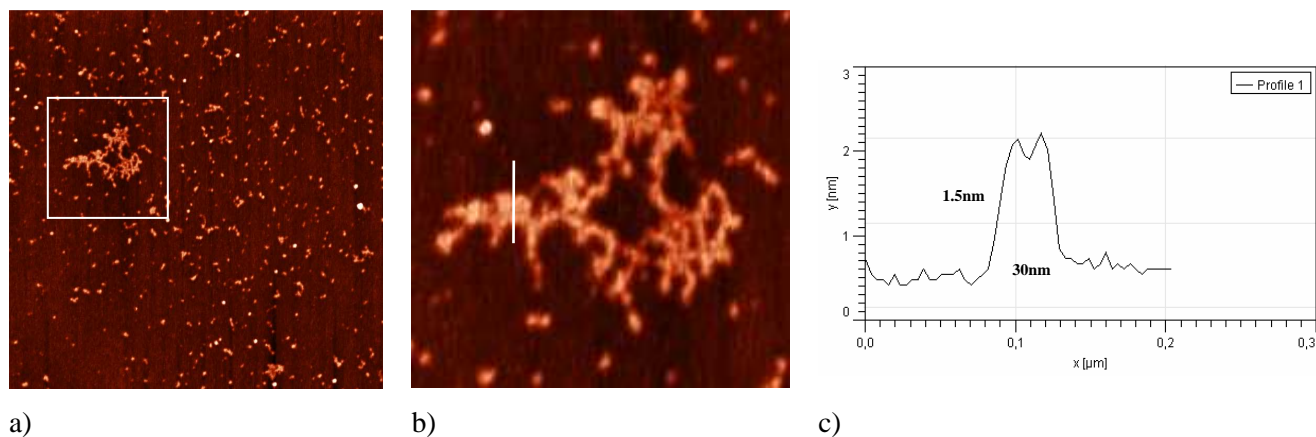

a)   b)   c)

Figure III-16. Arrangement of Y1+Y2 mixture in air on pretreated mica, deposition time t = 10min; a) Topography image of 2x2µm; b) zoom in the marked area of image (a) 0.5x0.5µm; c) cross-section of the macromolecule in the marked area of image (b).

Another example of the Y1+Y2 molecular assembling is shown in Figure III-17. In this case, small fragments do not form branched structures, but only linear structures with lengths between 8-112nm as on non pretreated mica surface (Figure III-11). Among these structures, a more complex macromolecule was found (Figure III-17b). This structure with a length of 466nm has a worm-like geometry with one bifurcation point which makes a loop in the bottom part of the molecule. As it can be seen from Figure III-17(c), height and thickness of the macromolecule are of 0.47nm and 2nm respectively, which is smaller than the sizes of the surrounding fragments (1.4nm and 4nm respectively).
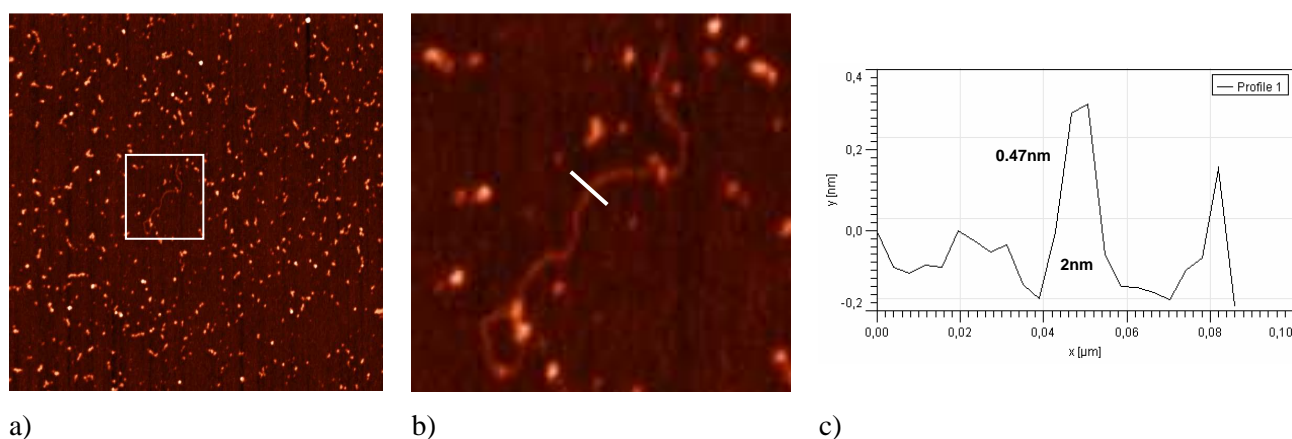

a)   b)   c)

Figure III-17. Arrangement of Y1+Y2 mixture in air on pretreated mica, deposition time t = 10min; a) Topography image of 2x2µm; b) zoom in the marked area of image (a) 0.4x0.4µm; c) cross-section of the macromolecule in the marked area of image (b).

146

Except in the bifurcation region (upper right part of the loop), the height and the thickness of the macromolecule are quite homogenous. This seems to indicate that only one type of molecular assembling is presented: the single double-stranded linear linkage.

Observed thickening in the tail of the macromolecule (from 0.4 to 0.9nm) is not fused in a structure as for the bifurcation region case. This latter can be related to the juxtaposition of a small double double-stranded molecular fragment onto the "tail" of the macromolecule.

X1+20 bases structures

On treated mica, the mixture of X1+20bases exhibited no or few fragments, as well as in the case of the deposition on non pretreated mica (Figure III-18a). However, among several scanned areas, a more complex structure was found, which is presented in Figure III-18b. This macromolecule shows two small and one large loop with a small tail, and has a lateral size of ~70nm and a vertical size of ~110nm. Taking into account these parameters together with the thickness of 7.8nm, it can be concluded that this molecule corresponds to a 2D assembling with a single double stranded linkage.
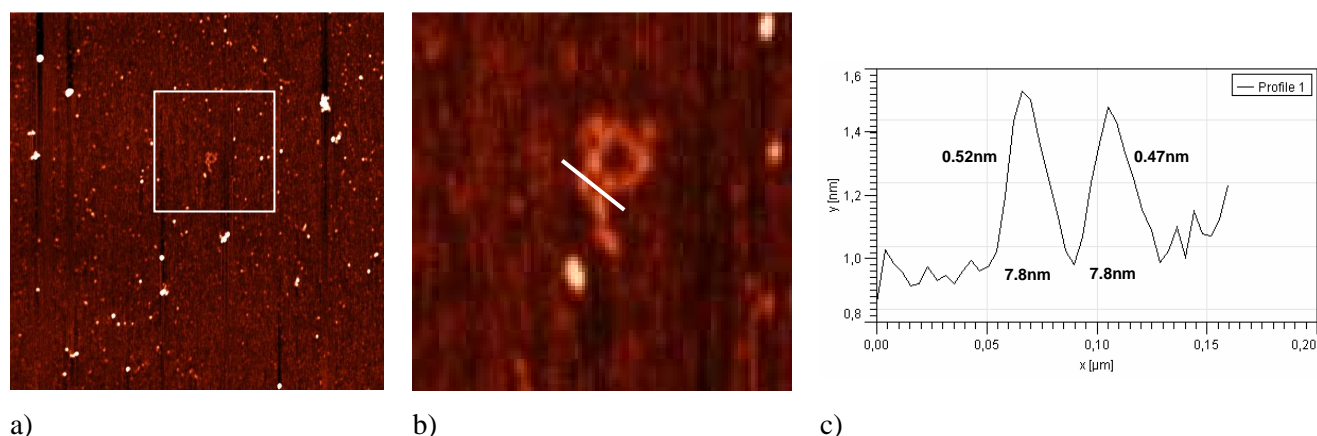

a)   b)   c)

Figure III-18. Arrangement of X1+20bases mixture in air on pretreated mica, deposition time t = 10min; a) Topography image of 2x2µm; b) zoom in the marked area of image (a) 0.2x0.2µm; c) cross-section of the macromolecule in the marked area of image (b).

Another macromolecule with a curled geometry was observed (Figure III-19a). This linear structure with length of 415nm has a height and a thickness of 0.33nm and 8.9nm respectively (Figure III-19c), quite similar to the previously described structure in Figure III-18(b). This macromolecule can also be described by a 2D assembling with a single double stranded linkage.
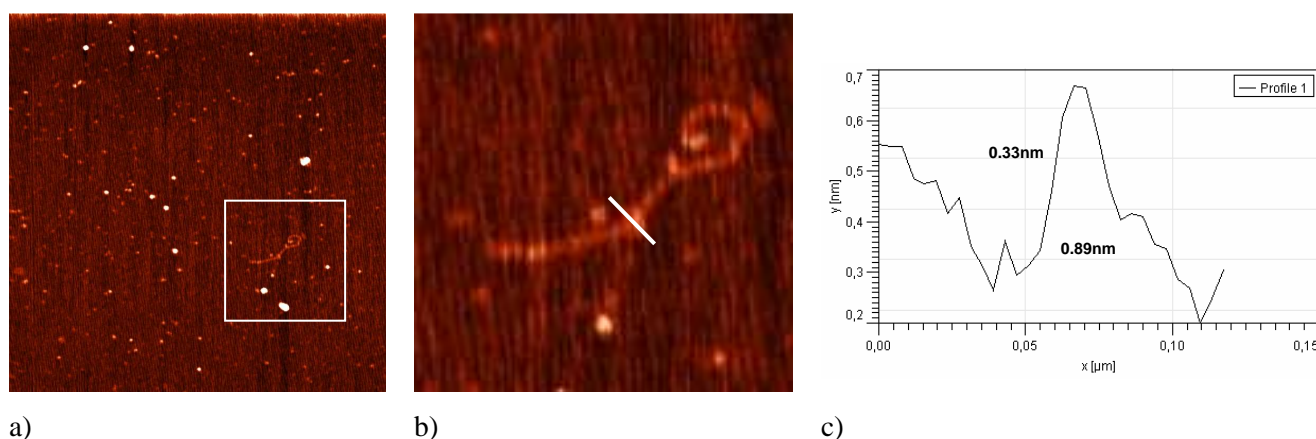
Figure III-19. Arrangement of X1+20bases mixture in air on pretreated mica, deposition time t = 10min; a) Topography image of 2x2µm; b) Zoom in the marked area of image (a) 0.3x0.3µm; c) cross-section of the macromolecule in the marked area of image (b).

II-1-4 Conclusion

This first AFM study of the structure assembly revealed the ability of each mixture to be arranged in different structures under ambient conditions, in air. It also demonstrates that the pre-treatment of the mica to facilitate the adsorption of structures, induces an effect in the organization of the structures on the mica.

Typically, on the non pretreated mica X1+X2 and Y1+Y2 mixtures generally formed small molecular fragments with double double-stranded structure and more rarely, worm-like large macromolecules with single double-stranded structure. Exceptionally, X1+X2 mixtures were observed to be assembled in complexes with combined 1D and 2D structures. On the contrary, X1+20bases mixture exhibited no branched structures neither small fragments on non pretreated mica. Rare straight molecules are visible at some places of the surface.

The $NiCl^{2+}$ pretreated mica provides the observation of numerous branched small fragments for the X1+X2 mixture and rare branched fragments for the Y1+Y2 mixture. Furthermore, large macromolecules have branched geometry with 2D structure and not worm-like 1D structure as on non treated mica (except one case for Y1+Y2 mixture). However, the pre-treatment does not affect significantly the arrangement of X1+20bases molecules, only a change in their conformation from straight to curled and loop-like was observed without any branching. The influence of pretreatement of mica on molecular organization suggests an important hypothesis. The $NiCl^{2+}$ treatment, increased the DNA/substrate interaction force, and then decrease the diffusion of species on the mica surface. One can consider that structures were "frozen" right after deposition, they remained at the same place where they were deposited. In the contrary, on non -treated mica, thermal energy of deposited molecules may exceed the DNA/substrate interaction, which is lower and can break intermolecular linkages. Diffusion is also possible. This can explain why complex branched architectures are observed on pretreated mica and more simple non branched structures on freshly cleaved mica. So, thermodynamical processes take place on non treated mica surface leading to a molecular reorganization of the initial DNA assembling.

II-2 Observation in Liquids

II-2-1 Experimental AFM conditions

AFM in liquid media was performed in a closed liquid cell equipped by a temperature controller (NT-MDT) which allows keeping the temperature at a set level with high accuracy (0.01°C). The liquid cell has increased volume and is hermetically closed with a silicon polymer membrane that ensures a complete limitation of evaporation of the liquid during experiment. Furthermore, such design provides additional protection from external acoustic noise. Figure III-20 presents a photo of the microscope cell with the membrane.
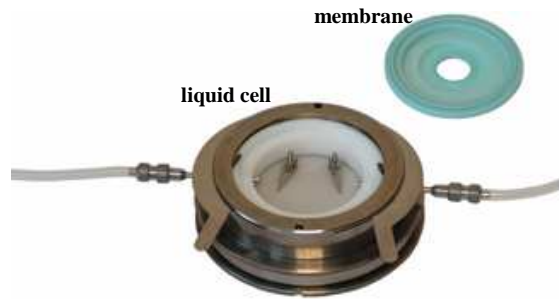

Figure III-20. Photo of the liquid cell with the membrane (NT-MDT)

Imaging was carried out using so called "hard tapping" mode where experimental A_{SP}/A_0 ratio was of 33-35% for chosen free amplitudes A_0 ranging between 15-20nm and working amplitudes A_{SP} = 5-7nm. Scanning of samples was performed with a rate between 0.8-0.9Hz when the cantilever was excited at its resonant frequency f_0 = 17-20kHz with relatively high quality factor Q ranging between 70 and 80, not typical in liquid. We used rectangular cantilevers with stiffness k = 0.025N/m and typical tip curvatures of 10nm.

AFM experiments were realized at the temperature T = 25°C in two solutions: Tris buffer (tris(hydroxymethyl)aminomethane) and HEPES buffer (*4-(2-hydroxyethyl)-1-piperazineethanesulfon acid*). The Tris buffer was chosen because in this solution, all DNA-based mixtures were supposed to be hybridized. The HEPES buffer was chosen for comparison and because it is often used in AFM imaging of DNA.

In all experiments, DNA-based mixtures were deposited onto $NiCl^{2+}$ pretreated mica because otherwise imaging was not possible due to the weak attachment of molecules onto substrate.

II-2-2 Deposition of mixtures onto pretreated mica surface

The mica was pretreated following exactly the same protocol as the one presented in paragraph II-1-2-2. Then, the mixtures were immediately, deposited following the dropping method previously described in paragraph II-1-2-1 but with some changes:

-   cdeposition from a drop of 2µL of the corresponding solution, using a micropipette,
-   incubation in air during 5min,
-   rinsing with the buffer solution,
-   keeping the sample immersed in the buffer solution.

The deposition was performed in ambient conditions with a drop of 2µL of the hybridized mixture using a standard micropipette. In order to prevent the drop from dryness, the deposition time was 5min. Once the sample was sufficiently incubated, the non adsorbed molecules were removed from the surface by rinsing with Tris or HEPES buffer. Rinsing was performed by using of 0.5mL of appropriate buffer solution, which was accurately dropped on the vertically placed mica surface in order to let the solution flow down under gravitational force.

After rinsing samples were immersed in the same type of solution with which they have been rinsed. Then, totally wet samples were placed in the AFM liquid cell filled with the appropriate liquid:

- Tris HCl 20mM + $MgCl^{2+}$ 10mM pH=7.2,

- HEPES 10mM + $NiCl^{2+}$ 1mM pH=7.2.

Keeping the samples in solution after rinsing avoids the use of intermediate liquid (like deionized water) and prevents molecular architectures from dryness. In the case of the Tris buffer, it makes possible AFM observation in an environment in which they were hybridized. In the case of the HEPES buffer, it is interesting to observe the molecular assembling in a solution different from the hybridized ("mother") solution but with an excess of $NiCl^{2+}$ ions.

II-2-3 AFM Imaging in the Tris buffer solution

X1+X2 structures

The deposition of X1+X2 mixture during 5min leads to the formation of structures with dendrimer-like boundaries which are connected with each other by thinner structures into one large network. A typical AFM image of the network is presented in Figure III-21(a). The network is more visible in the phase image (Figure III-21b), showing a clear compositional separation between mica substrate and deposited X1+X2 molecules (see chapter I).
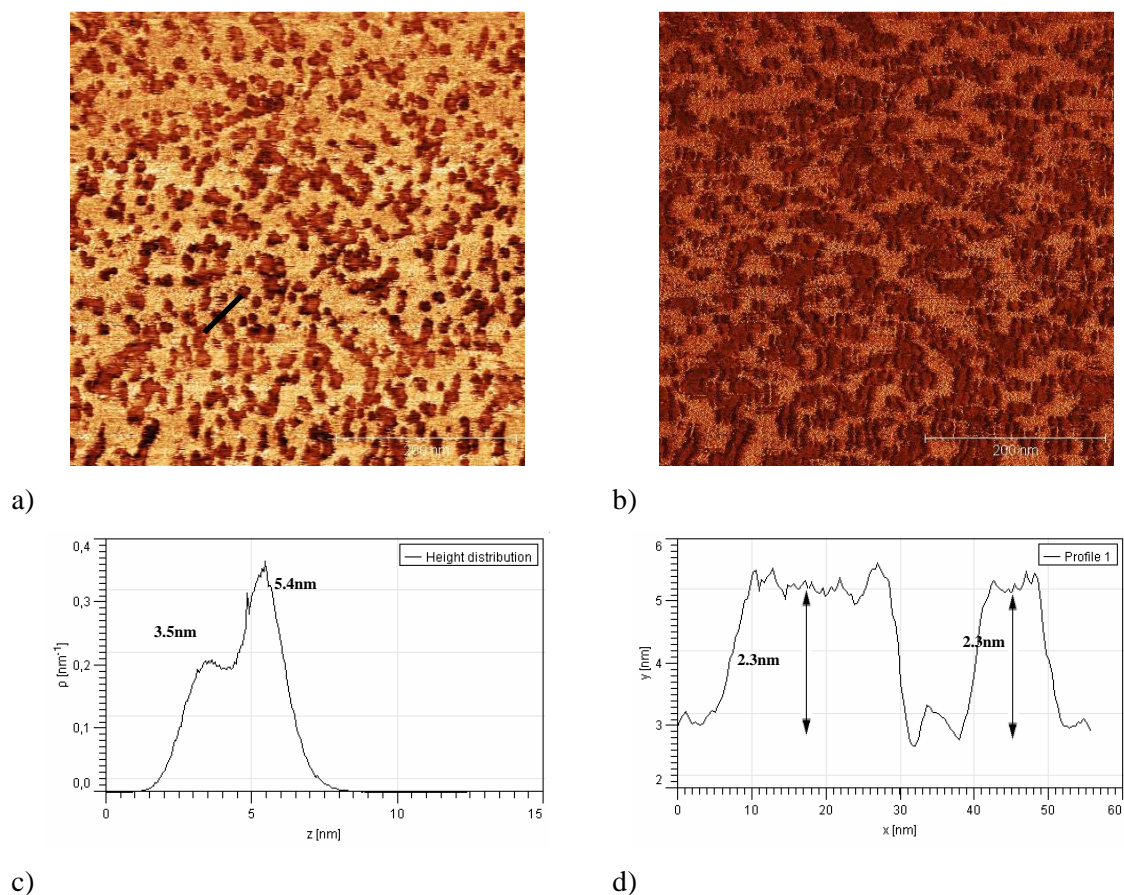
a)

b)

c)

d)

Figure III-21. Arrangement of X1+X2 mixture in Tris on pretreated mica, deposition time t = 5min;

a) Topography image of 500x500nm; b) respective phase image of 500x500nm;

c) histogram of the height distribution d) cross-section relative to the black line in (a).

There is no evidence of a preferred direction in the orientation of the dendrimers. However, their size is always larger than the space between them.

The network in Figure III-21(a) present a flat on the top surface. Its homogenous height along the whole surface indicates that the two-dimensional X1+X2 structures are well levelled, on the mica surface. The histogram of the height distribution (Figure III-21b) shows two peacks: a small one centred on $h_1 = 3.5nm$ and a high one centred on $h_2 = 5.4nm$. The difference between them gives the mean height of the network h = 1.9nm, which approximately corresponds to the DNA diameter and which indicates that this network is a monomolecular layer of assembled X1+X2 molecules.

A punctual measurement of the height give a slightly larger height of 2.3nm as can be seen on the cross-section profile (Figure III-20c). It is in agreement with the mean height value and the good homogeneity of the monomolecular layer.

<u>Y1+Y2 structures</u>

In the same deposition conditions, the Y1+Y2 mixture exhibits the formation of a network which almost completely covers the mica surface. Unlike the X1+X2 assembling, the Y1+Y2 molecules do not form dendrimer-like structures but a large layer perturbed by small holes of around 14nm in diameter at some places.
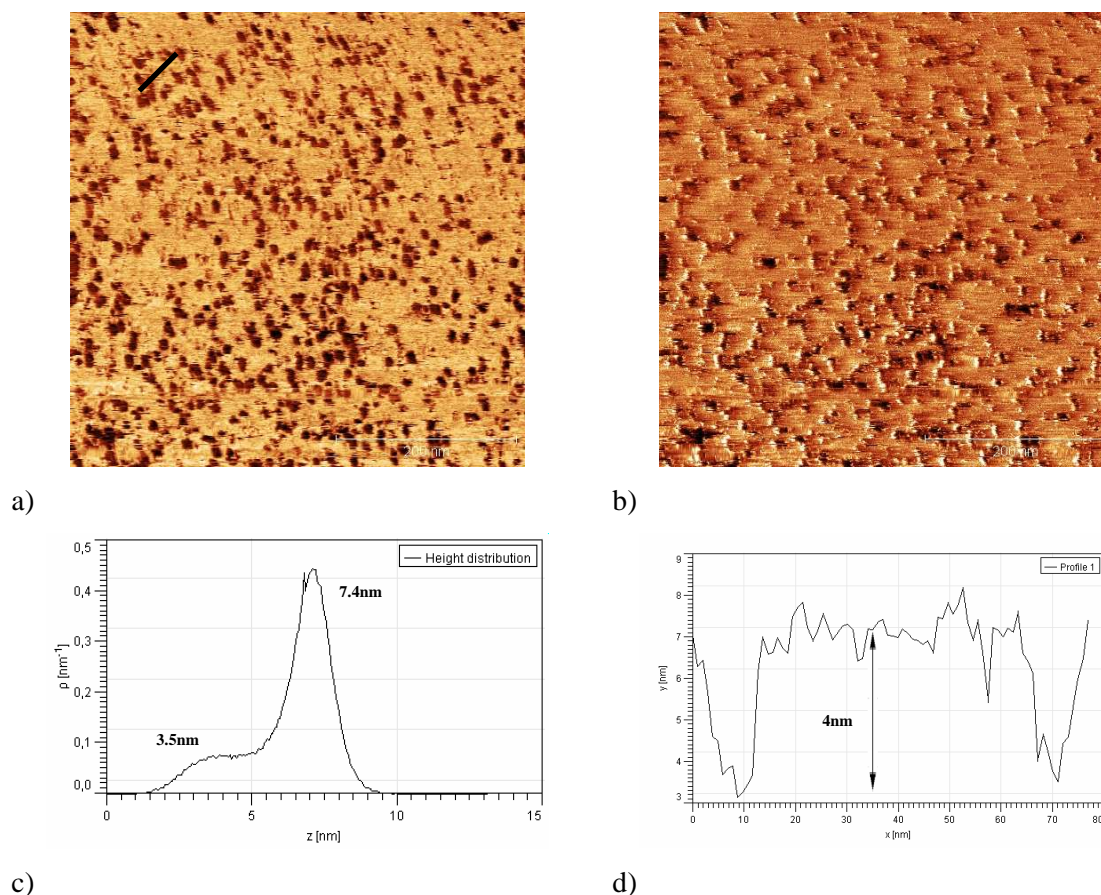

a)   b)

c)   d)

Figure III-22. Arrangement of Y1+Y2 mixture in Tris on pretreated mica, deposition time t = 5min;

a) Topography image of 500x500nm; b) Respective phase image of 500x500nm;

c) Histogram of the height distribution d) Cross-section relative to the black line in (a).

Figure III-22 (a, b) depict a flat surface of well levelled Y1+Y2 structures. In Figure III-22(c), the histogram presents two picks centred on $h_1 = 3.5\pm0.5$nm and $h_2 = 7.4\pm0.2$ nm which correspond to a mean height of $h = 3.9\pm0.5$nm. This means that the visible surface in Figure III-21(a) is the upper layer of a double-layered Y1+Y2 network. The cross-section in Figure III-22(d), gives local heights of around 4nm in agreement with this average height value.

X1+20bases structures

The X1+20bases does not exhibit a large flat surfaces but a more complex network, composed of dendrimer-like structures of non regular sizes separated from each other by numerous small holes (Figure III-23a). The phase image gives the same information with probably a better resolution inside the structure (Figure III-23b). The histogram in Figure III-23(c) presents a broadened peak centred on 11.8 ±0.2 nm, beginning at around 5nm which is representative of the juxtaposition of several structures, even up to 4 monolayers. The shape of the peak is also characteristic, it is enlarged on the low z values, which means that the image is dominated by the top layer but there are some information about structures above this layer. On the cross-section in Figure 22(d), a local height measurement of 3-4 monolayers is obtained.
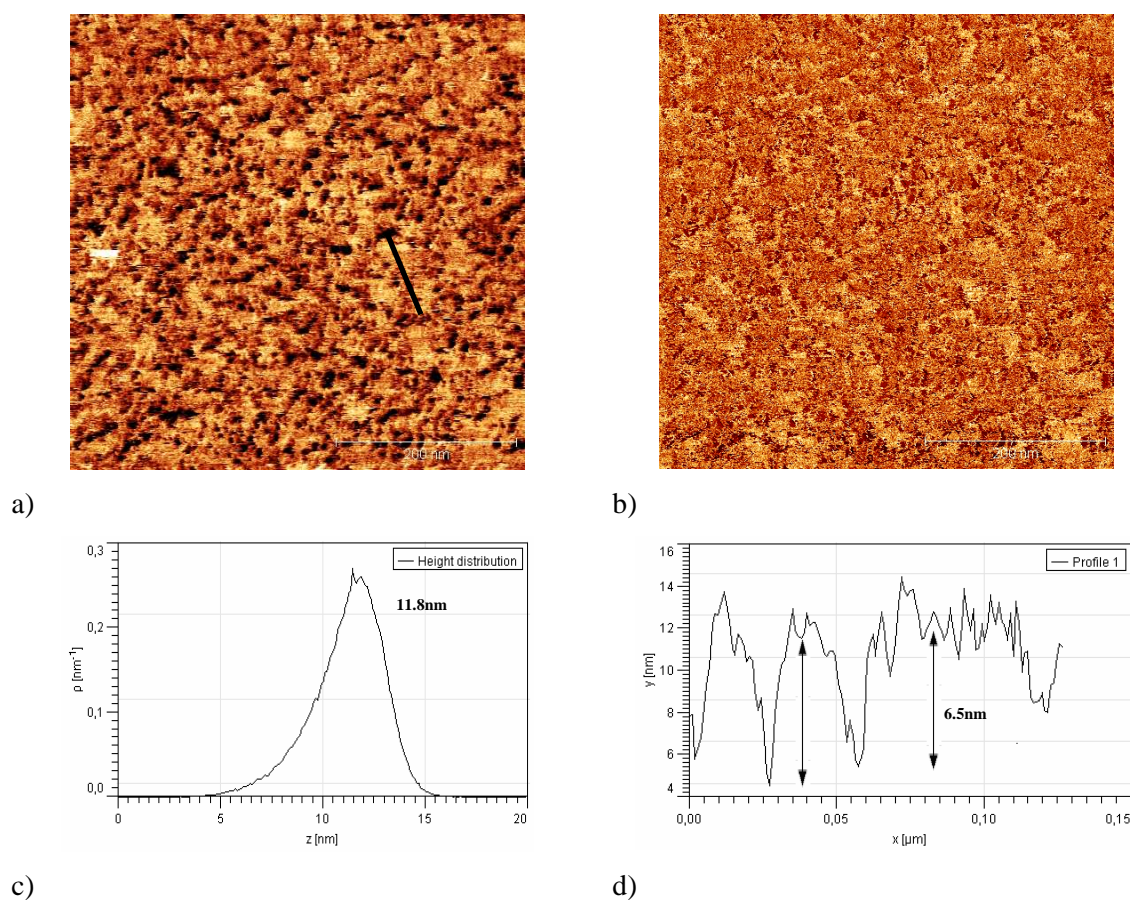

a)

b)

c)

d)

Figure III-23. Arrangement of X1+20bases mixture in Tris on pretreated mica, deposition time t = 5min;
a) Topography image of 500x500nm; b) respective phase image of 500x500nm;
c) histogram of the height distribution d) cross-section relative to the black line in (a).

II-2-4 AFM imaging in the HEPES buffer solution

X1+X2 structures

Elongated dendrimer-like structures are present densely on the surface (Figure III-24a). The phase image reveals the presence of 2 different zones, the dark one corresponds to the background and the bright one nearly to the higher features on Figure III-24a. In fact, this image shows that the dendritic islands present straight step edges, which sometimes extend into filaments connecting to other islands. There is no evidence of a preferred direction in the orientation of the dendrimers, they are randomly distributed on the surface.
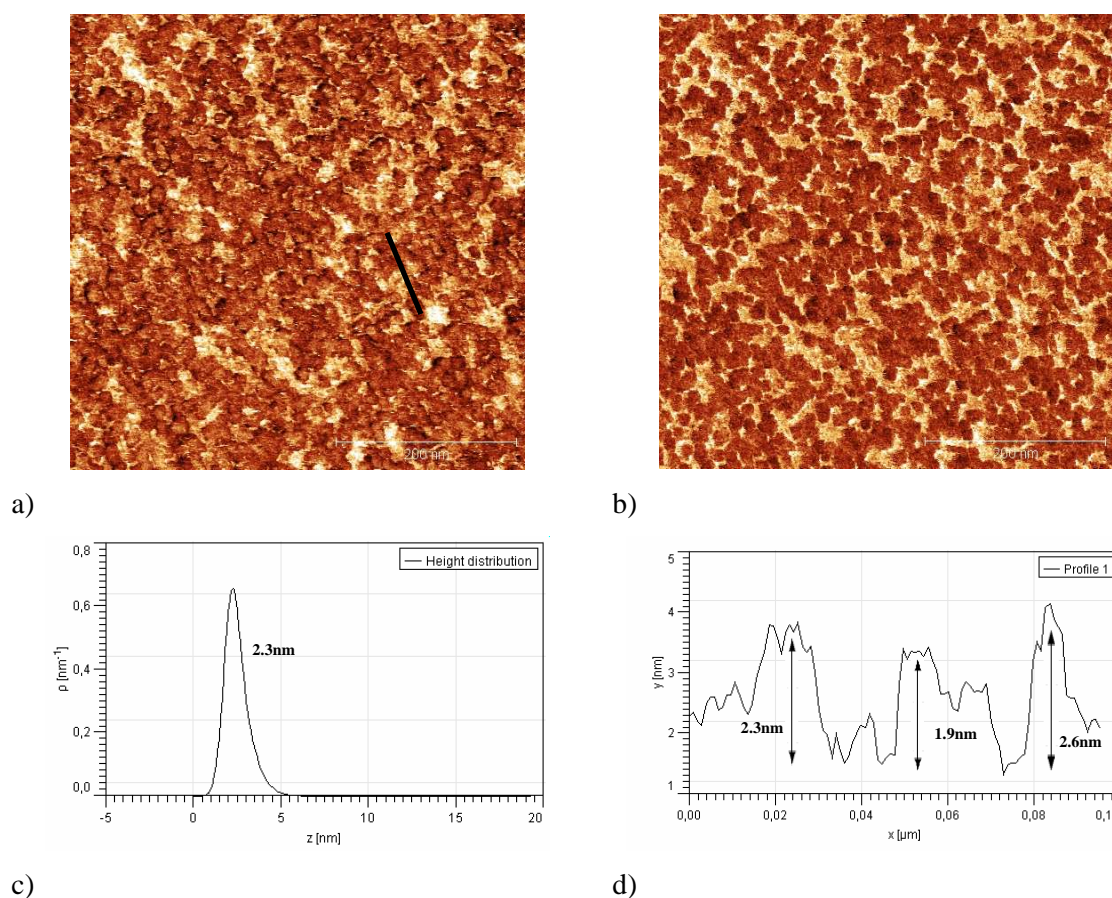

a)   b)

c)   d)

Figure III-24. Arrangement of X1+X2 mixture in HEPES on pretreated mica, deposition time t = 5min;
a) Topography image of 500x500nm; b) Respective phase image of 500x500nm;
c) Histogram of the height distribution d) cross-section relative to the black line in (a).

The height histogram presents one thin peak centred on 2.3±0.1nm slightly broadened on the right part, indicating the beginning of another peak difficult to situate (Figure III-24c). The roughness given by the cross-section image is in agreement with a monomolecular layer but the assembling seems to be less organized than in the case of the same mixture in Tris (Figure III-24d). The topographic image does not reveal so clearly a 2D behaviour, only some rounded holes randomly dispersed.

Another example of X1+X2 assembling is shown in Figure III-25. The topographical image is more constrasted and shows the presence of 2D dendritic structures connected, at some places, by filaments. Three different levels of color can be distinguished on the image in Figure III-25a, and on the zoom in Figure III-25b. The first dark level is the background, the second level the mean color of the filaments and 2D structures and the third color, brighter is present on top of some filaments and structures.
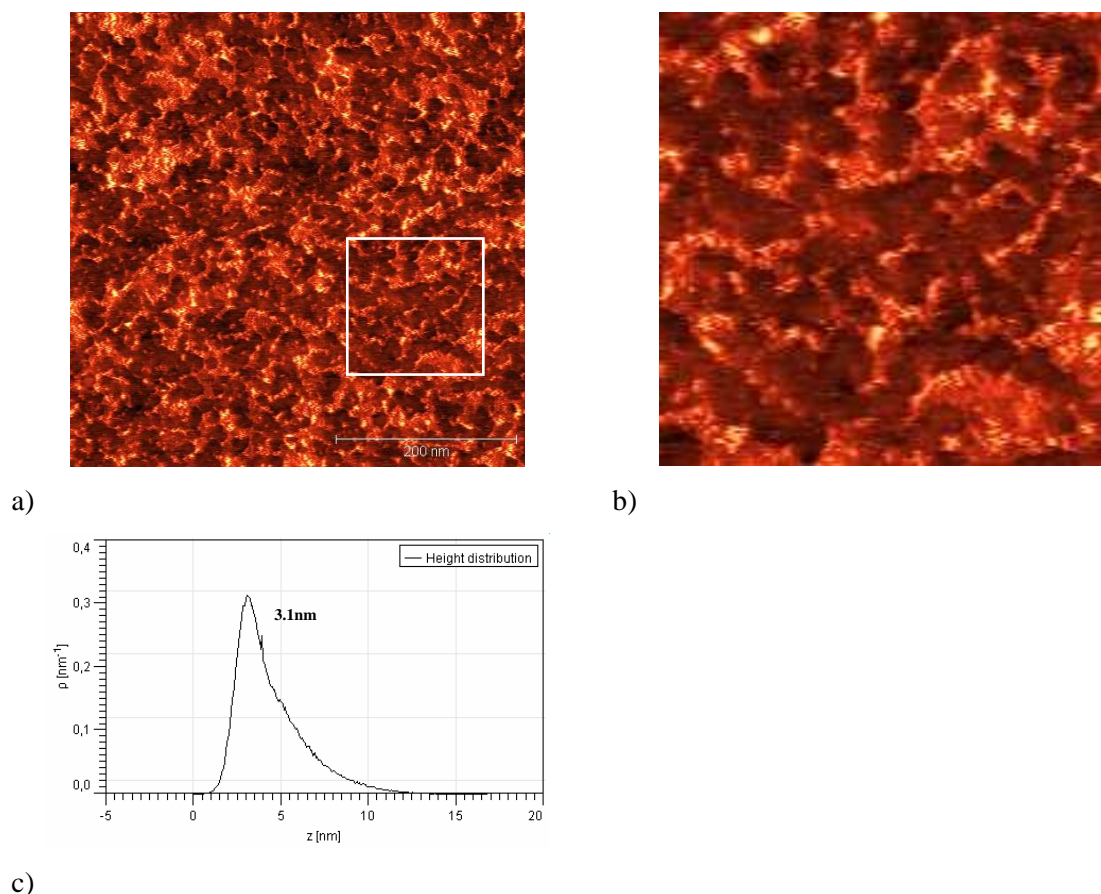

a)

b)

c)

Figure III-25. Arrangement of X1+X2 mixture in HEPES on pretreated mica, deposition time t = 5min;
a) Topography image of 500x500nm; b) Zoom in the marked area of image (a) 150nmx150nm;
c) Histogram of the height distribution

This is in good agreement with the shape of the histograms. On Figure III-25c, the histogram is centred on 3.1±0.2nm with a height distribution which starts around 1 nm this indicates a level of 2.1±0.2nm. The peak is enlarged on the right, a second peak is forming centred around 5±0.5nm and a third one is also forming further. Once again the structures present straight step edges, filaments have a stick shape with no preferential orientation. It seems that the assembly of the structures is also 2D, like in the Tris solution, but the layer is less complete for the same concentration and less organized. Moreover, a second layer appears at some places.

<u>Y1+Y2 structures</u>

Like in the Tris solution, the Y1 and Y2 molecules are more densely arranged, than the X1+X2 structures, in the HEPES solution (Figure III-26a). Obviously, three different level of colours are observed on the image of Figure III-26a and the zoom of Figure III-26b. the dark color corresponds to the background inside the holes, the intermediate color depicts a kind of mesh-like structure, with a lot of filaments, and the bright color, some higher isolated filaments and 2D higher part of the mesh. Figure III-26b reveals that, at some places, the mesh is composed of perpendicular filaments as can be seen inside the white circle of Figure III-26b. The histogram begins around 2nm and is centred on 4 nm, which indicates that a monomolecular layer is obtained, the intermediate color mesh. The peak is enlarged with a second peak around 6 nm, this corresponds to the start of the second monolayer height mesh.

a)   b)

c)   d)

Figure III-26. Arrangement of X1+X2 mixture in HEPES on pretreated mica, deposition time t = 5min;
a) Topography image of 500x500nm; b) Zoom in the marked area of image (a) 170x170nm^2;
c) histogram of the height distribution d) cross-section relative to the black line in (a).

;

It is clear that the assembly is less organized in the HEPES than in the Tris, the first layer is a mesh with a lot of holes and not a quasi complete monomolecular layer. The cross section in Figure III-26d shows the presence of holes of different depth, between structures.

The X1+20 bases mixture presents a very different assembly in HEPES than the other structures. The topography seems to be dominated by small rounded islands of ~ 15±0.5nmin diameter (Figure III-27a). They constitute a repeating pattern and cover mostly all the surface. Even when they joint each other, they can be individually identified. This small island is the elementary building block of the arrangement, no filaments are observed to connect islands. The phase image (Figure III-27b) does not provide of a contrast between deposited structures and the substrate.

However, the height histogram in Figure III-27(c) shows the mean height of 2.9nm which does not correspond to thickness of a double layer structure (it should be around 4nm). It can be explained by the fact that due to the dense structure of the background layer the surface of mica is not accessible and consequently it was possible to measure the height of only the second layer.

On the other hand, the cross-section (Figure III-27d) shows that height of X1+20bases architectures actually varies between 2.3nm and 3.2nm. This indicates that not all structures were successfully levelled during deposition.

a)

b)

c)

d)
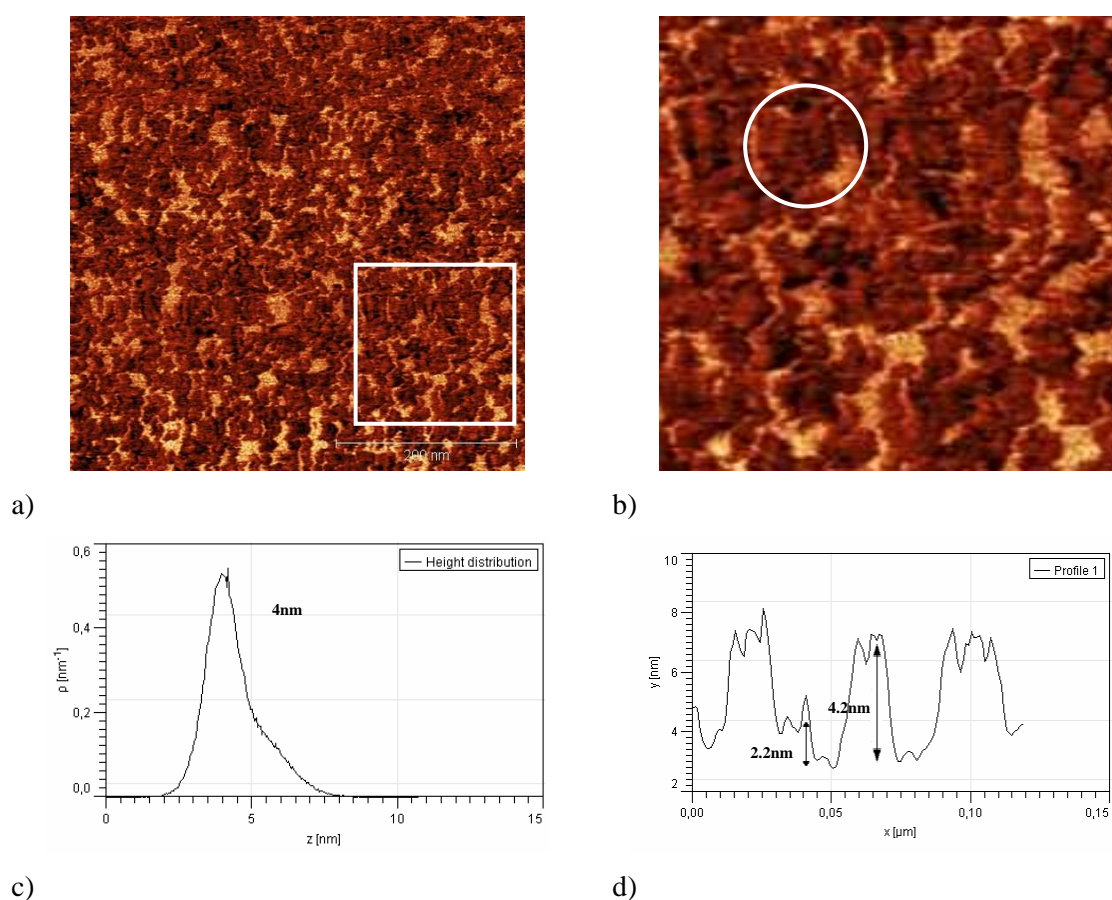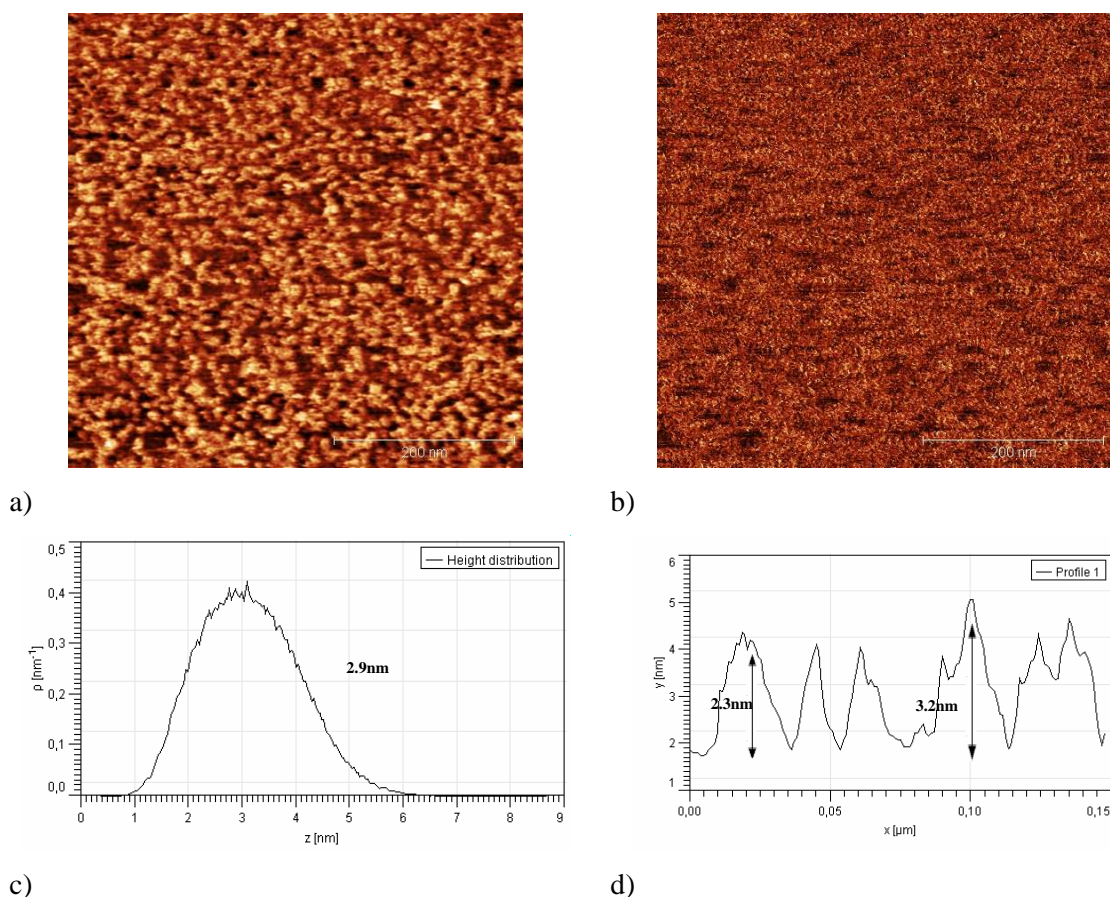
Figure III-27. Arrangement of X1+20bases mixture in HEPES on pretreated mica, deposition time t = 5min;
a) Topography image of 500x500nm; b) respective phase image of 500x500nm;
c) histogram of the height distribution d) cross-section relative to the black line in (a).

II-2-5 Conclusion

The AFM study of the X1+X2, Y1+Y2 and X1+20bases mixtures reveals their different arrangement in Tris and HEPES buffer solutions.

In the Tris solution, all mixtures exhibit a denser architecture with well levelled surfaces in comparison with structures observed in the HEPES solution. More precisely, the structures X1+X2 and Y1+Y2 tend to arrange in compact networks, dense monomolecular layers with few holes at some places, in the Tris buffer solution. They form less dense networks, some kind of mesh-like structure where 2D features present straight step edges and are connected by stick-like filaments.

The X1+20bases mixture present a different arrangement on the surface. In the Tris solution, it seems that there is no organisation on the surface, with a lot of holes of several monolayers in depth.

In the contrary, some small islands of 1 ML high randomly dispersed on the substrate are observed in the HEPES solution. They are not connected by filaments but juxtapose to each other to form the assembling.

The Tris buffer is the solution in which all mixtures were hybridized. The Tris or HEPES buffer solutions are the solution in which structures are maintained for AFM observation. In consequence, it was shown that HEPES buffer modifies the molecular arrangement of the already deposited structures.

In HEPES buffer, the molecular assembly is modified due to the change of the ionic strength of the solution. In other words, it means that the molecular reorganisation takes place even after the deposition on the pretreated mica.

It seems that the Tris buffer favors the homogeneity of the layers compared to the HEPES due to the interaction of the DNA molecules to each other, greater than their interaction with the mica surface. This is due to the fact that the Mg^{2+} cations, present in the Tris solution, have a higher affinity with the DNA molecules than with the mica. Moreover, Ni^{2+} cations have a higher affinity with muscovite mica than with DNA.

In addition, Mg^{2+} and Ni^{2+} cations have different ionic strengths in Tris and HEPES buffers. One should remember that, the ionic strength of a solution is a measure of the intensity of the electric field created by ions in the solution [65]. The ionic strength can be calculated according to the following expression:

$$I = \frac{1}{2}\sum_i z_i^2 n_{bi}$$
(eq.3.15)

Then, the ionic strength of Mg^{2+} in Tris buffer, I $MgCl^{2+}$ = 20mM and Ni^{2+} in HEPES buffer, I $NiCl^{2+}$ = 2mM in our experimental conditions.

Thereby, after immersing the samples in HEPES, the ionic strength of the solution decreases. This may lead to a decrease of the interaction between DNA and mica. Furthermore, a competition between Ni^{2+} and Mg^{2+} cations occurs which probably leads to a partial substitution of already adsorbed cations of Mg^{2+} by Ni^{2+} cations. This leads to the disruption of previously formed bonds between surface of mica and DNA

molecules. As a result, structures observed in HEPES are less dense than the one observed in the Tris solution. Molecules can not be well aligned on the surface due to their increased bonding with mica throw Ni^{2+} cations.

Observed in both solutions, double-layer (or more) structures suggest that interlayer interactions have electrostatic origin. Otherwise, if these structures were bonded to each other only by physical adsorption, then the upper layers should have been washed away during rinsing procedure. Consequently, the existence of such structures can be explained by the formation of salt bridges between juxtaposed layers, favoured by Mg^{2+} cations in Tris and by Ni^{2+} cations in HEPES.

By comparing the structures observed in air and in liquid, we can conclude that both liquids induce a 2D organisation of the DNA-based mixtures and that isolated filaments, sometimes worm-like wired structures, are only present in air. It is noticeable that it was difficult to observe structures in air, especially on non treated mica. It seems that in air, DNA-based networks are not stable and the few that have been observed remain in a dendritic structure on treated surface or a linear macromolecule on fresh mica.

In order to have a clear idea of how exactly the molecules are associated with each other, a 3D molecular model was built using a software for chemical simulation Schrödinger® (Figure III-28). This model was created for X1 and X2 molecules, hybridized in a linear double double-stranded chain. For X1+X2, Y1+Y2 and X1+20bases mixtures, the number of DNA bases is the same, so the geometrical parameters of this 3D structure are also relevant for other mixtures.
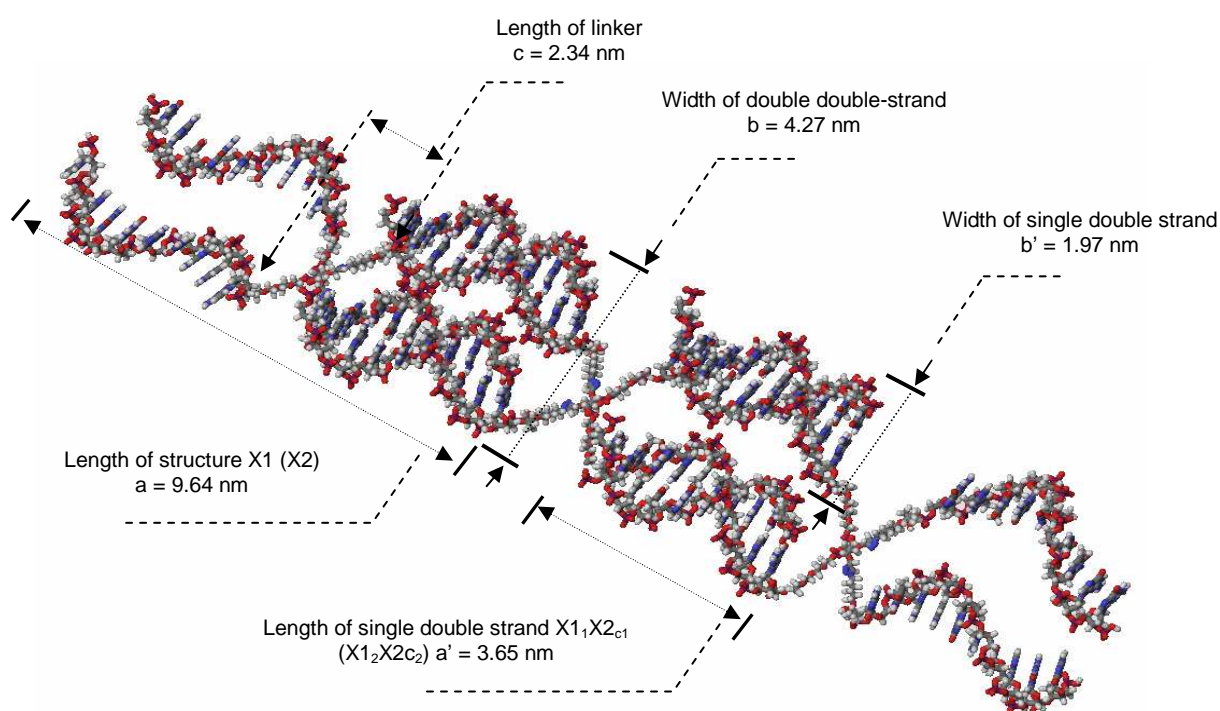

Figure III-28. Molecular 3D model for X1 and X2 molecules hybridized in linear double double-stranded chain.

According to the model in Figure III-28, the length of one X1 or X2 molecule (or Y1/Y2) is of 9.64 nm with a width of 4.27nm and a linker length of 2.34nm. The length and diameter of single double-strand are 3.65nm and 1.97nm, respectively.

It becomes possible to better understand how molecules are assembled with each others, by comparing the simulated 3D structure with the theoretically calculated molecular associations (Figures 4, 5, 6), and also, by taking into account geometries of observed structures. Models of the structures presented on Figure III-29a and b are proposed on Figures 29c and d.
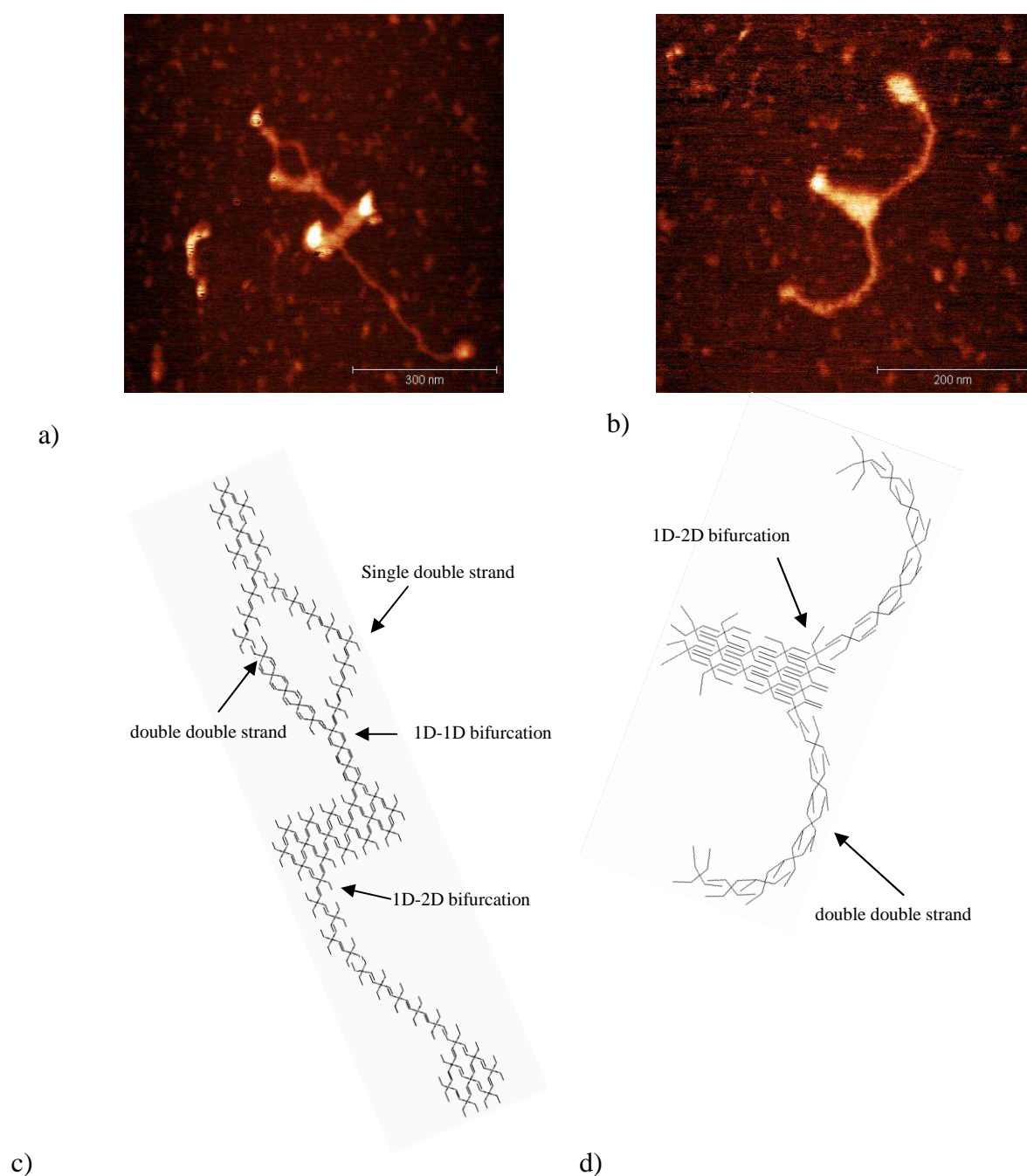

a)

b)

c)

d)

Figure III-29. Molecular 3D model for X1 and X2 molecules hybridized in linear double double-stranded chain.

Structures in Figure III-29a and b were already discussed in section "*AFM imaging on non treated mica surface*". They are good examples because they demonstrate all types of molecular associations observed for all mixtures. Namely, the structures shown in Figure III-29 a, b contain the juxtaposition of 1D and 2D architectures with several points of bifurcation.

The sketch in Figure III-28c proposes an interpretation of the molecular assembling of the structure shown in Figure III-28a. One can see a difference in the molecular assembling between single double-stranded and double double-stranded 1D and the origin of the bifurcations. Actually, there are two types of bifurcations:

1D-1D and 1D-2D bifurcations which are points of transition from 1D single double-stranded to 1D double double-stranded structure or from 2D to one of types of 1D structure. So, the molecular structure is determined by a number of linkages between molecules in longitudinal or latitudinal direction.

Figure III-28d is an interpretation of the molecular assembling of the structure shown in Figure III-28b. This structure does not contain single double-stranded chains and thus consists of 2D and 1D structures connected between them through 1D-2D bifurcations.

Using the principle of molecular association shown in the Figures 28c and d, it is possible to explain molecular assembling for all the other DNA-based mixtures. Resulting architectures depend on the number of connections involved in the interaction between molecules.

This number of intermolecular connections is also strongly dependent on the chemical properties of the substrate and the environment (air, Tris and HEPES).

III - References

[1] Watson, J. D.; Crick, F. H. C. Nature 1953, 171, 737-738.

[2] N.C. Seeman, J. Theor. Biol. 99 (2) (1982) 237–247.

[3] W.M. Shih, J.D. Quispe, G.F. Joyce, Nature 427 (2004) 618–621.

[4] P.W.K. Rothemund, Nature 440 (2006) 297–302.

[5] F. Mathieu, S. Liao, J. Kopatsch, T. Wang, C. Mao, N.C. Seeman, Nano Lett. 5 (4) (2005) 661–665.

[6] S.H.Park, R. Barish, H. Li, J.H. Reif, G. Finkelstein, H. Yan, T.H. LaBean, Nano Lett. 5 (4) (2005) 693–696.

[7] E. Winfree, F. Liu, L.A. Wenzler, N.C. Seeman, Nature 394 (1998) 539–544.

[8] T.H. LaBean, H. Yan, J. Kopatsch, F. Liu, E. Winfree, J.H. Reif, N.C. Seeman, J. Am. Chem. Soc. 122 (9) (2000) 1848–1860.

[9] C. Mao, T.H. LaBean, J.H. Reif, N.C. Seeman, Nature 407 (2000) 493–496.

[10] H. Yan, T.H. LaBean, L. Feng, J.H. Reif, Proc. Natl Acad. Sci. U. S. A 100 (4) (2003) 8103–8108.

[11] Y. Zhang, N.C. Seeman, J. Am. Chem. Soc. 116 (5) (1994) 1661–1669.

[12] R.P. Goodman, I.A.T. Schaap, C.F. Tardin, C.M. Erben, R.M. Berry, C.F. Schmidt, A.J. Turberfield, Science 310 (2005) 1661–1665.

[13] C.M. Erben, R.P. Goodman, A.J. Turberfield, J. Am. Chem. Soc. 129 (22) (2007) 6992–6993.

[14] a) X.D. Sun, I.S. Lee, 2 (2): 66-72, 2006. b) Um SH, Lee JB, Kwon SY, Li Y, Luo D. Nat Protoc 2006, 1:995–1000.

[15] C. Lin, Y. Liu, H. Yan, Nano Lett. 7 (2) (2007) 507–512.

[16] Winfree, E. In DNA Based Computing; Lipton, E. J., Baum, E. B., Eds.; Am. Math. Soc.: Providence; 1996; pp 199-219.

[17] Reif, J. H. DNA-Based Computers III; Rubin, H., Wood, D., Eds.; Providence: Am. Math. Soc. 1998; pp 217-254.

[18] Janoska, N. Karl, S. A. Saito, M. Rubin, H., Wood, D., Eds. Providence: Am. Math. Soc. 1998; pp 123-136.

[19] R.D.Barish, P.W.K.Rothemund, E.Winfree, Nano Lett. 5 (12) (2005) 2586–2592.

[20] C. Mao, T.H. LaBean, J.H. Reif, N.C. Seeman. Nature 407 (2000) 493–496.

[21] R. Chhabra, J. Sharma, Y. Liu, S. Rinker, H. Yan. Adv. Drug Delivery Reviews, 62 (6) (2010) 617-625

[22] D. Yang, M. J. Campolongo, T. N. N. Tran, R. C. H. Ruiz, J. S. Kahn, D. Luo. John Wiley & Sons, Inc. WIREs Nanomed Nanobiotechnol 2010 2 648–669

[23] Allison, D. P., P. S. Kerper, M. J. Doktycz, J. A. Spain, P. Modrich, F. W. Larimer, T. Thundat, and R. J. Warmack. 1996. Proc. Natl. Acad. Sci. USA. 93:8826–8829.

[24] van Noort, S. J., K. O. van der Werf, A. P. Eker, C. Wyman, B. G. de Grooth, N. F. van Hulst, and J. Greve. 1998. Biophys. J. 74:2840–2849.

[25] Pastré D, Piétrement O, Fusil S, Landousy F, Jeusset J, David MO, Hamon L, Le Cam E, Zozime A. Biophys J. 2003 Oct;85(4):2507-18.

[26] Lyubchenko, Y. L., Shlyakhtenko, L. S., Harrington, R. E., Oden, P. I. & Lindsay, S. M. (1993).. Proc. Natl Acad. Sci. USA, 90, 2137–2140.

[27] Lindsay, S. M., Tao, N. J., DeRose, J. A., Oden, P.I.&Lyubchenko, L.Y. (1992). Biophys. J. 61, 1570–1584.

[28] Lyubchenko L.Y., Lindsay S. M., DeRose J. A. & Thundat T. (1991). J. Vac. Sci. Technol. 9, 1288–1290.

[29] Schaper, A., Pietrasanta, L. I. & Jovin, T. M. (1993). Nucl. Acids Res. 21, 6004–6009.

[30] Rabke, C. E., Wenzler, L. A. & Beebe, T. P. J. (1994). Scanning Microsc. 8, 471–478.

[31] Bezanilla, M., B. Drake, E. Nudler, M. Kashlev, P. K. Hansma, and H. G. Hansma. 1994. Biophys. J. 67:2454–2459.

[32] Han, W., S. M. Lindsay, M. Dlakic, and R. E. Harrington. 1997. Kinked DNA. Nature. 386:563–564.

[33] Hamon, L.; Pastr_e, D.; Dupaigne, P.; Le Breton, C.; Le Cam, E.; Pi_etrement, O. Nucleic Acids Res. 2007, 35, e58.

[34] Kienberger, F.; Costa, L. T.; Zhu, R.; Kada, G.; Reithmayer, M.; Chtcheglova, L.; Rankl, C.; Pacheco, A. B.; Thalhammer, S.; Pastushenko, V.; Heckl, W. M.; Blaas, D.; Hinterdorfer, P. Biomaterials 2007, 28, 2403–2411.

[35] Pastré, D.; Hamon, L.; Mechulam, A.; Sorel, I.; Baconnais, S.; Curmi, P. A.; Le Cam, E.; Piétrement, O. Biomacromolecules 2007, 8, 3712–3717.

[36] Shlyakhtenko LS, Lushnikov AY, Li M, Lackey L, Harris RS, Lyubchenko YL. J Biol Chem. 2011 Feb 4;286(5):3387-95. Epub 2010 Dec 1.

[37] Hansma, H. G.; Laney, D. E. Biophys. J. 1996, 70, 1933–1939.

[38] Thomson, N. H.; Kasas, S.; Smith, B. L.; Hansma, H. G.; Hansma, P. K. Langmuir 1996, 12, 5905–5908.

[39] Pastr_e, D.; Hamon, L.; Landousy, F.; Sorel, I.; David, M. O.; Zozime, A.; Le Cam, E.; Pi_etrement, O. Langmuir 2006, 22, 6651–6660.

[40] Shao, Z., J. Mou, D. M. Czajkowksy, J. Yang, and J. Y. Yuan. 1996. Advances in Physics. 45:1–86.

[41] Jiao, Y., D. I. Cherny, G. Heim, T. M. Jovin, and T. E. Schaffer. 2001. J. Mol. Biol. 314:233–243.

[42] Liu, Z., Z. Li, H. Zhou, G. Wei, Y. Song, and L. Wang. 2005. Microsc Res Tech 66:179-185.

[43] Xiao, Z., Xu, M., Sagisaka, K., Fujita, D. Thin Solid Films 2003, 438-439, pp. 114-117.

[44] Hochella M. F., Jr. (1990). Rev. Mineral. 23, 87-132.

[45] T. Douglas. 2003. A bright bio-inspired future. Science 299:1192-1193.

[46] Cai L, Tabata H, Kawai T. Appl Phys Lett 2000, 77:3105–3106.

[47] Müller, K., Chang, C.C. Surface Science 1969, 14 (1), pp. 39-51.

[48] Ostendorf F, Schmitz C, Hirth S, Kuhnle A., Kolodziej J.J and Reichling M.2008,Nanotechnology, 19 305705.

[49] Dubochet, J., M. Ducommun, M. Zollinger, and E. Kellenberger. J Ultrastruct Res. 1971, 35:147-167.

[50] Lang, D., Bujard, H., Wolff, B. & Russell, D. (1967). J. Mol. Biol. 23, 163–181.

[51] Rivetti C, Guthold M, Bustamante C. J Mol Biol. 1996 Dec 20;264(5):919-32.

[52] Israelachvili, J. N. 1992. Academic Press Inc., San Diego.

[53] Pastré D, Piétrement O, Fusil S, Landousy F, Jeusset J, David MO, Hamon L, Le Cam E, Zozime A. Biophys J. 2003 Oct;85(4):2507-18.

[54] Rouzina, I., and V. A. Bloomfield. 1996. J. Phys. Chem. 100:4292–4304.

[55] Rouzina, I., and V. A. Bloomfield. 1996b. J. Phys. Chem. 100:4305–4313.

[56] Lau, A. W. C., and P. Pincus. 1999. Eur. Phys. J. B. 10:175–180.

[57] Lau, A. W. C. 2000. University of California, Santa Barbara, CA.

[58] Arenzon, J. J., J. F. Stilck, and Y. Levin. 1999. Eur. Phys. J. B. 12:79–82.

[59] Gier, S., and W. D. Johns. 2000. Applied Clay Science. 16:289–299.

[60] François Morvan, Albert Meyer, Anne Jochum, Charles Sabin, Yann Chevolot, Anne Imberty, Jean-Pierre Praly, Jean-Jacques Vasseur, Eliane Souteyrand and Sébastien Vidal. Bioconjugate Chem 18:1637 (2007) PMID 17658868

[61] John Santa Lucia Jr. (1998). Proc. Natl. Acad. Sci. USA 95 (4): 1460–5. doi:10.1073/pnas.95.4.1460. PMC 19045. PMID 9465037.

[62] M. Zuker. 3406–3415 Nucleic Acids Research, 2003, Vol. 31, No. 13

[63] Meinkoth, J. and Wahl, G. (1984). Analytical Biochemistry, 138, 267-284.

[64] T. H. Labean, H. Yan, J. Kopatsch, F. Liu, E. Winfree, J. H. Reif, N. C. Seeman. J. Am. Chem. Soc., Vol. 122, No. 9. (8 March 2000), pp. 1848-1860.

[65] G. N. Lewis, M. Randall, J. Am. Chem. Soc., 43, 1921, 1112.

General Conclusions

To summarize this work, we can see that the AFM technique is a powerful tool that offers a wide enough range of capabilities to perform direct studies of morphology of experimental samples and to obtain local information on the physical and mechanical properties of surfaces and isolated nanostructures.

In chapter I, we focussed on the technique, the different modes, the different forces involved, and the advanced approach for analysis of the images.

In an appropriate operation mode, depending on the chosen working parameters and the environment, different forces act between the tip and the sample. The interaction regime is in a large extent dependent on the sample properties that finally defines the scale of action of short-range repulsive Pauli force, long range van der Waals force and also electrostatic and magnetic forces. On the one hand, these forces may affect detectable information and thus may be undesirable, for example capillary force in the air or high viscoelastic forces on fragile biological samples. However, these forces may give additional information about the sample properties and about the regime of the tip-sample interaction. For example, the measurement of adhesion force provides information about mechanical properties of the sample. Or, in dynamic operation mode, depending on elastic properties of the sample and initial parameters (A, A_{sp}, ω_0), a bistable oscillation regime may take place where transitions between one state to another can be indicated by an inversion of phase shift.

One of the possible ways to avoid effect of capillary is to pass in liquid media. However, in this case the damping effect due to the higher viscosity of solution should be taken into account. In addition, AFM in a liquid media requires of more complex theoretical description of the tip-surface interaction forces such as the DLVO theory.

We showed by an example on a DNA chip, that information achieved in one regime of AFM operation can be successfully complemented by information obtained in another regime. This underlines the exceptional complementarity of the different modes of operation of the AFM. A clear example of this is the ability of the AFM to simultaneously detect information related to different physical properties of the sample. Especially, phase imaging is often performed together with a standard topographical imaging. Phase shift depends on working conditions and is also defined by the contribution of mechanical properties of the sample. Another example is the phase and amplitude spectroscopies, which can be realized simultaneously, in the same conditions, and thus give an idea about tip-sample interaction character even before scanning.

The experimental study of the phase and amplitude dependence on the tip–surface separation allowed to perform a quantitative description of the dissipative processes during AFM mapping of the DNA chip. It also made possible to characterize the tip-sample interaction regime by controlling the cantilever motion. In the other hand, it was shown that nonlinear dynamics of the cantilever is responsible of noise on the images and contrast artefacts.

Calculated from phase shifts data, the dissipation energy presents an evolution while changing of the A/A_0 ratio. This allows to establish the influence of the initial parameters (A, A_{sp}, ω_0) on the quality of the resulting images. However, in our case, this information is not sufficient to give of clear idea about the interaction regime of the tip with DNA molecule.

For this reason, we calculated the derivative of the experimental dissipation energy curve which offers unambiguous identification of the tip-sample interaction regime. For our concrete experimental system, this approach shows that dynamic dissipation processes on the DNA chip are mostly defined by a viscoelastic tip-sample interaction.

Because the maximum in the energy dissipation curves is about 30eV per cycle, material contrast may be achieved without introducing irreversible tip–surface modifications. Consequently, knowing the dynamics of the dissipation processes during the DNA-chip mapping, it becomes possible to predict appropriate experimental conditions in order to prevent damage of fragile DNA molecules.

This experimental study clearly demonstrated that the choice of the most adapted AFM operation mode added to a careful adjustment of experimental parameters can not only improve image quality, but also may significantly affect the correctness of measured quantities.

Moreover, after imaging in good conditions, it is also really important to interpret all the information given by the images. In this work, the spectral PSD-method for statistical analysis of the AFM images is proposed ; it gives a more complete description of the morphology in comparison with the conventional method of analysis. Different models are described in details in chapter I and used to characterize our study in chapter II.

In Chapter II, we studied the pentacene thickness-driven growth performed on two polymeric substrates, parylene and benzocyclobutene (BCB). AFM was used because we wanted to characterize the surface of pentacene at a nanometric scale, for small deposit thicknesses (at a submicronic scale). Our objective was to establish a link between the substrate nature, the morphology of the pentacene towards the deposited equivalent thickness and the mobility of the charges. On these organic materials, we showed that the AM-AFM mode is well appropriate to obtain the better resolution.

To understand the morphology for thicknesses of more than 30nm, the first step of the growth was studied, when equivalent thicknesses of 6 nm, 10nm and 15nm were deposited.

The morphology of the pentacene is different on the two substrates and to analyse in details these difference we used grain analysis, conventional and the PSD methode presented in Chapter I. The grain size distribution showed its nonlinear evolution versus the equivalent film thickness. Namely, for the range of the film thickness from 15nm to 60nm, the largest grain size was obtained for the thickness of 30nm on both substrates, around 500 nm for pentacene on parylene and 860 nm for pentacene on BCB. At the same time, the shape of the grains remained unchangeable for all thicknesses: a bulk-like grains on the parylene and a pyramid-like ones on the BCB. Therefore, the conventional methods of analysis showed the existence of a

certain critical thickness of the pentacene at 30nm, but for a more thorough study we had to apply additional methods of analysis.

Conventional methods of surface analysis gave information on sample properties determined by the distribution of heights on the surface. However, the PSD-method gave access to the surface properties in two dimensions i.e. in vertical and lateral directions. The application of this method to AFM images is possible thanks to their high spatial resolution. It allows their transformation into 2D reciprocal Fourier space and then representation in 1D graph (PSD curve). Analysis of experimental PSD-curves was performed with fractal and two nonlinear parametrical models (k-correlation and superstructural model) which provide exhaustive information not only on the accessible surface of the sample but also on its inner structural properties.

Actually, the fractal model made it possible to obtain fractal dimension of each sample, based on which it was elucidated that while deposition pentacene molecules can move more freely on the BCB than on the parylene. This information was completed by the k-correlation model which allowed us to establish mechanisms of growth of the pentacene films. According to this model, the growth of the pentacene films on parylene begins by an evaporation and condensation mechanism and evolves in a bulk diffusion mechanism for thicknesses higher than 30nm. For the pentacene on BCB, the growth begins by a viscous flow mode until a thickness of 35nm and changes in an evaporation and condensation mechanism for higher thicknesses. In addition, superstructures models give quantitative description of the lateral dimensions of the pentacene grains and their aggregates. The variation of the film thickness has caused the formation of superstructures with sizes ranging from 0.6µm to 1.1µm for pentacene on parylene from 1.3µm to 1.6 µm on BCB, where the largest sizes correspond to the thickness of 30nm. Furthermore, according to the superstructures model, variation of the size of the aggregates is not caused by variation of the size of the grains that form them but is mostly influenced by the quantity of grains in aggregates.

Evidenced by the k-correlation model, transitions at 30nm from one growth mechanism to another were already seen as peaks in the grain size distribution obtained by the superstructures model. In addition, measured by AFM spectroscopy, pentacene surface energies were the lowest at this thickness namely, for pentacene on parylene the surface energy values were 81.4 mJm^{-2} (pentacene 35nm) and 32.6 mJm^{-2} (pentacene 30nm). This change in surface energy is related to transition from orthorhombic to triclinic phase for pentacene growth on parylene. In a similar way, transition of the pentacene film polymorph occurs on BCB. Hence the growth mechanism can be described as follows: Pentacene molecules during the early stage of deposition have a tendency to stand vertically on a flat surface forming the orthorhombic crystalline structure. Further increasing of the film thickness leads to pentacene growth on gradually formed surface of grains hillsides. This causes additional inclination of pentacene molecules and as a result, the thin film phase and triclinic bulk phase are formed at higher film thicknesses.

Therefore, AFM imaging together with AFM spectroscopy and spectral methods of AFM image analysis allowed us to predict the relationship between morphology, molecular structure and growths mechanisms of pentacene thin films deposited on parylene and BCB. In addition, performed electrical

measurements on the pentacene based OFETs made it possible to relate theoretically predicted pentacene polymorph properties to its electrical performances. Namely, the best electrical performances were obtained for pentacene thickness of 30nm, which corresponds to the thickness of the film with the largest grain size.

Chapter III was devoted to the study of structure assemblies of X- and Y-shaped DNA-mixtures.

Our objective was to reveal their ability to be arranged in different structures under ambient conditions in air and in liquid media. After a brief description of the DNA arrangement in literature, the advantage of the mica surface as a substrate, the X and Y structures designed by our collaborators (F. Morvan et al Institut des Biomolécules Max Mousseron, UMR 5247, Universite de Montpellier 2) were presented and described in details.

The effect of the mica pre-treatment by Ni^{2+} ions was observed. The Ni^{2+} cations contribute to a strong interaction between DNA and the mica surface. The high affinity of the Ni^{2+} with the mica surface is explained by a high enthalpy of hydration in comparison with the Mg^{2+} which has a very close ionic radii (0.65 Å), but a enthalpy of hydration smaller than for Ni^{2+}.

It was shown that it provoked a competition between Ni^{2+} and $MgCl^{2+}$ cations in DNA/mica binding. This has a direct impact on the processes of molecular organization on the solid surface.

In the air, the pretreatment of the muscovite mica surface with $NiCl^{2+}$ cations considerably changes the molecular arrangement of X1+X2 and Y1+Y2 mixtures. Structures manifest by the presence of small molecular fragments with double double-stranded structure and worm-like large macromolecules with single double-stranded structure on the non treated mica. Large macromolecules with branched 2D geometry and not worm-like structure formed on pretreated mica. However, the pre-treatment does not affect significantly the arrangement of X1+20bases molecules. Non branched structure, are obtained straight on non pretreated mica and curled or loop-like on pretreated mica.

The $NiCl^{2+}$ treatment increases the DNA/substrate interaction force and then reduces the diffusivity of species. Therefore, the molecules are remained at the same place right after deposition. In the contrary, on non-treated surface, the larger thermal motion of weakly bounded to mica DNA molecules may provoke the breaking of the intermolecular linkage which results in the formation of more simple, non branched, and worm-like structures. So, less exhaustible thermodynamical processes on the non treated mica lead to a molecular reorganization of the initial DNA assembling.

Observation in Tris and HEPES buffer solutions revealed different arrangement of the X1+X2, Y1+Y2 and X1+20bases mixtures. In the Tris solution containing only Mg^{2+} cations, all mixtures exhibit a denser architecture with well levelled surfaces in comparison with structures observed in the HEPES solution. In HEPES which contains only Ni^{2+} cations, the ionic strength is 10 times lower, that leads to a decrease of the interaction between DNA and mica. However, DNA molecules do not move away due to a partial

substitution of already adsorbed cations of Mg^{2+} by Ni^{2+} cations which have a higher affinity with mica than Mg^{2+}. Disruption of previously formed bonds between mica and DNA molecules results in the formation of less dense structures, in HEPES, than previously observed ones, in the Tris solution. However, molecules can not be well aligned on the surface due to their increased bonding with mica throw Ni^{2+} cations. The presence of layered structures (2 or more layers) observed in both solutions can be explained by the formation of salt bridges between juxtaposed molecular layers, favoured by Mg^{2+} cations in Tris and by Ni^{2+} cations in HEPES.

The AFM study of the X1+X2, Y1+Y2 and X1+20bases mixtures in air and in liquid, made it possible to establish their molecular assembling in the native Tris solution and explore how it is influenced by changing the environment of observation while conserving initial conditions of adsorption. According to our results, we can conclude that both liquids favour a 2D organisation of the DNA-based mixtures and that isolated filaments, sometimes worm-like wired structures, are only present in air. It was elucidated that in air, DNA-based networks are not stable and the few that have been observed remain in a dendritic structure on treated surface or a linear macromolecule on fresh mica.

Annexe I. Surface energy measurements by sessile drop technique

The surface energy γ is defined as the reversible work required to form a unit area of new surface of the material [1]. For two plane surfaces of different materials separated by an interface the work of adhesion W_0 is the reversible work required to create two new surfaces across a unit area of this interface.

$$W_0 = \gamma_1 + \gamma_2 - \gamma_{12}$$

where γ_1 and γ_2 are surface energies of two materials and γ_{12} is the interfacial energy e.g. the additional energy of interaction between these materials.

The surface energy can be determined by the contact angle method [2]. This method consists in using a liquid droplet deposited on a flat solid surface in air. Once the droplet deposited, two distinct equilibrium states are possible: partial or complete wetting. When the liquid drop spreads on the solid surface, it results in a low value of contact angle, which is typical for a high wettability of the surface. On the contrary, if the deposited drop adopts a spherical shape, the contact angle becomes higher, indicating a low wettability of the surface. If pure water is used as a working liquid, the solid surface with the high/low wettability can be interpreted as a hydrophilic/hydrophobic surface, respectively. So, the contact angle is a direct measurement of the liquid ability to spread on a surface.

The measured contact angle is the angle between the tangent line drawn at the edge of the droplet, prolonged down to the surface, and the surface plane (as shown in Figure 1). The final droplet shape is governed by the surface tension given by the equilibrium state of the three interacting phases: solid, liquid and gas (as sketched in Figure1).
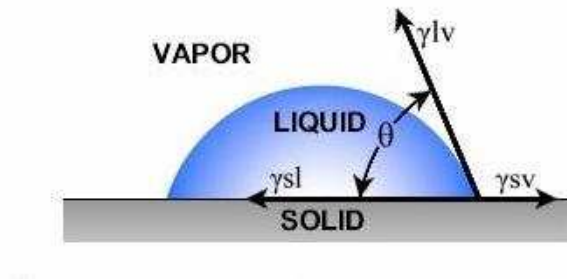

Figure 1. Scheme of the contact angle measurements

The contact angle is related to the surface energy and can be expressed by the Young's equation as follows:

$$\gamma_{lv} \cos\theta = \gamma_{sv} - \gamma_{sl}$$

where γ_{lv}, γ_{sv}, γ_{sl} are the interfacial tensions between, liquid and vapor, solid and vapor, and solid and liquid, respectively. θ is the contact angle measured experimentally.

Among the Young equation parameters, only the liquid/vapor component γ_{lv} and the contact angle θ can be determined experimentally. To calculate the other parameters, several models were developed. The most common models are Owens & Wendt and Good & Van Oss models [3, 4].

According to the *Owens & Wendt* model [3] the surface energy is described as:

$$\gamma_S = \gamma_S^d + \gamma_S^p$$

where:

- γ_S^d is the dispersive component of γ_{sv} (Lifshitz-Van der Vaals interactions)

- γ_S^p is the polar (non dispersive) component of γ_{sv} (Lewis acid base)

The relation between the contact angle and the tension components is then given by:

$$\gamma_L(1 + \cos\theta) = 2\sqrt{\gamma_S^d}\sqrt{\gamma_L^d} + 2\sqrt{\gamma_S^p}\sqrt{\gamma_L^p},$$

where γ_L^d and γ_L^p are dispersive and polar components of γ_{lv} respectively.

This contact angle model requires two different liquids for the surface energy calculation. However, the approximation on non dispersive interactions is considered as the geometrical mean of γ_S^p and γ_L^p. As a result, such approximation can not predict the behaviour of polar polymers in aqueous environment.

The *Good Van Oss* model [4] considers that the surface energy can be expressed as:

$$\gamma_S = \gamma_S^d + 2\sqrt{\gamma_S^+ \gamma_S^-},$$

where

- γ_S^d is the dispersive component (Lifshitz-Van der Vaals interactions)

- γ_S^+ and γ_S^- are the polar components (Lewis acid base)

The general equation of the surface energy is given by:

$$\gamma_L(1 + \cos\theta) = 2\left(\sqrt{\gamma_S^d}\sqrt{\gamma_L^d} + \sqrt{\gamma_S^+}\sqrt{\gamma_L^-} + \sqrt{\gamma_L^+}\sqrt{\gamma_S^-}\right)$$

In this model, three different liquids with known dispersive and polar components are necessary to calculate the surface energy.
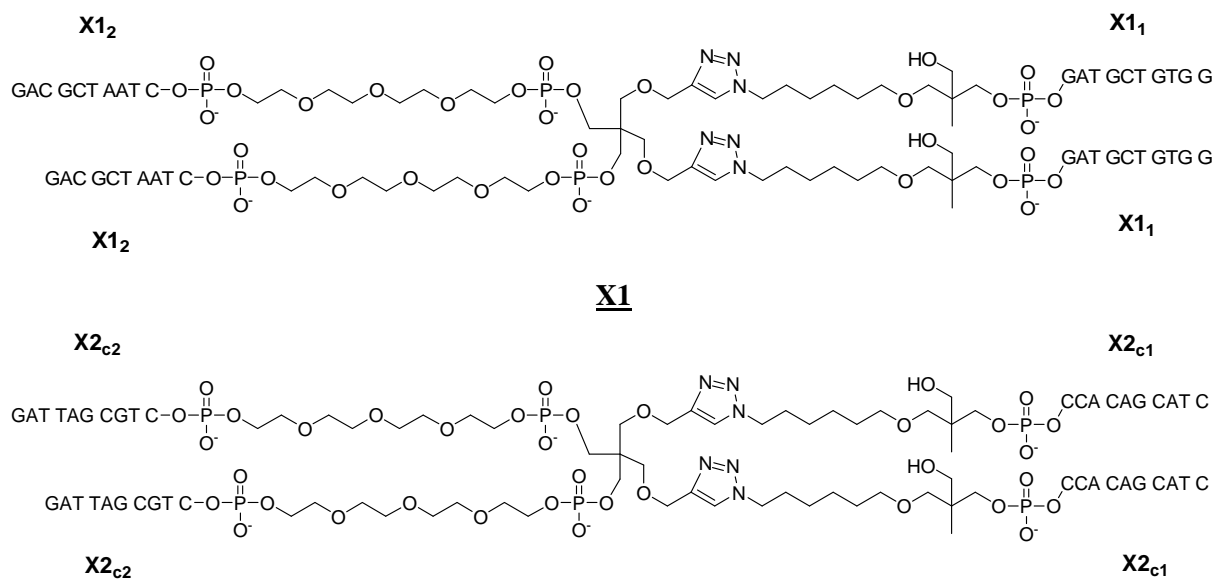
References

[1] Merril W.W., Pocius AV. Langmuir 7, (1991), 1975.
[2] Fowkes F.M. American Chemical Society: Washington, DC, 1964.
[3] D.K. Owens, R.C. Wendt – J. Appl. Polymer Sci. 13, (1979), 1741.
[4] C. J. van Oss, M. K. Chaudhury and R. J. Good. Advan. Colloid Interface Sci. 28, (1987), 35.

Annexe II. Synthesis of X and Y shaped DNA-based oligonucleotides
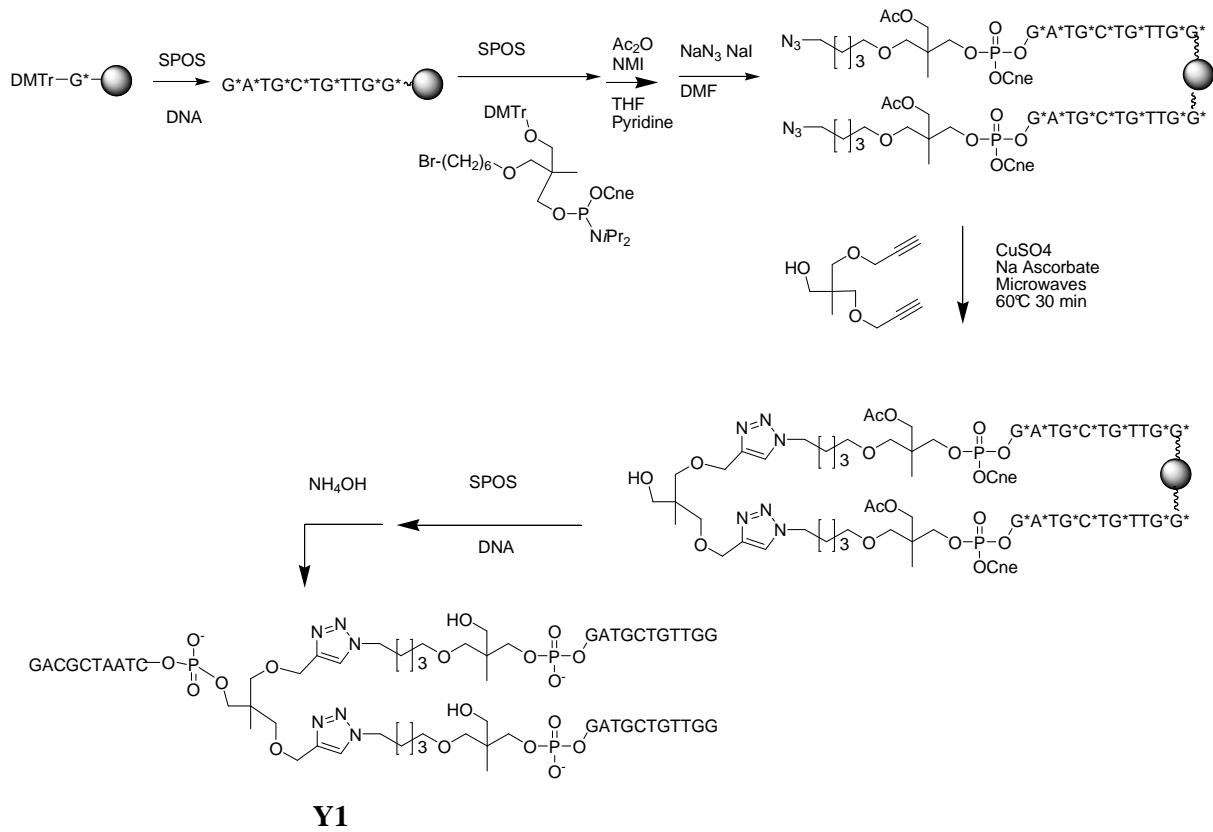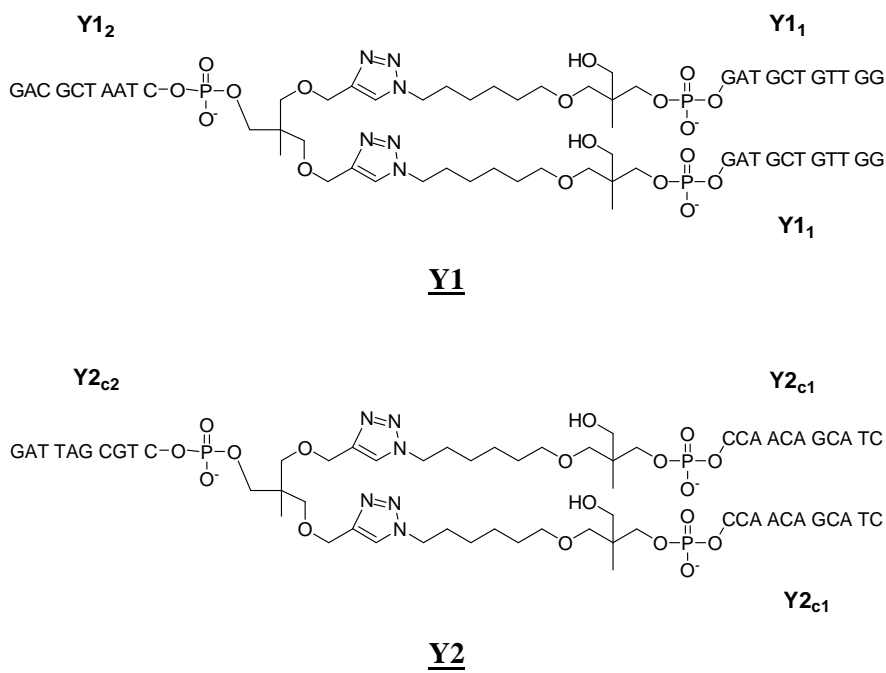
Synthesis of X-shaped molecule:

X1

Structure of molecules:

X1
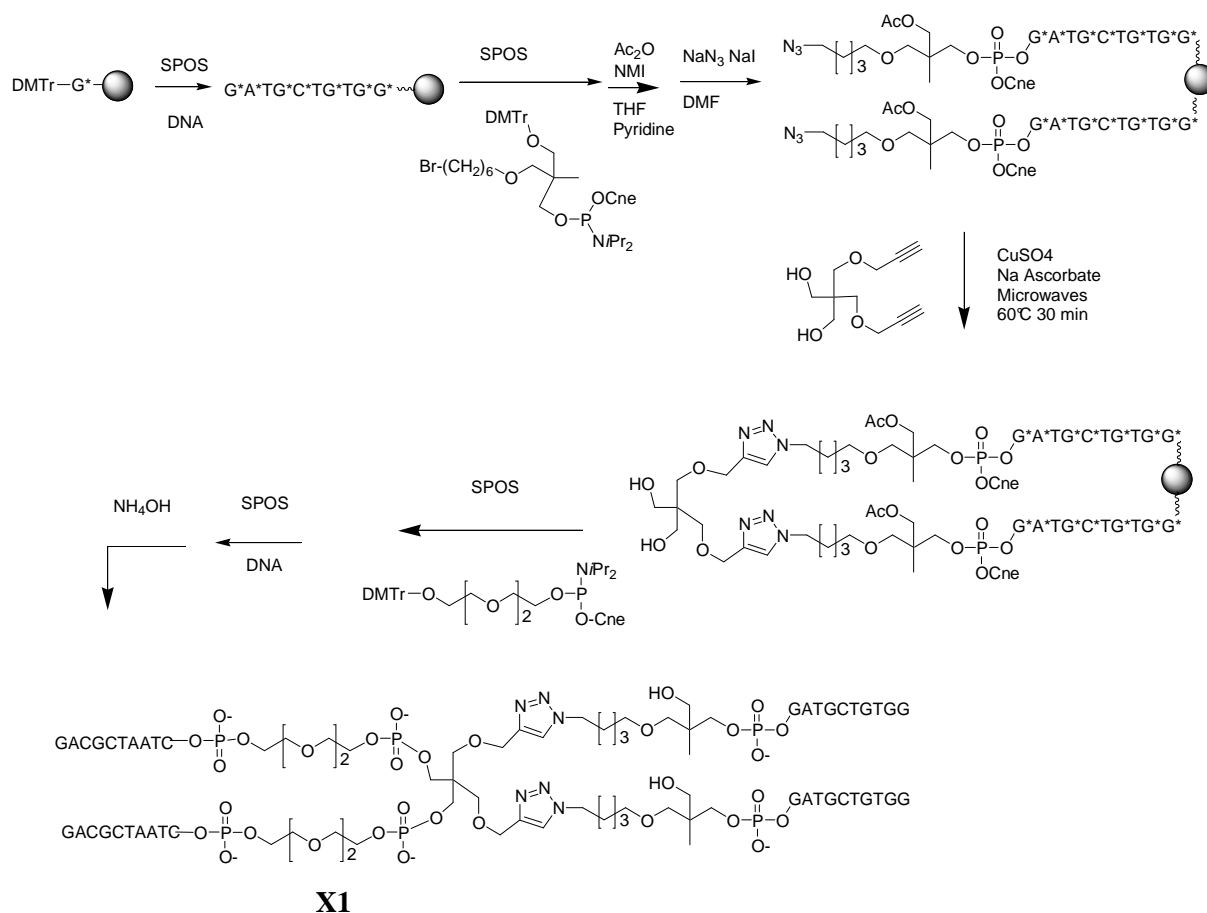
Synthesis of Y-shaped molecule:

Y1

Structure of molecules:

Y1₂

Y1₁

Y1₁

Y1

Y2_c2

Y2_c1

Y2_c1

Y2

X1 and 20bases

Structure of molecules:

X1
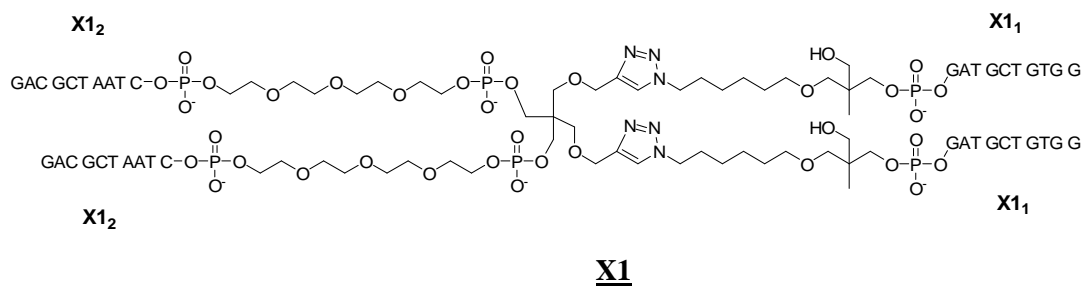
10mers$_{c2}$ 10mers$_{c1}$

CTA CGA CAC C – CTG CGA TTA G

20bases

References

[1] François Morvan. Institut des Biomolécules Max Mousseron, Département des Analogues et Constituants des Acides Nucléiques (DACAN), UMR 5247 CNRS-UM1-UM2, Universite de Montpellier 2, CC1704, Place E. Bataillon 34095 Montpellier Cedex 5, France

Annexe III. Deconvolution methods

In order to substract the effect of convolution of AFM tip with DNA molecules we firstly applied two known approaches. At first, we used a formula for a rectangular object and a spherical tip [1]:

$$D = 2\sqrt{2Rh - h^2} \ , \tag{1}$$

where D – is the real width, h – is the measured height, R – is the tip curvature.

Then, we also tried to use a formula for spherical sample and spherical tip [2]:

$$w = \sqrt{W^2 - 2RH} \ , \tag{2}$$

where w – is the real width, W – is the measured width, H – is the measured height, R – is the tip curvature.

These two approaches are efficient for samples which have rectangular or spherical geometry, and a size comparable to the size of the AFM tip, but it is not the case for DNA molecules. In our experiments, the tip curvature was larger than the diameter of a molecule (10 nm against 2 nm respectively)and the formulas (1) and (2) do not take into account an inevitable deformation of the DNAs during the AFM experiments. For example, in Fig. III-10 (c, d) one can see that the measured height depends on the width of the macromolecules (i.e. number of molecules in a macromolecule). Obviously, except a vertical deformation there is also effect of a side deformation, which is not detectable in our experiments. To solve this problem, we used the following assumption.

Since the DNA molecules form two types of 1D filaments (thin and thick), we considered that these configurations correspond to the "single-double strand" and "double-double strand" of DNA molecules. So their widths should be around 2 nm and 4 nm respectively. It is possible to obtain these values (2 and 4 nm) when it is assumed that the radius of curvature of the tip is R = 10 nm and the effect of convolution is 2R = 20 nm. This semi-empirical approach was used for the deconvolution of experimentally obtained data. So, all the widths in the cross-section images in the Chapter III present deconvoluted values.

In the contrary, the values of the measured heights correspond to those directly read from the graphs. This is because the effect of convolution takes place at the "edges" of the molecules and therefore the measured heights are the real heights (of course we must take into account the effect of deformation of the molecules by the AFM tip). For example, instead of the height of 2nm on "single-double strand" there is only 0.7 nm due to very important deformation. But on the "double-double strand" molecules it gives 1.53 nm and not 0.7 nm. So we can consider that for given experimental conditions a large tip of 10 nm causes a large enough deformation on the isolated molecules and less important on larger structures. According to the histograms of the heights of DNA arrays, we can see that the effect of the deformation is negligible.

However, it should be noted that the real geometry of the tip was unknown and we used several cantilevers during AFM experiments. Therefore the radius of curvature of the tip and its shape could be different for each selected cantilever.

References

[1] A.J. Gesquiere, T. Uwada, T. Asahi, H. Masuhara and P.F. Barbara, Single molecule spectroscopy of organic dye nanoparticles, Nano Lett 5 (2005), pp. 1321-1325.
[2] C. Y. Ngo, S. F. Yoon, D. R. Lim, V. Wong, and S. J. Chua, Appl. Phys. Lett. 93, 041912 (2008).

Abstract

This work reports the various aspects of the application of atomic force microscopy (AFM), for the characterization of organic semiconductors and DNA-based arrays, for organic electronics and biological applications. On these soft surfaces, the amplitude modulation AFM mode was chosen. This choice is argued by a study of dissipative processes, performed on a particular sample, a DNA chip. We showed the influence of experimental parameters on the topographic and phase image quality. By calculating the dissipative energy, it was shown that the dissipation on the DNA chip was mainly induced by a viscoelastic tip-sample interaction.

The AFM study of the "thickness-driven" pentacene growth was made to link the morphology to the nature of the substrate and to the electrical performance of created pentacene-based Organic Field Effect Transistor (OFET). Deposited on two polymer substrates, parylene and benzocyclobutene (BCB), pentacene has been characterized for nanoscale film thicknesses between 6 and 60nm. It has been shown that the larger grains were created for a deposited thickness of 30nm. Spectroscopic AFM mode was used as an alternative to the method of contact angles, to measure local surface energy. Decrease of surface energy is characteristic of a more ordered surface and was measured for a thickness of 30 nm of pentacene deposited on both substrates. Models of statistical analysis of spectral images, based on the Power Spectrum Distribution (PSD) have been used to explain the morphology of pentacene films. In addition, these models have provided a comprehensive description not only of the accessible surface of the sample, but also of its internal structural properties. Highlighted in the models, the critical thickness of 30 nm corresponds to a transition from the orthorhombic phase to the triclinic phase for pentacene molecules deposited on parylene. Similarly, a polymorphic transition occurs on the BCB. On OFETs, based on pentacene on BCB, the largest mobility of 3.1×10^{-2} cm²/Vs corresponds to the pentacene layer of 30nm, that shows a better ordering of the orthorhombic molecular packing in comparison with the triclinic packing.

The molecular arrangement of X and Y structures based on DNA was observed, by AFM, in air and in two buffer solutions of Tris and HEPES on a mica substrate. It was shown that the treatment of the mica by Ni^{2+} ions increases the strength of the DNA/substrate interaction and reduces the diffusivity of the molecules. In air, wired macromolecules containing one double-stranded structure are observed on untreated mica and macromolecules with a 2D geometry on pretreated mica. Onto a non-treated, the greater thermal motion of weakly bounded to mica DNA molecules leads to the rupture of intermolecular bonding and the forming structures are more simple and not branched. The organization is different in solutions of Tris and HEPES. In the Tris solution, containing Mg^{2+} cations, the arrangement leads to a well-organized 2D architecture. In the HEPES solution, containing Ni^{2+} cations, the ionic strength is 10 times lower, this leads to a breaking of the bonds previously formed between DNA and mica. However, DNA molecules are near each other due to a partial substitution of already adsorbed Mg^{2+} cations by Ni^{2+} cations of higher affinity with the mica. These results show that the two liquids promote a 2D assembly. In air, the networks are not stable and the few observed ones remain in a dendritic structure on the surface of pretreated mica and as a linear macromolecule on the untreated mica.

Résumé

Ce travail de thèse porte sur les divers aspects de l'application de la microscopie à force atomique (AFM), pour la caractérisation de semi-conducteurs organiques et de réseaux d'ADN, pour des applications en électronique organique et en biologie. Sur ces surfaces molles, le mode de fonctionnement Amplitude modulation de l'AFM a été choisi. Ce choix est argumenté par une étude des processus dissipatifs, réalisée sur un échantillon particulier, une puce à ADN. Nous avons montré l'influence des paramètres expérimentaux d'amplitude sur la qualité des images topographique et de phase. A partir du calcul de l'énergie dissipative, il a été montré que la dissipation sur la puce ADN était principalement induite par une interaction pointe-échantillon de type viscoélastique.

L'étude par AFM de la croissance "thickness-driven" du pentacène a été réalisée afin de relier sa morphologie à la nature du substrat et aux performances électriques pour la réalisation de transistors organiques à effet de champ, OFET (Organic Field Effect Transistor). Déposé sur deux substrats de polymères, le parylène et le benzocyclobutène (BCB), le pentacène a été caractérisé à l'échelle nanométrique pour des épaisseurs de film entre 6 et 60nm. Il a été démontré que les grains créés par le dépôt étaient les plus étendus pour une épaisseur déposée de 30nm. La spectroscopie AFM en mode contact a été utilisée, comme une alternative à la méthode des angles de contact, pour mesurer localement l'énergie de surface. Une énergie de surface minimale caractéristique d'une surface mieux ordonnée a été mesurée pour l'épaisseur de pentacène déposée de 30nm pour les deux substrats. Des méthodes spectrales d'analyse statistique d'images, à base de PSD (Power Spectrum Density), ont été utilisées pour expliquer la morphologie des films de pentacène. En outre, ces modèles ont fourni une description exhaustive non seulement de la surface accessible de l'échantillon, mais aussi de ses propriétés structurales intérieures. Mise en évidence dans les modèles, cette épaisseur critique de 30 nm correspond à une transition de la phase orthorhombique à la phase triclinique pour les molécules de pentacène déposées sur parylène. De même, une transition polymorphique se produit sur le BCB. Sur des OFET créés à base de pentacène sur BCB, la mobilité la plus importante de 3.1×10^{-2} cm²/Vs correspond à la couche de pentacène de 30nm, ce qui montre l'avantage de l' moléculaire orthorhombique en comparaison du triclinique.

L'assemblage moléculaire de structures en X et en Y à base d'ADN a été observé par AFM à l'air et dans deux solutions buffer de Tris et HEPES sur un substrat de mica. Il a été montré que le traitement du mica par des ions Ni^{2+} augmente la force d'interaction ADN/substrat et réduit la diffusivité des molécules. A l'air, des macromolécules filaires contenant une seule structure double brin sont observées sur le mica non traité et des macromolécules avec une géométrie 2D ramifiée, sur le mica prétraité. Sur une surface non-traitée, l'agitation thermique suffit à déplacer les molécules d'ADN faiblement liées au mica, ce qui conduit à la formation de structures plus simples 1D. L'organisation est différente dans les solutions de Tris et d'HEPES. Dans la solution de Tris, contenant des cations Mg^{2+}, les arrangements conduisent à une architecture 2D, bien organisée. Dans la solution d'HEPES, contenant des cations Ni^{2+}, la force ionique est 10 fois plus faible, qui conduit à une rupture des liaisons préalablement formées entre le mica et l'ADN. Cependant, les molécules d'ADN restent les unes près des autres en raison d'une substitution partielle des cations de Mg^{2+} déjà adsorbés par les cations de Ni^{2+} de plus grande affinité avec le mica. Ces résultats montrent que les deux liquides favorisent un assemblage 2D. Dans l'air, les réseaux ne sont pas stables et les rares qui ont été observés restent dans une structure dendritique sur la surface de mica traité ou sous forme de macromolécule linéaire sur le mica non traité.

AUTORISATION DE SOUTENANCE

Vu les dispositions de l'arrêté du 7 août 2006,

Vu la demande des Directeurs de Thèse

Madame M. PHANER-GOUTORBE et Monsieur V. SKRYSHEVSKYY

et les rapports de

Monsieur P. LECLERE
Directeur de Recherche - F.R.S. - F.N.R.S. Research Associate - Service de Chimie des Matériaux
Nouveaux - Centre de Recherche en Electronique et Photonique Moléculaires
Centre d'Innovation et de Recherche en Matériaux Polymères (CIRMAP) - Université de Mons
20, Place du Parc - 7000 MONS - Belgique

et de

Monsieur C. MOSKALENKO
Maître de Conférences HDR - Laboratoire de Physique - Ecole Normale Supérieure de Lyon
46 allée d'Italie - 69364 LYON cedex 7

Monsieur IAZYKOV Maksym

est autorisé à soutenir une thèse pour l'obtention du grade de **DOCTEUR**

Ecole doctorale MATERIAUX

Fait à Ecully, le 7 juin 2011

P/Le Directeur de l'E.C.L.
La Directrice des Etudes

M.A. GALLAND